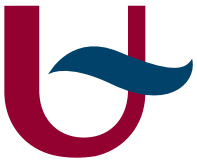

UNIVERSITEIT ANTWERPEN

Faculteit Wetenschappen

Departement Fysica

Vortex Structure and Critical Parameters in Superconducting Thin Films with Arrays of Pinning Centers

Proefschrift voorgelegd tot het behalen
van de graad van doctor in de wetenschappen
aan de Universiteit Antwerpen te verdedigen door

Golibjon Berdiyorov

Promotor: Prof. dr. F. M. Peeters
Co-promotor: Dr. M. V. Milošević

Antwerpen 2007

Contents

1

Introduction

Superconducting materials, which exhibit two characteristic properties, namely zero electrical resistance and perfect diamagnetism, are very important materials in the research field of solid state physics. However, the existence of superconductivity is restricted by three main parameters: the critical temperature T_c, the critical current I_c and the critical magnetic field H_c. During the last decades, a great deal of effort was directed towards an enhancement of these critical parameters because they are detrimental for technological applications of superconductors. A particular breakthrough was the discovery of high temperature superconductors in 1986. In addition, artificial pinning centers introduced by heavy ion irradiation have been shown to substantially increase the critical current. However, these defects are randomly distributed and have different pinning energies, causing a non-uniform dynamic behavior in the superconductor. Thus, a reduction of the latter topological and energetic dispersion is needed, which has been achieved over the last decade following advances in electron beam lithography, which allows to fabricate nanoscale artificial patterns on scales comparable to the coherence length ξ or magnetic penetration depth λ. These patterned superconducting samples exhibit a very different resistive and magnetic behavior. The introduction of periodic arrays of artificial pinning centers leads to shifts of the $T_c(H)$ phase boundary towards higher temperatures compared to non-patterned films. The presence of these

pinning sites gives rise to matching effects when the vortex lattice is commensurate with the array of pinning sites, which leads to a considerable increase of the critical current of superconductors.

The main objective of this thesis is to study the ***vortex structures and the critical parameters of superconducting thin films with periodic arrays of antidots and blind holes***. We also consider finite size ***mesoscopic superconducting samples*** where vortex structures are mainly defined by the geometry of the samples. The outline of the thesis is as follows:

Chapter 1 starts with a brief overview of the history of superconductivity. The derivation of the Ginzburg-Landau (GL) equations is given which are the main equations in the theoretical framework of this thesis. Magnetic properties of type-I and type-II superconductors are given, where in the latter case magnetic fluxes can penetrate in the form of quantized flux lines (vortices) and form the Abrikosov vortex state. We also discuss the pinning mechanism of vortices that prevent dissipation in samples. The possibility of increasing the critical current is shown using these pinning mechanisms. Finally we discuss the effect of the finite thickness of the films on our results.

Chapter 2 presents the results on the ***surface barrier for flux entry and exit*** in mesoscopic superconducting samples. The shape and the height of the surface barrier is investigated for different sizes of the samples and for different GL parameter κ. The results are compared with the ones obtained within the London theory.

Chapter 3 is devoted to the study the ***superconducting state and phase boundaries of mesoscopic square samples with antidots***. The stability of different vortex states, possible degeneracies and transition between them are discussed. The influence of different stable vortex states, due to the presence of antidots, to the $H-T$ phase diagram is considered.

In **Chapter 4** we report our results on the different ***vortex structures and the critical parameters of superconducting thin films containing a periodic array of antidots***. We construct the equilibrium structural phase diagram for the different ground-state vortex configurations as a function of size and periodicity of the antidots. Giant-vortex state, combination of giant- and multivortex states, as well as symmetry imposed ***vortex-antivortex states*** are found to be the ground state for particular geometric parameters of the sample. The antidot occupation number is calculated as a function of related parameters and comparison with existing expressions for the saturation number and with experiment is given. The stability of square pinned and unpinned (or partially pinned) triangular vortex structures are considered with lowering the pinning force. The ***enhanced critical current*** at integer and some rational matching fields is found, where the level of enhancement at given magnetic field directly depends on the stability of the vortex structures. Superconducting/normal $H-T$ phase boundary exhibits different regimes as antidots are made larger, and we transit from a plane superconducting film to a thin-wire superconducting network.

In **Chapter 5** we consider the ***interaction of a vortex with a circular hole in a superconducting film*** taking into account the ***finite size of the vortex core and its elastic properties***. Our calculations show that local compression of vortex current and their adhesion to the edge of the perforation may induce a local ***repulsive component*** to the generally ***attractive pinning force***. The resulting qualitative behavior of the interaction force therefore depends on the size of the hole and properties of the superconductor. A physical interpretation of the modulated pinning force is given and the implication of such interaction on the dynamic behavior of vortices under a dc-drive is discussed.

In **Chapter 6** we investigate the ***nucleation of superconductivity in a mesoscopic disk with a circular blind hole***, taking into account the smoothness, thickness and size of the blind hole. We show that the superconducting/normal transition field is increased and a gradual transition from a multivortex to a giant vortex state is observed with decreasing the bottom thickness of the blind holes.

Chapter 7 is devoted to the study pinning ***properties of a superconducting thin film with a square array of blind holes***. Although blind holes provide a weaker pinning potential than antidots, novel vortex structures are obtained for different size and thickness of the blind holes as the vortices pinned by the blind hole also act as the ones in the interstitial regions. Together with dimer, trimer and composite vortex states, combination of giant vortices located both in the pinning centers and at the interstitial sites, as well as combination of giant vortices with multivortices were found. For large blind holes ***vortex shell structures*** appear both in the blind holes and at the interstitial sites. The evolution of shell formation towards an Abrikosov lattice inside the blind holes are studied for different number of pinned vortices. We also consider a ***superconducting film with an array of superconducting pillars*** as a geometrically and physically inverted system, where pillars will serve as anti-pinning sites. The presence of the pillars changes vortex structures in the superconducting film considerably: a transition between triangular and square vortex lattices takes place with increasing the size and height of the pillars and for larger radius of the pillars vortex shell structures are obtained.

1.1 HISTORICAL OVERVIEW OF SUPERCONDUCTIVITY

After the initial discovery of superconductivity in Hg, by Kamerlingh Onnes in 1911 [1], almost 20 years went by before research was undertaken in alloys. Another 40 years would pass before organic superconductors were synthesized in the 1970s. Then, another decade would pass before superconducting cuprates were discovered in 1986, followed by fullerenes shortly after. There is a line of progression of structures from the very simple to the quite complex. At the same time, the critical temperature T_c has increased by a factor of 40 with the record T_c in cuprate perovskite; and there is a time span of 90 years between their discoveries. This seemingly slow development is governed by the general development of physics in a broader sense. Theoretical physics could not handle the many-body quantum theory necessary until the mid-1950s when the Bardeen-Cooper-Schrieffer (BCS) theory was worked out. And the mechanism developed there was one of the successful mechanisms to explain the superconductivity before superconducting cuprates were found 30 years later. Even today, more than 90 years after the initial discovery of superconductivity, there is a fierce debate about the mechanism for the high T_c cuprate superconductors. Superconductivity is still a subtle and very complex phenomenon.

Low-T_c superconductors. After superconductivity in Hg had been found, Sn and Pb followed suit. This brought T_c up from 4 K to 7 K. By the time the *Meissner effect* – the effect of magnetic field expulsion from the superconductor – was discovered [2], several more elements of the periodic table had been added to the list. Discovery of superconductivity was announced in tantalum in 1928 with T_c=4.4 K, thorium in 1929, with T_c=1.4 K, and Nb in 1930 with T_c=9.2 K.

In pure form the elements of the periodic table have provided excellent materials for scientific research in superconductivity. None of these pure elements have, however, contributed to applications of superconductivity in large scale, like wires and cables for magnets. However, on a small scale, Pb and Nb have been used for advanced development of Josephson technology. For SQUIDs (Superconducting Quantum Interference Device) niobium has been the best material overall, and is widely preferred in those particular low-T_c applications.

Research on binary alloys was started already in 1928 in Leiden by de Haas and Voogd [3]. They found superconductivity in SbSn, Sb_2Sn, Cu_3Sn, and Bi_5Tl_3. They noticed that the combination of a superconducting element with a non-superconducting one increased T_c 2-3 times compared to the critical temperature of pure elements. What was even more interesting, was that the magnetic threshold for destruction of superconductivity in these materials was much higher than in any of the elements known to be superconducting at the time. After an intense period of research on binary alloys around 1930, not much happened in the materials area until early 1950s. A number of new compounds were made, with impressively high T_c and high critical fields. Throughout the

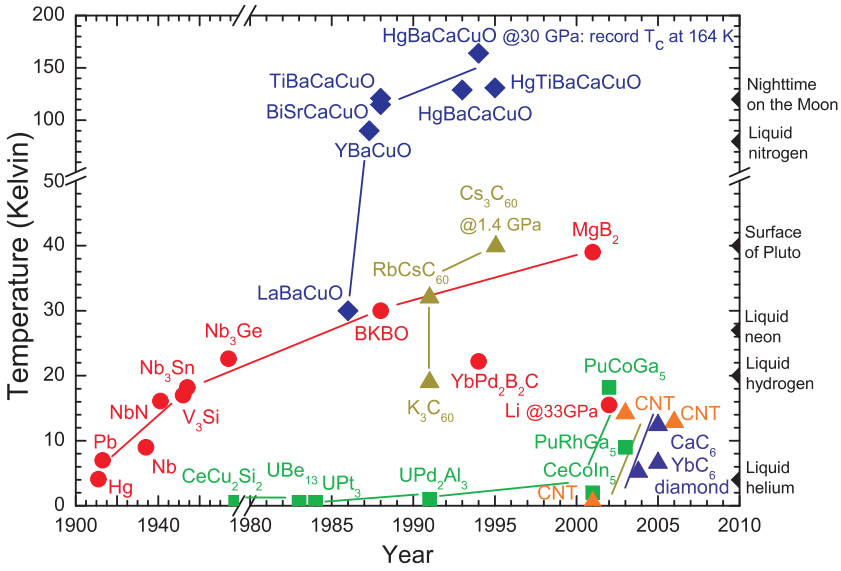

Fig. 1.1: The observed superconducting transition temperature (T_c) of variety of classes of superconductors as a function of time. Recent discoveries have increased the highest-observed T_c in a number of materials to unprecedented levels, such as in heavy fermion ($PuCoGa_5$), carbon nanotubes (CNTs), and graphite intercalated compounds (CaC_6) (from Ref. [4]).

1950s the materials that were developed for use as superconductors include: solid solutions of NbN and NbC with T_c = 17.8 K; V_3Si with T_c = 17 K; Nb_3Sn with T_c =18 K; NbTi with T_c =9 K. Later (1973) Nb_3Ge was added to this list with the highest T_c of all, at 23.2 K, a record that lasted until 1986. The history of the development of T_c is shown in Fig. 1.1 [4].

MgB_2 superconductor. Superconductivity in MgB_2 was discovered as late as 2001 [5], with T_c at 39 K, a record by far in ordinary metallic compounds. This value of T_c is close to what has been considered the maximum possible by pairing caused by electron-phonon interaction. The main disadvantage of early MgB_2 samples is their low critical magnetic field H_{c2}. But H_{c2} can be increased up to more than 40 T in bulk and up to near 60 T in oriented thin films by Carbon doping. Due to its enhanced mechanical properties, as compared to high-T_c superconductors this material is expected to be very promising for applications.

Organic superconductors. Superconductivity in a polymer material was first found in $(Sn)_x$ in 1975. This was followed by the discovery in 1979 of superconductivity in a molecular salt, $(TMTSF)_2FF_6$ under 1.2 Gpa pressure, and with a T_c of 0.9 K [6]. Since then, a long list of organic superconductors have been synthesized. T_c of those materials remains low, although it has

increased by a factor of more than 10 since the first discovery. In this sense progress has been remarkable. In another sense it has been disappointing, since predictions had been made for room-temperature superconductivity in stacked organic structures [7]. One of the carefully studied organic superconductors are fullerene-based materials. The initial discovery was made in K_3C_{60} with $T_c = 19.3$ K [8]. Critical fields of these materials are quite high, 28 T in K_3C_{60} and 38 T in Rb_3C_{60}. The critical temperature T_c as high as 40 K was observed in 1995 for Cs_3C_{60}.

High-T_c cuprate superconductors. The breakthrough to a new era in higher superconducting transition temperature came in 1986 with the discovery of superconductivity in the $La_{2-x}(Ba,Sr)_xCuO$ compounds at about 35 K (12 K better than the highest known critical temperature at the time, for Nb_3Ge) by two scientists at the IBM Zurich laboratory, J.G. Bednorz and K.A. Müller [9]. Subsequently, shortly after it was found that replacing lanthanum with yttrium, i.e. making YBCO, raised the critical temperature to 92 K, which was important because liquid nitrogen could then be used as a refrigerant. By 1993, cuprates with a T_c of 133 K at atmospheric pressure were found ($HgBa_2Ca_2Cu_3O_8$) [10]. After this discovery further efforts to find cuprates with higher T_c failed until 2000, when a slight increase in the transition temperature was detected for fluorinated Ha-1223 samples (T_c=138 K) [11]. At present a record T_c of 164 K was obtained for HgBaCaCuO cuprates under 30 GPa pressure (see Fig. 1.1). Table 1.1 shows the critical temperature and critical field of different types of superconductors.

1.2 APPLICATION OF SUPERCONDUCTORS

Superconductor technology divides naturally into two main categories: *small scale*, usually electronic components or devices, and *large scale* where magnets and energy applications are of most importance. The most important *small scale* electronic device applications so far are based on Josephson junctions – two superconducting electrodes separated by a thin dielectric tunnel barrier. Among these, SQUIDs have reached by far the widest range of useful implementations due to its unique property as the most sensitive and versatile device for detection and measurements of magnetic flux. It owes its sensitivity to the properties of the superconducting wavefunction phase which provides the basis for both flux quantization and Josephson tunneling. The broad versatility is due to the possibility it offers for high resolution measurements of any physical quantity which can be converted into magnetic flux. This is the case with quantities like magnetic field, magnetic susceptibility, magnetic field gradient,

[1]The coherence length $\xi = \xi_{ab}$ and the penetration depth $\lambda = \lambda_{ab}$ are given in the symmetry plane (called a,b plane) of anisotropic superconductors.

Table 1.1: Properties of some superconductors.

Superconductor	T_c (K)	B_{c2} (T)	ξ (nm)	λ (nm)
Al	1.2	0.01	550	40
Nb	9.3	0.21	38	39
Sn	3.7	0.031	230	34
Pb	7.2	0.078	83	37
Nb_3Ge	23.2	39	3	90
Nb_3Sn	17.9	24	3	65
V_3Si	17	23	3	60
$PbMo_6S_8$	15.2	60	2.2	215
$LaMo_8Se_8$	11	5		
MgB_2	39	19-40	2-5	85-180
UPd_2Al_3	2.0	∼40		
UPt_3	0.46	1.9	12-14	600
K_3C_{60}	19.3	17-32	∼3	240
Rb_3C_{60}	29.6	38	∼2	
$La_{2-x}Ba_xCuO_4$[1]; x=0.2	30		3.3	290
$YBa_2Cu_3O_{7-\delta}$[1]	93	115	2.5	150
$Bi_2Sr_2Ca_2Cu_3O_{10}$[1]	110	198	2.9	
$TbBa_2Ca_2Cu_3O_9$[1]	123			173
$HgBa_2Ca_2Cu_3O_{8+\delta}$[1] at 30 GPa	164	190	1.3	130

electrical current, and voltage. The SQUID has been under continuous development and improvements during several decades (see for example Ref. [12]).

The extreme sensitivity of SQUIDs make them ideal for studies in biology. Magnetoencephalography (MEG), for example, uses measurements from an array of SQUIDs to make inferences about neural activity inside brains. Because SQUIDs can operate at acquisition rates much higher than the highest temporal frequency of interest in the signals emitted by the brain (kHz), MEG achieves good temporal resolution.

Superconductors can have a dramatic impact on selected *passive microwave device applications* because of two properties that differ greatly from those of normal metals at high frequencies. First, much lower surface resistance is available using superconductors, a fact that transforms into much lower loss and much higher Q-values in superconducting microwave system components. Second, superconductors have a practically frequency independent depth in the microwave frequency range. This has the important consequence that superconductors introduce no dispersion into a microwave device up to 1 THz frequency in low-T_c superconductors, and well above this in high-T_c superconductors due to their larger gap frequency. Superconducting passive devices may work quite well in case where normal conductor devices would function very poorly or not

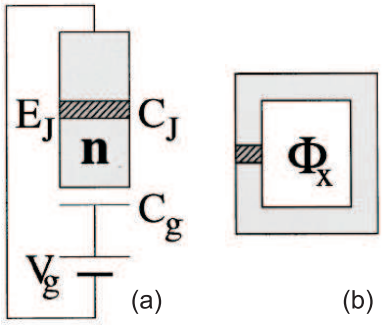

FIG. 1.2: The simplest Josephson charge qubit (a) and flux qubit (b).

at all. A normal metal component would, in many cases, have several orders of magnitude higher conductor loss than the superconducting ones. Important passive microwave device components are bandpass filters, which are becoming an essential component in mobile phone base stations. Other uses are in chirp filters which can provide improved resolution in radar images, and delay lines used in various contexts.

As a macroscopic quantum system, superconducting circuits have been proposed for *quantum computing* [13–16]. All proposed superconducting quantum circuits are based on superconducting structures containing Josephson junctions. There are two possibilities for constructing a superconducting qubit. They differ by the principle of coding the quantum information. The first approach is based on very small Josephson junctions, which are operated by maintaining coherence between individual states of electron Cooper pairs (Fig. 1.2(a)). This type of qubit is called a charge qubit. The charge states of a small superconducting island (a so-called electron box) are used as the basis states of this qubit. The second, alternative approach relies on the macroscopic quantum coherence between magnetic flux states in relatively large Josephson junction circuits (Fig. 1.2(b)). The latter qubit is known as the magnetic flux (phase) qubit. In fact, the flux qubit is based on a special realization of SQUIDs.

Large scale energy-related applications of superconductors mainly include generation, transport, transformation and storage of electrical power [4]. An high-T_c superconducting (HTS) *power cable* (Fig. 1.3) is a flat-conductor-based transmission line that carries large amounts of electrical current. Liquid nitrogen flows through the cable, cooling the HTS conductor to a zero-resistance state. The cable's most useful property is its compaction of large electrical currents into a small conductor area, i.e. high electrical currents density. Within the superconducting layer of new generation of superconducting cables, current densities are typically more than 10,000 times higher than those possible in copper.

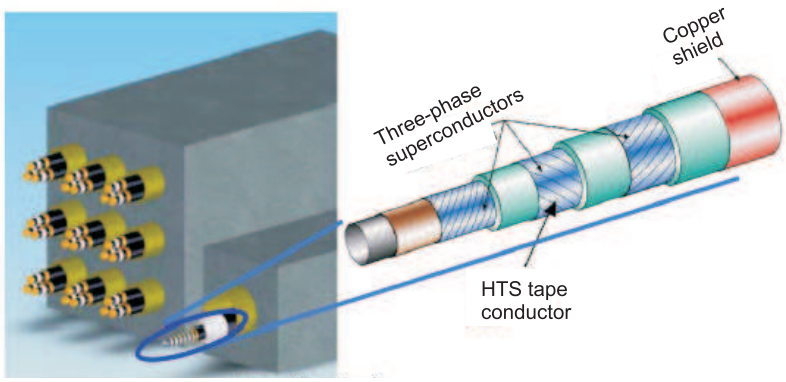

Fig. 1.3: Schematic comparison of the 3×3 duct bank of an underground copper distribution system vs. a single triaxial HTS cable operating at 13 kV and transferring 69 MVA of power (from Ref. [4]).

Superconducting magnets. Most of the low temperature superconducting (LTS) magnets are wound using conductors which are comprised of many fine filaments of a niobium-titanium (NbTi) or niobium-tin (Nb_3Sn) alloy embedded in a copper matrix, which gives mechanical stability and provides a path for the large currents in case the superconducting state is lost. These conductors have largely replaced the single filament conductors since their magnetic field more readily penetrates the fine filaments, resulting in greater stability and less diamagnetism. Another most outstanding feature of superconducting magnets is their ability to support a very high current density with a vanishingly small resistance. This characteristic permits magnets to be constructed that generate intense magnetic fields with little or no electrical power input.

LTS magnets are widely used in Resonance Imaging (MRI) Systems as the only economical way to provide the high magnetic field level of up to 3 T which is required for high resolution MRI pictures. An equally important application area of LTS magnets in the field of research is High-Energy Physics where the higher field level allows a large reduction of the radius of particle accelerator rings. Very recently the world's largest LTS magnet, called the Barrel Toroid because of its shape, was built at CERN's Large Hadron Collider (LHC) to provide a powerful magnetic field for particle detecting. LTS magnets are also essential for Fusion Research in providing the high magnetic fields to guide the plasma. For example, the "Large Helical Device" of National Institute for Fusion Science, Tokio, Japan is successfully in operation since 1998.

Although LTS magnetic systems represented an improvement over devices relying on conventional copper wire coils, their size, cooling demands and operational requirements made them expensive and technically challenging alternatives. Magnets that incorporate HTS wires offer a significant set of benefits

over older LTS devices. In a number of applications, HTS-based machines have demonstrated their reliability in uses such as magnetic separation, minesweeping, ion sources, beam switching magnet, vibrating sample magnetometry and high field insert coils. Advantages of HTS magnets stem from:

- *Simpler Cooling Systems*: Most HTS coils operate at 20-40 K compared to LTS coils that generally operate at less than 10 K. Higher operating temperatures mean that, unlike LTS coils and magnets, many HTS applications do not require actively-cooled shields. Their temperature can be controlled by simpler, standard industrial refrigeration systems.

- *Thermal Stability*: Coils and magnets operating at extremely low temperatures, such as those of LTS applications, are more vulnerable to quenching (sudden loss of superconducting properties) than HTS coils and magnets (which can operate at much higher temperatures). In addition, most LTS coils operate much closer to their critical temperature than their HTS counterparts. This means HTS coils and magnets can withstand greater temperature change without losing their superconducting properties.

- *Lower Cooling Costs*: Since LTS coils operate below 10 K, cooling costs are extremely high for any application that generates significant heat. Raising operating temperatures from the 4.2 K required by many LTS coils and magnets to the 20 K used for HTS coils and magnets cuts refrigeration costs by a factor of 10.

- *Higher Magnetic Fields*: The high upper critical fields of HTS wire can produce magnetic fields stronger than those possible with LTS wire alone. HTS inserts produce fields up to 25 Tesla when used in LTS generated background fields.

Superconducting transformers convert generation-level voltage to high transmission-level voltage, reducing the amount of energy lost in the transmission of power over long distances. Transformers are also needed to convert the voltage back to a distribution level. Small, quiet, lightweight, and efficient HTS transformers will be used primarily at substations within the utility grid. Environmentally friendly and oil-free, they will be particularly useful where transformers previously could not be sited, such as in high-density urban areas or inside buildings. Significant energy losses occur in conventional transformers as a result of the iron in the core and the copper in the windings.

HTS fault current limiters (FCL). A current limiter is designed to react to and absorb unanticipated power disturbances in the utility grid, preventing loss of power or damage to utility grid equipment. The superconducting FCL provides the same continuous protection as the conventional one, with no standby energy losses due to joule heating and no voltage drop. The superconducting FCL instantaneously limits the flow of excessive current by allowing itself

to exceed its superconducting transition temperature and switch to a purely resistive state, thus minimizing the fault current that passes through it.

HTS generators. By using superconducting wire for the field windings, losses in the rotor windings and armature bars are eliminated and the fields created in the armature by the rotor are not limited by the saturation characteristics of iron. As in the case of superconducting motors, the armatures are constructed without iron teeth, thereby removing another source of energy loss. An HTS generator will be one-third the overall volume of its conventional equivalent.

1.3 THEORY OF SUPERCONDUCTIVITY

1.3.1 London approach

More than 20 years after the discovery of superconductivity the brothers Fritz and Heinz London developed a phenomenological theory to describe the specific electrodynamic properties of superconductors [17]. They introduced the following constitutive relation complementary to the Maxwell equations:

$$\mathbf{E} = \frac{\partial}{\partial t}(\Lambda \mathbf{J}), \tag{1.1}$$

where $\Lambda = m/n_s e^2$, with m the effective mass of the electrons, n_s the density of superconducting electrons and e the electron charge. The London equation (1.1) together with the Maxwell equations lead to:

$$\nabla^2 \mathbf{h} = \frac{\mathbf{h}}{\lambda^2}, \tag{1.2}$$

where $\lambda^2 = mc^2/4\pi n_s e^2$ and c the speed of light in vacuum. This implies that a magnetic field is exponentially screened from the interior of a sample over a distance λ, thus accounting for the Meissner effect. The London equation (1.1) can be rewritten in a compact way, using the vector potential $\mathbf{A}$:

$$\mathbf{J} = -\frac{\mathbf{A}}{\Lambda c}. \tag{1.3}$$

The actual value of n_s is temperature dependent, starting from zero at $T = T_c$ and continuously increasing up to the total density of conduction electrons n when $T \to 0$. If this upper limit n is inserted in Eq. (1.3), the so called *London penetration depth* is obtained:

$$\lambda_L(0) = \left(\frac{mc^2}{4\pi n_s e^2} \right)^{1/2}. \tag{1.4}$$

Without giving a microscopic explanation of the superconducting mechanism, the London theory proved to be successful in describing the superconducting behavior of extreme type-II superconductors. However, for non-extreme

type-II superconductors, this theory fails to give sufficient accurate information about the superconducting state.

1.3.2 BCS theory

The microscopic mechanism of superconductivity was described by Bardeen, Cooper and Schrieffer in 1957 [18]. The formalism of this microscopic theory is more complicated than the one of the GL theory which will be used in this thesis. The vortex structure and the critical parameters can be precisely calculated using the GL theory and the microscopic level is not necessary for the purpose of this thesis. Therefore, the discussion of the BCS theory will be limited to the basics.

BCS theory starts from the assumption that there is an attraction between electrons, which overcome the Coulomb repulsion, and pairs of electrons, called Cooper-pairs [19], are formed. The electrons interact attractively indirectly in the following way: one electron slightly disturbs the lattice in its neighborhood. The resulting phonon interacts quickly with another electron, which takes advantage of the deformation and lowers its energy. The second electron emits a phonon by itself which interacts with the first electron and so on. It is that passing back and forth of phonons which couples the two electrons together and brings them into a lower energy state. Electrons in such a Cooper-pair are situated on the Fermi surface and have opposite momentum and opposite spin. These electrons form a cloud of Cooper-pairs which drift cooperatively through the crystal. In order to destroy one Cooper-pair, it is necessary to destroy all Cooper-pairs in a macroscopic region of the superconductor. It requires much energy and, consequently, the probability of the process is very small.

Since the electrons of a Cooper-pair have a lower energy than two separate electrons, the Fermi energy of the superconducting state may be considered to be lower than that for the non-superconducting state. The lower state is separated from the normal state by an energy gap E_g. The energy gap stabilizes the Cooper-pairs and prevents them from breaking apart. The scattering of the lattice atoms is eliminated because of the presence of the superconducting gap, which causes zero resistance.

The BCS microscopic theory gives an excellent account of the data in those cases where the energy gap E_g is constant in space. However, there are many situations in which the entire interest derives from the existence of spatial inhomogeneity. For example, in the intermediate state of type-I superconductors, one has to consider the interface where the superconducting state is joined onto the normal state. This sort of spatial inhomogeneity becomes all pervasive in the mixed state of type-II superconductors. In such situations, the fully microscopic theory becomes very difficult, and much reliance is placed on the more macroscopic Ginzburg-Landau theory, which we will consider in the next section. In 1959 Gor'kov showed that the Ginzburg-Landau theory was

just a limiting form of the BCS theory, valid near T_c and suitable to deal with spatially varying situations [20]. He showed that the order parameter Ψ can be seen as the wavefunction of the center-of-mass motion of the Cooper-pairs.

1.3.3 Ginzburg-Landau theory

In 1950, Ginzburg and Landau [21] proposed a generalization of the London theory, introducing a complex wavefunction $\Psi(r)$ ($|\Psi(r)|^2 = n_s/2$) of superconducting electrons as a complex order parameter which is zero in the normal state and has a finite value in the superconducting state. This theory is based on the theory of second-order phase transitions developed by Landau [22], according to which a phase transition of second order occurs when the state of a body changes gradually while its symmetry changes discontinuously at the transition temperature. The Gibbs[1] free energy density $\mathcal{G}_s$ in an applied magnetic field H can be expanded in a series of the form [23, 24]:

$$\mathcal{G}_s = \mathcal{G}_n + \alpha|\Psi|^2 + \frac{\beta}{2}|\Psi|^4 + \frac{1}{2m^*}\left|(-i\hbar\nabla - \frac{2e}{c}\mathbf{A})\Psi\right|^2 - \frac{(\mathbf{h}-\mathbf{H})^2}{4\pi}, \tag{1.5}$$

with $\mathcal{G}_n$ the free energy in the normal state, $m^* \approx 2m$ the effective Cooper-pair mass, $\hbar$ Planck's constant, $\mathbf{h}$ the local magnetic field. The parameters α and β have the approximate values $\alpha = \alpha_0(T - T_{c0})$ and $\beta = \beta_0$ with α_0 and β_0 are both defined as positive, so that $\alpha(T)$ vanishes at T_c and is negative below T_c. Minimizing this free energy with respect to Ψ and $\mathbf{A}$ leads to the following set of coupled nonlinear differential equations [23]:

$$\alpha\Psi + \beta|\Psi|^2\Psi + \frac{1}{2m^*}\left(-i\hbar\nabla - \frac{2e}{c}\mathbf{A}\right)^2\Psi = 0, \tag{1.6}$$

$$\mathbf{j} = -\frac{i\hbar e}{m^*}(\Psi^*\nabla\Psi - \Psi\nabla\Psi^*) - \frac{4e^2}{m^*c}|\Psi|^2\mathbf{A}, \tag{1.7}$$

where the superconducting current density $\mathbf{j}$ is given by

$$\mathbf{j} = \frac{c}{4\pi}\nabla\times\nabla\times\mathbf{A}. \tag{1.8}$$

These Ginzburg-Landau equations allow to determine the spatial variation of the order parameter and the current distributions. Note that expression (1.6) has the form of the usual quantum-mechanical Schrödinger's equation for a particle of mass $2m$, charge $2e$, energy $-\alpha$ and wavefunction $\Psi(r)$ in a potential

[1]For many calculations, making using of the Helmholtz free energy is awkward because normally quantities presumed to be constant for a body in an external magnetic field are the temperature and the external magnetic field. In the latter case, thermodynamic equilibrium is attained when another thermodynamic potential is a minimum, that is the Gibbs free energy.

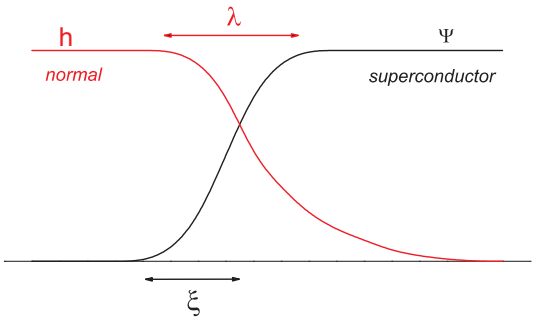

FIG. 1.4: The spatial distribution of the order parameter Ψ and the magnetic field h at the superconducting/normal surface boundary (after Ref. [23]).

$\beta|\Psi|^2$. In the limiting case of $|\Psi|$=const. Eq. (1.6) reduces to Eq. (1.2), thus the London approach appears as a result of a rigid Ψ. The phenomenological GL theory is one of the most elegant powerful concepts in physics, which was applied not only to superconductivity (see textbooks [23, 24]) but also to other phase transitions, to nonlinear dynamics, to dissipative systems with self-organizing pattern formation, and even to cosmology (for example, melting of a lattice of "cosmic strings" [25]).

The GL theory intoduces two important characteristic length scales: the *coherence length* ξ and the *penetration depth* λ. The coherence length ξ, which indicates the typical length scale over which the order parameter is allowed to vary without generating pair breaking kinetic energy (see Fig. 1.4), can be obtained from the first GL Eq. (1.6). In the case of zero applied field Eq. (1.6) in one dimension becomes

$$-\frac{\hbar^2}{2m^*}\frac{d^2\Psi}{dx^2} + \alpha(T)\Psi + \beta|\Psi|^2\Psi = 0. \tag{1.9}$$

On dividing by the parameter α we observe that an operator defined as $\frac{\hbar^2}{2m^*}\frac{d^2}{dx^2}$ in the first term of Eq. (1.9) must be dimensionless. Therefore, the quantity ξ defined by

$$\xi \equiv \left(\frac{\hbar^2}{2m^*\alpha(T)}\right)^{1/2}, \tag{1.10}$$

must have the dimension of a length. The temperature dependence of the coherence length is given as

$$\xi(T) = \xi_0(1 - T/T_{c0})^{-1/2}, \tag{1.11}$$

where the length ξ_0 is $\hbar/(2m^*\alpha_0)^{1/2}$.

The typical length scale λ over which the magnetic field can vary is the penetration depth (Fig. 1.4) and can be obtained from the second GL equation.

Neglecting the gradient of Ψ, Eq. (1.7) can be written in the following form

$$\nabla \times \mathbf{j} = -\frac{4e^2}{m^* c}|\Psi|^2 \nabla \times \mathbf{A}. \tag{1.12}$$

Using the Maxwell equation we can rewrite this as

$$\mathbf{h} + \lambda^2 \nabla \times \nabla \times \mathbf{h} = 0, \tag{1.13}$$

and the penetration depth λ is given by

$$\lambda(T) = \left(\frac{m^* c^2 \beta}{16\pi\alpha(T)e^2} \right)^{1/2}. \tag{1.14}$$

The coherence length also has the same temperature dependence as ξ

$$\lambda(T) \propto (1 - T/T_{c0})^{-1/2}. \tag{1.15}$$

The exact temperature dependence of ξ and λ depend on the purity of the materials, defined by the electron mean free path l_{el} [23, 24]

$$\xi(T) = 0.74\xi_0(1 - T/T_{c0})^{-1/2} \text{ when } l_{el} \gg \xi_0 \text{ (pure)}, \tag{1.16}$$

$$\xi(T) = 0.855\sqrt{\xi_0 l_{el}}(1 - T/T_{c0})^{-1/2} \text{ when } l_{el} \ll \xi_0 \text{ (dirty)}, \tag{1.17}$$

and

$$\lambda(T) = \frac{\lambda_L(0)}{\sqrt{2}}(1 - T/T_{c0})^{-1/2} \text{ when } l_{el} \gg \xi_0 \text{ (pure)}, \tag{1.18}$$

$$\lambda(T) = \frac{\lambda_L(0)}{\sqrt{2}}\sqrt{\frac{\xi_0}{1.33 l_{el}}}(1 - T/T_{c0})^{-1/2} \text{ when } l_{el} \ll \xi_0 \text{ (pure)}, \tag{1.19}$$

where λ_L is the specific theoretical limit value for a pure superconductor with local electrodynamics, as defined in the BCS theory.

A number of works have been devoted to find the exact temperature dependence of the coherence length and the penetration depth. For example, in recent experiments on Pb arrays of nanowires Stenuit *et al.* [26] found that the following temperature dependence of the coherence length and the penetration depth

$$\xi(T) = \xi(0)\sqrt{|1 - t^4|}/(1 - t^2), \tag{1.20}$$

$$\lambda(T) = \lambda(0)/\sqrt{|1 - t^4|}, \tag{1.21}$$

which leads to a temperature dependence of the GL parameter $\kappa = \kappa(0)/(1+t^2)$ with $t = T/T_{c0}$ and $\kappa(0) = \lambda(0)/\xi(0)$, agrees better with experiment.

Let us now establish the range of validity for the GL theory [23]. In the series expansion (1.5) of the Gibbs free energy density $\mathcal{G}_s$ in powers of $|i\hbar\nabla\Psi - (2e/c)\mathbf{A}\Psi|^2$, only the first term has been kept. This means that only slow changes of Ψ and $\mathbf{A}$ are assumed over distances comparable with the characteristic size of an inhomogeneity in the superconductor.

In the case of a clean superconductor, i.e. $l_{el} \gg \xi_0$, the GL theory is valid if $\xi(T)$, $\lambda(T) \gg \xi_0$. Since $\xi(T) \sim \xi_0(1 - T/T_c)^{-1/2}$, the quantity $\xi(T)$ always exceeds ξ_0 at $T \sim T_c$ and the first condition of validity is satisfied automatically. The second condition, $\lambda(T) \gg \xi_0$, represents the requirement that local electrodynamics is applicable, or, in other words, that the superconductor is of the London type. Since $\lambda(T) \sim \lambda(0)(1 - T/T_c)^{-1/2}$ and $\kappa \sim \lambda(0)/\xi_0$, the condition $\lambda(T) \gg \xi_0$ expresses again that temperature must be close to T_c.

In dirty superconductors ($l_{el} \ll \xi_0$), the validity interval for the GL theory is much wider. In this case, the characteristic scale of inhomogeneity is the mean free path l_{el} and the GL theory can be applied if $\xi(T)$, $\lambda(T) \gg l_{el}$. Since $\xi(T) \sim (\xi_0 l_{el})^{1/2}(1 - T/T_c)^{-1/2}$, the condition $\xi(T) \gg l_{el}$ reduces to $\xi_0/l_{el} \gg 1 - T/T_c$. Furthermore, since $\xi_0 \gg l_{el}$, this condition is much less strict than the general condition of validity for the Landau theory of the second-order phase transitions, $T_c - T \ll T_c$. Consider the second condition: $\lambda(T) \gg l_{el}$. Recalling that, for dirty superconductors, $\lambda(T) \sim \lambda(0)(\xi_0/l_{el})^{1/2}(1 - T/T_c)^{-1/2}$ and $\kappa \sim \lambda(0)/l_{el}$, it can be rewritten as $\kappa^2(\xi_0/l_{el}) \gg 1 - T/T_c$. If $\kappa \sim 1$, we find once again that it is less strict than the general condition $T_c - T \ll T_c$.

Although the GL theory has been derived only close to the superconducting/normal transition it turns out that its validity range is much larger. In particular, in mesoscopic superconductors the GL theory has been successfully used deep into the superconducting phase (see for example Refs. [26–28]). Moreover, the GL theory [27] was able to explain experimental results for superconducting samples with sizes smaller than the coherence length ξ [29].

1.4 TWO TYPES OF SUPERCONDUCTORS

A classification of superconductors can be made depending on their behavior in an external applied magnetic field. This division is based on the fact that the surface energy σ_{ns}, which is proportional to the difference $(\xi - \lambda)$, of a boundary between a normal and superconducting region has a different sign. This energy depends on the value of the GL parameter $\kappa = \lambda/\xi$ (see table 1.1) and changes sign at $\kappa = 1/\sqrt{2}$ [30]. If $\kappa < 1/\sqrt{2}$ the superconductor is classified as *type-I*. On the other hand the condition $\kappa > 1/\sqrt{2}$ (*type-II* superconductors) implies a negative surface energy, favoring the formation of superconducting-normal boundaries and the flux penetrates in small tubes (*vortices*) each one carrying a quantized amount of flux, or *superconducting flux quantum*:

$$\Phi_0 = hc/2e = 2.07 \cdot 10^{-15}\ \mathrm{Tm}^2. \tag{1.22}$$

Type-I superconducting bulk samples are in the Meissner state for applied fields up to the *thermodynamic critical field* $H_c(T)$, given by:

$$H_c(T) = \frac{\Phi_0}{2\sqrt{2}\pi\lambda(T)\xi(T)}. \tag{1.23}$$

In this perfect diamagnetic state all magnetic field is expelled from the interior of the sample. Above $H_c(T)$ superconductivity cannot be sustained and the sample turns to the normal state. Bulk type-II superconductors are in the Meissner state for fields smaller than the *first critical field* H_{c1}:

$$H_{c1}(T) = \frac{\Phi_0}{4\pi\lambda^2(T)} \ln\kappa. \tag{1.24}$$

For fields $H_{c1}(T) < H$ (*mixed state*), vortices start to penetrate the superconductor [30] until the cores overlap at H_{c2}. This *second critical field* can be expressed as,

$$H_{c2}(T) = \frac{\Phi_0}{2\pi\xi^2(T)}. \tag{1.25}$$

In the region $H_{c2} < H < H_{c3}$, superconductivity only exists at a thin layer of thickness $\xi(T)$ near the sample edges, while the inner side of the sample is in the normal state. For bulk type-II superconductors in parallel to the surface magnetic fields the *third critical field* H_{c3} is approximately equal to $H_{c3} = 1.69H_{c2}$ [24]. In obtaining the latter expression it was assumed that the medium has flat boundary and it is semi-infinite, which allows one to ignore all other surfaces. In general the coefficient for H_{c3} is geometry dependent. For example, for a thin film in a parallel field the critical field for nucleation of surface superconductivity is approximately twice the critical field for bulk superconductivity, i.e. $H_{c3} = 2H_{c2}$ [23]. If the surface of a superconductor is covered with a layer of normal metal, it causes a reduction of H_{c3} to a value very close to H_{c2}.

The different phases (Meissner, mixed and normal) can be easily identified by the equilibrium magnetization

$$\mathbf{M} = \frac{\mathbf{B} - \mathbf{H}}{4\pi}, \tag{1.26}$$

where, $\mathbf{B}$ is magnetic induction and can be obtained by averaging the local magnetic field over the sample volume. Fig. 1.5 shows the magnetization $-M$ plotted as a function of the applied field H for bulk type-I and type-II superconductors. In the Meissner state all magnetic flux is expelled ($B = 0$) from the interior of the sample and therefore $M = -H/4\pi$. For absolute values of the field $H > H_{c1}$, type-II superconductors are in the mixed state. The incoming magnetic flux causes a smooth decrease of the magnetization $|M|$ down to zero at the second critical field H_2, where superconductivity is suppressed.

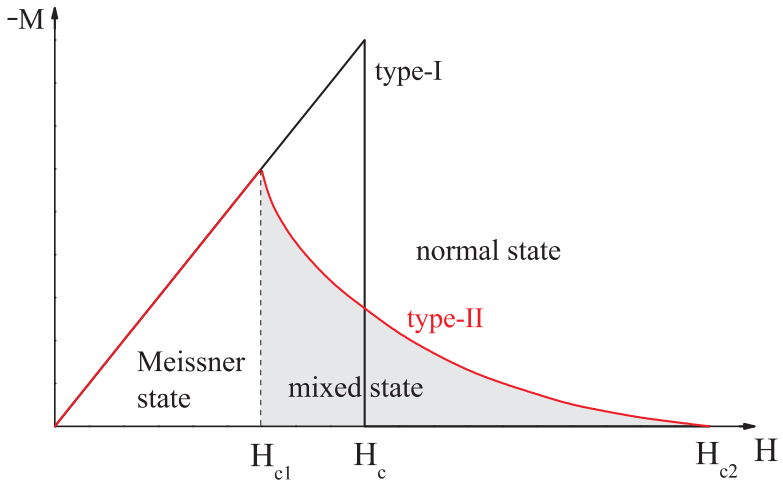

FIG. 1.5: The magnetization as a function of the applied magnetic field for bulk type-I and type-II superconductor.

1.5 VORTEX STRUCTURE IN TYPE-II SUPERCONDUCTORS

1.5.1 Fluxoid quantization

The quantization condition can be easily derived from the second GL equation (1.7), which can be written in the following form by introducing the magnitude $|\psi|$ and the phase ϕ of the order parameter:

$$\mathbf{j} = \frac{2e\hbar}{m}|\psi|^2\nabla\phi - \frac{4e^2}{mc}|\psi|^2\mathbf{A}. \tag{1.27}$$

The line integral of Eq. (1.27) around a closed circuit gives

$$\oint \mathbf{j}\cdot\mathbf{dl} = \frac{2e}{m}|\psi|^2\oint(\hbar\nabla\phi - \frac{2e}{c}\mathbf{A})\cdot\mathbf{dl}. \tag{1.28}$$

Using Stokes' theorem and the definition of the vector potential $\mathbf{A}$, $\oint \mathbf{A}\cdot\mathbf{dl} = \int(\nabla\times\mathbf{A})\cdot\mathbf{dS} = \int \mathbf{h}\cdot\mathbf{dS} = \Phi$ leads to

$$\frac{mc}{4e^2|\psi|^2}\oint \mathbf{j}\cdot\mathbf{dl} + \frac{2e}{c}\Phi = \oint \hbar\nabla\phi\cdot\mathbf{dl}. \tag{1.29}$$

Since the complex superconducting order parameter ϕ is single-valued, this requires that the phase must change by integral multiples of 2π in a closed circuit:

$$\frac{mc}{4e^2|\psi|^2}\oint \mathbf{j}\cdot\mathbf{dl} + \Phi = n\frac{hc}{2e} = n\Phi_0 \tag{1.30}$$

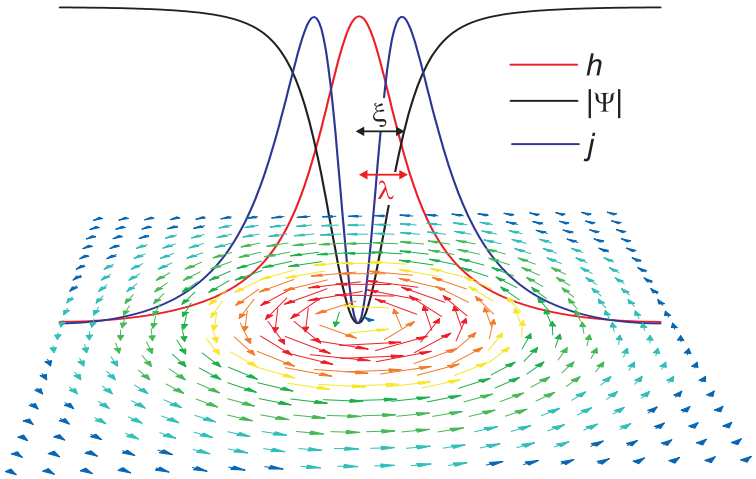

Fig. 1.6: Cross section and vector plot of the super-currents of an isolated vortex in a type-II superconductor. The modulus of the order parameter $|\Psi|$, the local magnetic field h and the the circulating screening currents j are shown as a function of the radial distance from the center of the vortex.

with Φ_0 given by Eq. (1.22). This equation expresses the condition whereby the sum of the enclosed flux Φ and the line integral involving the current density $\mathbf{j}$ is quantized.

1.5.2 Isolated vortex line

In type-II superconductors, for $H > H_{c1}$, vortices penetrate into the sample. Each of the vortices has a normal core of radius ξ where the superconducting electron density n_s falls to zero as shown in figure 1.6. The local field $h(r)$ is maximum at the center of the vortex and vanishes over a distance λ due to superconducting screening currents $j(r)$ around the core. As long as the separation between vortices is large compared to λ, there will be negligible overlap or interaction between the vortices. In this limit, each vortex can be treated as isolated. In the extreme type-II limit $\kappa = \lambda/\xi \gg 1$, $|\Psi|$ can be treated as constant, except in the vortex core. Thus, for the $r > \xi$ region, the currents and fields can be calculated by using London's equation. In order to include the normal core, the London equation (1.1) needs to be extended to account for the fluxoid quantization Eq. (1.30):

$$\frac{4\pi\lambda^2}{c}\nabla \times \mathbf{j} + \mathbf{h} = \mathbf{z}\Phi_0\delta(r), \tag{1.31}$$

where $\mathbf{z}$ is a unit vector along the vortex and $\delta(r)$ a δ-function at the location of the core. Combining Eq. (1.31) with the Maxwell equation $\nabla \times \mathbf{h} = 4\pi/c\mathbf{j}$

we obtain:

$$\lambda^2 \nabla^2 \mathbf{h} + \mathbf{h} = \mathbf{z}\Phi_0 \delta(\mathbf{r}). \tag{1.32}$$

The exact solution of this equation gives an expression for the local magnetic field as a function of the radial distance r from the vortex core [24]:

$$h(r) = \frac{\Phi_0}{2\pi\lambda^2} K_0(r/\lambda), \tag{1.33}$$

with K_0 the zero-order Bessel function. $K_0(r/\lambda)$ decreases as $\exp(-r/\lambda)$ at larger distances and diverges logarithmically as $\ln(\lambda/r)$ for $r \to 0$. By taking the derivative of Eq. (1.33), we can obtain the local current flowing around the vortex core:

$$j(r) = \frac{c\Phi_0}{4\pi^2\lambda^2} K_1(r/\lambda). \tag{1.34}$$

Here, K_1 is the Bessel function of first order which diverges as $1/r$ at short distances and decreases as $\exp(-r/\lambda)$ at large distances. The free energy per unit length of a vortex can be calculated by considering the contributions from the field and the kinetic energy of the currents, yielding

$$\epsilon_l = \left(\frac{\Phi_0}{4\pi\lambda}\right)^2 (\ln(\lambda/\xi) + \epsilon_0), \tag{1.35}$$

with ϵ_0=0.12 a small contribution coming from the vortex core. The line energy of a vortex ϵ_l is a quadratic function of Φ_0, therefore it is energetically unfavorable in homogenous superconductors to form multi-quanta vortices carrying more than one flux quantum Φ_0.

1.5.3 Interaction between vortex lines

Using the high κ approximation we can estimate the interaction energy between vortices. Consider two parallel flux lines located at $\mathbf{r_1}$ and $\mathbf{r_2}$, respectively. The

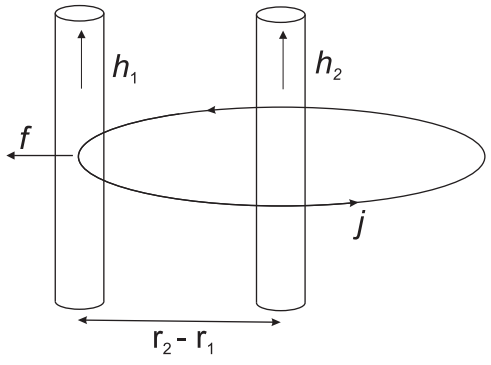

FIG. 1.7: Repulsive interaction force f between two parallel vortices.

total magnetic field will be given by:

$$\lambda^2 \nabla^2 \mathbf{h} + \mathbf{h} = \mathbf{z}\Phi_0[\delta(\mathbf{r} - \mathbf{r_1}) + \delta(\mathbf{r} - \mathbf{r_2})], \tag{1.36}$$

with solution $\mathbf{h} = \mathbf{h_1} + \mathbf{h_2}$ resulting from the superposition of the fields $\mathbf{h_1}$ and $\mathbf{h_2}$ due to the vortices (1) and (2), with $h_i(r) = \frac{\Phi_0}{2\pi\lambda^2} K_0(\frac{r-r_i}{\lambda})$. The results for the total increase in free energy per unit length can be written as the sum of the two individual line energies plus the interaction energy, given by [23]:

$$F_{12} = \frac{\Phi_0 h_1(r_2)}{4\pi} = \left(\frac{\Phi_0^2}{8\pi^2\lambda^2}\right) K_0\left(\frac{r_1 - r_2}{\lambda}\right). \tag{1.37}$$

thus,

$$\Delta F = \frac{\Phi_0}{8\pi}\left[h_1(r_1) + h_2(r_2) + h_1(r_2) + h_2(r_1)\right] = \frac{\Phi_0}{4\pi} h_1(r_1) + \frac{\Phi_0}{4\pi} h_1(r_2). \tag{1.38}$$

This interaction is repulsive in case that both vortices have the same direction and attractive when they are anti-parallel. The force per unit length (see Fig. 1.7) on an individual vortex line can be computed by taking the derivative of the interaction energy F_{12}. This results in:

$$f = j \times \frac{\Phi_0}{c}, \tag{1.39}$$

where j is given by Eq. (1.34). The repulsive interaction between vortices is very weak when the vortices are far apart. The forces between vortices are fairly short-range with the penetration depth a measure of the range, and they must be sufficiently close together, compared to λ, for their interaction to be appreciable.

1.5.4 Vortex lattices

The repulsive interaction between flux lines gives rise to a regular arrangement of vortices forming a flux line lattices, the Abrikosov vortex lattice [30]. It has been shown that a triangular array is the energetically most favorable vortex configuration [31] with a nearest neighbor distance

$$a_\triangle = 1.1(\Phi_0/H)^{1/2}. \tag{1.40}$$

The next configuration very close in energy consists of a square array of vortices (see Fig. 1.8). Here the nearest neighbor distance is given by

$$a_\square = (\Phi_0/H)^{1/2}. \tag{1.41}$$

Thus, for a given flux density in a homogeneous superconductor, $a_\triangle > a_\square$. Taking into account the repulsion of the vortices, it is reasonable that the vortex

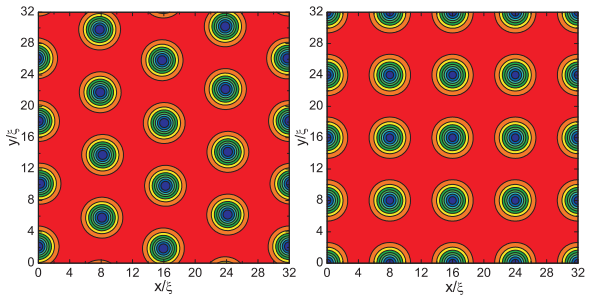

FIG. 1.8: Abrikosov vortex lattices: (a) triangular (β_A=1.16) and (b) square (β_A=1.18).

configuration with the greatest separation of the nearest neighbors would be favored. The flux line lattice was for the first time visualized by U. Essmann and H. Träuble in 1967 [32] by using magnetic decoration consisting in the evaporation of ferromagnetic powder which is attracted by the stray field of the vortices. It is important to stress that there is a small energy difference between a triangular and square flux line lattice in a homogeneous superconductor. Abrikosov [30] showed that the parameter $\beta_A = \overline{|\psi|^4}/(\overline{|\psi|^2})^2$, determining the relative stability of various possible periodic vortex configurations, turned to be 1.18 for a square lattice of Abrikosov vortices. Later on Kleiner *et al.* [31] demonstrated that the triangular vortex lattice has β_A=1.16 and therefore it is energetically the most favorable. In some materials, the symmetry of the underlying crystal structure dominates over this small energy difference, leading to the observation of square or even rhombic vortex arrays [33]. Also defects in the material may introduce sufficient inhomogeneity to destroy the regular array entirely. Abrikosov vortex lattices in superconductors can be visualized using scanning tunelling microscopy, scanning probe magnetometry, Bitter decoration, magneto-optical imaging etc. Examples of vortex images are shown in Fig. 1.9.

1.6 FLUX PINNING

An applied current J passing though a superconductor in the mixed state, will force the vortices to move transverse to the current due to the Lorentz force per unit volume:

$$f_L = \mathbf{J} \times \frac{B}{c}. \tag{1.42}$$

These vortices moving with a velocity $\mathbf{v}$ induce an electrical field

$$E = B \times \frac{\mathbf{v}}{c}, \tag{1.43}$$

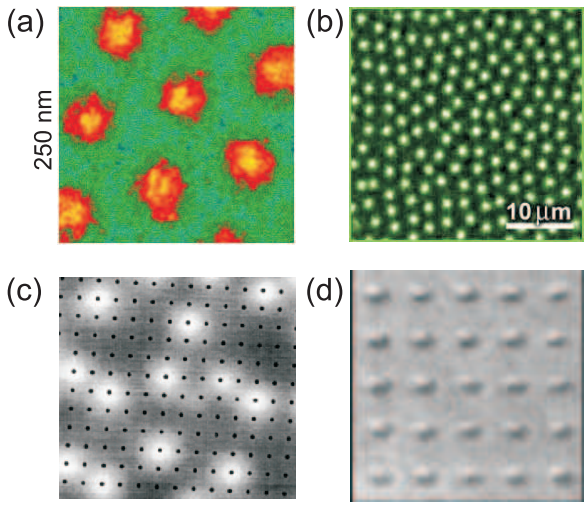

Fig. 1.9: Images of vortices: (a) scanning tunnelling microscope image of Abrikosov vortices in MgB_2 [35], (b) magneto-optical image the vortex lattice in $NbSe_2$ [36], (c) scanning Hall probe microscopy [37] and (d) Lorentz microscopy [38] images of vortices in superconducting films with arrays of artificial pinning sites.

which is parallel to J if we neglect the small contribution of the transverse Magnus force [34], i.e. the effect of the circulating current around the vortex to its path through the superconductor is neglected. The relation between J and $\mathbf{v}$ corresponds to the current-voltage or $E(J)$ characteristic from which useful information about the vortex motion can be obtained. The electric field produces a resistive voltage and therefore an energy dissipation occurs, thus limiting the potential application of superconductors. In order to sustain high currents without resistance through a superconductor, it is necessary to compensate the Lorentz force with a pinning force f_p. The critical current or depinning current density J_c is defined as the maximum current density that a superconductor can carry without resistance [23]. The total force acting on a flux line is given by [39]:

$$\mathbf{f} = \mathbf{f}_L - \mathbf{f}_p - \mathbf{f}_M - \eta\mathbf{v}, \tag{1.44}$$

with $-\eta\mathbf{v}$ a viscous damping force and $\mathbf{f}_M$ the Magnus force. The average macroscopic pinning force per unit volume is related through the critical current density by the following formula:

$$f_p = J_c H. \tag{1.45}$$

Consequently, the better the pinning the higher the critical current density J_c. The upper limit for the critical current density is the depairing current density

J_d at which the superconducting Cooper pairs are destroyed [23],

$$J_d = \frac{c}{3\sqrt{6}\pi} \frac{H_c(T)}{\lambda(T)}, \tag{1.46}$$

where c is the speed of light. Although simple theoretical estimates for optimal columnar defects give J_c/J_d ratios of $\sim$1, the J_c/J_d ratios above $\sim$0.1-0.2 have not yet been achieved [4].

1.6.1 Pinning mechanism

Although numerous realizations of vortex pinning have been proposed and analyzed, all pinning mechanisms can be divided in two main groups: core pinning and electrodynamic pinning [40].

Electromagnetic pinning is due to the perturbation of the supercurrents around vortices and of their local magnetic fields by the defects, which are always present in real superconductors or can be manufactured artificially (see below). The usual rotational symmetry of the screening currents is broken by the defects. The kinetic energy of the supercurrents can be lowered when vortices are situated on the pinning sites, resulting in an attraction between vortices and pinning centers. The important length scale here is the penetration depth λ [41].

At point defects *core pinning* is the origin of the attractive interaction between vortices and defects. A local variation of T_c or κ at the defect results in a minimization of the free energy when the vortex core is located at the position of the defect. Other examples of core pinning sites are dislocations and grain boundaries. More effective core pinning is achieved when the size of the pinning site is of order ξ or λ.

1.6.2 Artificial pinning centers

For any application of superconductors (see Refs. [4, 12]), it is essential to properly include the working temperature, the current these devices carry, and the present magnetic fields. It is well known that penetration of magnetic flux lines (i.e. vortices) into the superconductor leads to a finite resistance and consequently energy dissipation in the presence of an applied current. Ordinarily, most materials have intrinsic defects that pin the vortices, which strengthen superconductivity. To improve the functionality of superconductors, one can therefore manufacture pinning centres artificially, using e.g. heavy-ions irradiation [42, 43]. However, these defects are randomly distributed and have different pinning energies [44], causing a non-uniform dynamic behaviour across the device. Thus, a reduction of the latter topological and energetic dispersion is needed, which has been achieved over the last decade following advances in

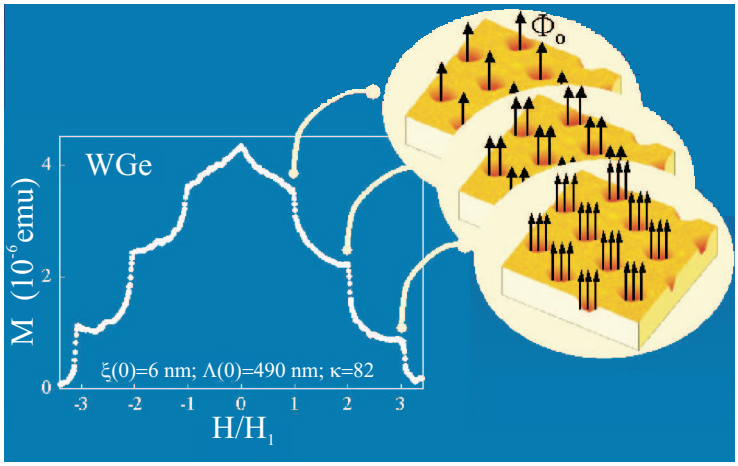

Fig. 1.10: The magnetization of a WGe film (thickness 60 nm) with antidot lattice (radius of the antidots is 0.17 μm and the period equals 1 μm) as a function of the magnetic field in units od the first matching field. Insets show the image of the sample and stable vortex configurations at the matching fields (from Ref. [46]).

lithography. Modern fabrication techniques allowed building of artificial pinning centres (e.g. antidots [45–50], or magnetic dots [51–55]) on nano-scale, with precise optimization of their size and arrangement.

Artificial pinning centers arranged periodically gives rise to commensurability phenomena between the vortex lattice and the periodic pinning potential. The stable vortex configurations, reproducing the symmetry of the pinning array, give rise to local enhancement of the magnetization $M(H)$ and the critical current $j_c(H)$ (see Fig. 1.10). These pronounced maxima, so-called matching features, occur at integer multiples of the first matching field $H = nH_1$, which is defined as the field at which the density of vortices equals the density of pinning sites. Furthermore, also rational multiples of the first matching field ($H_{p/q}$, p and q integers) can produce a reduced mobility of the vortex lattice. Important to mention is that matching effects are typically observed at temperatures close to T_c. On the one hand, this can be attributed to the divergence of $\lambda(T)$ at temperatures close to T_c, leading to a strong vortex-vortex interaction. On the other hand, commensurability features due to the periodic pinning array are progressively masked by the intrinsic pinning as temperature is decreased.

The first observation of the matching phenomena in a periodic pinning potential was reported by Daldini *et al.* [56]. They studied the interaction of the vortex lattice with a one-dimensional periodic thickness modulation of an Al film and found peaks in the critical current density at well-defined field values. A few years later experiments on two-dimensional arrays of holes were

reported [57, 58]. Later on square and triangular arrays of pinning centers were widely studied [46–48, 59–62]. In these systems, the flux line lattice configurations for different fields have been directly visualized by Lorentz microscopy [38], magnetic force microscopy [63], scanning Hall probe microscopy [64–66], and Bitter decoration [67].

An important intrinsic property of an artificial array of pinning sites is the maximum number of flux quanta that can be trapped inside a pinning center. This so called saturation number n_s depends on the ration between the size of the pinning site and the coherence length [68–70]. For fields $H > n_s H_1$, incoming vortices will no longer sit at the pinning centers, but instead they will occupy interstitial positions, in between the holes. These interstitial vortices are much more mobile than vortices trapped into the pinning sites, thus resulting in a sharp decrease of the critical current. However, as we will show in the Chapter 4 of the thesis, this composite vortex lattice containing a mixture of interstitial vortices and vortices trapped by the antidots, can still be stable. This stability is due to the strong repulsion between interstitials and vortices inside the saturated antidots.

As mentioned above, periodic arrays of pinning centers enhance the critical current whenever the density of vortices matches the underlying pining landscape. However, these peaks in the critical current decrease quickly for applied fields away from the matching fields, especially for larger separation of the pinning centers. Moreover, at high temperatures those commensurability

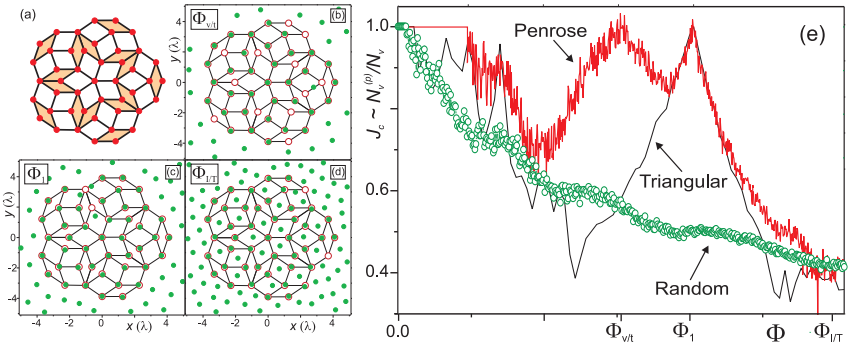

FIG. 1.11: (a) An example of a fivefold Penrose lattice, consisting of thick and thin rhombuses. (b-d) The location of vortices (green dots) and the Penrose lattice of pinning sites (red open circles connected by black lines) for (b) the flux $\Phi = 0.757\Phi_1$ (vortices occupy all the pinning sites except those in one of the two vertices of each thin rhombus), (c) $\Phi = \Phi_1$ (all the pinning sites are occupied by the vortices) and (d) $\Phi = 1.482\Phi_1$ (vortices occupy both the pinning sites and the interstitial positions inside each thick rhombus). (e) The critical current for Penrose lattice (red line), for triangular lattice (black line) and for random pinning arrays (green circles) (from Ref. [71]).

effects occur only in a very narrow window of fields. One way to circumvent these difficulties is the use of quasiperiodic arrays of pinning sites with high degree of order. An example of such a system is a superconductor with arrays of pinning centers placed on the nodes of a fivefold Penrose lattice [71] (Fig. 1.11(a)). Such a Penrose lattice has many periodicities and each period provides stable vortex configurations. Examples of such vortex lattices are shown in Figs. 1.11(b-d). The proliferation of matching peaks associated with the local symmetry of the underlying pinning arrays give rise to a wide field range of enhanced critical current. A comparison of the critical current for the Penrose lattice with the ones for triangular and random pinning arrays is shown in Fig. 1.11(e). It is seen from this figure that the Penrose lattice leads to a very broad enhancement of the critical current compared to the triangular and random arrays of pinning centers. These theoretical predictions for the critical current enhancement using the quasiperiodic Penrose lattice were recently confirmed experimentally [72].

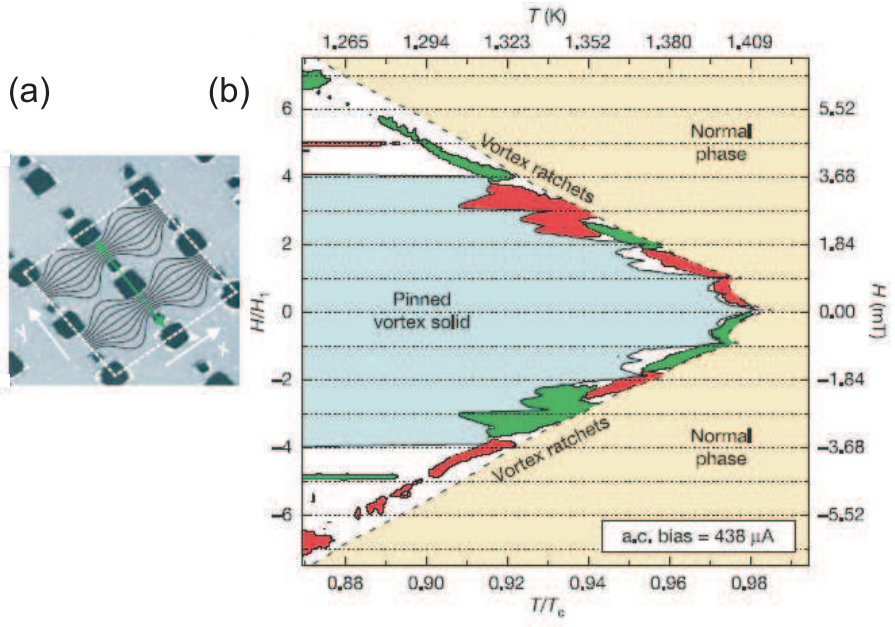

Fig. 1.12: (a) Atomic force micrograph of a superconducting film with arrays of big (a=600 nm) and small (a=300 nm) antidots (with period $W = 1.5$ μm). (b) $H - T$ dynamical phase diagram at applied ac current. The green and red areas correspond to positive and negative voltage, respectively, originated from the vortex motion (from Ref. [73]).

Many superconducting materials in nature, especially high temperature superconductors, have structural defects at different length scales (forming a pinning landscape) and in a wide variety of shapes. In the presence of such pining landscape different static and dynamic effects can be observed. As an example, a pronounced ratchet effect was observed [73, 74] in a Al superconducting film with a composite square array of pinning sites (with period $W = 1.5$ μm), with its unit cell consisting of a small ($a = 300$ nm) and a big ($a = 600$ nm) square antidot separated by a narrow superconducting wall (see Fig. 1.12(a)). Such arrangement of antidots generates a potential with one minimum with period W and two local minima per period. Fig. 1.13(a) shows such a double-well ratchet potential (green curves) and the relative characteristics energies of each pinning well (the energy of a well plus the energy of the trapped particles) and their respective occupancies for the number of particles 1 to 4. The ratchet effect in such a system strongly depends on the number of interacting particles in the potential: the inter-particle interactions captured by the ratchet potential leads to multiple drift reversals, with the drift sign alternating from positive to negative as the number of particles per ratchet period changes from odd to even. This pinning mechanism is illustrated in Fig. 1.13(b). Transport measurements in the above superconducting sample confirms this ratchet effect (see Fig. 1.12(b)).

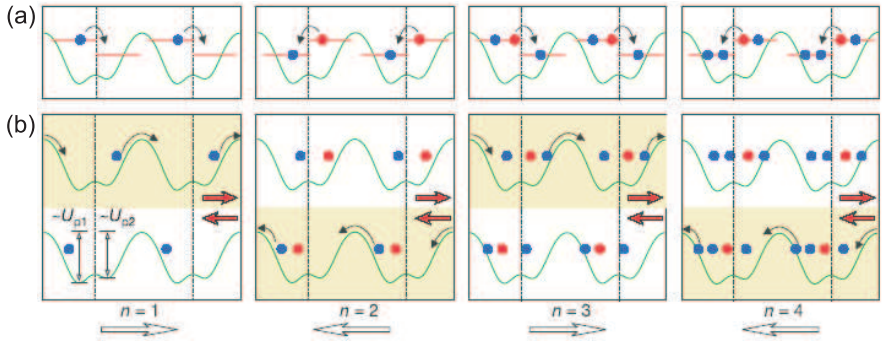

FIG. 1.13: (a) A double-well ratchet potential (green curves) and the relative characteristic energies of each pinning well and their respective occupancies. (b) Schematic demonstration of the ratchet mechanism when the chain of particles is exited by an ac force (red arrows). Yellow backgrounds highlight the motion of the chain in the corresponding drive direction, whereas white backgrounds indicate that the chain is pinned. Black arrows show the direction of motion of the whole chain (from Ref. [73]).

1.7 THIN SUPERCONDUCTING FILMS

For thin superconducting plain films with a thickness d much smaller than the penetration depth, $d \ll \lambda$, the superconducting screening currents are limited by the thickness of the film. This results in a larger effective penetration depth given by [23, 24]:

$$\lambda_{eff} \simeq \frac{2\lambda(T)^2}{d}. \tag{1.47}$$

On the other hand, the perforation leads to a renormalization of the penetration depth, where the superconducting volume corrections have to be taken into account. This can be interpreted as a consequence of a much easier flux line penetration through the holes in a perforated film in comparison with a reference film, where λ_{eff} should be used. In this case λ should be modified according to [75]:

$$\lambda_a(0) = \lambda(0)/\sqrt{1 - 2S_a/S_t}, \tag{1.48}$$

where S_a is the area occupied by the holes and S_t the total area of the superconducting film.

In thin films with the applied field perpendicular to the sample plane, vortices can be considered as strait lines, and the vortex lattice is almost two-dimensional. The smallness of the film thickness d has consequences for the individual vortex structure. The local field around a single vortex in a thin film is less effectively screened at large distances. Instead of the exponential decrease of the local magnetic field for large distances from the vortex core in bulk superconductors, in thin films the local field around a vortex decreases as $1/r^3$. On top of that, the repulsive energy between two vortices decreases like $1/r$. This means that the repulsive interaction between vortices in thin films is of longer range than in bulk superconductors.

For an infinite long cylinder, an applied field along the axis induces shielding currents flowing in the surface, with a constant value along the cylinder. This creates a spatially uniform magnetic field along the superconductor. However, at the top and bottom surface of a finite sample, the tangential magnetic field is not continuous and extra shielding currents are also there induced. For example, in a thin superconducting film strong demagnetization effects are responsible for a sharp rise in the local magnetic field H_{eff} at the edges in comparison with the actual field value H. As a result, higher values of current are necessary to shield the applied magnetic field, yielding larger values of the magnetization. Additionally, it is clear that the thinner the sample, the larger this effect [76].

The effective field H_{eff} originates from the contribution of the demagnetization field $-\tilde{\nu}\mathbf{M}$ with $\tilde{\nu}$ a shape dependent tensor. Taking into account demagnetization effects, one obtains [77]:

$$\mathbf{B} = \mathbf{H} + 4\pi(1 - \tilde{\nu}) \cdot \mathbf{M}. \tag{1.49}$$

For superconductors in the Meissner state, all flux in the interior of the sample is expelled ($B = 0$), leading to $\mathbf{M} = -\mathbf{H}_{eff}$ thus, $\mathbf{H}_{eff} = \mathbf{H}/(1-\nu)$. For a long cylinder with an applied field parallel to the axis of the cylinder, $\nu = 0$, since field lines are not distorted. In contrast, for $\mathbf{H}$ perpendicular to the axis of the cylinder, $\nu \sim 2/3$. For superconducting films this number is even larger, leading to an effective field, which is substantially larger than the applied field. Consequently, the critical field H_{c1} will be strongly reduced in thin films.

1.8 MESOSCOPIC SUPERCONDUCTORS

In mesoscopic samples, whose size is comparable to the coherence length ξ and penetration depth λ, the properties of a superconductor are considerable influenced by the confinement effects. Therefore, the nucleation of the superconducting state depends strongly on the boundary conditions imposed by the sample shape, i.e., on the topology of the system, which makes the behavior of mesoscopic samples significantly different from the bulk ones. In mesoscopic samples, the distinction between type-I and type-II superconductors is determined not only by κ and thickness of the sample d, but also by the lateral dimensions of the sample (see e.g. Ref. [78]). In such samples there is a competition between the triangular Abrikosov distribution of vortices, as being the lowest energy configuration in bulk material and thin films, and the sample boundary which tries to impose its geometry on the vortex distribution [78, 79]. It was shown that [80] vortices form shell structures in superconducting disks and for large radius of the disks the influence of the boundary diminishes and the triangular lattice may reappear (see Fig. 1.14(a)) [81]. Concentric shell structures of vortices were recently obtained experimentally using the Bitter decoration technique (Fig. 1.14(b)) [82].

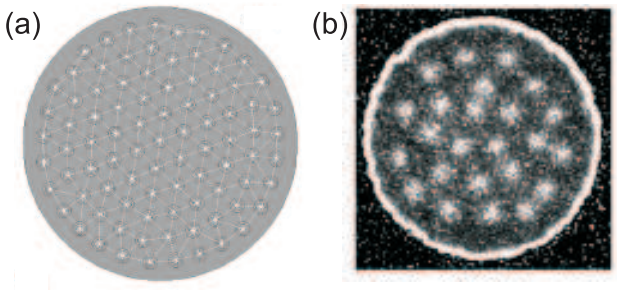

FIG. 1.14: (a) The vortex structure in a superconducting disk with vorticity $L = 88$ (from Ref. [81]) and (b) scanning electron microscope image of vortex patters in a disk of radius $R = 5.0$ μm (from Ref. [82]).

A rich variety of vortex matter in mesoscopic samples was predicted depending on the geometry, the size, the applied field and temperature. For example, giant-, multi-vortex states or a combination of them (with same or opposite polarity) can be nucleated in mesoscopic superconductors. Recently, Kanda *et al.*, developed the multiple-small-tunnel-junction (MSTJ) method, in which multiple small tunnel junctions with high tunnel resistance are attached to a mesoscopic superconductor in order to detect small changes in the local density of states under the junctions [83]. This setup allows one to make the distinction between the giant vortex states and multivortex states. Moreover, a magnetic field induced rearrangement and combination of vortices can be also studied experimentally. It was shown that [28] the temperature dependence of the vortex expulsion fields is closely related to the vortex states in mesoscopic superconductors. Namely, the expulsion field increases with temperature for multivortex states, while for giant vortex states it is almost temperature independent. Calculations within GL theory describes well these experimental findings.

1.9 DETAILS OF THE NUMERICAL APPROACH

In this thesis, we use the Ginzburg-Landau equations (1.6, 1.7) which can be rewritten using dimensionless variables and the London gauge div$\mathbf{A}$=0 in the following form:

$$(-i\nabla - \mathbf{A})^2 \Psi = \Psi \left(1 - |\Psi|^2\right), \tag{1.50}$$

$$-\kappa^2 \triangle \mathbf{A} = \frac{1}{2i} \left(\Psi^* \nabla \Psi - \Psi \nabla \Psi^*\right) - |\Psi|^2 \mathbf{A}. \tag{1.51}$$

Here the distance is measured in units of the coherence length $\xi = \hbar/\sqrt{-2m^*\alpha}$, the order parameter in $\Psi_0 = \sqrt{-\alpha/\beta}$ and the vector potential in $c\hbar/2e\xi$. $\kappa = \lambda/\xi$ is the Ginzburg-Landau parameter and $\lambda = c\sqrt{m^*/\pi/4e\Psi_0}$ is the penetration depth. The magnetic field is measured in the second critical magnetic field $H_{c2} = c\hbar/2e\xi^2 = \kappa\sqrt{2}H_c$, where $H_c = \sqrt{4\pi\alpha^2/\beta}$ is the thermodynamic critical field.

The temperature dependence in our calculations is included through the characteristic lengths ξ and λ, following from GL theory (see the Sec. 1.3.3)

$$\xi(T) = \xi(0)/\sqrt{|1 - T/T_{c0}|}, \tag{1.52}$$

$$\lambda(T) = \lambda(0)/\sqrt{|1 - T/T_{c0}|}, \tag{1.53}$$

$$H_{c2}(T) = H_{c2}(0)\,|1 - T/T_{c0}|\,, \tag{1.54}$$

where $H_{c2}(0) = c\hbar/2e\xi(0)^2$ and T_{c0} is the critical temperature at zero magnetic field.

The boundary condition for the order parameter in a superconductor in contact with an insulator or with vacuum is given by

$$\mathbf{n} \cdot (-i\nabla - \mathbf{A})\Psi\Big|_{boundary} = 0, \tag{1.55}$$

where $\mathbf{n}$ is the unit vector normal to the surface of the superconductor. This condition expresses that no current can pass perpendicular to the sample boundary (Neumann boundary condition). For a superconductor-normal metal interface the boundary condition must be modified. The more general expression for the boundary condition can be written as [24]

$$\mathbf{n} \cdot (-i\nabla - \mathbf{A})\Psi\Big|_{boundary} = \frac{i}{b}\Psi\Big|_{boundary}, \tag{1.56}$$

where b is the extrapolation length, which denotes the distance from the interface over which the order parameter Ψ is still finite in the normal metal, due to the proximity effect. For vacuum or an insulator $b \to \infty$, for ferromagnets $b \to 0$ and for normal metals $b > 0$. The boundary condition for the vector potential is such that the total magnetic field far away from the superconductor equals the applied magnetic field (the contribution of the field of the supercurrents diminishes as one goes further away from the superconductor).

In the case of an infinite superconducting film the following boundary conditions for $\mathbf{A}$ and Ψ are used [84]

$$\mathbf{A}(\rho + \mathbf{b}_i) = \mathbf{A}(\rho) + \nabla\eta_i(\rho), \tag{1.57}$$

$$\Psi(\rho + \mathbf{b}_i) = \Psi \exp(2\pi i \eta_i(\rho/\Phi_0)), \tag{1.58}$$

where $\mathbf{b}_i$, $i = x, y$ are the lattice vectors, and η_i is the gauge potential which cannot be chosen freely but must preserve the single valuedness of $\mathbf{A}$ and Ψ. These boundary conditions mean that $\mathbf{A}$ and Ψ are invariant under lattice translations combined with specific gauge transformations. Other quantities, such as the magnetic field, the current and the modulus of the order parameter are periodic. One should notice that these boundary conditions reduce to their standard form for $\eta_i = 0$. The adequate choice of the gauge potential η_i will be discussed for particular applied magnetic fields through the thesis.

In this thesis we consider thin superconductors, mainly with thickness smaller than the characteristic lengths of the superconductors. It was shown [23] that the current and the vector potential for such thin superconductors may be considered constant over the thickness of the sample. Consequently, they have no z-component, and the boundary condition (1.55) is automatically fulfilled at top and bottom surface of the superconductor. From the first GL equation (1.50) then follows the behavior of the order parameter, and, as far as the order parameter is concerned the 3D problem is reduced to a 2D problem. We use this property and average the GL equations (1.50) and (1.51) over the

superconductor thickness. They take the form

$$(-i\nabla_{2D} - \mathbf{A})^2 \Psi = \Psi \left(1 - |\Psi|^2\right), \tag{1.59}$$

$$-\Delta_{3D}\mathbf{A} = \frac{d}{\kappa^2}\delta(z)\,\mathbf{j}_{2D}, \tag{1.60}$$

where

$$\mathbf{j}_{2D} = \frac{1}{2i}\left(\Psi^*\nabla_{2D}\Psi - \Psi\nabla_{2D}\Psi^*\right) - |\Psi|^2\,\mathbf{A}, \tag{1.61}$$

is the density of the superconducting current. The indices 2D, 3D refer to two- and three-dimensional operators, respectively. Note that the 3D nature of the magnetic field distribution following from Eq. (1.60) is completely retained.

For the fixed applied magnetic field, we solved the two coupled GL equations self-consistently introducing the complex link variable [85]

$$U_\mu^{r_1 r_2} = exp\left(\int_{r_1}^{r_2} \mathbf{A}_\mu(\mathbf{r})\mathbf{d}\mu\right), \tag{1.62}$$

with $\mu = x, y$. These link variables are used in order to preserve the gauge-invariant properties of the GL equations. A finite-difference representation of the order parameter and the vector potential is given on a uniform cartesian space grid (x, y) with a typical grid spacing less than 0.1ξ. In order to provide time relaxation and ensure convergence of our calculations, we add the time derivatives of the order parameter and the vector potential to the left side of Eqs. (1.59) and (1.60), respectively, which are then iterated over time. According to Kato *et al.* [85], the time dependent GL equation (1.59) can be written as

$$\frac{\partial\Psi}{\partial t} = -\frac{1}{12}\left[\left(\frac{\nabla}{i} - \mathbf{A}\right)^2 \Psi + (1-T)\left(|\Psi|^2 - 1\right)\Psi\right] + \tilde{f}(\mathbf{r}, t), \tag{1.63}$$

where $\tilde{f}(\mathbf{r}, t)$ is a dimensionless random force. For computer simulations, it is convenient to discretize the system. The first and second derivatives of Eq. (1.63) are given by

$$\left(\frac{1}{i}\frac{\partial}{\partial x} - A_x\right)\Psi \rightarrow -i\frac{U_x^{kj}\Psi_k - \Psi_j}{a_x}, \tag{1.64}$$

$$\left(\frac{1}{i}\frac{\partial}{\partial x} - A_x\right)^2 \Psi \rightarrow \frac{U_x^{kj}\Psi_k - 2\Psi_j + U_x^{ij}\Psi_i}{a_x^2}, \tag{1.65}$$

respectively, where a_x is the lattice constant in x direction and superscripts and subscripts $j, k, ...$ denote the lattice points as shown in Fig. 1.15. We then obtain the discretized time dependent GL equation from Eq. (1.59) as

$$\begin{aligned}\frac{\partial\Psi}{\partial t} = \quad & \frac{1}{12}\Big[\frac{U^{kj}\Psi_k}{a_x^2} + \frac{U^{ij}\Psi_i}{a_x^2} + \frac{U^{mj}\Psi_m}{a_y^2} + \frac{U^{kg}\Psi_g}{a_y^2} - \frac{2\Psi_j}{a_x^2} - \frac{2\Psi_j}{a_y^2} \\ & + (1-T)\left(|\Psi_j|^2 - 1\right)\Psi_j\Big] + \tilde{f}_j(t).\end{aligned} \tag{1.66}$$

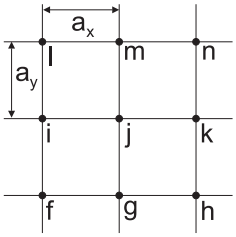

FIG. 1.15: The uniform Cartesian grid-point lattice used in the simulations (after [85]).

First, we solve the linearized GL equation, setting the non-linear part in Eq. (1.66) to zero. This solution is then substituted in the non-linear equation, and a new solution is found, which is substituted back in the equation. In this recurrent procedure based on a Gauss-Seidel iteration technique, convergence is finally reached and the first GL equation is solved [78]. The values of Ψ is used to calculate the current densities j_x and j_y in every grid point. From the supercurrents a new value for the vector potential can be calculated using the second GL equation (1.60). Finally, this vector potential is substituted back in the first GL equation (1.59) and the whole procedure described above is repeated until a convergent solution of both GL equations is found.

In this way, we solve self-consistently two coupled GL equations for fixed magnetic field. Once a solution is obtained at a given magnetic field, the field is increased (or decreased) and this solution is used as the initial value in the new calculation. In doing so, the program stays within the same local minimum of the free energy and follows this minimum as a function of the magnetic field. At a certain field, the minimum ceases to exist and the program runs towards a new minimum which is a different solution of the GL equations. Then, the magnetic field is changed further and one can investigate the magnetic field range over which the new minimum is stable by sweeping the field up and down.

In order to calculate the Gibbs free energy of the system, we start from the expression (1.5), which can be written in dimensionless form as follows:

$$\begin{aligned} F &= \frac{\mathcal{G}_s - \mathcal{G}_n}{H_c^2 V/8\pi} \\ &= \int \left[-2|\Psi|^2 + |\Psi|^4 + 2\left|(-i\nabla - \mathbf{A})\,\Psi\right|^2 + 2\kappa^2(\mathbf{h}-\mathbf{H})^2 \right] dV, \end{aligned} \tag{1.67}$$

where the integration is carried out over the entire space. Using mathematical transformations and the Gauss theorem $\int \nabla \cdot \mathbf{A} dV = \oint \mathbf{n} \cdot \mathbf{A} dS$, the third term

in the integrand in Eq. (1.67) can be written as

$$\int |(-i\nabla - \mathbf{A})\Psi|^2 \, dV = \oint \mathbf{n} \cdot \left[\Psi^* \left(-i\nabla - \mathbf{A}\right) \Psi\right] dS + \int \Psi^* \left(-i\nabla - \mathbf{A}\right)^2 \Psi dV. \tag{1.68}$$

The first term on the right side equals to zero due to the boundary conditions both for the superconducting vacuum boundary (Eq. (1.55)) and periodic boundary (Eqs. (1.57, 1.58)). The second term is rewritten with the help of the first GL equation (1.59) and finally we have

$$\int |(-i\nabla - \mathbf{A})\Psi|^2 \, dV = \int \left(|\Psi|^2 - |\Psi|^4\right) dV. \tag{1.69}$$

Therefore,

$$F = \int \left[\left(\mathbf{h} - \mathbf{H}\right)^2 \kappa^2 - 1/2|\Psi|^4\right] dV, \tag{1.70}$$

where $\mathbf{H}$ =rot $\mathbf{A}$. Using the vector relations $\nabla\cdot(\mathbf{a} \times \mathbf{b}) = \mathbf{b}\cdot(\nabla \times \mathbf{a}) - \mathbf{a}\cdot(\nabla \times \mathbf{b})$ and $\mathbf{a} \times (\nabla \times \mathbf{a}) = 0$, and the London gauge $\nabla \cdot \mathbf{A} = 0$, the free energy becomes

$$F = V^{-1} \int \left[2 \left(\mathbf{A} - \mathbf{A}_0\right) \cdot \mathbf{j} - |\Psi|^4\right] d\mathbf{r}, \tag{1.71}$$

where $\mathbf{A_0}$ denotes the vector potential of the applied magnetic field H in the absence of the superconductor and the dimensionless supercurrent is given by Eq. (1.61).

2

Surface barrier for flux penetration and expulsion in thin mesoscopic superconductors

2.1 INTRODUCTION

Vortex matter in superconducting samples with sizes on the scale of the coherence length ξ and penetration depth λ has attracted much attention in recent years [29, 86, 87]. In such small confined systems the interaction between the vortices and the sample surface, which tries to impose the symmetry of the sample boundary on the vortex configurations, becomes important. This interaction of vortices with the surface manifests itself through the existence of hysteresis behavior and different phase transitions [27, 29, 78, 86, 88–91]. The hysteresis effect is a consequence of the presence of an energy barrier between the states with vorticity L and $L+1$, known as the Bean-Livingston energy barrier [92], (see also Ref. [93]) which increases the first-vortex entry field H_s beyond the first critical field H_{c1}. According to this model the surface barrier appears due to a competition between the vortex attraction to the sample walls by its mirror image and its repulsion by screening currents. This model was further developed for cylindrical samples [94–96], thin disks [81, 97, 98], rings [99–102] and strips [103–107]. Most of these barrier models are based on the London theory and do not account for the process of vortex formation (vortices are treated as point particles) and describe only the vortex motion far from the sample boundary. In this limit it is possible to find an analytical

expression for the energy and forces for an arbitrary arrangement of vortices inside the superconductor.

The origin of barriers for flux penetration and expulsion has been considered recently through a numerical study of the Ginzburg-Landau (GL) equations [108–112]. Within the GL theory vortices are extended objects where the superconducting condensate vanishes over a length scale ξ, which is very different from the London theory where vortices are point particles, i.e. $\xi \to 0$. The allowed vortex configurations correspond to different minima of the free energy in configurational space and the lowest barrier between those two minima is a saddle point which corresponds to the flux penetration and expulsion state. Schweigert and Peeters [109] presented an approach for finding the saddle point states in thin disks and calculated numerically the heights of the free energy barriers separating the stable states with a different number of vortices. Their approach was later extended to the case of superconducting rings [111].

In this chapter we study the surface barrier in mesoscopic disks, rings and squares for different values of the GL parameter κ though a numerical solution of the GL equations using analytical expressions for the phase of the order parameter as obtained from the London approach. Previous studies were limited to the London theory or assumed the limit of very thin disks such that only the first GL equation had to be solved. In our approach, both GL equations are solved self-consistently and by fixing the phase of the order parameter locally we are able to move the vortex through the sample. We compare our results with those obtained from the London theory.

The chapter is organized as follows. The theoretical formulation of the problem is given in Sec. 2.2. The Bean-Livingston barrier for a single vortex entry/exit in a small radius disk is studied in Sec. 2.3 for different thickness of the disk and for different values of the GL parameter κ. In Sec. 2.4 we compare our calculations with the results obtained from the London theory. The $L = 2$ giant vortex state in a superconducting disk is considered in Sec. 2.5, and the break up into a multivortex state is investigated. The surface barrier for vortices in a superconducting ring and in a square sample is investigated in Secs. 2.6 and 2.7, respectively. The results of the present paper are summarized in Sec. 2.8.

2.2 THEORETICAL FORMALISM

2.2.1 Ginzburg-Landau theory

We consider thin superconducting samples with thickness $d < \xi, \lambda$ immersed in an insulating medium in the presence of a perpendicular uniform magnetic field H. Measuring the distance in units of the coherence length ξ, the vector potential $\mathbf{A}$ in $c\hbar/2e\xi$, the magnetic field in $H_{c2} = c\hbar/2e\xi^2 = \kappa\sqrt{2}H_c$, and the

order parameter Ψ in $\sqrt{-\alpha/\beta}$ with α, β being the GL coefficients, the system of GL equations can be written in the following form [78]:

$$\left(-i\nabla_{2D} - \mathbf{A}\right)^2 \Psi = \Psi\left(1 - |\Psi|^2\right), \tag{2.1}$$

$$-\Delta_{3D}\mathbf{A} = \frac{d}{\kappa^2}\delta(z)\,\mathbf{j}_{2D}, \tag{2.2}$$

$$\mathbf{j}_{2D} = \frac{1}{2i}\left(\Psi^*\nabla_{2D}\Psi - \Psi\nabla_{2D}\Psi^*\right) - |\Psi|^2\,\mathbf{A}, \tag{2.3}$$

where the indices 2D, 3D refer to two- and three-dimensional operators, respectively, and $\mathbf{j}_{2D}$ is the density of the superconducting current. The boundary conditions to Eqs. (2.1, 2.2) correspond to zero superconducting current at the sample boundaries and an uniform external magnetic field far from the sample $\mathbf{A}_{|\mathbf{r}|\to\infty} = \frac{1}{2}[\mathbf{r}\times\mathbf{H}]$, respectively. To solve the coupled set of nonlinear Eqs. (2.1, 2.2) we follow the numerical approach of Schweigert and Peeters [78, 88].

The Gibbs free energy, in units of $F_0 = H_c^2 V/8\pi$, for the given vortex states is calculated from

$$F = V^{-1}\int_V \left[2\left(\mathbf{A} - \mathbf{A}_0\right)\cdot\mathbf{j}_{2d} - |\Psi|^4\right] d\mathbf{r}, \tag{2.4}$$

where integration is performed over the sample volume V, and $\mathbf{A}_0$ is the vector potential of the uniform magnetic field. For *Al* disks with 1.3 μm (0.2 μm) radius and 0.13 μm (0.01 μm) thickness the unit F_0 is of the order $\sim 10^3$ eV (2 eV) (see for example Ref. [29]). The dimensionless magnetization is defined as

$$M = (\langle h\rangle - H)/4\pi, \tag{2.5}$$

where $\langle h\rangle$ is the magnetic field averaged over the sample.

2.2.2 London approach and phase of the order parameter

In thin films, within the limits $S \gg \xi$ (where S are the transverse dimensions of the film) and $H \ll H_{c2}$, $|\Psi|^2$ is practically constant throughout the specimen, except at distances $\sim\xi$ from the vortex cores or the interface. These conditions are satisfied in the London limit, and one may consider $|\Psi|^2 = $ const. with singularities in the phase of Ψ at the vortex core positions. Considering the magnetic field pointing in the z direction, the second GL equation reduces to the London equation,

$$h_z + \frac{4\pi\Lambda}{c}(\nabla\times\mathbf{J})_z = \Phi_0\sum_{k=1}^{L}\delta\left(\mathbf{r} - \mathbf{r}_k\right), \tag{2.6}$$

where $\mathbf{J} = \int_0^d \mathbf{j}dz \approx \mathbf{j}d$, $\Lambda = \lambda^2/d$, and $\mathbf{r}_k$ is the position of vortex k.

In order to solve the London equation one may consider taking $\mathbf{J} = \nabla \times \hat{z}g$, where $g(\mathbf{r})$ is the streamline function [113]. This function has the property that $g_\Gamma = \text{const.}$, where g_Γ represents the value of $g(\mathbf{r})$ at the specimen edges. For samples without holes, one may consider $g_\Gamma = 0$. Otherwise, $g(\mathbf{r})$ may take different constant values at each hole and at the edges [102, 114]. In addition, in thin films where $\Lambda \gg S$, demagnetization effects can be disregarded, and $h_z \approx H$ in Eq. (2.6). This makes the London equation of the Poisson type

$$-\frac{4\pi\Lambda}{c}\nabla^2 g = \Phi_0 \sum_{k=1}^{L} \delta\left(\mathbf{r} - \mathbf{r}_k\right) - H, \tag{2.7}$$

which can be solved by standard techniques. Analytical solutions, for example, of the problem of a vortex in a thin disk [97, 98] or in a ring [102], have been found. Such analytical expressions – from which the energy of the system can be calculated – are suitable for simulations of systems containing a large number of vortices [81].

As pointed out by Fetter [97] g_v, which is the streamline function for a vortex inside the mesoscopic superconductor with zero external magnetic field, and θ (in two dimensional systems) are related by the real and imaginary parts of a complex function, $\Omega(z)$, since both g_v and θ satisfy Laplace equation (except at the vortex core positions). This allows one to obtain analytic expressions for the phase of the order parameter, θ. For a disk, the phase of the order parameter is given by the imaginary part of [81, 97] (see also [115])

$$\Omega = \sum_{j=1}^{L} \ln\left[\left(\frac{z - (R/z_j)^2 z_j}{z - z_j}\right)\frac{r_j}{R}\right], \tag{2.8}$$

where $z = r\exp(i\phi) = x + iy$, $z_j = r_j \exp(i\phi_j)$ is the position of vortex j, and R is the disk radius. For the case of rings with inner (outer) radius a (b), θ – for one vortex at $(x, 0)$ – is the imaginary part of

$$\begin{aligned}
\Omega &= \ln\left[\frac{A(z,x))}{B(x)}\right] - \left[N + \frac{\ln(b/x)}{\ln(b/a)}\right]\ln(z/a), \\
A(z,x) &= \frac{\mathrm{cn}[2\gamma\ln(x/a), m]}{\mathrm{sn}[2\gamma\ln(x/a), m]} - \frac{\mathrm{cn}[\gamma\ln(x/z), m]}{\mathrm{sn}[\gamma\ln(x/z), m]}, \\
B(x) &= \frac{\mathrm{cn}[2\gamma\ln(x/a), m]}{\mathrm{sn}[2\gamma\ln(x/a), m]} - \frac{\mathrm{cn}[\gamma\ln(x/a), m]}{\mathrm{sn}[\gamma\ln(x/a), m]},
\end{aligned} \tag{2.9}$$

where N is the number of vortices inside the hole, $(a \le x \le b, 0)$ is the vortex position, cn and sn are the Jacobi elliptic functions, $\gamma = \mathrm{K}(m)/\ln(b/a)$, $\mathrm{K}(m)$ is the complete elliptic integral and the parameter m is determined by the relation $\mathrm{K}(1-m)\ln(b/a) = \pi\mathrm{K}(m)$ according to Ref. [102].

For a rectangle with dimensions $0 \leq x \leq a$ and $0 \leq y \leq b$, the complex function which is a solution of Eq. (2.7) (for $H = 0$) is given by

$$\Omega = \sum_{j=1}^{L} \ln \left[\frac{\mathrm{sn}^2(\mathrm{K(m)}z/a, m) - \mathrm{sn}^2(\mathrm{K(m)}z_j^*/a, m)}{\mathrm{sn}^2(\mathrm{K(m)}z/a, m) - \mathrm{sn}^2(\mathrm{K(m)}z_j/a, m)} \right], \qquad (2.10)$$

which is the same as for the problem of an electric charge inside a rectangle held at zero potential (see Ref. [116]). The value of m is now chosen to satisfy $\mathrm{K}(1-m) = (b/a)\mathrm{K}(m)$ and $z_j* = r_j \exp(-i\phi_j)$ is the conjugate of the position of vortex j.

2.3 SUPERCONDUCTING DISK

2.3.1 A single vortex: estimation of the H_{c1}

In earlier works (see for example Refs. [27, 78, 88]) which were devoted to the study of the properties of superconducting disks, vortex configurations were obtained through a minimization of the energy. In this work we investigate the energy and magnetization of a superconducting disk, by fixing vortices in an arbitrary position for different applied magnetic field. In general, such vortex configurations are not stable. In experiments this can be realized e.g. by pinning vortices through a weak pinning potential. However, for strong pinning potential the system may become different leading to different vortex structures (see Secs. 2.4 and 6.3.2).

First, we consider a superconducting disk with radius $R = 4.0\xi$ and different thickness d. Fig. 2.1 shows the free energy and the magnetization of the sample as a function of the radial position of the vortex. For the given parameters of the disk, the $L = 1$ state is stable in the magnetic field range $H/H_{c2} = 0.125-0.71$. As for the bulk case [92], an energy barrier to flux penetration and expulsion in the disk exists in some magnetic field range. Below this magnetic field range the function $F(\rho_v)$, where ρ_v is the radial position of the vortex, has only one extremum which is a maximum at $\rho_v = 0$, i.e. the vortex will leave the sample (curve 1). At low fields vortices are unstable inside the sample and there is an energy cost associated with vortex entrance. For higher fields it is energetically favorable for the vortex to sit inside the sample and $F(\rho_v)$ is a function with a single minimum at $\rho_v = 0$ (curve 2). The increase of the disk thickness does not change the qualitative behavior of the free energy but shifts the free energy to lower energy (red curves in Fig. 2.1(a)). For small fields the magnetization curves show paramagnetic response (i.e. $M > 0$) when the vortex is located close to the center and $-M$ increases with shifting the vortex from the center of the sample. This paramagnetic behavior for the total magnetization results from the existence of the energy barrier. Increasing the disk thickness leads to more flux expulsion from the sample.

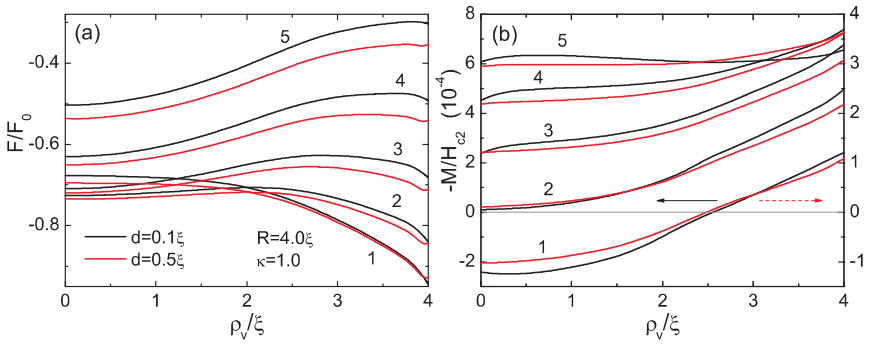

FIG. 2.1: The free energy (a) and the magnetization (b) of the $L = 1$ state as a function of the radial position of the vortex for different values of the applied magnetic field: $H/H_{c2} = 0.1$ (curve 1), $H/H_{c2} = 0.2$ (curve 2), $H/H_{c2} = 0.3$ (curve 3), $H/H_{c2} = 0.4$ (curve 4) and $H/H_{c2} = 0.5$ (curve 5). The radius of the disk is $R = 4.0\xi$, the thickness is $d = 0.1\xi$ (black curves) and $d = 0.5\xi$ (red curves referred to the right axis for the magnetization). The GL parameter is $\kappa = 1.0$.

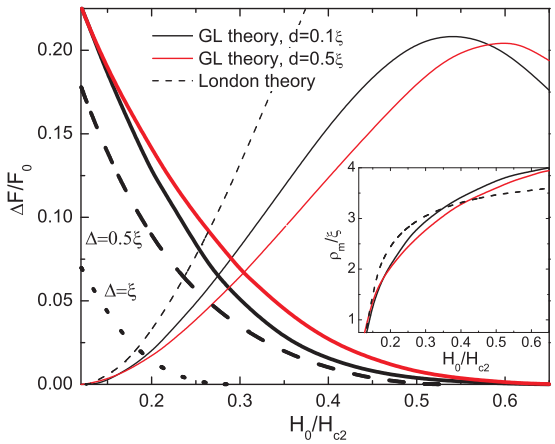

FIG. 2.2: Energy barrier for the vortex penetration (thick curves) and escape (thin curves) as a function of the applied field for a disk with $R = 4.0\xi$, $d = 0.1\xi$ (solid black curves) and $d = 0.5\xi$ (solid red curves) and for $\kappa = 1.0$. The inset shows the position of the barrier maximum ρ_m as a function of the applied field. The results of the London theory are given by the dashed curves for two different values of the cutoff parameter Δ.

Fig. 2.2 presents the energy barrier for vortex penetration (thick curves), $\Delta F_{penetration} = F_{max} - F_{\rho_v=R}$, and expulsion (thin curves), $\Delta F_{expulsion} = F_{max} - F_{\rho_v=0}$, as a function of the applied field for $d = 0.1\xi$ (solid black curves) and $d = 0.5\xi$ (solid red curves). As seen from this figure, the barrier for flux escape disappears at low fields, while the barrier for vortex entry increases. Increasing the external field leads to an increase of the barrier for vortex expulsion and to a decrease of the barrier for vortex penetration. The first critical field H_{c1} is the field at which the energy for a vortex inside the superconductor is the same as the energy of the vortex at the sample edge, i.e. $\Delta F_{penetration} = \Delta F_{expulsion}$. Therefore, the crossing point of the two barriers determines the first critical field H_{c1}. This barrier is influenced by the sample thickness: the expulsion barrier decreases and the penetration barrier and critical field H_{c1} increases by increasing the thickness. The latter indicates the larger repulsion of the vortex from the surface of the sample with larger thickness. The London theory (dashed curves in Fig. 2.2) predicts a much larger energy barrier for vortex expulsion (near H_{c1} it is almost a factor of 2 larger). Because the London theory fails close to the sample boundary (i.e. $F \to -\infty$ when $r \to R$), we need to introduce a cutoff distance Δ in order to find finite value for $\Delta F_{penetration}$. Therefore, within the London theory, we defined $\Delta F_{penetration} = F_{max} - F_{\rho_v=R-\Delta}$. The results for two different choices, i.e.

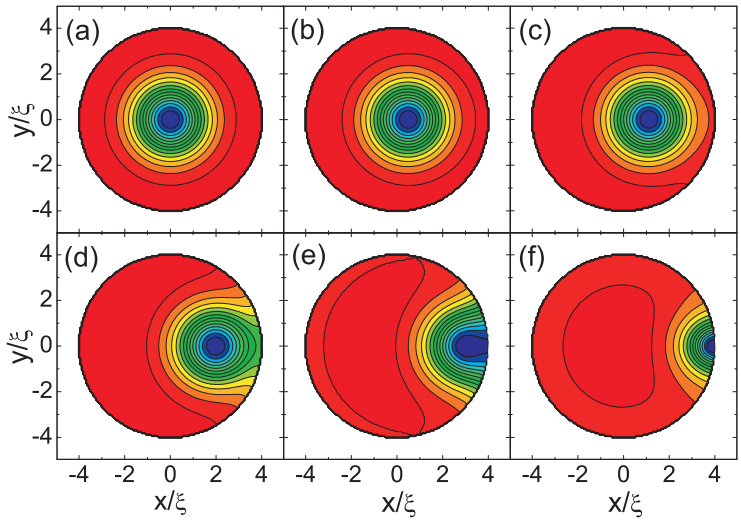

Fig. 2.3: Contour plots of the Cooper pair density distribution in the disk with radius $R = 4.0\xi$, thickness $d = 0.1\xi$, $\kappa = 1.0$ at $H/H_{c2} = 0.2$ for different values of the vortex position: a) $\rho = 0\xi$, b) $\rho = 0.5\xi$, c) $\rho = 1.0\xi$, d) $\rho = 2.0\xi$, e) $\rho = 3.0\xi$, and f) $\rho = 3.85\xi$. Red (blue) color corresponds to large (small) value of the Cooper pair density.

$\Delta = \xi$ (dotted curve) and $\Delta = 0.5\xi$ (dashed curve), are shown in Fig. 2.2. For both choices we find that the penetration barrier and the magnetic field range over which this barrier exists, is much smaller within the London approach as compared to the one in the GL theory. These results show clearly the limited applicability of the surface barrier when obtained from the London theory in case of finite values of the GL parameter. When calculating the saddle point states, Schweigert and Peeters [109] found a better agreement with the London theory, and a small difference was found only beyond H_{c1}. The position of the barrier maximum ρ_m (see the inset of Fig. 2.2) is shifted from the center of the sample to the sample boundary with increasing applied field. For small fields ρ_m calculated from the London theory is larger compared to the one obtained from the GL theory and for larger fields the reverse is found.

We found that there is no energy barrier when we place an antivortex inside the disk for any radius of the sample and any positive applied field. The energy minimum is at the edge of the disk and consequently the antivortex will leave the sample.

The spatial distribution of the Cooper-pair density $|\Psi|^2$ calculated for different vortex positions ρ_v is plotted in Fig. 2.3 for $H/H_{c2} = 0.2$ and for disk thickness $d = 0.1\xi$. Notice the non circular shape of the contour lines, when the vortex is close to the sample boundary.

The dependence of the surface barrier on the GL parameter κ is shown in Fig. 2.4. This figure gives the free energy of the disk with radius $R = 4.0\xi$ and thickness $d = 0.1\xi$, as a function of the vortex position ρ_v for different values of κ, at $H/H_{c2} = 0.15$ (a) and $H/H_{c2} = 0.3$ (b). It is seen from this figure that the free energy strongly depends on κ: with increasing GL parameter from $\kappa = 0.1$ (corresponding to an effective GL parameter $\kappa^* = \kappa^2\xi/d = 0.1$) to

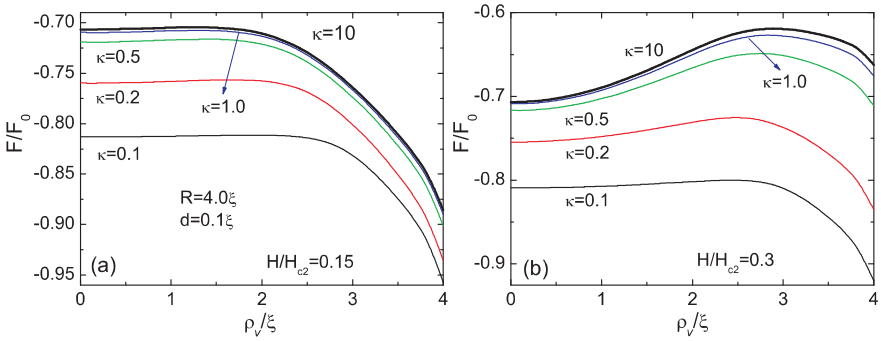

FIG. 2.4: The free energy as a function of the radial position of the vortex ρ_v for different values of the GL parameter κ and for the applied fields $H/H_{c2} = 0.15$ (a) and $H/H_{c2} = 0.3$ (b). The radius of the disk is $R = 4.0\xi$ and the thickness is $d = 0.1\xi$.

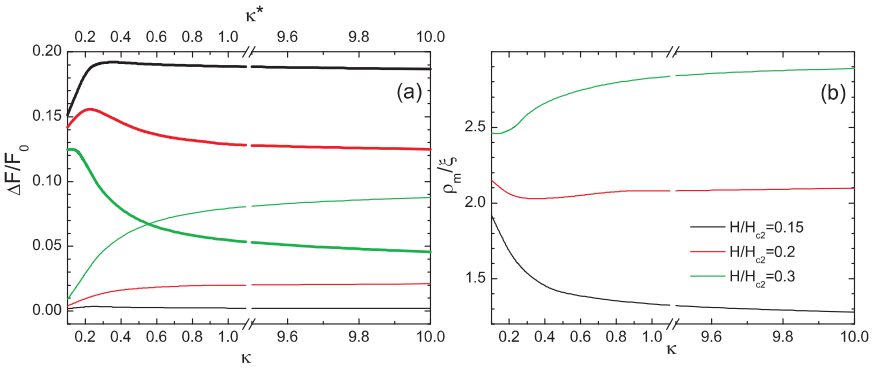

Fig. 2.5: Energy barrier (a) for flux penetration (thick curves) and escape (thin curves) and the position of the barrier maximum ρ_m (b) as a function of the GL parameter κ for the applied fields $H/H_{c2} = 0.15$ (black curves), $H/H_{c2} = 0.2$ (red curves), and $H/H_{c2} = 0.3$ (green curves), with a break at $\kappa = 1.1$.

$\kappa = 1.0$ ($\kappa^* = 10.0$) (blue curve) the free energy increases considerably, which is due to the larger penetration of the field inside the sample; further increase of κ (thick black line) leads only to a minor increase of the free energy. We found that the results for $\kappa = 10$ ($\kappa^* = 1000$) is identical to the results for $\kappa \geq 100$.

Figs. 2.5(a,b) show the height of the barrier for vortex penetration (thick curves) and expulsion (thin curves) and the position of the barrier maximum as a function of κ. At low fields (black line) the maximum in the expulsion barrier (thin curves) is found for small values of κ and the barrier decreases with further increase of κ. For higher fields (green curve) the expulsion barrier increases with increasing κ and we see the crossing of the curves for penetration and expulsion barrier. At small fields the position of the barrier maximum (Fig. 2.5(b)) decreases with increasing κ and for higher fields a minimum appears in the plot of the barrier position.

2.3.2 Comparison with London theory

The London theory fails close to the sample boundaries at distances of order ξ and for small inter-vortex distances. As a consequence the applicability of the London theory for very small mesoscopic samples is questionable. Therefore, we will consider larger disks and compare the results of the London theory with our GL calculations. In this case the London approach, in which the superconducting density is assumed to be a constant, gives rather accurate results. This model was extended to arbitrary radius of the disk by taking into account the spatial nonuniformity of the modulus of the order parameter in Refs. [81, 109]. This improved version of the London theory was shown to be

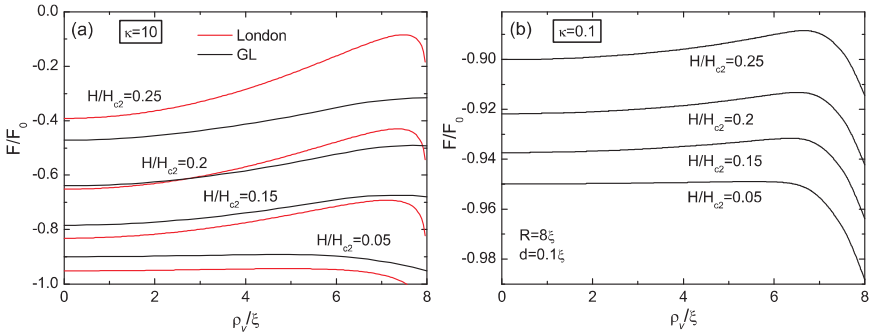

FIG. 2.6: The free energy of the disk with radius $R = 8.0\xi$ and thickness $d = 0.1\xi$ as a function of the radial position of the vortex ρ_v for different values of the applied magnetic field. The results from the London theory are given by dashed (red) curves and the results of the GL theory are given by solid curves for $\kappa = 10$ (a) and $\kappa = 0.1$ (b).

in good agreement with the GL theory below the nucleation field $H = H_n$ and breaks down for higher fields.

Fig. 2.6 shows the free energy of the superconducting disk with radius $R = 8.0\xi$ as a function of the vortex position ρ_v, calculated from the London theory (red curves) and the GL theory (black curves) for $\kappa = 10$ (a) and $\kappa = 0.1$ (b) at different applied fields. The disk thickness is $d = 0.1\xi$ whose value is less important in the GL theory for larger κ (see Eq. (2.2). The free energy shows a similar qualitative behavior in both cases: the appearance of the energy barrier at high fields and its disappearance at lower fields. But the value of the free energy is not the same: at low fields the free energy from the London theory is lower than the free energy of the GL theory which is opposite at higher fields. For small κ the free energy calculated within the GL theory is lower than in the corresponding case of $\kappa = 10$, which is the reason why the results of the London theory are not shown in Fig. 2.6(b).

The height of the energy barrier for the vortex penetration (thick curves) and expulsion (thin curves) is given in Fig. 2.7 as a function of the applied field. It is seen from this figure that for larger value of κ and at small fields our results for the expulsion barrier show good agreement with the one from the London approach for $H < H_{c1}$. At higher fields the London theory gives a larger expulsion barrier. The penetration barrier within the London limit is calculated for two different values of the cutoff parameter $\Delta = 0.5\xi$ (tick dotted curve) and $\Delta = \xi$ (thick dashed curve). For $\Delta = \xi$ a reasonable good agreement with the GL-approach is found for $H > H_{c1}$. For small κ (Fig. 2.7(b)) a surface barrier is found over a larger range of magnetic field, while the barrier itself is smaller than for the larger κ case. If we compare these results with the one for

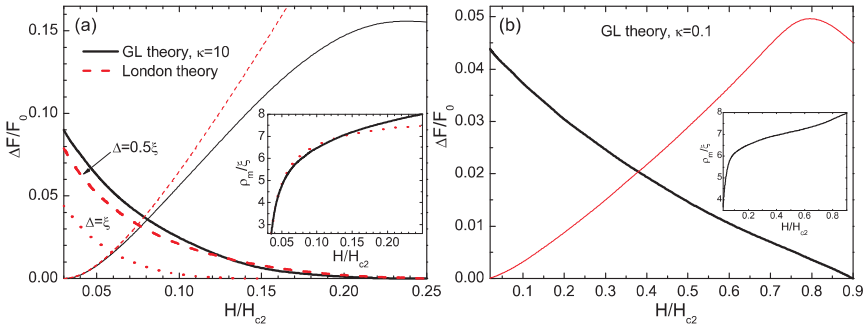

Fig. 2.7: Energy barrier for vortex penetration (thick curves) and escape (thin curves) as a function of the applied magnetic field for the disk of Fig. 2.6. Dashed curves are the results of the London theory and solid curves are the one of the GL theory for $\kappa = 10$ (a) and $\kappa = 0.1$ (b). The insets show the position of the barrier maximum ρ_m as a function of the applied field.

a smaller disk radius (Fig. 2.2) we see that the barrier height and the magnetic field range, where this barrier exists, decreases with increasing R for fixed κ.

2.3.3 The $L = 2$ state in the disk

For larger disk radius (i.e. $R \geq 3.0\xi$), several vortices can enter the sample at once (see for example Ref. [110]), indicating that at the entrance field the energy barriers separating the different vortex states become very small. In such samples many different superconducting states can exist at a given magnetic field. Our approach allows us to study the transitions between these states and calculate the energy barrier as a function of the vortex position for any number of vortices L.

We start with the most simple case – the $L = 2$ state, which was studied in Ref. [110] within the modified London approach. Fig. 2.8(a) shows the free energy for a disk with $R = 4.0\xi$ and $d = 0.1\xi$ as a function of the inter-vortex distance a for different applied fields. It is seen that, at larger magnetic fields (green curve, $H = 0.55H_{c2}$), the free energy has a minimum when both vortices are located in the center implying that the giant vortex state is preferred. With decreasing magnetic field (red curve, $H = 0.35H_{c2}$) the free energy has a minimum when the vortices are separated at a distance $a = 3.22\xi$ and has a maximum for $a = 5.7\xi$, which shows that at this magnetic field the multivortex state is energetically favorable. The inset of Fig. 2.8 shows the height of the energy barrier for the transition from this multivortex state to the giant vortex state (solid curve) and for the transition from the multivortex state to the $L = 0$ state (dashed curve, referred to the right axis). Further decreasing the field (black line, $H = 0.2H_{c2}$) there is no energy barrier for vortex expulsion

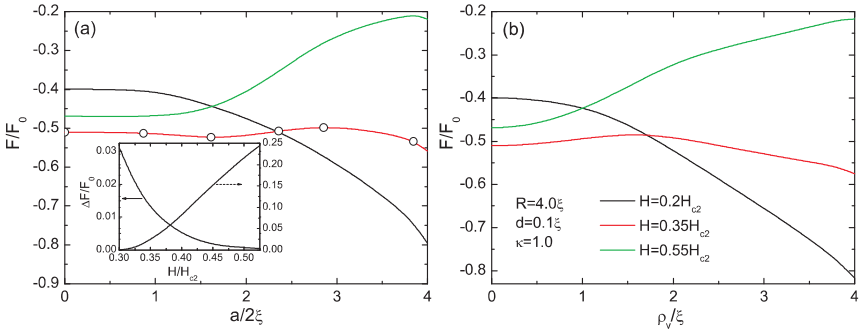

FIG. 2.8: The free energy of the multi-vortex ($L = 2$) state (a) as a function of the inter-vortex distance a, and the free energy of the giant vortex ($L = 2$) state (b) as a function of the radial position of the giant vortex ρ_v for different magnetic fields. The inset shows the height of the energy barrier for the transition from the multivortex $L = 2$ state to the giant vortex $L = 2$ state (solid curve) and for the transition from multivortex $L = 2$ state to the $L = 0$ state (dashed curve, referred to the right axis) as a function of the applied field. The radius of the disk is $R = 4.0\xi$, the thickness is $d = 0.1\xi$, and $\kappa = 1.0$.

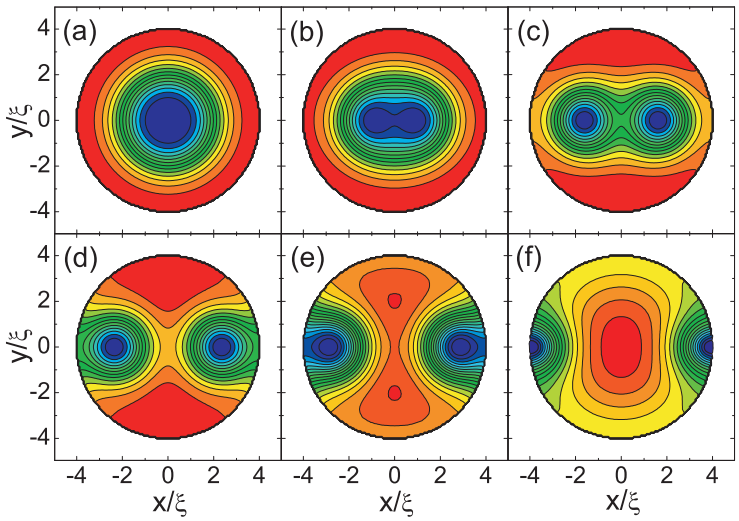

FIG. 2.9: Contour-plot of the Cooper pair density for a disk with $R = 4.0\xi$, $d = 0.1\xi$, $\kappa = 1.0\xi$ at $H/H_{c2} = 0.35$ and the distance between vortices is: a) $a/2 = 0\xi$, b) $a/2 = 0.87\xi$, c) $a/2 = 1.61\xi$, d) $a/2 = 2.36\xi$, e) $a/2 = 2.85\xi$, and f) $a/2 = 3.85\xi$.

and vortices leave the sample. To compare with the multi-vortex state, we plotted in Fig. 2.8(b) the free energy of the giant vortex state with $L = 2$ as a function of the radial position of the giant vortex. It is seen from this figure that the giant vortex behaves similar to what we found for a single vortex: at small fields there is a barrier for the giant vortex to enter the sample which disappears with increasing applied field. The distribution of the Cooper-pair density for different values of a, which are indicated by open circles in Fig. 2.8, is shown in Fig. 2.9.

2.3.4 Temperature dependence of the energy barrier

Recently the temperature dependence of the vortex penetration and expulsion magnetic fields were investigated experimentally for mesoscopic superconducting disks [28] and squares [117] using the small-tunnel-junction method [83] to determine the transition fields between the different vortex states. It was found that the penetration fields decrease with increasing temperature for all values of the vorticity, while the expulsion fields may increase, decrease or be independent of temperature. Theoretical calculations based on Ginzburg-Landau calculations show that the expulsion field is almost independent of temperature when the superconductor is in the multi-vortex state. When, on the other hand, the last vortex state is a giant-vortex state, the expulsion field increases with increasing temperature. Magnetization measurements on high T_c superconductors have shown that [118] the flux penetration field decreases linearly with increasing temperature with anomalous changes in the slope close to T_c . The linear temperature dependence of the penetration and expulsion fields was also theoretically shown in Ref. [119]. As the hysteresis behavior of superconductors are due to the surface barrier, one can expect from those experimental results the linear dependence of the surface energy barrier on temperature.

In this section we investigate the temperature dependence of the surface barrier for the first vortex penetration and expulsion in a superconducting disk. As an example we consider a superconducting disk with radius $R = 1.5$ μm, thickness $d = 100$ nm, the coherence length $\xi(0) = 120$ nm and the penetration depth $\lambda(0) = 140$ nm. The $H - T$ phase diagram of this sample is given in Fig. 6.13. Fig. 2.10 shows the temperature dependence of the penetration (red curves) and expulsion (black curves) barrier ΔF for different applied fields. At small applied fields there is no barrier for flux expulsion, while the barrier for the vortex penetration is maximal. This barrier increases with increasing temperature and decreases close to $T_c(0)$. At higher fields the penetration barrier always decreases with temperature but no linear dependence is obtained. The expulsion barrier has similar temperature dependence for different magnetic fields: it increases with temperature and decreases faster at higher temperatures. The position of the maximum of the barrier shifts to lower temperatures for larger fields. This behavior of the expulsion barrier is in good agreement

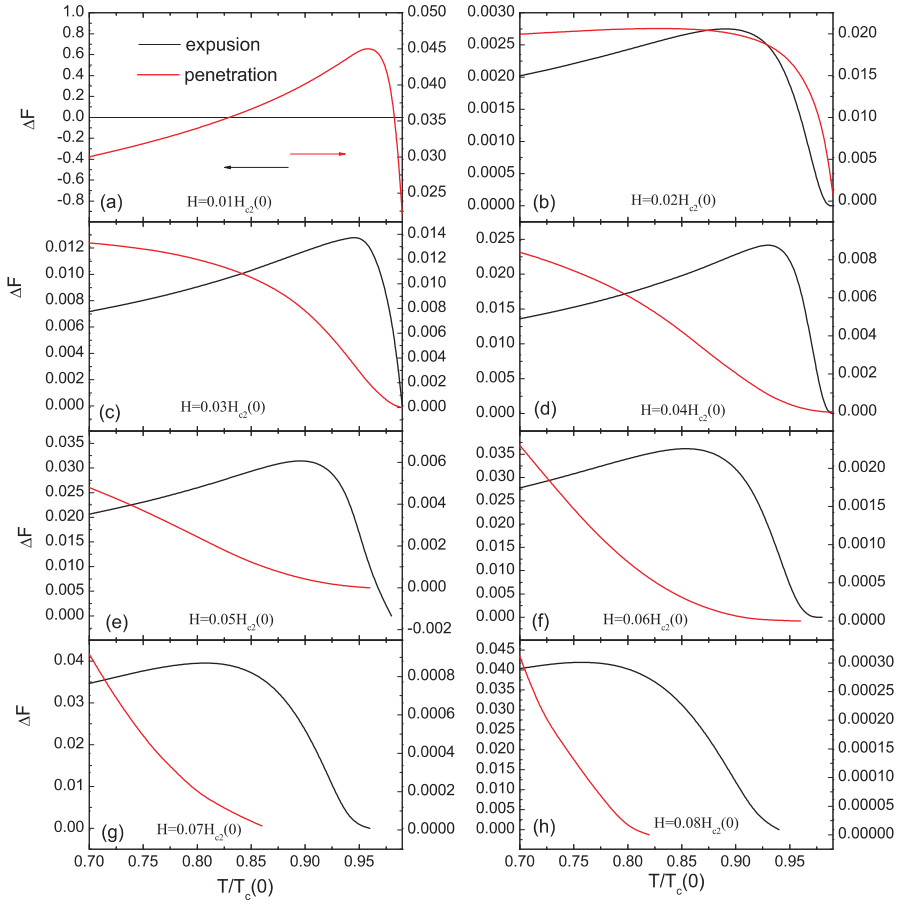

FIG. 2.10: The energy barrier for the vortex penetration(red curves) and expulsion (black curves) as a function of temperature for different applied magnetic fields for a disk with radius $R = 1.5$ μm and thickness $d = 100$ nm. The coherence length is $\xi(0) = 120$ nm and the penetration depth is $\lambda(0) = 140$ nm.

with the experimentally obtained temperature dependence of the expulsion field in mesoscopic superconductors [28, 117].

2.4 SUPERCONDUCTING RING

Although the problem of flux quantization in large superconducting rings was shown experimentally a long time ago [120], recently there was renewed interest for fluxoid dynamics in such a geometry (see for example Ref. [100]), where

jumps in the magnetization curve corresponding to changes of the vorticity larger than unity [99] were observed. These jumps appear due to the presence of several metastable states with different vorticity L at a given field and strongly depends on the stability condition for those metastable states [101]. Transitions between these states were investigated within the GL theory in

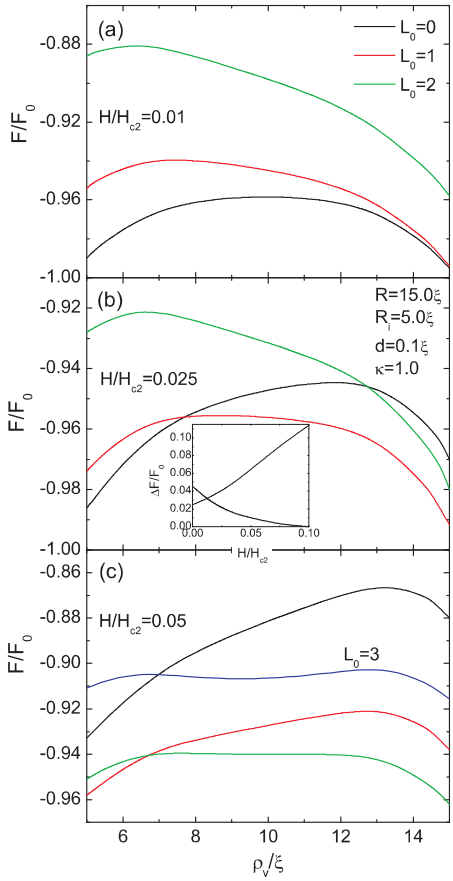

Fig. 2.11: The free energy of the superconducting ring with outer radius $R = 15\xi$, inner radius $R_i = 5\xi$, thickness $d = 0.1\xi$, and $\kappa = 1.0$ as a function of the radial position of the vortex ρ_v for three values of the applied field $H = 0.01H_{c2}$ (a), $H = 0.025H_{c2}$ (b), and $H = 0.05H_{c2}$ (c). The number of vortices inside the hole is $L_0 = 0$ (black curves), $L_0 = 1$ (red curves), and $L_0 = 2$ (green curves). Blue curve (c) corresponds to $L_0 = 3$ and $H = 0.075H_{c2}$. The inset in (b) shows the height of the energy barrier for flux penetration (thick curve) and expulsion (thin curve) for $L_0 = 0$ as a function of the applied field.

Ref. [111] through the saddle point, i.e. the lowest barrier between two different energy minima. The time for flux penetration and expulsion is determined by the height of the energy barrier. In this section we consider superconducting rings with different inner and outer radii and calculate the energy barrier for flux penetration/exit. This problem was recently considered in Ref. [102] in the London limit.

As an example, we consider a superconducting ring with outer radius $R = 15\xi$, inner radius $R_i = 5\xi$, thickness $d = 0.1\xi$, and $\kappa = 1.0$. Figs. 2.11(a-c) show the free energy of the ring as a function of the radial position of the vortex ρ_v for different values of the applied field. At low fields (a) and when there is no vortex trapped inside the ring ($L_0 = 0$) the maximum of the barrier is in the center of the superconducting region of the ring and the free energy is lowest at the outer ring edge indicating that it costs energy to add an additional vortex inside the ring. When increasing the field the barrier maximum shifts to the outer boundary of the sample (Fig. 2.11(b,c)). The inset of Fig. 2.11 shows the height of the energy barrier for flux penetration (thick curve) and escape (thin curve) as a function of the applied field. It is seen from this figure that even for zero applied field there is a barrier for vortex expulsion and we have to apply negative field to transit to the $L = 0$ state. If there are one or more vortices inside the ring the energy barrier shifts to the inner boundary of the sample and the vortex prefers to leave the sample. For some critical value of the applied field and for a given number of vortices inside the ring the energy has a local minimum in the superconducting region of the ring (green and blue

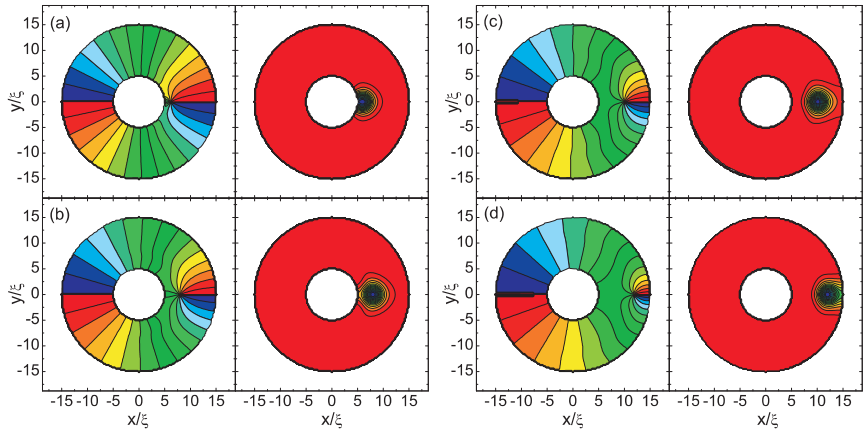

FIG. 2.12: Contour plots of the phase of the order parameter (left columns) and Cooper pair density (right columns) at $H/H_{c2} = 0.01$ for $L_0 = 1$ for the ring of Fig. 2.11. Phases near zero are given by blue regions and phases near 2π by red regions. The position of the vortex is $\rho_v = 6.0\xi$ (a), $\rho_v = 8.0\xi$ (b), $\rho_v = 10.0\xi$ (c), $\rho_v = 12.0\xi$ (d), and $\rho_v = 14.0\xi$ (e).

curves in Fig. 2.11(c)) indicating that a vortex can be trapped in a metastable state in the superconducting region of the ring. This is more pronounced when there are more vortices inside the ring and the field is higher (blue curve in Fig. 2.11(c)). For $H/H_{c2} = 0.05$ it is clear from Fig. 2.11(c) that energetically it is more favorable to add one extra vortex inside the sample when $L_0 \leq 3$. Fig. 2.12 shows contour plots of the phase of the order parameter (left column) and Cooper pair density (right column) for $L_0 = 1$ and different position of the vortex. Notice that a closed path within $\rho < \rho_v$, we correctly have a change in the phase of 2π (i.e. one flux is trapped inside the ring). If, otherwise, we choose a closed path including the vortex position, ρ_v, the phase changes by 4π. The contour lines of the Cooper pair density are nearly circular close to the vortex core, but are distorted farther away due to the geometry of the sample.

2.5 SUPERCONDUCTING SQUARE

The energy barrier for flux penetration and exit in mesoscopic superconductors is partly due to a geometric barrier, which depends on the shape of the sample, and is even more pronounced for superconductors with rectangular cross section. In such samples the edge barrier is caused by a delayed penetration of flux lines at the four corners and exhibits hysteretic behavior even if the sample is free of pinning centers [104–106]. Therefore, in this section we consider a square superconducting sample to study the influence of its edges to the surface barrier. Superconducting cylinders with rectangular cross section were

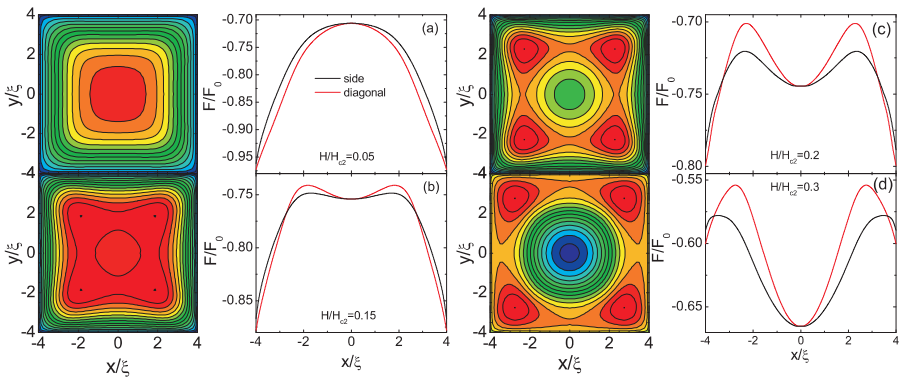

Fig. 2.13: Contour plots of the dependence of the free energy (left column) on the position of the vortex. Cross section for $y = 0$ (black curves) and diagonal $x = y$ (red curves) cross sections (right column) in a square sample with side $a = 8.0\xi$ and thickness $d = 0.1\xi$ and $\kappa = 1.0$ for four values of the applied field: $H/H_{c2} = 0.05$ (a), $H/H_{c2} = 0.15$ (b), $H/H_{c2} = 0.2$ (c), and $H/H_{c2} = 0.3$ (d).

recently considered in Ref. [121] within the London theory in the presence of an axial magnetic field. Calculations show that the energy barrier is higher in the corners and the first vortex tends to enter the sample through the middle of the edges [122].

Fig. 2.13 shows the contour plot of the free energy of the square superconductor with size $a = 8.0\xi$, thickness $d = 0.1\xi$, and $\kappa = 1.0$ for four different values of the applied field, where red regions correspond to higher energy. At small fields (Fig. 2.13(a)) the energy is maximum when the vortex is at the center of the sample and decreases when the vortex approaches to the boundary. The plot of the cross sections (right column) shows that the energy is lower in the corners. An increase of the magnetic field leads to the appearance of an energy barrier (Fig. 2.13(b,c)) which is higher near the corners of the sample. By further increasing the applied field (Fig. 2.13(d)) the position of the barrier shifts to the sample boundary. It is seen from the plot of the cross sections of the barrier energy that the barrier disappears first near the edges of the sample, which means that the vortex penetrates the sample through the center of the edges and not through the corners of the sample. Fig. 2.14 shows the energy barrier for vortex penetration (thick curves) and expulsion (thin curves) along the diagonal (dashed curves) and side (solid curves) of the square. It is seen from this figure that the vortex feels the largest barrier along the diagonal of the sample. This also means that a vortex placed in the square center has more freedom to wander laterally towards the edges than along the diagonals of the square.

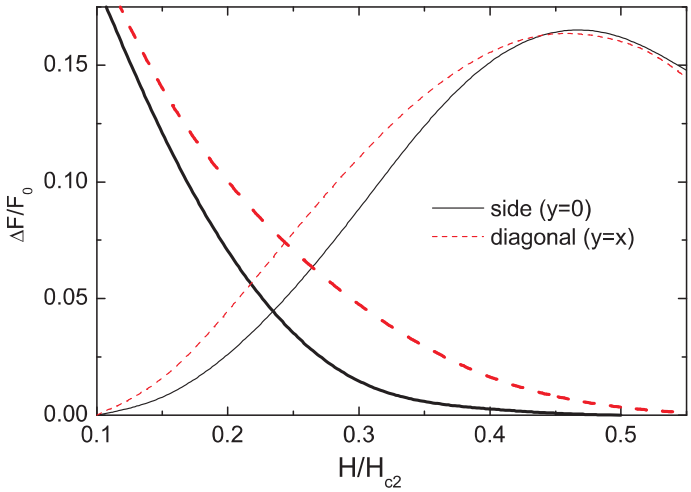

FIG. 2.14: The energy barrier for vortex penetration (thick curves) and expulsion (thin curves) along the side (solid curves) and diagonal (dashed curves) of the sample as a function of the external field for the sample of Fig. 2.13.

2.6 CONCLUSIONS

We have presented an approach to calculate the energy barrier when a single vortex enters or exits superconducting mesoscopic finite size sample. Our approach is based on a numerical solution of the coupled nonlinear GL equations using analytical expressions for the phase of the order parameter obtained from the London theory.

First we calculated the energy barrier in superconducting disks with small radius and for different values of the disk thickness and GL parameter κ. These results for the energy barrier show clearly the limitations of the London theory which considerably overestimates (underestimates) the barrier for vortex expulsion (penetration). The discrepancy between the results from the GL approach and the one from the London theory decreases with increasing size of the disk. The energy barrier strongly depends on the GL parameter κ: the magnetic field range over which the barrier exists is larger (consequently, the first critical field H_{c1}) for small values of κ, for which the sample behaves like a type-I superconductor. We also calculated the energy barrier for the vortex entry and exit at different temperatures and found the nonlinear dependence of the barrier on temperature, in contrast to previous predictions. We also studied the $L = 2$ state in the disk and found for some values of the field an energy barrier between the multivortex and the giant vortex state.

We also considered a superconducting ring and a square disk. For a superconducting ring we found a minimum in the free energy in the superconducting region of the sample for some range of magnetic field values when there are a number of vortices inside the hole, indicating that a vortex can be trapped in a metastable state in this region. For a superconducting square the vortex feels a larger barrier along the diagonal of the sample, while the lowest barrier is found along the middle of the sides of the square. The results for the square confirm the vortex entry laterally, through the sample edge.

Publications. The results presented in this chapter were published as:

- G.R. Berdiyorov, L.R.E. Cabral, F.M. Peeters, *Surface barrier for flux entry and exit in mesoscopic superconducting systems*, Journal of Mathematical Physics **46**, 095105 (2005).

3

A superconducting square with antidots

3.1 INTRODUCTION

Recent progress in microfabrication and measurement techniques made it possible to study the properties of superconducting samples with sizes comparable to the penetration depth λ and the coherence length ξ. For such mesoscopic samples nucleation of the superconducting state depends strongly on the boundary conditions imposed by the sample shape [123], i.e. on the topology of the system. Many different topologies have been studied experimentally and theoretically, which can be classified into: simple single loops [90, 123–126], multiloop structures [127–130] and large infinite networks [48]. For superconducting structures, containing a large number of antidots it is not a simple exercise to take into account the vortex-vortex interaction due to the very large number of interacting vortices. From this point of view, a microdot with an antidot cluster (2×2, 3×3, etc.) with a small number of interacting vortices is a very promising "intermediate" system between a single superconducting loop with a finite strip width [90] and a superconducting film with a large regular array of antidots. The reduced number of interacting vortices simplifies the calculations and the results may be extrapolated to the analysis of the vortex state in substantially larger antidot arrays. Moreover, the different vortex states can

be studied on a macroscopic level and they can even be visualized using scanning tunelling microscopy [35], scanning Hall probe magnetometry [37], Bitter decoration [82], magneto-optical imaging [36] and Lorentz microcopy [38].

In the last decade, several experimental studies [128, 129] were published, where the vortex state of superconducting 2×2 antidot clusters made of different kinds of superconducting material were investigated. In Ref. [128] the authors studied the transport properties of a superconducting Pb/Cu microdot with a 2×2 antidot cluster, measuring the superconducting/normal (S/N) phase boundary, the magnetoresistance, the critical currents, and the $V(I)$ characteristics. They compared their experimental results with calculations in the London limit of the Ginzburg-Landau theory and in the framework of the de Gennes-Alexander model. It was shown that vortices can be pinned by the antidots forming a cluster and that the ground-state configurations of the vortices are noticeably modified by the current sent through the structure. The authors of Ref. [129] considered a 2×2 aluminium antidot cluster and a microsquare containing two submicron holes. It was found that the S/N phase boundary $T_c(H)$ of these structures shows quite different behavior in low and high magnetic fields.

The theories used to explain experimental results for the $H(T)$ boundary of these structures were mainly based on the linearized Ginzburg-Landau theory, using either the London limit, where the modulus of the order parameter is assumed to be spatially constant, or the de Gennes-Alexander formalism [127], allowing $|\Psi(x)|$ to vary along (but not across) the strands. Fomin *et al.* [126] studied the superconducting state in a narrow mesoscopic square loop and analyzed phase boundaries on the basis of a self-consistent solution of the Ginzburg-Landau equations. Baelus and Peeters [90] considered mesoscopic superconducting disk structures containing a circular antidot and investigated the vortex structures and the $H-T$ phase boundary using the complete Ginzburg-Landau formalism.

In this chapter, we investigated the superconducting state of mesoscopic square samples containing two and four antidots in the presence of a uniform perpendicular magnetic field (Fig. 3.1). Our theoretical analysis is based on a full self-consistent numerical solution of the coupled nonlinear GL equations. As an example we took the Ginzburg-Landau parameter $\kappa = 0.28$, which is typical for *Al* thin disks [29]. The magnetic field profile near and in the superconductor is obtained self-consistently, and therefore the full demagnetization effect is included in our approach. We calculated quantities like the free energy, the magnetization, the cooper-pair density, the total magnetic field profile and the current density distribution. Due to the interplay of the different kinds of symmetry, there exists a qualitative difference in the nucleation of the superconducting state in samples with different number of antidots. In small systems vortices may overlap so strongly that it is more favorable to form one big giant vortex. In order to see clear multi-vortex configurations we chose sufficiently large values for the sizes of the samples. A square sample with side $W = 7.0\xi$

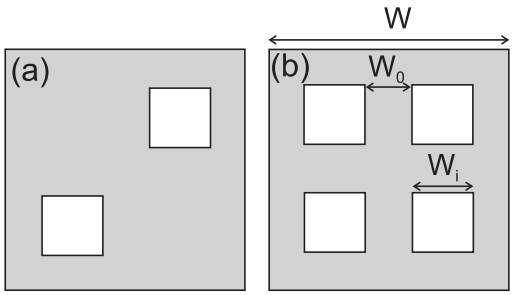

Fig. 3.1: Model configurations: superconducting square samples with two (a) and four (b) antidots. W denotes the size of the sample, W_i is the size of the antidots and W_0 is the distance between the antidots. The sample thickness is $d = 0.1\xi$.

is taken as a reference sample. The dimensions of the holes for all structures was taken the same $W_i = 2.0\xi$, and $W_0 = 1.0\xi$ is the lateral distance between the anti-dots. The thickness of all samples is taken $d = 0.1\xi$.

The chapter is organized as follows. The theoretical formulation of the problem is presented in Sec. 3.2. The free energy and magnetization of the samples are given in Se. 3.3. The stability and the configuration of different vortex states is studied in Sec. 3.4. In Sec. 3.5 we present the superconducting/normal phase boundary for the 2×2 antidot cluster. The $H - T$ diagram of this structure is compared with experimental results. Our results are summarized in Sec. 3.6.

3.2 THEORETICAL FORMALISM

In the present paper, we consider thin flat superconducting samples of different geometry which are immersed in an insulating medium in the presence of a perpendicular uniform magnetic field H. For the given system we solve two-coupled GL equations (1.59, 1.60) following the numerical approach of Schweigert and Peeters [78]. The superconducting wavefunction satisfies the boundary condition (1.55) at the sample surface and the vector potential is given by $\mathbf{A} = \frac{1}{2}H\rho\mathbf{e}_\phi$ far away from the superconductor.

To find the different vortex configurations, which include the metastable states, we search for the steady-state solutions of Eqs. (1.59, 1.60) starting from different randomly generated initial conditions. Then we increase/decrease slowly the magnetic field and recalculate each time the exact vortex structure. We do this for each vortex configuration in a magnetic field range where the number of vortices stays the same. By comparing the dimensionless (in units of $F_0 = H_c^2 V/8\pi$) Gibbs free energies (1.71) of the different vortex configurations we find the ground state, the metastable states, and the magnetic field range over which the different states are stable. The dimensionless magnetization,

which is a direct measure of the expelled magnetic field from the sample, is defined as

$$M = \frac{\langle h \rangle - H}{4\pi}, \tag{3.1}$$

where H is the applied magnetic field. $\langle h \rangle$ is the magnetic field averaged over the sample, i.e. superconductor and holes, and $\mathbf{h}$ =rot $\mathbf{A}$.

3.3 FREE ENERGY AND MAGNETIZATION

The free energy and magnetization of the mesoscopic superconducting samples give us plenty of information on the physical processes in the superconductor, and therefore we will first compare the free energy and magnetization for our different superconducting samples. Figs. 3.2(a-c) show the free energy for the reference sample and for the square superconductor with two and four holes, respectively, as a function of the applied magnetic field. The insets show an enlargement of the free energy of the states with large vorticity. In the reference sample (Fig. 3.2(a)) vortex states up to $L = 11$ can nucleate. At lower magnetic fields states with vorticity L =2, 3, 4, 5 and 6 are multivortex states (see [79]). Further increase of the magnetic field leads to the formation of the giant vortex state in the center of the sample.

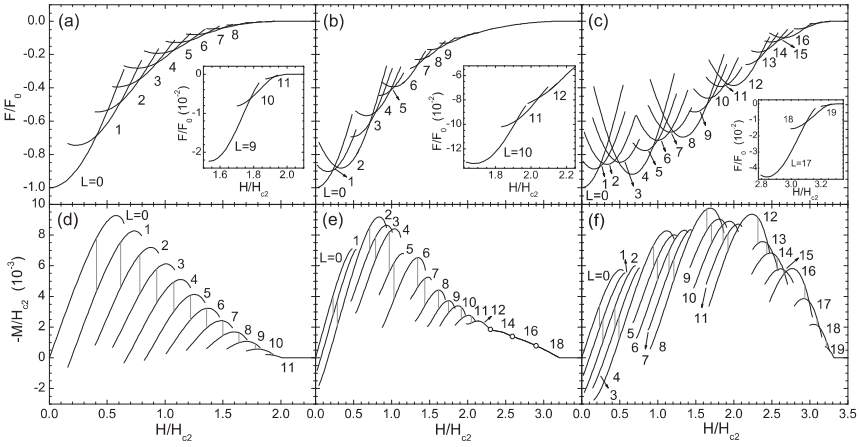

FIG. 3.2: The free energy (a-c) and magnetization (d-f) as a function of the applied magnetic field for a filled square (a,d) and for the square with two (b,e) and four (c,f) antidots. The insets show the free energy for higher vorticity. The vertical lines show the ground state transitions between different vortex states and open circles indicate continuous transitions between different vortex states. The GL parameter is $\kappa = 0.28$.

The insertion of antidots in the sample changes the free energy of the sample considerably (Fig. 3.2(b)). In this case all ground state transitions between different vortex states occur at lower magnetic fields. The $L = 2$ state is stable over a much larger magnetic field range than the other states. Notice also that the superconducting/normal transition field is larger. This field is $H/H_{c2} = 2.01$ for the reference sample and $H/H_{c2} = 3.22$ for the superconductor with two holes. The 60 % increase of the critical magnetic field is completely due to the narrow superconducting area in the corners of the sample. It is well-known that superconductivity is enhanced [131] in such corners. The maximum vorticity which can be accommodated in the full square is $L = 11$, while for the sample with two holes, this is 18. Contrary to the results for the reference sample, here we found with increasing magnetic field $\Delta L = 2$ transitions such as $L = 2 \rightarrow L = 4$, $L = 6 \rightarrow L = 8$, $L = 12 \rightarrow L = 14$, $L = 14 \rightarrow L = 16$, and $L = 16 \rightarrow L = 18$. Notice that the last three transitions are continuous and for these transitions $\Delta L = 2$; i.e. states with vorticity $L = 13$, 15, 17 do not become the ground state. The continuous vortex transitions are a consequence of the non-circular geometry of the sample and are analogous to those found earlier in ring-like structures with non-uniform width [90, 125]. The energy of all superconducting states are lower and the ground state transitions occur at lower magnetic fields as compared to the previous sample. Notice also that the superconducting state with even vorticity are more stable than those with odd vorticity.

The most interesting case is the superconductor with four antidots. The free energy of this sample is given in Fig. 3.2(c). Notice that each of the vortex states have a larger stability region, the energy of the different superconducting states are lower as compared to all previous cases, the transitions between different L states occur at lower magnetic fields and all thermodynamic equilibrium transitions are discontinuous with $\Delta L = 1$. Vortex states with vorticity up to $L = 19$ can be nucleated and the S/N transition field $H/H_{c2} = 3.32$ is the highest of all the six considered structures. There is also a clear enhancement of the stability for states with L =4, 8, 12 and 16.

Figs. 3.2(d-f) shows the magnetization of the different vortex states for the considered samples. The magnetization (3.1) is a measure of the expelled flux from the sample and is calculated after averaging the field only over the superconducting region excluding the holes. In these figures the vertical gray lines indicate the ground state transitions. Notice that in the rest of the text we define the magnetization as $-M$, i.e. the difference between applied magnetic field and averaged magnetic field. In the absence of the antidots (see Fig. 3.2(d)) the maxima in the magnetization curve decreases with increasing L which is not so for the other samples. For the two antidot sample the largest flux expulsion is reached for $L = 2$, i.e. it equals the number of antidots. The sample with four antidots behave very different and we found that $-M$ is maximal for $L = 8$. There is also a clear bunching of the magnetization curves with increasing number of antidots which is absent in our reference sample.

The number of curves which are bunched together increases with the number of antidots. Only the vortex states with vorticity less or equal to the number of antidots exhibit a paramagnetic response. Note that for the reference sample a paramagnetic response [132] can be realized in a small magnetic field region of the L =1, 4, 5 states. It should be stressed that the superconductor is in a metastable state when such a paramagnetic response is found.

3.4 STABILITY OF DIFFERENT VORTEX STATES

Fig. 3.3(a) shows the magnetic field range ΔH_s over which the vortex state with vorticity L is stable (i.e. $\Delta H_s = H_{penetration} - H_{expulsion}$) as a function of the vorticity L. The stability of each individual superconducting state is very sensitive to the topology of the sample. For the reference sample $\Delta H_s(L)$ decreases with increasing L, except for the $L = 4$ state which exhibits an enhanced stability and which is clearly a consequence of the commensurability of the square vortex lattice with the square geometry of the sample as we pointed out earlier [79]. For the samples with antidots, the vortex states with even vorticity are more stable than the ones with odd vorticity. For the 4 anti-dot system vortex states in which L are multiples of 4 have the highest stability. The L-states with enhanced stability are clearly a consequence of matching phenomena. The magnetic field range over which each of the vortex states are the ground state ΔH_g are shown in Fig. 3.3(b). The ground state region ΔH_g also shows similar features as the stability region ΔH_s. There is one main difference, ΔH_s exhibits an overall decrease with increasing L in the larger magnetic field region which is not present in ΔH_g. In all cases, the vortex states show enhanced stability for commensurate vorticity, namely when the

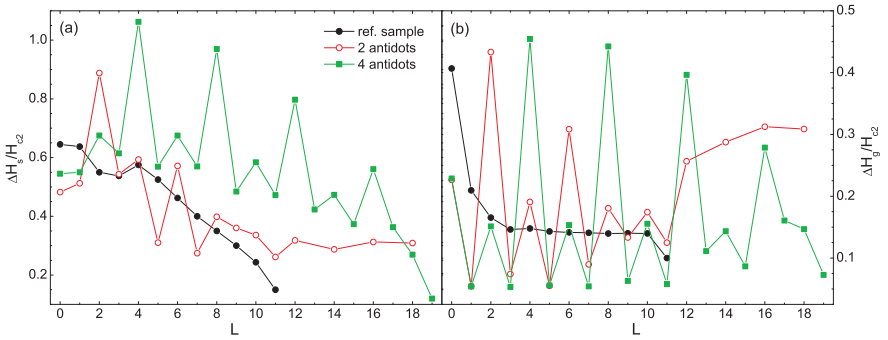

FIG. 3.3: The magnetic field region ΔH_s over which the state with vorticity L is stable (a) and the magnetic field region ΔH_g over which the state with vorticity L is the ground state (b) as a function of the vorticity L for the reference sample (black curves) and for the samples with two (red curves) and four (green curves) antidots.

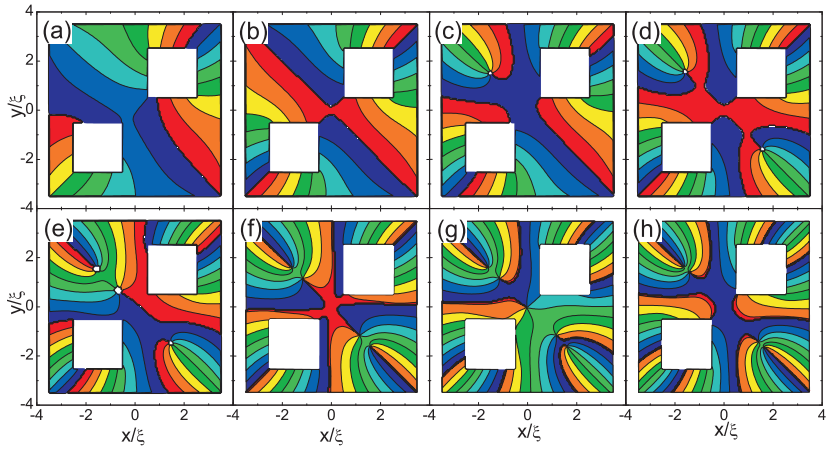

Fig. 3.4: The phase of the order parameter for the superconductor with two holes for the states with L =3 (a), 4 (b), 5 (c), 6 (d), 7 (e), 8 (f), 9 (g) and 10 (h) at H/H_{c2} =0.76, 0.87, 1.02, 1.1, 1.38, 1.51, 1.67, and 1.81, respectively. Phases near zero are given by blue regions, phases near 2π by red regions. The GL parameter is $\kappa = 0.28$.

number of vortices penetrating the sample is a multiple of the number of holes. However, for higher magnetic field these commensurability effects disappear or are less pronounced, which is due to the finite size of the sample.

The sample with two antidots is more symmetric than the reference sample and this symmetry will have an influence on the position of the vortices. We show in Figs. 3.4(a-h) the phase of the order parameter for the states with vorticity $L = 3 - 10$ at H/H_{c2} =0.76, 0.87, 1.02, 1.1, 1.38, 1.51, 1.67, 1.81, respectively. At these magnetic fields the vortex states in question correspond to the ground state. The $L = 1$ and $L = 2$ vortex configurations are trivial. For $L = 1$ there is one vortex in one of the antidots and the groundstate is *degenerate* with respect in which antidot the vortex is located. When $L = 2$ each antidot contains a single vortex. For $L = 3$ the extra vortex is located in one of the antidots (Fig. 3.4(a)) and the superconducting state is again degenerate. When $L = 4$ two vortices nucleate in each of the antidots (Fig. 3.4(b)). The fifth and the sixth vortex are situated in the superconducting region along the diagonal (Figs. 3.4(c,d)). When the 7^{th} vortex enters the superconductor, its position is close to the center of the sample (Fig. 3.4(e)). This non symmetric vortex arrangement with respect to the diagonal passing through the antidots is energetically preferred because of the narrow superconducting region between the two antidots where superconductivity is enhanced [131]. Fig. 3.4(f) shows that for $L = 8$ there are two vortices in each hole and the other vortices are along the diagonal in the superconducting region forming two clusters each consisting of two closely spaced vortices. The 9^{th} vortex is stabilized in the center

of the sample (Fig. 3.4(g)). When the 10^{th} vortex enters the superconductor, it initially forms a giant vortex in the center with vorticity $L = 2$, but we found that this giant vortex is not stable and eventually the giant vortex decays in two separate vortices, each of them moves to each of the holes (Fig. 3.4(h)). Till the $L = 16$ state all other vortices are situated along the diagonal. Increasing further L we found that the number of vortices in each hole increases with one unit. Superconductivity is then only preserved in the corners of the sample where the holes are placed and that the rest of the sample is practically in the normal state.

For the sample with four antidots the vortices are, up to high magnetic fields, located in the antidots. As a consequence the phase of the superconducting condensate Ψ contains less information and therefore we show in Figs. 3.5(a-h) the magnetic field distribution for the sample with 4 holes for the states with vorticity L =1-4, 12, 13, 14 and 17 at H/H_{c2} =0.25, 0.33, 0.46, 0.67, 1.2, 2.36, 2.48 and 2.97, respectively. At these values of the magnetic fields, the considered states correspond to the ground state of the superconductor. The applied magnetic field is always given by the same grey color. Up to the first penetration field, the magnetic field is expelled from the superconductor and we see an increased magnetic field near the boundary of the superconductor. But even in this case there is some increased magnetic field in all antidots. At $H/H_{c2} = 0.5575$ the first vortex enters the superconductor. One can expect that the position of this vortex can be in any of the 4 holes (Fig. 3.5(a)) (for a much smaller size of the superconductor this vortex can be located in

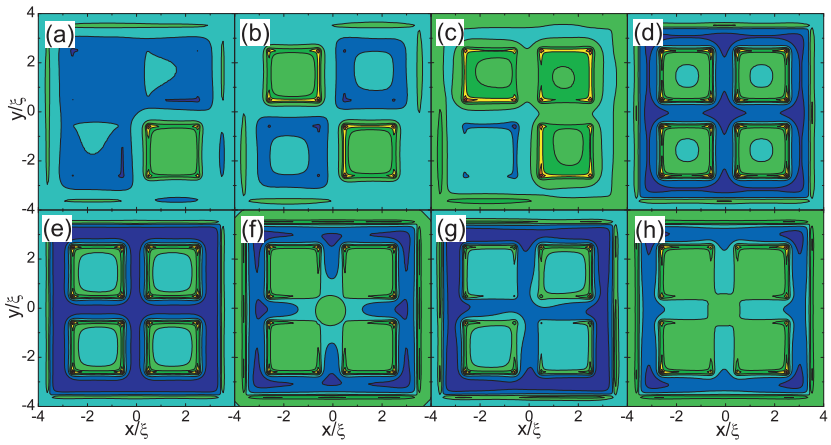

FIG. 3.5: The magnetic field distribution for the superconductor with 4 holes for the states with vorticity L =1 (a), 2 (b), 3 (c), 4 (d), 12 (e), 13 (f), 14 (g) and 17 (h) at H/H_{c2} =0.25, 0.33, 0.46, 0.67, 1.2, 2.36, 2.48 and 2.97, respectively. Higher magnetic field is given by red regions and lower by blue regions. The GL parameter is $\kappa = 0.28$.

the center of the superconductor). The second vortex is situated in the hole opposite to the hole containing the first vortex (Fig. 3.5(b)). The probability for the third vortex to be located in one of the remaining two holes is equal. In the depicted configuration the third vortex is in the top right hole, as shown in Fig. 3.5(c). For the $L = 4$ state all antidots contain a single vortex (Fig. 3.5(d)). This rule of filling the antidots with vortices is repeated up to the 12^{th} vortex (Fig. 3.5(e)). The 13^{th} vortex appears in the center of the sample (Fig. 3.5(f)), which is due to the small sizes of the holes which prevent them to capture more vortices at those fields and the fact that if the extra vortex would go to one of the antidots a very asymmetric configurations would be obtained which is energetically unfavored. When the 14^{th} vortex appears in the superconductor, the symmetry can be restored by moving two vortices to the holes (Fig. 3.5(g)). Starting from $L = 17$, the superconductivity in the central region of the sample is destroyed and vortices move to the center. After the 19^{th} vortex the sample transforms into the normal state.

3.5 SUPERCONDUCTING/NORMAL PHASE TRANSITION

In this chapter, we investigate the influence of temperature on the superconducting state in the square sample with four antidots. The temperature dependence of the coherence length ξ and the magnetic field H_{c2} (see Eqs. 1.52 - 1.54) will be included in our calculation. Therefore, the distances are now expressed in units of $\xi(0)$, magnetic field in $H_{c2}(0)$ and temperature will be rescaled by the critical temperature T_{c0} at zero magnetic field.

In order to compare our results with the experimental ones, we used the parameters from Ref. [129] where the nucleation of superconductivity in an unform perpendicular magnetic field in aluminium microsquares containing a few (two and four) submicron holes was investigated. They used the coherence length $\xi(0) = 92$ nm, and the penetration depth $\lambda(0) = 140$ nm which was found for a full square superconductor as well as for the microsquares with antidots. The parameters of our samples are as follows (see Fig. 3.1): $W/\xi(0) = 22.17$, $W_i/\xi(0) = 5.0$, $W_0/\xi(0) = 5.0$, $d/\xi(0) = 0.26$, and $\kappa = 1.52$. The calculated $H - T$ phase boundary, using these values, is presented in the inset of Fig. 3.6, which shows clear oscillations in the superconducting/normal state boundary. Moreover, the period of the oscillation and the peak amplitude for the state with vorticity $L = 4$ is larger than for the other states, which is due to a commensurability effect when the number of vortices is a multiple of the number of holes. Comparing our results with experiment (see Ref. [129]), we notice a clear qualitative agreement. But the theoretical predicted S/N transition at a fixed L occurs at higher temperatures than observed experimentally. Also the transitions between the successive L states appear at slightly larger fields in our calculations. This quantitative disagreement between our theory and

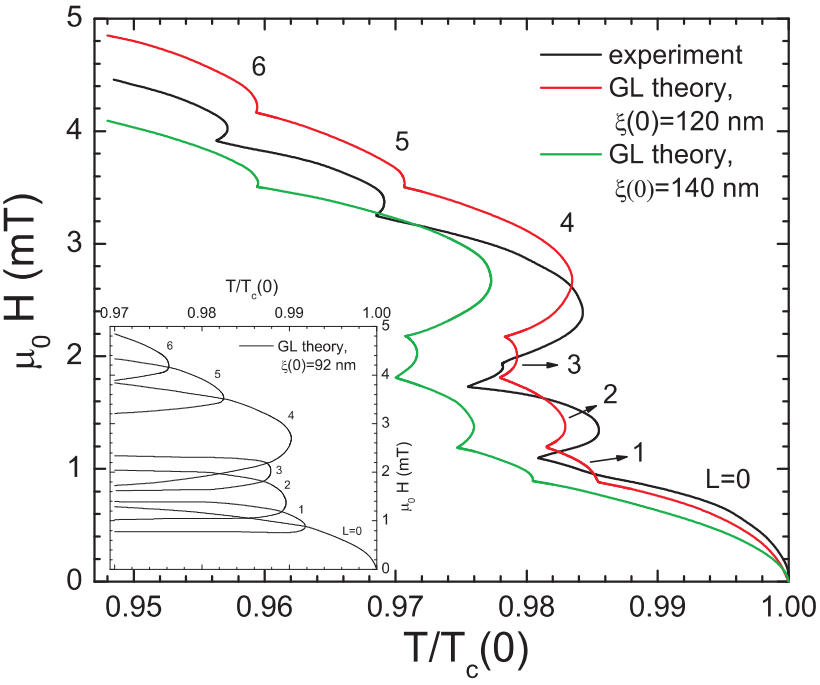

FIG. 3.6: The $H-T$ phase diagram for the superconducting sample with 4 holes for $\xi(0)=120$ nm (red curve) and for $\xi(0)=140$ nm (green curve). The parameters of the superconductor are $W=17.0\xi(0)$, $W_i=3.83\xi(0)$, $W_0=3.83\xi(0)$, $d=0.2\xi(0)$, $\kappa=1.17$ for $\xi=120$ nm, and $W=14.57\xi(0)$, $W_i=3.29\xi(0)$, $W_0=3.29\xi(0)$, $d=0.17\xi(0)$, $\kappa=1.0$ for $\xi=140$ nm. The black curve is experimentally obtained result. The inset shows the $H-T$ phase diagram for the superconducting sample with 4 holes when $\xi(0)=92$ nm. The parameters in this case are $W=22.17\xi(0)$, $W_i=5.0\xi(0)$, $W_0=5.0\xi(0)$, $d=0.26\xi(0)$, $\kappa=1.52$.

the experiment can be due to: (i) the uncertainties in the dimensions of the sample (holes), (ii) the criteria used for determining whether the sample is in the superconducting (normal) state or not, and/or (iii) the assumed value of the coherence length at zero temperature. To explore the latter possibility, we repeated the calculation and varied $\xi(0)$ keeping all other parameters fixed.

The $H-T$ phase diagram for the four-antidot superconductor is shown in Fig. 3.6 for the states with vorticity up to $L=6$. The solid curve was obtained experimentally in Ref. [129] and the red curve is the theoretically calculated $H-T$ phase diagram for $\xi(0)=120$ nm. For this value of the coherence length the correspondence is obviously much better, since the transition temperatures in our theoretical curve closely follows those from the experimental results. Still, a small difference in the transition fields exists. In our model,

the transitions occur at slightly higher temperatures. This can be explained by the different criteria for the determination of the S/N transition. Namely, in the experiment, one assumes that superconductivity is destroyed when the region between the contacts becomes normal. In our model, for the same magnetic field, superconducting regions would still be present in the corners of the sample [131, 133]. Our transition fields are related to the destruction of superconductivity in the whole sample, and therefore, they are higher than the experimental ones. In Ref. [129] the authors mentioned also another value for the coherence length $\xi(0) = 140$ nm, which was deduced for the 2×2-antidot system on the basis of de Gennes-Alexander (dGA) model [127]. The green curve in Fig. 3.6 shows the result of our calculations for such value of $\xi(0)$. Our previous analysis still holds but now the theoretical transition temperatures are lower than the experimental ones and the transition fields are also lower.

In Fig. 3.7 we compare the low magnetic field part of the experimentally obtained $T_c(H)$ (black curve) with the $T_c(H)$ obtained in our calculations for $\xi(0)$ =120 nm (red curve) and for $\xi(0)$ =140 nm (green curve), where a parabolic background

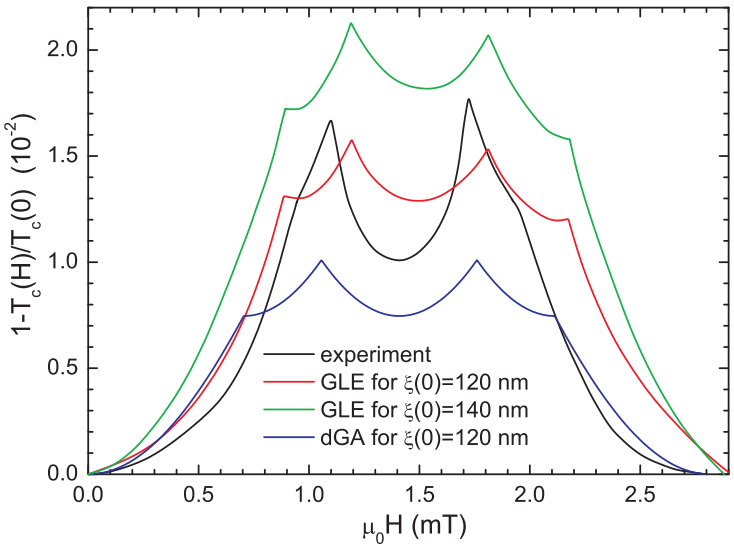

Fig. 3.7: Low-field part (single period) of the experimentally obtained $T_c(H)$ phase boundary (black curve, Ref. [129]) of the four-hole sample (where a parabolic background has been subtracted) compared with the theoretically calculated ones for $\xi(0)$ =120 nm (red curve) and for $\xi(0)$ =140 nm (green curve). The blue curve is the phase diagram calculated using the dGA model for a 2×2 cell network made of one-dimensional strips for $\xi(0)$ =120 nm, and the red curve illustrates the results of the GL simulation.

$$1 - \frac{T_c(H)}{T_c(0)} = \frac{\pi^2}{3}\left(\frac{\omega\xi(0)\mu_0 H}{\Phi_0}\right)^2 \tag{3.2}$$

was subtracted. This formula was obtained in Ref. [129] for a 2×2-cell network consisting of one dimensional strips with finite width ω. We also give the $T_c(H)$ phase boundary calculated from the dGA model for a 2×2 cell network made of one-dimensional strips (see Ref. [128]) for $\xi(0)$ =120 nm (blue curve). Although the dGA model gives a rather good qualitative agreement of the observed transition fields, our theoretical results lead to a better overall quantitative agreement. Qualitatively, the only difference is that in our calculations the transition fields between the different vortex states occur at slightly higher fields.

3.6 CONCLUSIONS

We have investigated the superconducting state and critical parameters superconducting square samples containing two and four submicron antidots. We calculated the free energy as a function of the applied magnetic field, which shows the considerable influence of antidots to the number of possible vortex states, their stability and transitions between them. For the reference sample vortex states up to L=11 can nucleate, with S/N transition field $H_{c3}/H_{c2} = 2.01$, while for the sample with two (four) antidots these numbers are L=18 (19) and H_{c3}/H_{c2}=3.22 (3.32). Increasing the number of holes in the sample decreases the free energy for a fixed L and ground state transitions between different vortex states occur at lower magnetic fields. We also found that the stability of each individual superconducting state is very sensitive to the topology of the sample: the states with even vorticity are more stable than the ones with odd vorticity. The vortex states show enhanced stability for commensurate vorticity, i.e. when the number of vortices is a multiple of the number of holes. However, due to the finite size of the samples this effect is less pronounced at high magnetic field. For the reference sample and for the four-antidot sample we found only transitions between successive L states, i.e. $\Delta L = 1$ in increasing field, where all transitions correspond to a jump in the free energy curve. But for the two antidot sample transitions between vortex states with high vorticity occur continuously with possible $\Delta L = 2$ transitions. The magnetization is strongly influenced by the presence of the antidots. For the reference sample the maximum of the magnetization correspond to the Meissner state, i.e. $L = 0$ state, while this state becomes less stable for the samples with antidots. For the two-antidot sample the largest flux expulsion is reached for $L = 2$. The sample with four antidots behave very different and maximum magnetization is reached for $L = 8$. For the samples with antidots paramagnetic response (i.e. $-M < 0$) was found for the sates with vorticity less or equal to the number

of antidots, while for the reference sample this effect occur for the $L = 1, 4, 5$ states.

We also studied S/N phase boundaries for the four-antidot sample and compared the results with experiment. The calculated $H - T$ phase diagram shows clear oscillations in the S/N boundary. Contrary to the full square superconductor, in the four-antidot sample the period of the oscillations and the peak amplitude is not the same for all vortex states, which was explained by the stability of the different vortex states. We also studied the influence of the value of $\xi(0)$ on the S/N boundary. The theoretically calculated $H - T$ diagram shows good agreement with the experimental results.

Publications. The results presented in this chapter were published as:

- G.R. Berdiyorov, B.J. Baelus, M.V. Milosevic, and F.M. Peeters, *Stability and transition between vortex configurations in square mesoscopic samples with antidots*, Phys. Rev. B **68**, 174521 (2003).
- G.R. Berdiyorov, B.J. Baelus, M.V. Milosevic, and F.M. Peeters, *The superconducting state in square mesoscopic samples with two and four antidots*, Physica C **404**, 56-60 (2004).

4

Superconducting thin films with an antidot lattice

4.1 INTRODUCTION

Periodically engineered systems with an energy landscape with many degenerate minima can be found in various areas of physics and they often exhibit mutually common phenomena. Typical examples are colloidal crystals on periodic substrate or light arrays [134], biomolecular chains formed in an array of obstacles [135], ordering of atoms and molecules absorbed on corrugated surface [136], the electron configurations in arrays of quantum dots [137], or lattice of superfluid vortices in Bose-Einstein condensates interacting with periodic optical traps [138].

In superconductivity, a similar system has been realized in films with regular arrays of antidots. Namely, direct imaging experiments [38], magnetization, transport, and *ac*-susceptibility measurements [46, 48, 59, 61], have shown that the vortices form highly ordered configurations at integer $H_n = n\Phi_0/S$ and at some fractional $H_{p/q} = \frac{p}{q}\Phi_0/S$ (n, p, q being integers) matching fields, where $\Phi_0 = hc/2e$ is the flux quantum, and S is the area of the primitive cell of the artificial lattice. These commensurability effects between the pinning centers and the vortex lattice are reflected in an enhancement of the critical current, resulting from the collective locking of vortices to the pinning sites.

Following the experimental studies on perforated superconductors, significant efforts have been made on the theoretical side as well. For example, extensive molecular dynamics simulations [139–142] have been performed within the London limit to study the vortex structure and their dynamics in a periodic pinning potential. Although the description of the general behavior of vortex lattices was satisfactory, the made approximations are valid only in a limited parameter space because vortices were considered as classical point-particles and the pinning was introduced through an attractive potential (often a Gaussian). As a consequence, a lot of interesting physics was left out which cannot be described adequately in such a crude approximation. Vortices are extended objects which interact in a non-trivial way with the antidot lattice leading to new phenomena which have not been anticipated up to now. Here, we will apply the full Ginzburg-Landau theory which allows for any vortex rearrangement, their merging, coupling, and any other feature imposed by the geometry and/or pinning strength of the antidot-lattice. As will be shown in this chapter, such features lead to novel commensurability phenomena and new vortex structures.

Most of the experiments on perforated superconducting films are carried out in the effective type-II limit ($\kappa^* = \lambda^2/d\xi \gg 1/\sqrt{2}$, d being the thickness of the superconducting film and λ the magnetic penetration depth). In this regime, the vortices act like charged point particles and their interaction with periodic pinning potential can be described using molecular dynamic simulations [139–142]. However, the overlap of vortex cores (with size $\sim \xi$), and the exact shape of the inter-vortex interaction (depending on the superconducting material properties reflected through κ), may significantly modify the vortex structures and consequently the critical current when this criteria is no longer satisfied.

Besides, the vortex-pinning and the critical current enhancement, higher critical field (H_{c3}) near an open circular hole in a thin film (the so-called "surface superconductivity") has been predicted theoretically [143] and confirmed experimentally [144]. Cusps in the $H - T$ boundary were observed, which occurs when the number of vortices which nucleate inside the hole increases by one, similarly to the known Little-Parks effect [7]. The ratio between the critical fields in perforated samples was estimated in limiting cases: $H_{c3}/H_{c2} = 1$ when $R \to 0$ (or $R << \xi$) and $H_{c3}/H_{c2} = 1.695$ when $R \to \infty$.

In this chapter of the thesis superconducting films with square arrays of antidots are treated within the phenomenological Ginzburg-Landau theory. This approach considers vortices as extended objects and no approximations have to be made on e.g. the vortex-vortex interaction and/or the vortex-antidot interaction. In Sec. 4.2, the details of our numerical formalism are given. Sec. 4.3 deals with vortex lattices in perforated films in homogeneous magnetic field, with emphasis on the number of pinned and interstitial vortices as function of the antidot-size and interhole distance. The vortex structures in perforated

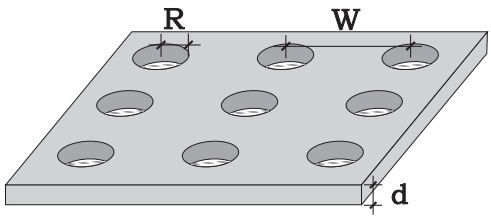

Fig. 4.1: Schematic view of the sample: a superconducting film (thickness d) with a regular array (period W) of circular antidots (radius R).

type-I superconducting films are investigated in Sec. 4.4. In Sec. 4.5, we address the behavior of critical current in the sample as function of the applied field, for different geometrical parameters, and temperature. The dependence of the critical field on temperature, and different regimes in the $H-T$ phase diagram are discussed in Sec. 4.6 for different antidot-size. All presented findings are then summarized in Sec. 4.7.

4.2 THEORETICAL FORMALISM

We consider a thin superconducting film (of thickness $d \ll \xi, \lambda$) with a square array of holes (radius R, period W) immersed in an insulating media in the presence of a perpendicular uniform applied field H (see Fig. 4.1). The superconducting state of the sample is described by the Gibbs energy functional (1.67), which takes into account not only the intrinsic energy of the sample, but also the energy contribution due to the deformation of the magnetic field lines around the superconductor. In Eq. (1.67), all distances are scaled by the coherence length ξ, the vector potential $\mathbf{A}$ by $c\hbar/2e\xi$, the magnetic field $\mathbf{h}$ by $H_{c2} = c\hbar/2e\xi^2 = \kappa\sqrt{2}H_c$, and the order parameter ψ by its equilibrium value in the absence of the magnetic field.

The minimization of Eq. (1.67) leads to the well known GL equations, which we averaged over the superconductor thickness (being much smaller than the characteristic lengths ξ and λ), mapped on a uniform Cartesian grid (with more than 10 points per ξ), and solved self-consistently for $\mathbf{A}$ and Ψ using the iterative procedure from Ref. [78] in combination with the link-variable approach [85] given by Eq. (1.62). Our simulation region is a $W_S \times W_S$ square, mostly with $W_S = 4W$ where W is the period of the antidot-array (i.e. we simulate a 4×4 supercell). In order to include periodicity in our calculation, we apply the periodic boundary conditions (1.57, 1.58) for $\mathbf{A}$ and Ψ, where the gauge potential η_i fulfils the Landau gauge $\mathbf{A}_a = Hx\mathbf{e}_y$ for the external vector potential (e.g. $\eta_x = HW_S y$, $\eta_y = 0$). Note that the chosen values of H must

provide the *flux quantization per supercell*, as required by the virial theorem [84].

4.3 VORTEX STRUCTURE IN PERFORATED SUPERCONDUCTING FILMS

4.3.1 Equilibrium vortex configurations

We studied the vortex structure of a superconducting film (with thickness d) with a square array of circular holes (of radius R) exposed to a homogeneous magnetic field H (see Fig. 4.1). For a given magnetic field the final vortex configuration depends on the geometrical parameters of the antidot-lattice. As a representative example, we constructed the equilibrium vortex phase diagram for the 4^{th} matching field ($H = H_4$), as a function of W and R, shown in Fig. 4.2 for $d = 0.1\xi$ and $\kappa = 0.45$ ($\kappa^* = 2.025$). Out of 4 vortices per unit cell, n_o vortices are captured by the hole, and the remaining ones sit at interstitial sites. From this phase diagram we notice: 1) that the occupation number (n_o) of each hole depends not only on the hole-radius R (as discussed in previous works [68]), but also on W, i.e. the proximity of the neighboring holes in the lattice. 2) The final configuration of the flux-lines is determined not only by their mutual repulsion, but also by the attraction by the antidots and the repulsion by there pinned vortices. Therefore, instead of having an Abrikosov lattice, for close spacing $W(< 15\xi)$, the flux-lines form square-shaped lattices regardless of n_o (see the insets on the right of Fig. 4.2). Note that these configurations have been observed experimentally using Lorentz microscopy in Ref. [38]. 3) With decreasing period W, the interstitial vortices become strongly caged between the neighboring antidots, resulting in the disruption of the individual-vortex lattice. The best example is the part of the diagram for $n_o = 1$, where caging effect first causes the formation of triangular multivortices (MV) at interstitials, with chosen orientation that minimizes the energy between the neighboring cells. However, these triangular structures do not follow the imposed square symmetry, and with further decrease of W, the confinement causes the formation of the *giant-vortex* (GV) at each interstitial site (yellow area in Fig. 4.2). The GV state was predicted previously for superconducting disks [78] and recently observed experimentally [83]. This is the first time that such a state is anticipated for an open geometry. 4) Surprisingly, there is a small area in the phase diagram where a vortex-antivortex (VAV) pair is created, resulting in a configuration with 4 vortices in a square MV, with an antivortex in the center (resulting in five zeros of the order parameter, see the leftmost inset of Fig. 4.2). These symmetry imposed VAV states are in essence very similar to the ones found in finite superconducting polygons [145–147]. As compared to previous studies of nanostructured superconducting films, it is important to

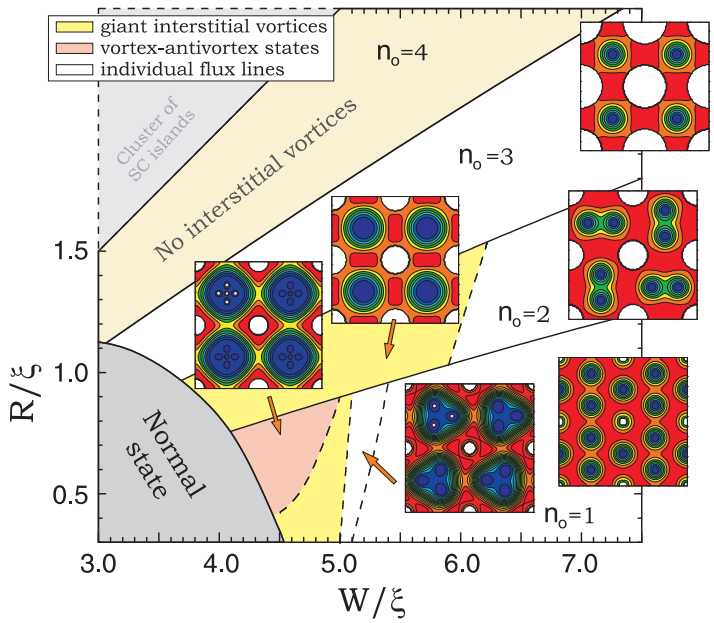

Fig. 4.2: The equilibrium vortex lattices at $H = H_4$, as a function of the radius (R) and the period (W) of the antidots. The solid lines denote the first order transitions between the states with different antidot occupation number (n_o), and dashed ones depict second order configurational transformations. The insets denote the Cooper-pair density plots (blue/red-low/high density, white color-antidots) of the corresponding states (open dots are a guide to the eye indicating the position of the zeros of the order parameter).

emphasize here that it is not only the commensurability between number of vortices and the number of pinning sites (so-called "matching") that carries important physics in superconductors with antidot arrays, but also the here predicted *commensurability in geometry* between the antidot- and the vortex lattice.

In order to verify these findings, and show they are not peculiar for one chosen field, we repeated our analysis for the rational matching field $H = H_{9/2}$. The ground-state $W - R$ diagram is shown in Fig. 4.3. For sufficient spacing between the antidots, the vortex configuration consists of individual vortices, where a kind-of vortex lattice is established by one extra vortex (compared to $H = H_4$) being shared between the adjacent cells. Alternatively, every other interstitial site contains this extra vortex (at each site a MV is formed, but with different vorticity). As a consequence, for a dense antidot lattice, the confinement/symmetry does not act equally on adjacent cells - e.g. for $n_o = 1$, at one site MV with vorticity 4 obeys the imposed symmetry, whereas the

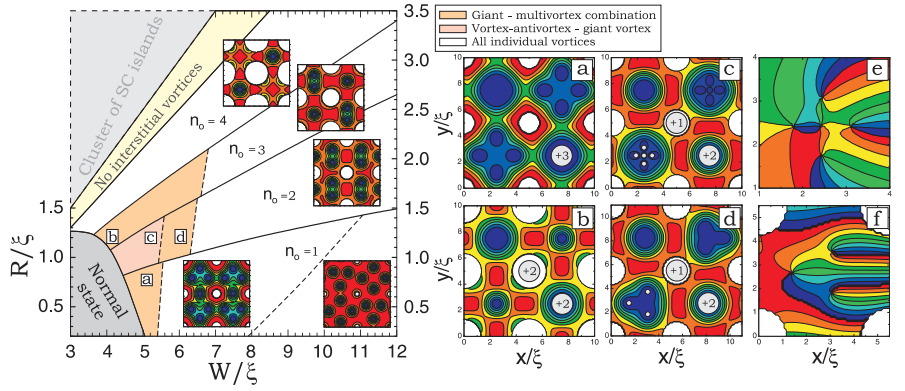

FIG. 4.3: The ground-state vortex lattices at $H = H_{9/2}$ fractional matching field (same notation as in Fig. 4.2 is used). Figs. (e-f) show the phase of the order parameter (blue/red-$0/2\pi$ phase) of the bottom left unit cell for the vortex configurations depicted in Figs. (c-d), respectively.

neighboring triple vortex is compressed into a giant form (Fig. 4.3(a)). The simultaneous presence of a *stable giant and a multi vortex* is unique and has never been predicted before. For $n_o = 2$, 3 vortices at one of the interstitials are not favored by symmetry (Fig. 4.3(d)), and for small spacing W a VAV configuration is induced, in combination with a giant vortex at adjacent site (Fig. 4.3(c)), illustrating the remarkable variety of possible vortex structures.

4.3.2 Influence of temperature on the stability of the vortex-antivortex pairs

As follows from our formalism, all the sizes in our analysis so far were expressed in units of the coherence length ξ. In order to direct the experiment, we will now use conventional units and introduce temperature in the calculation through the $\xi(T) = \xi(0)/\sqrt{1 - T/T_c}$ dependence.

Fig. 4.4(a) shows the $H - T$ equilibrium diagram for a Pb sample ($\xi(0) \approx 40$ nm, $\kappa \approx 1$) with $W = 600$ nm and $R = 110$ nm, at magnetic fields between the 3^{rd} and 6^{th} matching field. These parameters were chosen such that we are located in the middle of the VAVs region in Fig. 4.2 at $H = H_4$. Then by removing or adding vortices one by one (due to the virial theorem [84]), and changing the temperature, we constructed the $H - T$ diagram for the stability of different VAV configurations. Notice that e.g. for $H = H_5$ a new reentrant behavior (non-VAV vs. VAV states) is found as a function of temperature. For $T \approx T_c(H_5)$, $\xi(T)$ is large, only one vortex can be pinned by each antidot and the remaining 4 are compressed into a giant interstitial vortex. As T decreases, so does $\xi(T)$, vortices gain more space and the GV may split into

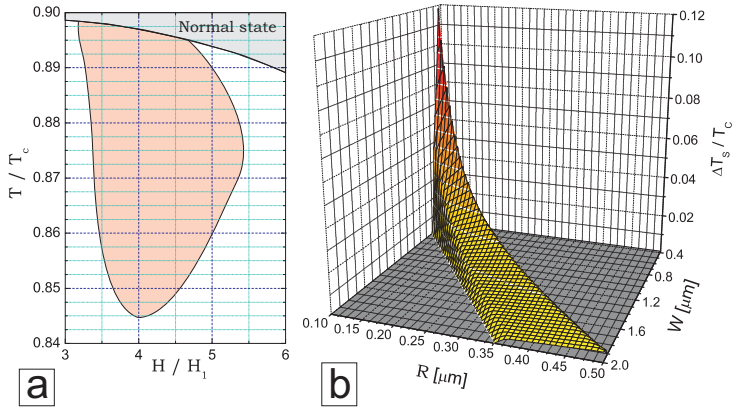

Fig. 4.4: (a) The $H-T$ area of stability of different VAV states for W =600 nm, R =110 nm, and κ^*=2. (b) ΔT stability range of the VAV-GV state (see Fig. 4.3(c,e)) as a function of the geometrical parameters of the antidot lattice, for $H = H_{9/2}$.

a more energetically favorable multi-vortex. However, further decrease of T makes the holes larger in units of ξ and enables them to capture two vortices each. When left with only 3 vortices per interstitial site, the unit cell imposes the square geometry and the VAV configuration nucleates (analogous to the one of Fig. 4.3(c,e)). When the unit cells become too large compared to the vortices, the imposed symmetry influences less the local vortex structure and acts on a vortex lattice as a whole. As a result, a square lattice of individual vortices is formed.

As shown in Fig. 4.4(a), the VAV-GV state at $H = H_{9/2}$ is stable almost 5% of T_c deep in the superconducting state. Being important for experimental observation, we calculated the temperature range of VAVs stability in equilibrium at $H = H_{9/2}$, for different geometrical parameters of the antidot lattice. The obtained results for $\Delta T(W, R)$ are shown in Fig. 4.4(b), for Pb films. VAVs were found stable for $W/R \approx 3.81 \div 5.76$ (see Fig. 4.3), and ΔT increases with decreasing size of the unit cell and radius of the antidots. The maximal value of $\Delta T/T_c = 11.3\%$ is obtained for $W = 400$ nm and $R = 100$ nm. In order to securely stay within the limits of current lithographic techniques, but also within limitations of the GL theory, we did not decrease further W and R, but the tendency of even further increase of ΔT is evident from Fig. 4.4(b). Note that similar conclusions can be drawn from Ref. [146] for VAV stability in mesoscopic superconducting squares, but the vortex-antivortex spacing in our case is significantly larger than in the superconducting polygons ($> 0.75\xi$, see Fig. 4.3(e)).

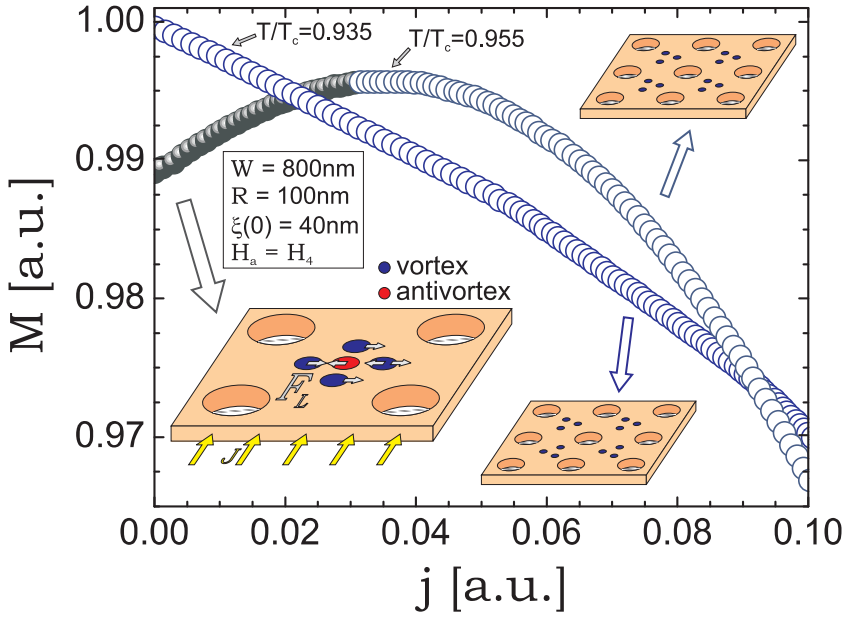

FIG. 4.5: Magnetization as a function of the applied current (see illustrations), in the case when VAV pairs are present in the sample (dark grey dots) and when not (blue dots).

The previous temperature stability analysis shows good prospects for the experimental verification of the predicted VAV states. In this respect, we suggest a convenient method, based on the response of the sample to an applied electric current. The idea relies on the Lorentz force, which for an applied dc current acts in the opposite direction on vortices and antivortices, causing their annihilation (see bottom-left inset of Fig. 4.5). We calculated the magnetization of a perforated Pb film, as a flux expelled from the superconductor 20 nm above the sample, over a 1 μm$\times$1 μm area directly above the chosen interstitial site ($4\pi M = \langle h \rangle - H$), corresponding to a Hall measurement by a probe of the proposed size. The results are shown in Fig. 4.5, for $W = 800$ nm and $R = 100$ nm, at $H = H_4$, for two temperatures, $T/T_c = 0.955$ and 0.935. For qualitative comparison, both magnetization and applied current are expressed in arbitrary units. As one can easily recalculate and compare with Fig. 4.2, for $T/T_c = 0.955$ we are in a VAVs equilibrium, whereas for $T/T_c = 0.935$ the three vortices at interstitial sites form triangular multivortex states (see insets of Figs. 4.2 and 4.5). When a small current j is injected in the sample, one expects a monotonous decrease of magnetization on j, characteristic for SC films. However, in the VAV state, under the influence of the Lorentz force

the vortex and the antivortex slowly approach each other and annihilate, effectively enhancing superconductivity (increasing magnetization). After all VAV pairs disappear, the magnetization curve exhibits a negative slope. At lower temperature, when no VAVs are present, the applied current acts equally on all present vortices, and since they become smaller in size with decreasing T, the magnetization response linearizes, and more importantly - the $M(j)$ curve always has a negative slope. Therefore, the $M(j)$ behavior for small currents can be used for the indication of the presence of VAV states, given by the change of slope from positive to negative. The conventional visualization techniques (Hall probe or Lorentz microscopy) are presently limited by their sensitivity, and the scanning tunnelling microscopy shows best results at temperatures further from T_c, but should not be excluded as potential alternatives for the observation of the variety of novel vortex states predicted in this Letter.

4.3.3 The hole occupation number n_o

Let us compare our numerical results for the hole-occupation number n_o with existing theoretical predictions. The saturation number n_s ($n_s = n_o$ for larger fields) is usually estimated as $n_s = R/2\xi(T)$ [68]. Fig. 4.6(a) shows the hole occupation number n_o obtained from this expression and the one from our GL calculation for different period of the antidots. It is seen from this figure that this expression underestimates n_o for small period W (slid black and red curves). This is due to the fact that the last expression does not account for the interaction between vortices sitting at different holes. For larger period W the occupation number is smaller in our calculation for a given radius of the holes (blue curve). A more accurate analysis was presented by Buzdin [143] for bulk superconductors within the London approach. However, his estimation of the critical hole radius $R/\xi \approx (W/\xi)^{2/3}$ (for $W \ll \lambda$) and $R/\xi \approx \kappa^{2/3}$ (for $\lambda \ll W$) corresponding to the transition from single flux-quantum to two flux-quanta captured by the hole, differ from our numerically exact results, i.e. the magnitude of the critical hole radius is largely overestimated in Ref. [143] for both small and large period W (see Fig. 4.6(b)).

The maximum number of flux quanta that can be trapped in a pinning center in a thin superconducting film was recently studied experimentally using scanning Hall probe microscopy [64] and ac susceptibility measurements [148]. In the latter case the saturation number was obtained from the transition to different dynamic regimes, as the interstitial vortices have higher mobility than those pinned by the antidots. They studied thin Pb films containing a square antidot array of period $d = 1.5$ μm. The antidots had circular (square) shape with radius $R = 330$ nm (size $a = 0.8$ μm), the film thickness was $d = 80$ nm ($d = 100$ nm) and the coherence length at zero temperature was estimated $\xi(0) = 30$ nm ($\xi(0) = 33$ nm) in Ref. [64] (Ref. [148]). Let us first discuss the results for the sample of Ref. [64], where the experimentally obtained saturation

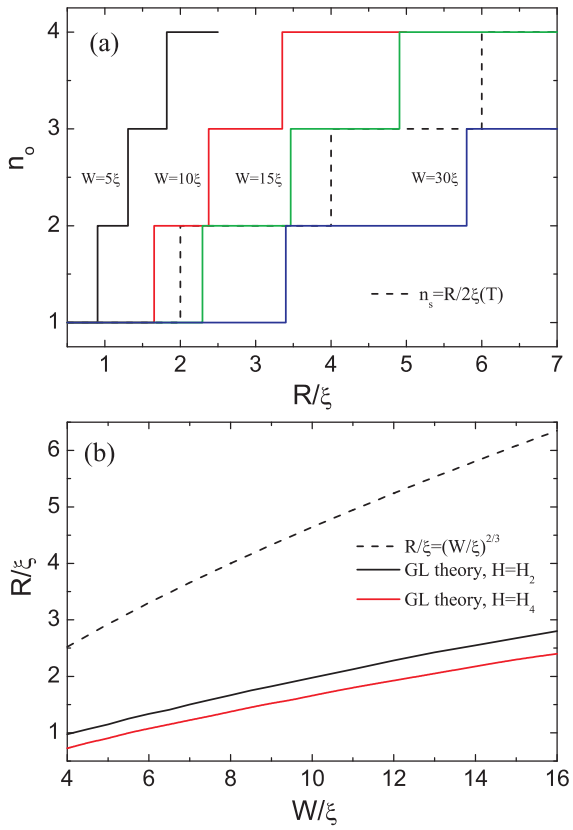

FIG. 4.6: (a) The antidot occupation number as a function of the antidot radius from the London theory [68] $n_s = R/2\xi(T)$ (dashed line) and from the GL theory for the period $W = 5\xi$ (back curve), $W = 10\xi$ (red curve), $W = 15\xi$ (green curve) and $W = 30\xi$ (blue curve) for the fourth matching field and $\kappa^* = 10$. (b) The critical hole radius corresponding to $n_o = 1 \rightarrow n_o = 2$ transition as a function of the period W. Dashed curve is obtained from the London theory [143] and solid black (red) curve is the result from the GL theory for $H = H_2$ ($H = H_4$) and $\kappa^* = 10$.

number was n_s=2 at $T/T_{c0} = 0.77$. Fig. 4.7(a) shows the antidot occupation number n_o as a function of temperature for different applied matching fields. At small applied fields ($H \leq H_3$) the occupation number is equal to two, which is in agreement with the experimentally obtained n_s. With increasing applied field $H > H_3$ one more vortex is trapped by the holes, i.e. $n_o = 3$, which is now larger than the experimental value. At higher temperatures $T > 0.89T_{c0}$, n_o again becomes equal to two. In this case one would estimate the saturation number from $n_s \approx R/2\xi(T)$ [68] to be $n_s = 1$ for $0.967T_{c0} < T < T_{c0}$ and $n_s = 2$ for $0.868T_{c0} < T < 0.967T_{c0}$. We found the occupation number equal to $n_o = 1$

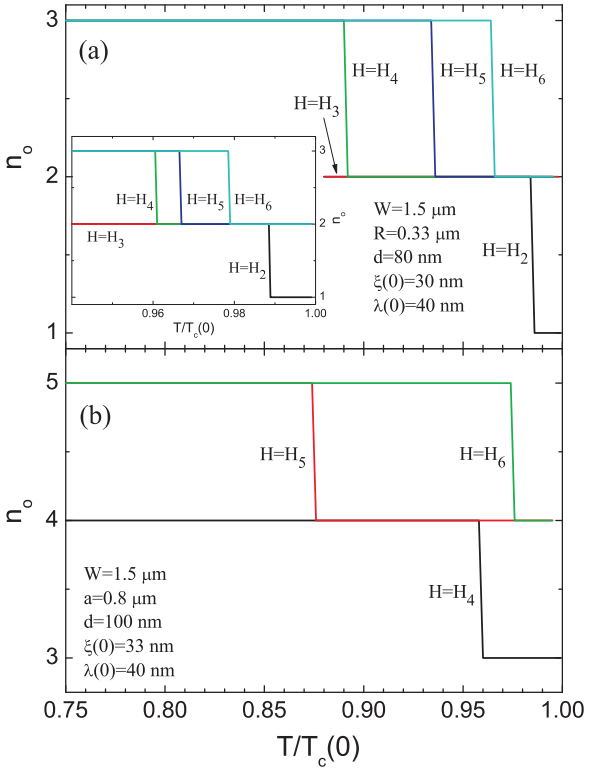

Fig. 4.7: The antidot occupation number n_o as a function of temperature T/T_{c0} for different matching fields for circular antidots ($R = 0.33$ μm) (a) and square ($a = 0.8$ μm) (b) holes. The lattice period for both samples is $W = 1.5$ μm and film thickness is $d = 80$ nm (a) and $d = 100$ nm (b). The inset in (a) shows the hole occupation number n_o of the same sample as a function of temperature for a different temperature dependence given by Eqs. (1.20) and (1.21).

only for the second matching field at the temperature range $0.985T_{c0} < T < T_c$. The estimation of Buzdin [143] for the critical hole radius $R^3 < \xi(T)\lambda(T)^2$, where the transition from $n_o = 1$ to $n_o = 2$ occurs, gives the temperature range $T < 0.985T_{c0}$. We found this transition at this temperature only for the second matching field. For larger fields the occupation number is always larger than unity. The giant vortex state is found only at $H = H_4$ for $T > 0.984T_{c0}$ and the vortex-antivortex state is formed at $H = H_5$ for the temperatures $T > 0.986T_{c0}$.

Up to now we use the temperature dependence for the coherence length and penetration depth given by Eqs. (1.52) and (1.53), which is obtained from the BCS theory [23] and is valid near T_c. In this case the GL parameter κ is

temperature independent. We also calculated the hole occupation number n_o for the temperature dependence of the coherence length and the penetration depth given by Eqs. (1.20) and (1.21). The results are shown in the inset of Fig. 4.7(a). It is seen from this figure that the transition from $n_o = n$ to $n_o = n$-1 occurs now at higher temperatures, but the results are qualitatively similar with the earlier results.

4.4 VORTEX STRUCTURE IN EFFECTIVE TYPE-I SUPERCONDUCTING FILM WITH AN ANTIDOT ARRAY

It is well known that the vortex-vortex interaction changes sing at the point $\kappa = 1/\sqrt{2}$. For $\kappa > 1/\sqrt{2}$, vortices repel each other while for $\kappa < 1/\sqrt{2}$ they attract. To see how this attractive interaction modifies the different vortex lattice configurations we consider a sample with small κ. Fig. 4.8 shows the contour plots of the Cooper-pair density for $\kappa^* = 10$ (type-II regime) and $\kappa^* = 0.1$ (type-I regime) for the second, third and fourth matching fields. For the

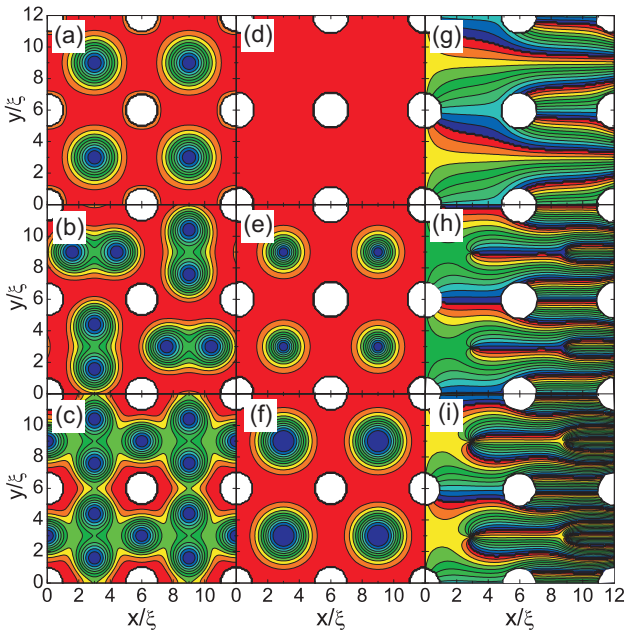

FIG. 4.8: Contour plots of the Cooper-pair density for $\kappa^* = 10$ (a-c) and $\kappa^* = 0.1$ (d-f). The lattice period is $W = 6\xi$ and the radius is $R = 1\xi$. Figures (g-i) show the phase of the order parameter of the states shown in (d-f). The first row is for $H = H_2$, the second for $H = H_3$ and the bottom row for $H = H_4$.

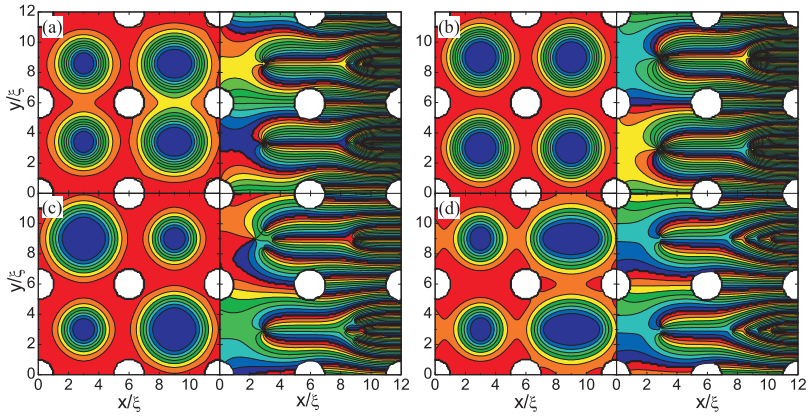

Fig. 4.9: Contour plots of the Cooper-pair density and the corresponding phase of the order parameter of the sample in Fig. 4.8 for different metastable vortex states at $H = H_4$ and $\kappa^* = 0.1$.

given parameters of the sample and for $\kappa^* = 10$ each hole pins one vortex and the remaining vortices sit at interstitial sites (Figs. 4.8(a-c)). The occupation number of each hole is increased to two in the type-I sample (see Figs. 4.8(d-i)) due to the enhanced expulsion of the magnetic field by the superconductor. Moreover, because of the attractive interaction between vortices, giant vortices become energetically more favorable contrary to the case for $\kappa^* = 10$. Due to the instabilities of vortex states, which is common for type-I superconductors, variety of metastable vortex structures can be found. As an example we show in Fig. 4.9 different metastable vortex states of the sample in Fig. 4.8 for $\kappa^* = 0.1$. The free energies of those states are: F/F_0 =-0.3268 (a), -0.2823 (b), -0.2787 (c) and -0.2755 (d). The ground state free energy (Fig. 4.8(f,i)) is $F/F_0 = -0.3759$. Notice that because of the attractive interaction a giant vortex state is always favored.

We have shown in previous section that a rich variety of ordered vortex structures: a combination of giant vortices with mltivortices and vortex-antivortex pairs are found in perforated superconducting samples for fractional matching fields. Here we consider the dependence of these vortex states on the effective GL parameter κ^*. As an example we constructed the equilibrium vortex phase diagram for $H = H_{9/2}$ rational matching field (i.e. 4.5 flux quanta per antidot) as a function of R and W, and for $\kappa^* = 10$ (Fig. 4.10(a)) and $\kappa^* = 0.1$ (Fig. 4.10(b)). The vortex lattice configurations for $\kappa^* = 10$ are similar to the one obtained for $\kappa^* = 2.025$ (see Fig. 4.3).

Fig. 4.10(b) shows the ground-state phase diagram found for $\kappa^* = 0.1$. Compared to Fig. 4.10(a), the threshold antidot-radius for capturing another vortex decreases due to the enhanced screening of the applied field. Due to

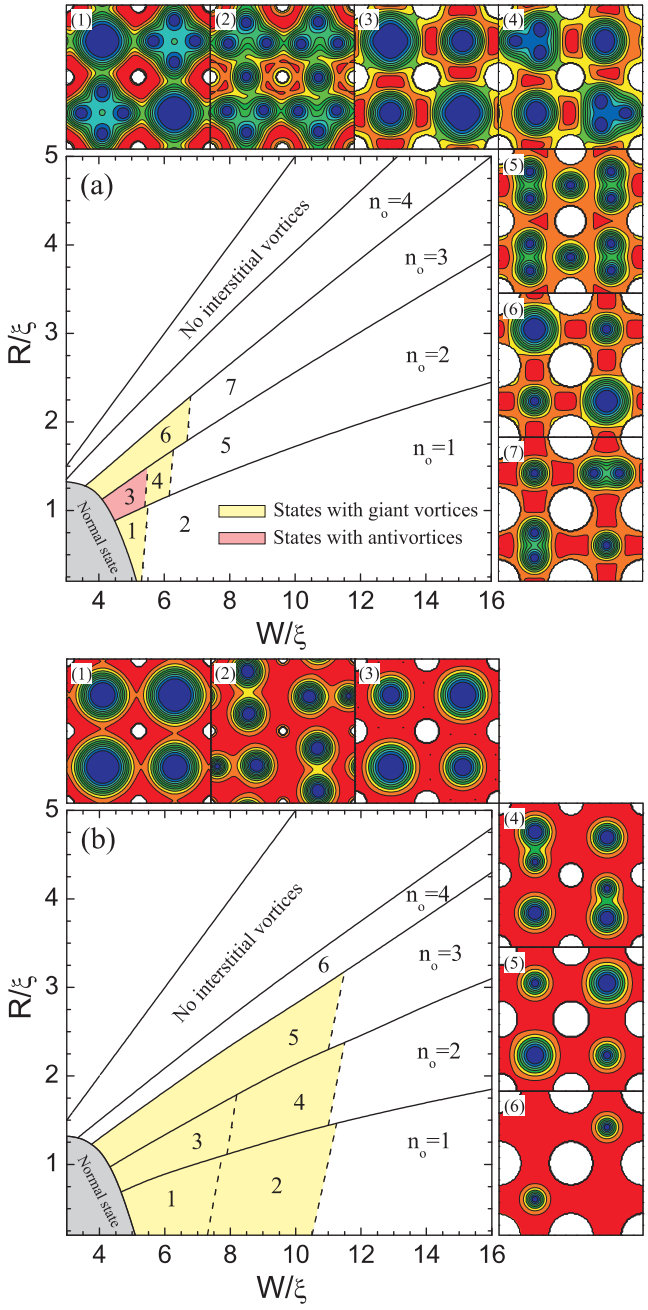

FIG. 4.10: The ground-state vortex lattice at $H = H_{9/2}$ as a function of the antidot-radius R and their periodicity W, for $\kappa^* = 10$ (a) and $\kappa^* = 0.1$ (b). The solid lines denote the first order transitions between the states with different antidot-occupation number n_o, and dashed ones depict second order configurational transitions. The insets show the Cooper-pair density plots of the corresponding states indicated by the numbers in the phase diagram.

the attractive vortex-vortex interaction in type-I samples, giant-vortex states become energetically favorable at the interstitial sites and spread over the majority of the $W - R$ phase diagram (light yellow areas). For a dense antidot lattice, giant vortices with different vorticity are found in adjacent cells ($L = 3$ and $L = 4$ (inset 1), and $L = 2$ and $L = 3$ (inset 3)). Contrary to the type-II case, these giant vortices can split to smaller giant vortices for larger spacing of antidots. They exhibit single-vortex behavior, forming the lattice of 2-quanta and single-quanta vortices (insets 2 and 4). Such new quasi-Abrikosov lattices of giant-vortices result from the competition of vortex-vortex attraction and imposed square symmetry of pinning. At the same time, these competing interactions cause the complete disappearance of the vortex-antivortex structures as found in type-II samples.

4.5 WEAK PINING CENTERS: STABILITY OF PINNED SQUARE AND PARTIALLY PINNED VORTEX STRUCTURES

It is well known that the regular triangular vortex lattice has the lowest energy in defect free superconductors [31] and the square lattice of pinning sites impose its own symmetry on the vortex structure. If the vortex-pinning strength in a periodic square array is reduced, the vortex-vortex repulsion starts to dominate over the pinning force and the triangular lattice is recovered. Calculation in the London theory [149], where vortices are considered as point like particles, show that depending on the strength and length scale of the pinning potential the triangular vortex lattice with some vortices are pinned by the pinning sites and others are located between them forms the ground state. A phase diagram for the transition between these two vortex states was given, which strongly depends on the type of the periodic pinning potential, the parameters of which are difficult to relate to any growth parameters of the sample. This kind of partially pinned (PP) vortex lattices were found in recent experiments on charged macroscopic particles [150]. The transition between the square totally pinned (TP) and the PP states occur sharply with decreasing pinning strength in the experiment.

Therefore we studied the different vortex configurations in superconducting films with arrays of weak pinning sites within the Ginzburg-Landau theory. Here we present our results about vortex structures in a superconducting film of thickness $d = 0.1\xi$ with a square array of antidots (holes) of radius R and interhole distance W for the first three matching fields. In order to decrease the pinning force in our calculations we just reduced the radius of the antidots R for a given period of antidot lattice W.

Fig. 4.11 shows the two most frequently observed vortex configurations for different matching fields. At the first matching field there are states where all vortices are pinned by the holes (i.e. the TP state) (Fig. 4.11(a)) and

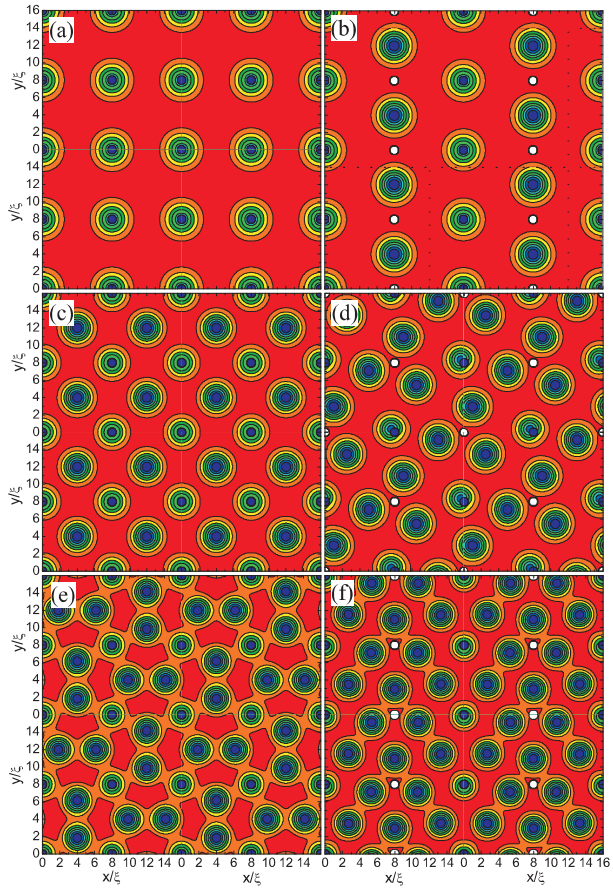

FIG. 4.11: Contour plots of the Cooper-pair density in the superconducting film of thickness $d = 0.1\xi$ with antidots of radius $R = 0.5\xi$ and interhole distance $W = 8\xi$ for the matching fields: $H = H_1$ (a,b), $H = H_2$ (c,d) and $H = H_3$ (e,f). The left column shows the totally pinned (TP) vortex configurations and the right column shows the partially pinned (PP) vortex states.

there are states where half of the vortices are pinned by the holes and the others are depinned and located between the antidots (i.e. the PP state) (Fig. 4.11(b)). This alternating rows of pinned and unpinned vortices restore the triangular symmetry of the vortex lattice. This vortex state is the same as was found in the experiment [150] and as predicted by the London theory [149]. At the second matching field in the TP state all pinning centers are

occupied and the remaining vortices are located in the interstitial region (Fig. 4.11(c)). The PP state is the one with one hole occupied by the vortices and the next one is empty. Three unpinned vortices form a cluster around the empty holes. A small difference of the PP state at $H = H_2$ with the experimentally obtained one is that non of those three vortices around the empty hole is located between the holes. However, for very large period W we found the state which is close to the experimentally obtained one. The PP state at $H = H_3$, consists of alternating rows of occupied and unoccupied holes with zig-zag structure of interstitial vortices (Fig. 4.11(f)). This nearly triangular lattice was found in molecular dynamic simulations [151], where a logarithmic vortex-vortex interaction potential was used. In the TP state all the holes are occupied by a single vortex and the others are located in the interstitials alternating in position (Fig. 4.11(e)).

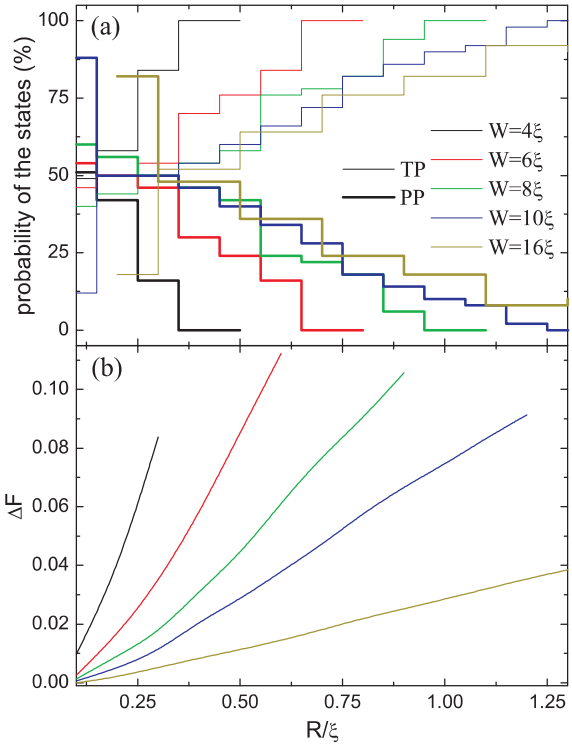

Fig. 4.12: (a) The probability of the totally pinned (TP) (thin curves) and partially pinned (PP) (thick curves) vortex states as a function of the holes radius R for different periods W. (b) The energy difference ΔF between the TP and PP vortex states as a function of the radius R. The applied magnetic field is $H = H_1$.

Usually, in experiments so called "field cooling" measurements are carried out and the most frequently observed patters are referred as stable configurations and less frequent states are considered as metastable configurations. However, recent Bitter decoration experiments on the vortex structures in mesoscopic superconducting samples [82] show that some theoretically predicted vortex states were never seen in the experiment and some of them are found in few cases, and, therefore, were considered as metastable states. On the other hand, the experimentally observed vortex configurations are in better agreement with those predicted for finite systems of charged particles and vortices in liquid helium. Although calculations within the London theory [149] and experiments with charged particles [150] show that the PP state can be obtained as the ground state (or it is degenerate with the TP state as was mentioned in Ref. [150]), we could not find PP states with lower energy than the TP states.

To resolve this problem we performed a "field cooling" experiment, which gives us the possibility to study the statistics of the TP and the PP states. In our calculations we started each time from a random initial vortex distribution

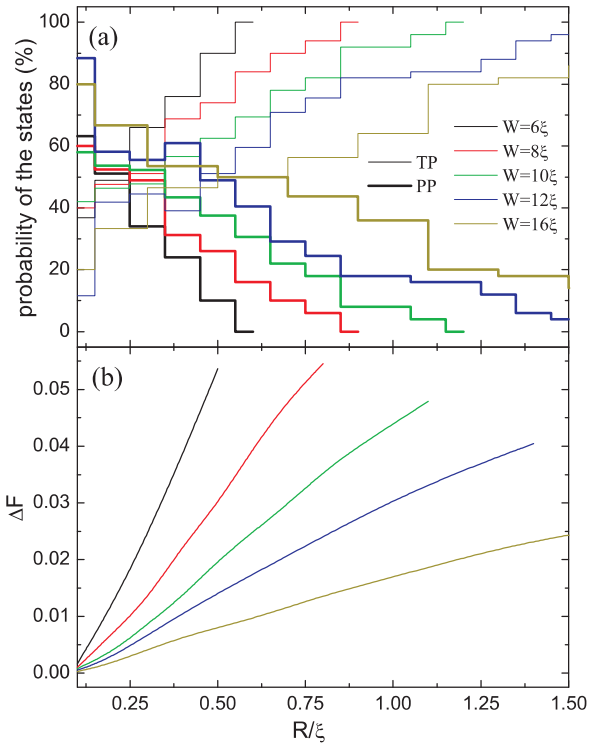

FIG. 4.13: The same as in Fig. 4.12 but for $H = H_2$.

(calculations were done typically with 50 different random distributions for a given field and sample parameters). The results are shown in Fig. 4.12(a) for $H = H_1$. It is seen from this figure that the PP state (thick curves) is obtained more frequently than the TP state (thin curves) for small pinning force (i.e. small hole radius R). The increase of the hole radius leads to a decrease of the probability to obtain the PP state. Larger period W requires larger radius R in order to have 100% the TP state. Fig. 4.12(b) shows the difference between energies of the PP and TP states ΔF as a function of the radius R for different period W. As we see from this figure, the TP state always has lower energy than the PP state. ΔF is smaller for larger period W for a fixed radius R. The same behavior of the PP and TP states is found for the second matching field (see Fig. 4.13(a,b)).

From the fact that the PP vortex configurations are observed more frequently than the TP vortex state for small pinning strengths, one can conclude that the PP state has a larger interval of stability. To check that we calculated the

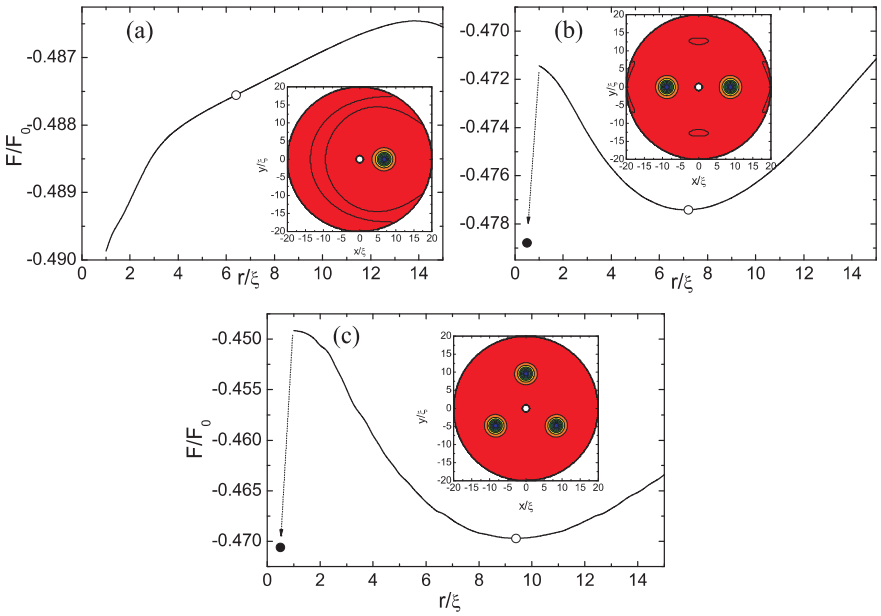

Fig. 4.14: The free energy of the superconducting disk of radius $R = 20\xi$ with a hole in the center ($R_0 = 1\xi$) as a function of the radial position of the vortex r for the vorticity $L = 1$ (a), $L = 2$ (b) and $L = 3$ (c). The insets show the Copper-pair density plots corresponding to open circles in the free energy curve. The solid circles in (b) and (c) show the free energy when one vortex is pinned by the hole and the others are located around the hole. The applied magnetic field equals $H = 2n\Phi_0/S$, where Φ_0 is the flux quantum and S is the disk surface.

free energy of a superconducting disk with a hole (we considered larger disks, in order to reduce the effect of the boundary) as a function of the position of vortices inside the disk. The applied magnetic field was $H = 2L\Phi_0/S$, where L is the number of vortices, Φ_0 is flux quantum and S is the surface of the superconductor. When there is only one vortex in the disk it interacts attractively with the hole (Fig. 4.14(a)). The presence of the second vortex changes this attractive interaction (Fig. 4.14(b)). Now there is no attraction to the hole which is due to the repulsive interaction of the vortices. The free energy has a very broad minimum with the separation of the vortices $\sim 17\xi$ from each other. However, if one of the vortices comes close to the hole and occupies it (or the vortex is initially in the hole) the free energy of the system becomes even lower (black dot in Fig 4.14(b)). But this minimum in the free energy is very narrow. Therefore, in order to find the ground state vortex configuration, we have to put one vortex exactly in the hole, otherwise they will drop to that larger energy minimum. The situation is the same for $L = 3$ state (Fig. 4.14(c)), where vortices form a trimer around the hole. The vortices are located equidistantly from the hole, whereas in the calculations (and in the experiment [150]) they are not because of the influence of other vortices.

4.6 THE CRITICAL CURRENT OF PATTERNED SUPERCONDUCTING FILMS

4.6.1 Influence of the geometrical parameters

In the previous sections we showed that vortex configurations that are commensurate with the periodic arrays of antidots exhibits well-defined matching phenomena, which leads to pronounced peaks in the critical current (see for example Ref. [47]). However, the stability of these vortex states strongly depend on the parameters of the sample. For example, a multi-quanta vortex state become energetically favorable for large radius of the holes, while small holes can capture only a single vortex. The additional vortices located in interstitial sites reduces the critical current considerably. Therefore, we first investigate the critical current of our sample as a function of the relevant antidot parameters.

The first step to calculate the critical current is to accurately determine the vortex ground state for given applied magnetic field, in a manner described in previous section. Then the applied current in the x direction is simulated by adding a constant A_{cx} to the existing vector potential of the applied external field [152]. With increasing A_{cx} we find a critical value of A_{cx} such that a stationary solution to GL equations cannot be found since a number of vortices is driven in motion by the Lorentz force. The current j_x in the sample corresponding to the given value of A_{cx} is obtained after integration of the

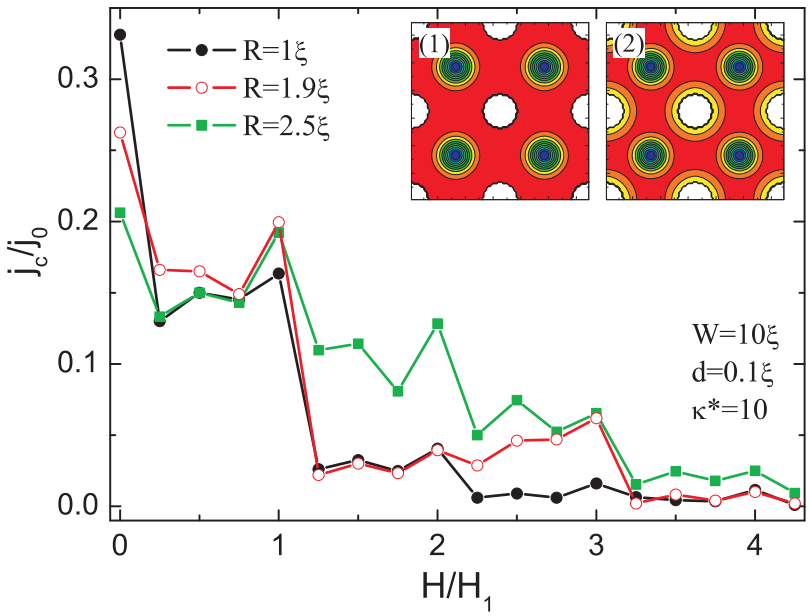

Fig. 4.15: Critical current density (in units of $j_0 = cH_{c2}\xi/4\pi\lambda^2$) as a function of the applied magnetic field (in units of the first matching field H_1) for three values of the antidot radius: $R = 1\xi$ (black curve), $R = 1.9\xi$ (red curve) and $R = 2.5\xi$ (green curve). The antidot lattice period is $W = 10\xi$, the film thickness is $d = 0.1\xi$ and the effective GL parameter is $\kappa^* = 10$. The insets show the contour plots of the Cooper-pair density at the second (1) and third (2) matching fields for $R = 1.9\xi$.

x-component of the induced supercurrents in the y-cross-section. The maximal achievable value of j_x denotes the critical current j_c.

Fig. 4.15 shows the critical current density j_c (in units of $j_0 = cH_{c2}\xi/4\pi\lambda^2$) as a function of applied magnetic field (normalized to the first matching field H_1) for different values of the antidot radius R for fixed value of the antidot lattice period W. For small radius (balck curve), where only one vortex can be pinned by the hole, the peaks at the matching fields decrease with increasing applied field. The opposite behavior is found when there is a *caging effect*, i.e. $j_c(H_n) < j_c(H_{n+1})$, which e.g. is found for radius $R = 1.9\xi$ (red curve) for $n_o = 1$ and $n_o = 2$. This effect occurs when there are the same number of interstitial vortices but the number of pinned ones are different at the different matching fields. In this case the interstitial vortices feel a stronger repulsive interaction when there are a larger number of pinned vortices. As is shown in Fig. 4.15 (red curve), a higher critical current is found for the third matching field, when a double vortex occupies each hole and a single one is located at the interstitial, than for the second matching, with one vortex in each hole and

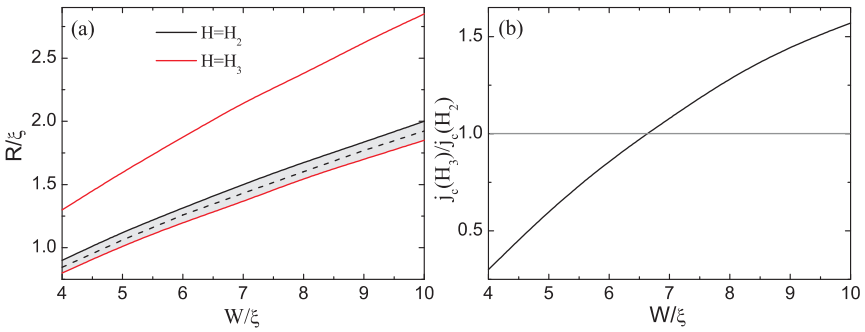

FIG. 4.16: (a) The dependence of the antidot occupation number n_o as a function of the radius R and the period W of the antidots. The solid black (red) line indicates the transition between the states with different n_o at $H = H_2$ ($H = H_3$). The shadowed area indicates the vortex state with a single interstitial vortex for both applied fields (the occupation number in this region is $n_o = 1$ for $H = H_2$ and $n_o = 2$ for $H = H_3$). (b) The ratio of $j_c(H_3)/j_c(H_2)$ as a function of the period W, where the radius of the antidots correspond to the dashed line in the middle of the dashed area.

a single interstitial vortex (see the insets of Fig. 4.15). This effect disappears with further increasing the radius R due to the different occupation number n_o, i.e. no interstitial vortices at $H = H_2$.

In order to show the range of radius R and period W of antidots, where this caging effect is active, we constructed a $R-W$ phase diagram for $H = H_2$ and $H = H_3$, shown in Fig. 4.16(a). The shadowed area indicates the vortex state with a single interstitial vortex for both $H = H_2$ (solid black) and $H = H_3$ (red curves). Fig. 4.16(b) shows the ratio $j_c(H_3)/j_c(H_2)$ as a function of period W. The critical radius R is taken from the middle of the region (dashed curve). It is seen from this figure that, although we have the same vortex structure for all values of the period $4\xi \leq W \leq 10\xi$, the enhancement of j_c is found only for $W \gtrsim 6.6\xi$. For small period the pinned vortices at $H = H_3$ suppresses superconductivity around the holes and interstitial vortices are easily set into motion, reducing the critical current.

Fig. 4.17 shows the critical current density as a function of the field for two values of the period: $W = 4\xi$ (black curve) and $W = 8\xi$ (red curve) at $R = 1.25\xi$. As we showed above, the $j_c(H)$ curve shows pronounced maxima at integer fields H_1, H_2 and H_3 and at some of the fractional matching fields. However, while the qualitative behavior of $j_c(H)$ in Fig. 4.17 is as expected, its quantitative behavior reveals a counterintuitive phenomenon. Namely, one expects higher critical current in the sample with larger interhole distance, simply due to the presence of more superconducting material. Indeed, that is the case for $H \leq H_1$, where the superconductor is able to compress all flux lines in the holes. However, for higher magnetic fields, the critical current drops

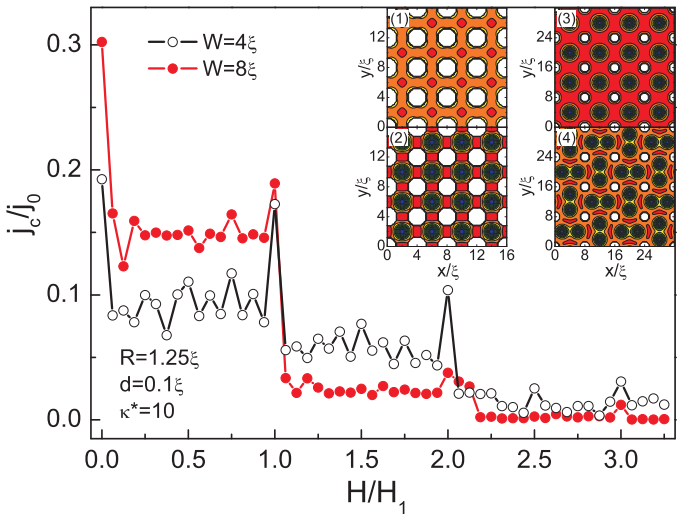

Fig. 4.17: Critical current density of the superconducting film as a function of the applied magnetic field for two values of the antidot lattice period: $W = 4\xi$ (black curve) and $W = 8\xi$ (red curve). The insets show contour plots of the Cooper-pair density at the second (1,3) and third (2,4) matching fields for $W = 4\xi$ (1,2) and $W = 8\xi$ (3,4). The radius of the holes is $R = 1.25\xi$, the film thickness is $d = 0.1\xi$ and the effective GL parameter is $\kappa^* = 10$.

sharply immediately after the first matching field H_1, which is related to the appearance of interstitial vortices. On the other hand, the smaller interhole distance affect the hole occupation number, and the additional vortices after $H = H_1$ are still captured by the holes (as illustrated by Cooper-pair density plots in the inset of Fig. 4.17). Consequently, the critical current in this case is larger for smaller periodicity. Note that even for smaller periodicity a sharp drop in j_c is observed for $H > H_1$, as every additional vortex disturbs the stability of the vortex lattice. Even at $H = H_2$, although all vortices are captured by the holes, the critical current is lower, due to a stronger suppression of the order parameter around the holes compared to the $H = H_1$ case. The height of the matching peaks is decreasing with further increasing field (due to the presence of interstitial vortices), which agrees with experiment (see Ref. [47]), and these peaks strongly diminish for higher fields as the vortex-flow overwhelms the pinning potential.

When we apply a *dc* current into the superconductor the vortex lattice is distorted before the vortices start moving. To illustrate this phenomenon, we plot in Fig. 4.18 the Cooper pair density of the superconducting film at the applied currents (in y direction) $j = 0$ (first column), $j = 0.5j_c$ (second column) $j = 0.95j_c$ (third column) for different matching fields. At the first

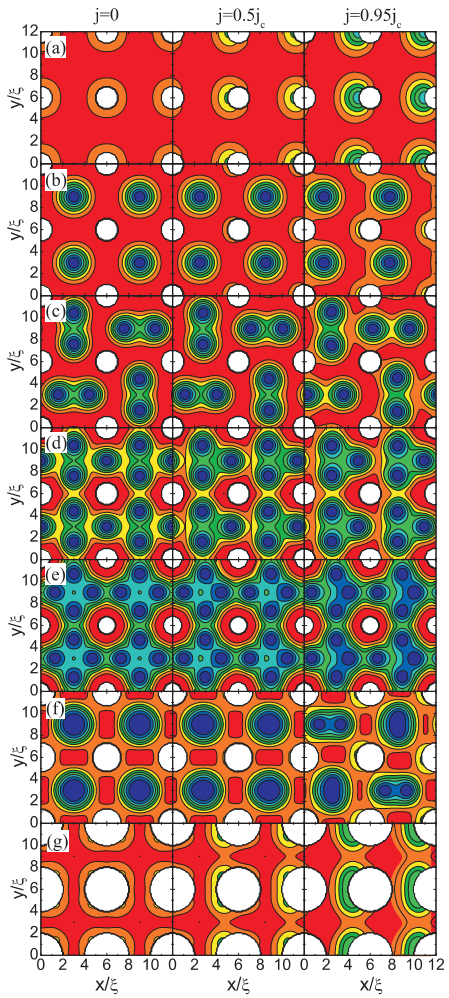

FIG. 4.18: Contour plot of the Cooper-pair density for $H = H_1$ (a), $H = H_2$ (b), $H = H_3$ (c,g), $H = H_4$ (d,f), and $H = H_5$ (e), and for the applied current $j = 0$ (first column), $j = 0.5j_c$ (second column) and $j = 0.95j_c$ (third column). GL parameter is $\kappa^* = 10$, the period of the antidots lattice is $W = 6\xi$ and the radius of the antidots is $R = 0.8\xi$ (e), $R = 1\xi$ (a-d), $R = 1.3\xi$ (f) and $R = 2\xi$ (g).

(Fig. 4.18(a)) and second (Fig. 4.18(b)) matching fields all the vortices are displaced over the same distance, conserving the square symmetry in the lattice of vortices. At larger fields, when there is a large number of interstitial vortices (Fig. 4.18(c-e)), the vortex configuration is changed by the current and some of the vortices are jammed at the interstitial sites. If we initially have giant

vortices (Fig. 4.18(f)) they can be split into multivortices with increasing j. Our calculations also show that there is no transition from the multivortex state to the giant vortex state when we increase the applied current, and the occupation number of the antidots n_o is found to be independent of j.

Another interesting feature following from the displacement is found for fractional matching fields. For example, in the insets 6 and 7 of Fig. 4.10 shows alternating two-vortex - single vortex structure at $H = H_{9/2}$, where applying small current in y-direction can shift the excess-vortex from one interstitial site to another. Note that resulting state has identical configuration and energy as the previous one. In order to estimate the energy barrier between these two vortex states we performed calculations for a superconducting film of thickness $d = 13$ nm with an array of antidots with period $W = 1$ μm, radius $R = 0.13$ μm, at temperature $T = 0.9T_c$. We take $\xi(0) = 40$ nm and $\lambda(0) = 80$ nm, which are typical values for Pb thin films. We found an energy barrier of $\Delta F = 6.2$ meV, which is significantly higher than the thermal activation energy at this temperature ($kT = 0.56$ meV), but still low enough for successful switching by a relatively weak current. Moreover, when an *ac* current is applied to the sample, the vortex can shift back and forth between the adjacent cells, resulting in resonant dissipation.

4.6.2 Temperature dependence of the critical current

So far, we presented results at a fixed temperature. In what follows, we include temperature in our numerical analysis through the temperature dependence of the coherence length ξ (see Eq. (1.52)). We now consider the superconducting film with thickness $d = 20$ nm, interhole distance $W = 1$ μm, and antidot radius $R = 0.2$ μm. We choose the coherence length $\xi(0) = 40$ nm and the penetration depth $\lambda(0) = 42$ nm, which are typical values for Pb films. Fig. 4.19 shows the calculated critical current of the sample as a function of the applied field normalized to the first matching field at temperatures $T/T_{c0} = 0.86 \div 0.98$. As expected, decreasing the temperature leads to a larger critical current for all values of the applied field. The relative height of the peak at zero field with respect to one at the first matching field increases with increasing temperature. At higher temperatures, i.e. for $\xi(T) > R$, a certain suppression of the order parameter is present around the antidots as the core of pinned vortices overlaps with the interstitial regions. Consequently, the suppressed order parameter leads to a smaller j_c. The caging effect is found for temperatures $T \leq 0.93T_{c0}$ (see the inset Fig. 4.19) and it disappears with temperature when approaching T_{c0}, since the vortices entirely cover the interstitial regions and effectively destroy superconductivity.

This effect that the critical current is larger for larger fields was recently observed experimentally [153]. The considered sample was a Pb film of thickness 50 nm, with square antidots of size $a = 0.5$ μm and period $W = 1.5$ μm. The

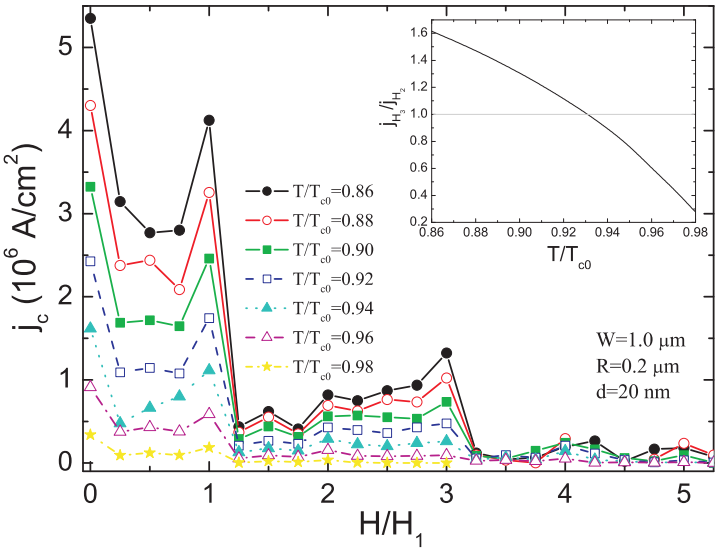

FIG. 4.19: Critical current density of the perforated superconducting film as a function of the applied magnetic field (in units of the first matching field H_1) at temperatures $T/T_{c0} = 0.86 \div 0.98$. The inset shows the ratio of $j_c(H_3)/j_c(H_2)$ as a function of temperature. The lattice period is $W = 1$ μm, the antidot radius is $R = 0.2$ μm, and film thickness is $d = 20$ nm.

coherence length and the penetration depth at zero temperature were estimated to be $\xi(0) = 40$ nm and $\lambda(0) = 80$ nm. Although plotted for other purposes, Fig. 6(b) in Ref. [153] demonstrates a clear overshoot of the critical current at $H = H_3$ with respect to the one at $H = H_2$, at the temperature $0.974T_{c0}$. Fig. 4.20 shows the comparison of the calculated critical current density (dots) with experiment (solid line). Our $j_c(H)$ curve shows the same qualitative behavior as the experimental one, though a quantitative agreement is lacking for the experimentally estimated values of $\xi(0)$ and $\lambda(0)$. Better correspondence was achieved for smaller values of $\xi(0)$, indicating somewhat "dirty" sample in the experiment. No further attempts were made to improve the quantitative agreement with experiment because of the different determination of j_c in the experiment and in our theory. In our calculations we use a dynamical criterium, i.e. we assume normal state as soon as vortices are set in motion, whereas in transport measurements a certain value of the threshold voltage was used to determine the critical current and the surface barrier at the edges is important. Therefore, our result should be considered as a lower limit to the experimental critical current. The qualitative behavior of j_c at the matching fields should not be influenced by these facts.

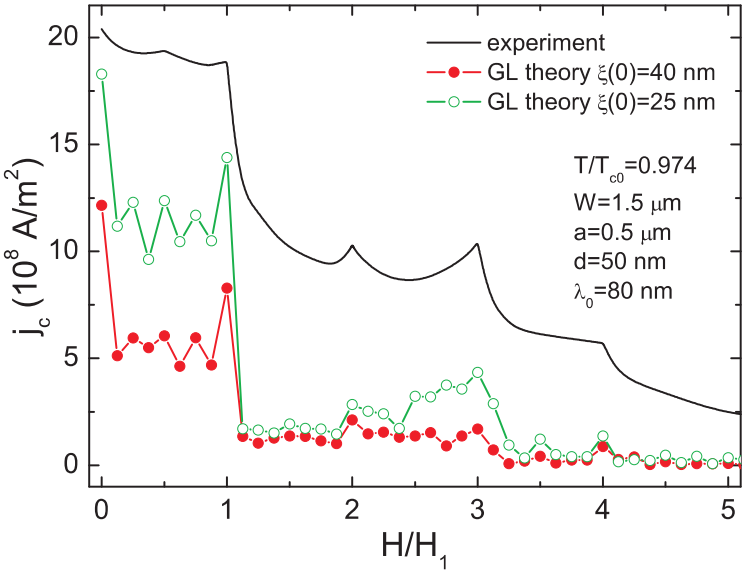

FIG. 4.20: Numerically obtained $j_c(H)$ characteristics of the superconducting film with antidot arrays (parameters given in the figure) for the coherence length at zero temperature $\xi(0) = 40$ nm (red curve) and $\xi(0) = 25$ nm (green curve). The solid curve denotes experimental data (taken from Ref. [153]).

4.7 $H-T$ PHASE DIAGRAM

The presence of antidot lattice in a superconducting film not only enhances the vortex-pinning, which was discussed in the previous section, but also affects substantially the nucleation of superconductivity. Due to the superconducting/vacuum interface at the antidots, surface superconductivity will be important around each antidot, at fields above the bulk critical field $H_{c2}(T)$. This makes it possible to enhance the critical field in patterned superconducting films above $H_{c2}(T)$ and even beyond the third critical field $H_{c3}(T)$. The ratio $H_{c3}(T)/H_{c2}(T)$ tends to the value 1.69, the enhancement factor for a semi-infinite slab [24]. However, for a dense antidot lattice a much larger enhancement can be achieved. Namely, if the antidots are sufficiently closely spaced, almost the entire sample may become superconducting at high fields through surface superconductivity.

The critical field of superconducting Pb films with a square array of antidots was investigated in Ref. [154] by the magneto resistance measurements. The experimentally obtained $H-T$ phase boundary shows a cusp-like behavior with cusps at integer and some fractional matching fields. The amplitude of

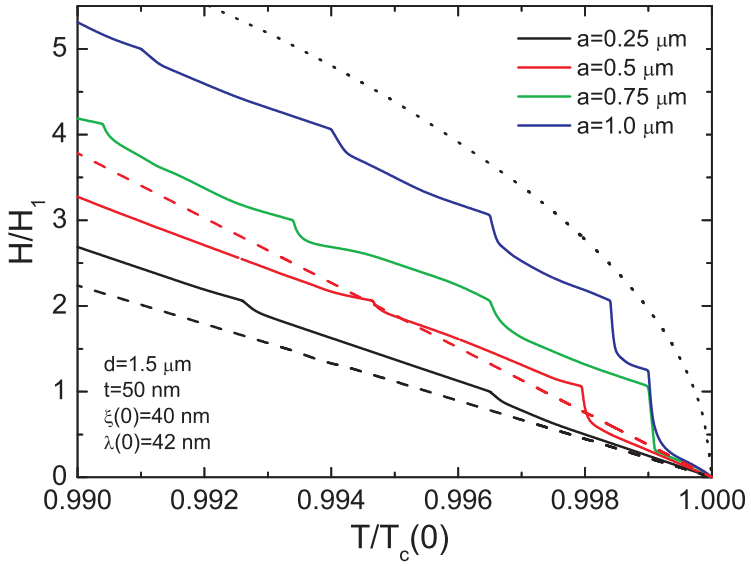

FIG. 4.21: $H-T$ phase boundary for the superconducting film with an antidot array. The film thickness is $d = 50$ nm, the period of the antidot lattice is $W = 1.5$ μm, the antidot size is varied as $a = 0.25$ μm (solid black curve), $a = 0.5$ μm (solid red curve), $a = 0.75$ μm (green curve), and $a = 1.0$ μm (blue curve). Black dashed curve denotes the upper critical field (H_{c2}) of the plain superconducting film (Eq. (4.1)), red dashed curve gives the third critical field $H_{c3} = 1.69H_{c2}$ for a plain superconductor-vacuum boundary, and dotted curve is the critical field of a superconducting strip with thickness $\omega = 0.5$ μm (Eq. (4.2)).

the cusps depend on the resistive criterion – the cusps become sharper and their amplitude increases with decreasing this criterion.

We investigated numerically the $H-T$ phase boundary for a superconducting film of thickness $d = 50$ μm in the presence of a regular array of square antidots with lattice period $W = 1.5$ μm. We take the coherence length at zero temperature as $\xi(0) = 40$ nm and penetration depth as $\lambda(0) = 42$ nm. Fig. 4.21 shows the calculated $T_c(H)$ phase diagram for different sizes of the antidots: $a = 0.25$ μm (solid black curve), $a = 0.5$ μm (solid red curve), $a = 0.75$ μm (green curve), and $a = 1.0$ μm (blue curve). For comparative reasons, we plotted also the phase boundary for a plain film (dashed black) with the same coherence length $\xi(0) = 40$ nm, obtained from the well-known expression for the upper critical field

$$H_{c2} = \frac{\Phi_0}{2\pi\xi^2(T)} = \frac{\Phi_0}{2\pi\xi^2(0)}\Big(1 - T/T_{c0}\Big). \tag{4.1}$$

It can be easily seen that the antidot lattice has a profound influence on the critical magnetic field, as compared to a reference non-patterned film. The critical temperature is enhanced at every field, and vice versa, regardless of the size of the antidots. Note also that matching features are present in $T_c(H)$ at integer matching fields. For small radius of the antidots matching peaks at higher integer matching fields $H > H_2$ are weakly pronounced, due to the small hole-saturation number. We did not observe clear evidence of fractional matching features.

For small radius of the antidots the sample basically acts as a non-patterned film for temperatures close to T_{c0} and the dependence of the critical temperature on the applied field is almost linear. For larger sizes of the antidots (e.g. green and blue curves in Fig. 4.21), the critical field becomes substantially higher than the third critical field of a semi-infinite slab (red dashed curve), and the peaks at matching fields are more pronounced. In addition, $T_c(H)$ exhibits a parabolic background as for a thin slab in a perpendicular field, as well as to a thin film in a parallel field, which can be described in the London limit by [23]

$$H_{c3} = \frac{\sqrt{12}\xi(T)}{\omega} H_{c2}(T), \tag{4.2}$$

where ω stands for the width of the superconducting strip.

4.8 CONCLUSIONS

We have studied the vortex structure of a thin superconducting film with a regular array of antidots, which shows a rich variety of ordered vortex lattice configurations for different matching and fractional matching fields H_n. For small radius of the holes, the vortex configurations with one vortex captured in each hole and the others located in the interstitial sites are realized, where interstitial vortices form regular patterns, either as multi- or giant vortices, or combination of giant- and multi-vortex states. For particular geometrical parameters of the sample and the applied field, a symmetry imposed vortex-antivortex configuration is found. Depending on the ratio between the hole radius R and the interhole distance W, multi-quanta vortices may be forced into the antidots, in spite of their low saturation number at smaller magnetic fields. To illustrate the transition between possible multi-quanta states in the holes we showed a diagram of the occupation number n_o as a function of the radius of the holes and interhole distance for different values of the effective GL parameter. n_o increases with decreasing κ^* due to the enhanced expulsion of the magnetic field from the superconductor and giant vortices become energetically favorable because of the attractive interaction between the vortices. When the pinning force of the antidots is small, i.e. small radius of the antidots, the triangular vortex lattice becomes energetically favorable. Depending on the applied field

all the vortices can be located between the antidots, or some of them are pinned by the antidots and some of them are located between the pinning centers. Although these partially pinned vortex structures are obtained more frequently in field cooling experiments than the square pinned vortex lattice, we could not find them as a ground state vortex configuration contrary to the results from the London approach [149] and experimental results on charged macroscopic particles [150].

The critical current j_c of the sample shows well defined peaks at different matching H_n and fractional matching fields, indicating that vortices are strongly pinned by antidots. However, the level of j_c enhancement at particular magnetic field strongly depends on the antidot occupation number n_o. For certain parameters of the sample, the critical current becomes larger at higher matching fields, contrary to conventional behavior.

We also studied the $T_c(H)$ phase boundary of regularly perforated superconducting film. When an antidot array is present the critical temperature $T_c(H)$ is enhanced compared to a non-patterned film and distinct cusps in the phase boundary are found for different matching fields, which is in agreement with the experiment [154]. This behavior is in contrast to the Little-Parks [7] like structures found in finite size superconductors. The increase of the antidot size for given lattice period leads to the change of the $T_c(H)$ background from linear to parabolic behavior except for temperatures near T_{c0}.

Publications. The results presented in this chapter were published as:

- G.R. Berdiyorov, M.V. Milosevic, and F.M. Peeters, *Vortex lattice in effective type-I superconducting films with periodic arrays of submicron holes*, Physica C **437-438**, 25-28 (2006).
- G.R. Berdiyorov, M.V. Milosevic, and F.M. Peeters, *Superconducting films with antidot arrays -Novel behavior of the critical current*, Europhys. Lett., **74** (3), 493-499 (2006).
- G.R. Berdiyorov, M.V. Milosevic, and F.M. Peeters, *Novel Commensurability effects in superconducting films with antidot arrays*, Phys. Rev. Lett. **96**, 207001 (2006).
- G. R. Berdiyorov, M. V. Milosevic, and F. M. Peeters, *Vortex configurations and critical parameters in superconducting thin films containing antidot arrays: Nonlinear Ginzburg-Landau theory*, Phys. Rev. B **74**, 174512 (2006).
- G. R. Berdiyorov, M. V. Milosevic, and F. M. Peeters, *New commensurate vortex structures in type-I and type-II superconducting films with antidot arrays*, to appear in Physica C (2007).

5

Vortex-cavity interaction

5.1 INTRODUCTION

Although simple by appearance, the problem of interaction of an object core with a rigid obstacle has recently drawn a lot of attention. For example, the deformation of an emulsion droplet on nanoengineered defects in caterpillars is essential for modern microfluidic devices [155]. In magnetic elements, the core of the magnetic vortex state has been recently observed [156]. Artificial pinning of such a vortex is currently a prominent study object, as it might be advantageous for applications to move the vortex core between defects, instead of reversing the magnetization of the whole element [157]. In biology, vacuoles are known to deform by extending membrane pseudopodia around an obstacle. In a similar fashion, phagocytes engulf bacteria in living organisms [158]. Although in all these systems the initial and the equilibrium state are well-defined, the exact dynamics in between is still an open question.

Analogous problem exists in superconductivity, where interaction of vortices with columnar defects has been extensively studied [38, 59, 68, 69, 73, 74, 139–142, 159]. It is now well-known that flux-lines are attracted by defects in superconductors, and that, due to this pinning, vortices contribute less to overall dissipation. The exemplary estimation of the vortex pinning by a cylindrical cavity in a bulk superconductor was derived in 1972 by Mkrtchyan and Shmidt

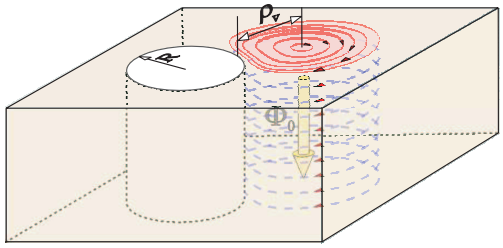

FIG. 5.1: Oblique view of the system: vortex currents interacting with a cylindrical cavity (with radius R) in a superconducting film. The distance of the vortex singularity from the edge of the cavity is denoted by ρ_v.

[68], later extended by Nordborg and Vinokur [69], both made within the London approximation. However, this approach does not account for the finite size of the vortex core, and core dynamics in the vicinity of the artificial defect. Priour and Fertig were the first to employ the Ginzburg-Landau formalism for this issue [159]. However, their prediction of the core deformation close to the hole by roughly 400% of the vortex size seems rather obscure. That the question of vortex core interaction with defects is not just a marginal extension of previous works was shown in Refs. [73, 74], where deformation of the core on asymmetric pinning sites was found directly responsible for particular features of the observed ratchet effect. Yet, used theoretical model did not incorporate the properties of the vortex core. Instead, vortices were described as particles with apparent mass. While the interaction of a moving vortex with a defect can be seen through certain inertia, it is by no means obvious how vortex core deformation results in a constant mass.

Therefore, in this section, we show numerically exact calculation of the vortex-cavity interaction in a superconducting film. Knowledge of this interaction potential is of fundamental importance. Up to now this interaction has not been calculated properly and is in most papers modeled by an *ad hoc* Gaussian function. Without taking any assumptions nor approximations, we find the distribution of the superconducting order parameter and local currents around the cavity, as a function of the vortex position. The pinning force is then derived from the evolution of the energy of the system along the vortex path. As a main result, new analytical fit and explanation of the modulated pinning force are given, taking into account the presence of the vortex core and all relevant parameters - coherence length ξ, penetration depth λ, and the radius of the cylindrical cavity R (see Fig. 5.1). As another main objective, the implications of such interaction on the dynamic behavior of vortices under a dc-drive are demonstrated.

5.2 THEORETICAL FORMALISM

Our theoretical approach relies upon the Ginzburg-Landau theory. In the stationary case, we solve self-consistently a set of mean field differential equations for the order parameter Ψ and the vector potential $\mathbf{A}$

$$(-i\nabla - \mathbf{A})^2\Psi = (1 - |\Psi|^2)\Psi, \tag{5.1}$$

$$-\kappa^*\nabla \times \nabla \times \mathbf{A} = \mathbf{j}, \tag{5.2}$$

averaged over the sample thickness d [88]. The latter is the Maxwell-Ampère equation with a current density given by Eq. (1.61). κ^* is the sample property and equals $\lambda^2/d\xi$. Solution of Eqs. (5.1, 5.2) minimizes Gibbs free energy (Eq. (1.71)), where periodic boundary conditions (1.57, 1.58) were imposed on the outer edges of the square simulation region. The latter consists of a single hole in the center. At the same time, the condition $j_\perp = 0$ (Eq. (1.55)) was used on the boundaries of the artificial cavity.

5.3 DEFINITION OF THE VORTEX CORE

As a textbook problem, it can be shown that an isolated vortex in a superconducting film is best described by the characteristic length ξ over which the order parameter rises away from the vortex center, and the decay length of the magnetic field λ. However, this rather simple picture directly results in a complicated question - how to define the vortex core - as there is no abrupt change in either Ψ or magnetic field to clearly bound the vortex as a rigid object. On the other hand, the circulating supercurrents around the vortex are resulting from both phase change and applied magnetic vector potential, and should therefore vanish both in the center of a vortex and far from it. Consequently, the maximum of the current in between can be theoretically associated with the vortex core. Solid lines in Fig. 5.2 show the radial distribution of the supercurrent density (in units of $j_0 = cH_{c2}\xi/4\pi\lambda^2$) around the vortex, obtained in our numerical procedure for different values of the effective GL parameter κ^*. Plotted current exhibits maximum at distance ρ_j from the vortex center, which increases with increasing κ^* (in the simulation, ξ and d are fixed, and we actually change λ) and saturates to its maximal value $\rho_j^{max} = 1.692\xi$ (see the inset of Fig. 5.2). Therefore, the size of the vortex core (following the chosen definition) *does not depend on* λ in extreme type-II superconductors, and is *significantly larger than* ξ.

To obtain the analytic expression for the vortex current, we fitted the numerically obtained data utilizing the non-linear χ^2-fitting and a number of function-classes. As a result, we obtained the following approximate expression for the supercurrent around the vortex

$$j = \zeta\rho^\omega \exp(-\sigma\rho), \tag{5.3}$$

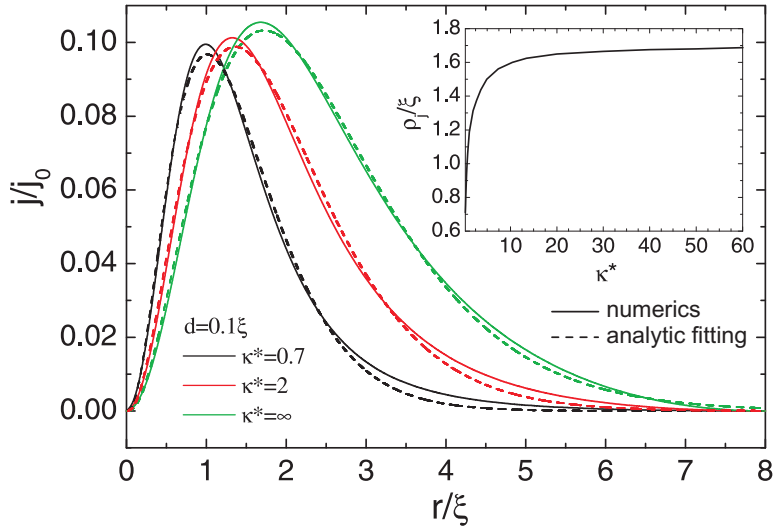

FIG. 5.2: The numerically obtained spatial distribution of the vortex current for different λ to ξ ratios. The dashed curves illustrate the analytic fits (Eq. (5.3)). The inset shows the position of the maximum of the vortex current ρ_j as a function of the effective GL parameter κ^*.

where the coefficients ζ, ω and σ are given by $\zeta = 0.3\exp[1.28/(\kappa^* + 0.3)]$, $\omega = 2.3\exp[0.03/(\kappa^* - 0.23)]$ and $\sigma = 1.35\exp[0.63/(\kappa^* + 0.38)]$. Note that this expression is valid only for type-II superconductors, i.e. $\kappa > 1/\sqrt{2}$. As we will show, such a modified Box-Lucas model for the vortex-current profile in superconducting films will strongly reflect on the interaction of a vortex with an artificial pinning center.

5.4 THE PINNING POTENTIAL

In order to construct the vortex pinning potential of a circular hole, we calculated the free energy of the system F as a function of the vortex distance from the edge of the hole (ρ_v). For each initial vortex localization ρ_v, we kept the phase of the order parameter θ fixed within the area of radius less than 0.5ξ around the vortex center. This additional "boundary" condition ensures the 2π circulation of phase around the chosen grid-point, and numerically fixes the vortex during the process of self-consistent solving of Eqs. (5.1-5.2). In the next step, the derivative of the $F(\rho_v)$ energy landscape reveals the profile of the cavity-vortex attractive force f. This vortex-pinning force is plotted in Fig. 5.3(a) for several radii of the cavity R.

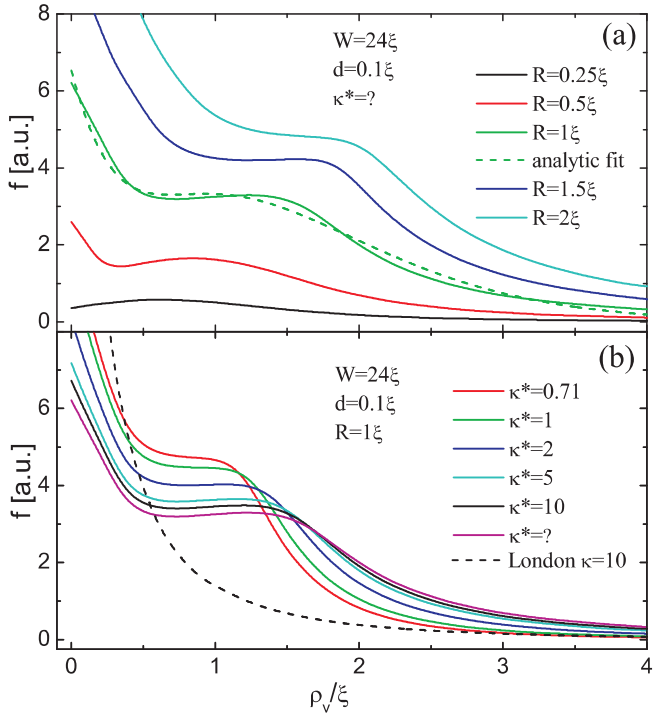

Fig. 5.3: The vortex-cavity interaction force f vs. the vortex position away from the cavity ρ_v: (a) for different radius of the cavity R, and (b) for different values of κ^*. The dashed curve in shows (a) the analytic fit of the $R = \xi$ data (Eq. (5.4)) and (b) the result from the London theory [69].

At this point, it is important to emphasize that the known results within London theory [68, 69] predict an attractive force that monotonically increases as the vortex approaches the hole (dashed curve in Fig. 5.3(b)). However, as shown in Fig. 5.3, our study reveals an *unexpected local maximum* in the $f(\rho_v)$ curve close to the cavity. We observed that the position of the latter maximum shifts further from the hole with increasing radius of the cavity, while the maximum itself diminishes. Note also that R scales with $\xi(T) = \xi(0)/\sqrt{1 - T/T_c}$ in our calculations, and therefore Fig. 5.3(a) indirectly illustrates the temperature dependence of the vortex pinning force for given size of the hole in real units. Thus, not only the pinning force weakens with increasing temperature as shown in Ref. [160], but also *its qualitative behavior* changes.

The vortex-cavity interaction force is also dependant on the GL parameter κ^* (see Fig. 5.3(b)). With increasing λ (and consequently κ^*), the local maximum of the force becomes comparatively more pronounced, shifts further from the cavity, resulting in a stronger long-range vortex-cavity interaction.

Interestingly enough, *no change in the pinning potential* has been observed for $\kappa^* > 15$, indicating that the nature of the vortex-cavity interaction hides behind the vortex currents (which show similar behavior, see Fig. 5.2).

Following the fitting procedure described earlier, we have been able to approximate the cavity-vortex force by the following expression

$$f = \zeta(\rho^{\omega} + \delta)\exp(-\sigma\rho). \tag{5.4}$$

One should note here that the above pinning force shows essentially the same qualitative behavior as the vortex current (see Eq. (5.3)), apart from the shift δ which models the novel repulsive component in the generally attractive interaction. However, unlike Eq. (5.3), the coefficients here depend not only on κ^* but also on the radius of the hole R, and are thus difficult to fit analytically. For example, for radius $R = \xi$ the dependence of the coefficients on κ^* is given by $\zeta = 0.0021 + 0.0065/(\kappa^* + 0.45))$, $\omega = 2.71 - 0.11/(\kappa^* + 0.007))$, $\sigma = 2.11 - 1.1/(\kappa^* + 0.42))$, and $\delta = 0.31 - 0.56/(\kappa^* + 2.62))$. Yet, most of the thin superconducting films commonly used in experiments behave as extreme type-II superconductors, i.e. having large κ^*. In this case, the dependence of the coefficients of Eq. (5.4) on radius R becomes more general: $\zeta = 0.0044 - 0.011/(R + 3.6))$, $\omega = 3.01 - 0.95/(R + 1.77))$, $\sigma = 1.06 + 1.41/(R + 0.5))$, and $\delta = 4.82 - 28.23/(R + 5.4))$.

5.5 THE VORTEX-CAVITY PHAGOSOME

Having in mind the similarities in Eqs. (5.3) and (5.4), let us now address the behavior of the $f(\rho_v)$ curves in Fig. 5.3(a) from the perspective of vortex currents. When the vortex approaches the hole, supercurrents gradually reach the cavity. Although a fraction of the flux becomes captured by the hole, the majority of the currents still remains trapped between the vortex and the edge, unable to circumvent the cavity (Fig. 5.4(a)). It is this high current density between the vortex center and the cavity that is responsible for a local repulsive force contribution to the global attractive force visible in Fig. 5.3. The maximal adhesion of currents to the cavity is achieved when vortex core (i.e. maximal current) reaches the hole (see Figs. 5.2 and 5.3 in comparison) and starts deforming around it. Finally, when close to the hole, remaining vortex currents engulf the hole (Figs. 5.4(b-c)), dragging the vortex inside the hole. However, the adhesion of the currents to the cavity quantitatively depends on the size of the hole; smaller holes are easier to circumvent, and only tighter isolines of current close to the vortex adhere to the cavity, when vortex already gradually slides towards its equilibrium position in the cavity (see black line in Fig. 5.3(a)). For a more comprehensible analogy, one may think of a liquid droplet sliding down a tilted surface towards a cylindrical perforation. Moreover, the interaction of droplets with circular roughness of the substrate

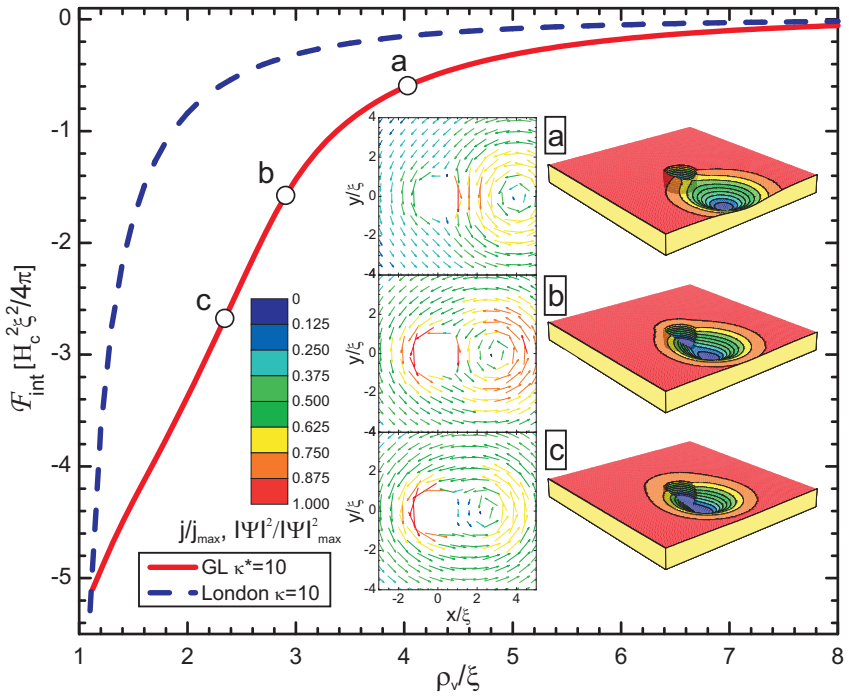

Fig. 5.4: The vortex-cavity interaction energy (per unit length) as a function of the vortex position (solid line – GL theory, dashed one – London approach [69]). Insets (a-c) show the $|\Psi|^2$-profiles (right panel) and the corresponding vectorplots of the supercurrent (left) for indicated vortex positions.

(with given radius of the curvature) is essential for modern microfluidic ratchet devices, as wetting and de-wetting of such curved surface textures create a gradient in the surface-energy of the droplet.

Fig. 5.4 also shows the vortex-hole interaction energy ($\mathcal{F}_{int} = F - F_v$, with $\mathcal{G}_v$ being the energy of a single vortex far from the hole) as a function of ρ_v for $R = \xi$ and $\kappa^* = 10$. The behavior of the energy is significantly different from the one obtained within the London theory for a bulk superconductor (reported earlier in Refs. [68, 69]) and has no linear dependence on ρ_v as predicted in Ref. [159]. We also failed to reproduce extensive vortex elongation ($\approx 4\xi$) close to the cavity as found in Ref. [159]. Quite contrary, we found a gradual deformation of the vortex core around as well as towards the hole. Though latter deformation is sizeable and clearly visible, it does not exceed 15% of the size of the vortex core (see Fig. 5.4(a-d)). Still, this stationary picture may differ from the case when vortex is driven across the hole, as different core dynamics is expected during pinning and de-pinning.

5.6 DYNAMIC CONSEQUENCES

To understand the dynamics in this system, we studied a thin superconducting square (with side $a = 32\xi$) with a cylindrical hole, using the time-dependent GL equation [161]

$$\frac{u}{\sqrt{1+\Gamma^2|\Psi|^2}}\left(\frac{\partial}{\partial t}+\mathrm{i}\varphi+\frac{\Gamma^2}{2}\frac{\partial|\Psi|^2}{\partial t}\right)\Psi = \\ =(\nabla-\mathrm{i}\mathbf{A})^2\Psi+(1-|\Psi|^2)\Psi, \tag{5.5}$$

coupled with the equation for the electrostatic potential $\Delta\varphi = \mathrm{div}\big(\mathrm{Im}(\Psi^*(\nabla - \mathrm{i}\mathbf{A})\Psi)\big)$. Here, time is scaled by $\tau_{GL} = \pi\hbar/8k_BTu$, and the electrostatic potential by $\varphi_0 = \hbar/2e\tau_{GL}$. $\Gamma = 2\tau_E\Psi_0/\hbar$, with τ_E being the inelastic electron-collision time. Typical values of Γ for low-T_c superconductors are in the 10-10^3 range (we used $\Gamma = 100$). Parameter u is taken equal 5.79 [161]. Current leads were attached along the two parallel sides of the sample (with injected current j_{ext}), and simulated as normal metal-superconductor contacts, i.e. with $\Psi = 0$ and $-\nabla\varphi = j_{ext}$.

Using the above formalism, we investigated the current-voltage characteristics for different radii of the cavity. Initially, we stabilized a single vortex inside the cavity by applying a homogeneous field of $H = 0.01H_{c2}$. When a dc current is applied to the sample, vortex experiences Lorentz force and can be set in transverse motion across the sample by a sufficiently strong drive. In that case, vortex is depinned from the hole, and with time leaves the sample, only to reenter it from the opposite side and become pinned again. These dynamical phases are indicated in Fig. 5.5(a) for a fixed drive of $j_{ext} = 0.01j_0$ ($j_0 = cH_{c2}\xi/4\pi\lambda^2$), in the transverse voltage vs. time curves (dV/dt enhances the pinning features). In the absence of pinning, one expects approximately linear behavior of $V(t)$ curves between the extremes related to the vortex entry and exit. As shown in Fig. 5.5(a), increasing of the hole-radius results in a more pronounced voltage drop. Since the discrepancy from the linear behavior is present both during pinning and depinning, it is unclear how this phenomenon is related to the vortex-core deformation. For that reason, we plot the position of the vortex-center ($\Psi = 0$) vs. time in Fig. 5.5(b). In proof of our previous assessments, we observed different vortex behavior for different radii of the hole - for $R = \xi$, vortex monotonously speeds towards the hole, whereas for larger R it slows down prior to entering the cavity. For $R > 1.8\xi$, we found that monotonous behavior is restored (vortex even accelerates in front of the cavity), but with higher velocity. Therefore, the existence of the repulsive component in the pinning force is confirmed in transport simulations, even though the driving force and non-uniformity of the applied current around the hole partially mask the effect.

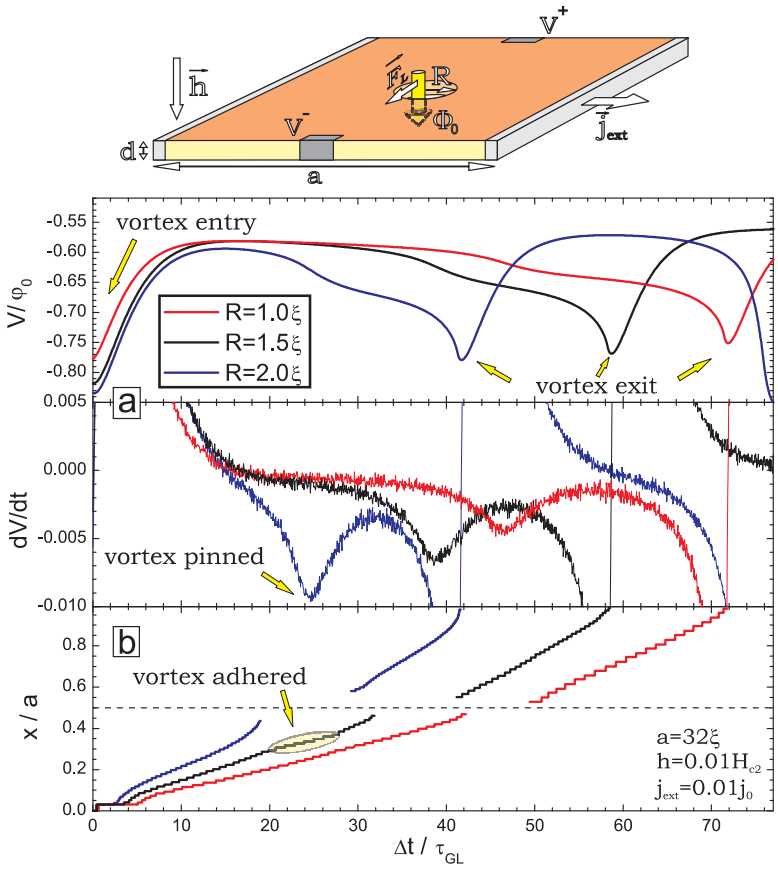

FIG. 5.5: Vortex dynamics in a superconducting square with a hole of radius R: $V(t)$ and $dV/dt(t)$ curves for different R, and the corresponding vortex position as a function of time.

5.7 CONCLUSIONS

We have studied the interaction of a vortex with a circular antidot in a superconducting thin film using the nonlinear GL theory. Calculations show that due to the local compression of vortex currents and their adhesion to the edge of the perforation, a local repulsive component to the generally attractive pinning force is found. The value of this component depends on the size of the antidot and vanishes for very big and small radii of the antidots. The dynamic consequences of this adhesion effects was considered in the case of finite superconductor with external applied current. The $I-V$ characteristics show different regimes in the presence of a hole in the sample. The obtained results

are of great interest in understanding complex dynamic processes [73, 74] in superconducting samples in the presence of different kinds of pinning centers. Besides having a clear impact on numerous vortex-dynamics studies and fluxonic devices, our model for the pinning force relates to the interaction of a magnetic vortex with defects in magnetic elements (with local moments taking the role of the vortex currents), and dynamic deformations of biological entities during phagocytosis (where membrane is imitated by the vortex core).

Publications. The results presented in this chapter were published as:

- G. R. Berdiyorov, M. V. Milosevic, and F. M. Peeters, *Qualitative Modification of the Pinning Force due to Vortex-Cavity Adherence* (submitted to Phys. Rev. Lett.).

6

A superconducting disk with a blind hole

6.1 INTRODUCTION

The properties of mesoscopic superconductors are very different compared to those of bulk superconductors as the vortex configurations and the critical parameters for mesoscopic samples are strongly influenced by the size and topology (boundary) of the samples. Theoretical studies [78, 79, 88, 89] have shown that different kinds of vortex states can appear in such samples: giant vortex states, where the order parameter has a single zero, multivortex states consisting of several singly quantized vortices (mostly situated on shells [162]) and symmetry imposed vortex-antivortex states [145, 147, 163–165]. In addition, the non-quantized penetration of magnetic field in the vortex state of superconductors is observed [132, 166], which lead to so-called *fractional* and *negative* vortices.

Conventional experiments on mesoscopic superconductors have measured the resistivity [123, 167] and the magnetization [29, 132] of the different vortex states. With this technique it is possible to investigate the dependence of the critical parameters on the sample geometry, but it does not provide clear information about the real vortex structure. To describe these experimental results one can linearize the GL equations, simplifying the problem considerably. Another method to investigate the superconducting state is through Hall magnetometery [29, 86, 132], which gives indirect information on the vortex structure

deep inside the superconducting region. Recently, Kanda *et al.* [83] developed the multi-small-tunnel-junction, in which several small superconductor-insulator-normal junctions are attached to a nesoscopic superconductor to detect small changes in the local density of states caused by supercurrents. This method is able to distinguish directly between multivortex states and giant vortex states. The static and dynamic behavior of individual vortices can also be directly observed using the Bitter decoration technique [82], electron holography [168], scanning probe [169] and Lorentz [38] microscopy. In the case of superconductors with holes it is impossible to visualize the vortices in the cavity because of the absence of any magnetic contrast: the supercurrents constituting the vortex are forced to flow at the outer edge of the hole, confining the vortex in space. This can be circumvented by putting a thin superconducting layer under the sample (or equivalently by depositing a thin superconducting film inside the hole) and due to the so-called "flux compression" method [170], multiquanta vortices are visualized.

A superconducting film with a blind circular hole was investigated theoretically in Ref. [67] using the linearized GL equation. It was shown that the value of the critical field is sensitive to the bottom layer thickness, but the number of vortices which nucleate inside the hole was not influenced. But recent experiments [171] on superconducting films with arrays of blind holes show that blind holes provide a weaker pinning potential than antidots. It was also found that the maximum number of flux quanta trapped by a pinning site is lower for the blind hole array.

In this chapter of the thesis we investigate nucleation of superconductivity in a superconducting disk containing a blind hole. In our approach, the full non-linear GL-theory is used and the dependence of various quantities (free energy, order parameter and magnetization) on the thickness of the blind hole is studied. This allows us to obtain the actual vortex structure inside the blind hole which will act as a pinning site, when embedded in an infinite extended superconducting film. We also consider the influence of the smoothness of the edges of the blind hole on the superconducting state. In two limiting cases (see Fig. 6.1): i) $d_i = d$, i.e. for the superconducting disk and ii) $d_i = 0$, the case of rings, we recover our previous results.

The chapter is organized as follows. The theoretical formulation of the problem is presented in Sec. 6.2, where we extend our previous approach to systems with variable thickness. The influence of the steepness of the edges and thickness of the blind hole on the vortex configuration and critical parameters is studied in Sec. 6.3 for small (Sec. 6.3.1) and for larger (Sec. 6.3.2) disks. The non-symmetrical case, when the blind hole is moved from the center of the sample over a distance a is also considered. The $H - T$ phase diagram is given in Sec. 6.4 and our results are summarized in Sec. 6.5.

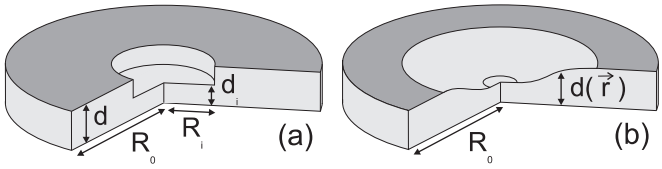

Fig. 6.1: The configurations: a superconducting disk with radius R_0 and thickness d with: a) a sharp edge, or b) a smooth blind hole with radius R_i and thickness $d(x, y)$, which is placed in the center of the disk.

6.2 THEORETICAL FORMALISM

We consider a superconducting disk with radius R_0 and thickness d with a blind hole in the center with radius R_i and thickness d_i (see Fig. 6.1). The superconducting sample is immersed in an insulating medium (e.g. vacuum) and exposed to a homogeneous perpendicular magnetic field $\mathbf{H} = (0, 0, H)$. For the given system we solve the non-linear GL equations taking into account the demagnetization effects. All the calculations are done for the Gl parameter $\kappa = 1$.

First we derive the GL equations for a thin sample with variable thickness d(x,y). The total Gibbs free energy is [23, 24]

$$\begin{aligned}\mathcal{G}_{sH} = \quad & \mathcal{G}_{nH} + \int \Big\{\alpha|\Psi|^2 + \frac{1}{2}\beta|\Psi|^4 + \frac{1}{4m}\Big|\Big(-i\hbar\nabla - \frac{2e}{c}\mathbf{A}\Big)\Psi\Big|^2 \\ & + \frac{1}{8\pi}\Big(\mathbf{h} - \mathbf{H}\Big)^2\Big\} dV, \end{aligned} \tag{6.1}$$

where h is the local magnetic field and G_{nH} is the free energy of the magnetic-field-exposed superconductor in the normal state. For thin disks we are allowed to assume that the superconducting condensate is homogeneous along the z-direction and consequently we may take for the volume of the sample $dV = d(x, y)dxdy$, where $d(x, y)$ is the coordinate dependent thickness of our sample. To derive the GL equations we use the Euler equation:

$$\frac{\partial\Omega}{\partial\Psi^*} - \frac{\partial}{\partial x}\frac{\partial\Omega}{\partial\left(\frac{\partial\Psi^*}{\partial x}\right)} - \frac{\partial}{\partial y}\frac{\partial\Omega}{\partial\left(\frac{\partial\Psi^*}{\partial y}\right)} = 0, \tag{6.2}$$

where Ω is the integrand appearing in Eq. (6.1). After simple transformations we obtain the expression

$$\left[\alpha\Psi+\beta\Psi\left|\Psi\right|^2+\frac{1}{4m}\left(-i\hbar\nabla-\frac{2e}{c}\mathbf{A}\right)^2\Psi\right]d(x,y)$$
$$-\frac{i\hbar}{4m}\left(-i\hbar\nabla\Psi-\frac{2e}{c}\mathbf{A}\Psi\right)\nabla d(x,y)$$
$$+\frac{i\hbar}{4m}d(x,y)\nabla\left(i\hbar\nabla\Psi+\frac{2e}{c}\mathbf{A}\Psi\right)=0, \tag{6.3}$$

which gives us the boundary condition (1.55) and the first Ginzburg-Landau equation (see also Ref. [172]):

$$\frac{1}{2m}\left(-i\hbar\nabla-\frac{2e}{c}\mathbf{A}\right)^2\Psi=-\alpha\Psi-\beta\Psi|\Psi|^2$$
$$+\frac{i\hbar}{2m}\left(-i\hbar\nabla-\frac{2e}{c}\mathbf{A}\right)\Psi\frac{\nabla d(x,y)}{d(x,y)}, \tag{6.4}$$

The last term in Eq. (6.4) describes the effect of the sample thickness variation on the superconducting condensate. In case of a sharp hole with radius R_i the latter term becomes a delta function which results in a discontinuity of the derivative of the order parameter at $\rho=R_i$, while the order parameter itself is continuous. Thus at the edge $\rho=R_i$ the radial component of the current density $\mathbf{j}$ will exhibit a jump but the total current, $\mathbf{I}=\mathbf{j}\cdot d$, has to be continuous. The second Ginzburg-Landau equation reads:

$$\nabla\times\nabla\times\mathbf{A}=\frac{4\pi}{c}\mathbf{j}, \tag{6.5}$$

with the superconducting current density

$$\mathbf{j}=\frac{e\hbar}{im}\left(\Psi^*\nabla\Psi-\Psi\nabla\Psi^*\right)-\frac{4e^2}{mc}\left|\Psi\right|^2\mathbf{A}. \tag{6.6}$$

The actual boundary condition corresponds to the preservation of the total current in the perpendicular cross-section of the sample, which can be written as the condition of no current leaking in the insulator media $\left(-i\nabla-\mathbf{A}\right)\Psi\big|_n=0$, where the subscript n denotes the component normal to the disk surface. The boundary condition for the vector potential has to be taken far away from the disk, where H equals the applied field, i.e. $\mathbf{A}=\mathbf{A}_0=0.5H\rho\mathbf{e}_\phi$ for $\rho\gg R_0$. Here $\mathbf{e}_\phi$ denotes the azimuthal direction, and ρ the radial distance from the disk center.

Using dimensionless variables and the Landau gauge, $\mathrm{div}\mathbf{A}=0$, we rewrite the system of coupled nonlinear Eqs. (6.4, 6.5) in the following form:

$$\left(-i\nabla-\mathbf{A}\right)^2\Psi=\Psi\left(1-\left|\Psi\right|^2\right)+i\left(-i\nabla-\mathbf{A}\right)\Psi\frac{\nabla d(x,y)}{d(x,y)}, \tag{6.7}$$

$$-\frac{k^2}{d(x,y)}\Delta\mathbf{A} = \frac{1}{2i}\left(\Psi^*\nabla\Psi - \Psi\nabla\Psi^*\right) - |\Psi|^2\,\mathbf{A}, \tag{6.8}$$

and we solve this system by following the numerical approach of Schweigert and Peeters [78]. Here the distance is measured in units of the coherence length $\xi = \hbar/\sqrt{-2m\alpha}$, the order parameter in $\psi_0 = \sqrt{-\alpha/\beta}$, the vector potential in $c\hbar/2e\xi$. $\kappa = \lambda/\xi$ is the Ginzburg-Landau parameter, and $\lambda = c\sqrt{m/\pi}/4e\psi_0$ is the penetration depth. We scale the superconducting current in units of $j_0 = cH_c/2\pi\xi$ and the magnetic field in $H_{c2} = c\hbar/2e\xi^2 = \kappa\sqrt{2}H_c$, where $H_c = \sqrt{-4\pi\alpha/\beta}$ is the critical field. For nonzero temperature T, the temperature dependence of ξ and H_{c2} is given by Eq. (1.52, 1.54). This scaling allows us to relate our numerical results to the experimental measurements performed at nonzero temperature.

The difference between the superconducting and the normal state Gibbs free energy measured in $F_0 = H_c^2V/8\pi$ units can be expressed through the integral

$$\begin{aligned} F = \quad & V^{-1}\int_V \Big[2\left(\mathbf{A}-\mathbf{A}_0\right)\cdot\mathbf{j} - |\Psi|^4 \\ & +i\left(-i\nabla-\mathbf{A}\right)\Psi\frac{\nabla d(x,y)}{d(x,y)}\Big]d(x,y)dxdy, \end{aligned} \tag{6.9}$$

where integration is performed over the sample volume V, and $\mathbf{A}_0$ is the vector potential of the applied uniform magnetic field. The dimensionless magnetization, which is defined as

$$M = (\langle h\rangle - H)/4\pi, \tag{6.10}$$

where $\langle h\rangle$ denotes the magnetic field averaged over the sample.

6.3 EFFECT OF THE EDGE STEEPNESS AND THICKNESS OF THE BLIND HOLE ON THE VORTEX CONFIGURATIONS

6.3.1 Small disks

First we investigate the influence of the smoothness of the blind hole edges on the vortex configurations, by changing the smoothness and the slope of the edges of the blind hole. In order to avoid Dirac-delta-functions in the differential equation (6.7) which appear in the case of a step-like change in $d(x,y)$, we introduced a gradual thickness variation, modeled by the function $f(\rho) = (1-\exp(-\rho/\eta))/(1+\exp(R_i-\rho)/\eta)$. In the limit $\eta\to 0$ the function $f(\rho)$ reduces to the Heaviside step function. The thickness of our sample is defined as $d(\rho) = a + bf(\rho)$, where $a = d_i$ and $b = d - d_i$.

We consider a small superconducting sample with $a = 0.3\xi$, $b = 0.3\xi$, $R_i = \xi$, $R_0 = 2.0\xi$ and η/ξ =0.0, 0.05, 0.1, 0.2. It was shown in Ref. [88] that for small radius disks the confinement effects are dominant and this imposes

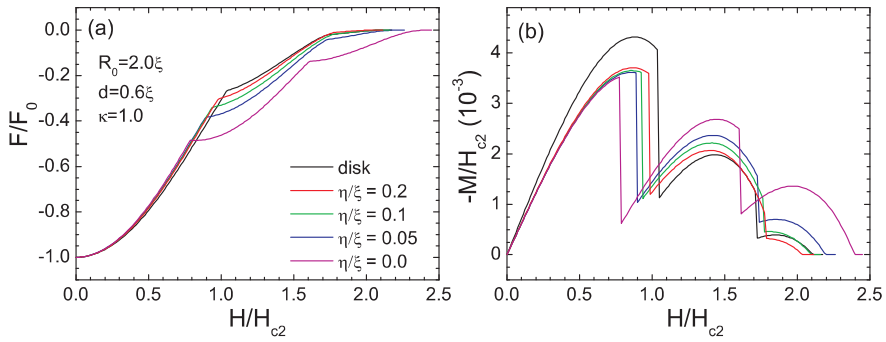

FIG. 6.2: The ground state free energy (a) and the corresponding magnetization (b) as a function of the applied magnetic field for a disk (black curve) with radius $R_0 = 2.0\xi$ and thickness $d = 0.6\xi$ and for samples containing a blind hole with different steepness: $\eta/\xi = 0.2$ (red curve), 0.1 (green curve), 0.05 (blue curve), and 0.0 (magenta curve).

a circular symmetry on the superconducting condensate. Therefore, following the approach of Ref. [88] we solve the GL equations assuming $\Psi(\rho) = F(\rho)\exp(iL\phi)$, where ρ and ϕ are cylindrical coordinates, and consequently both the vector potential and the superconducting current are directed along $\mathbf{e}_\phi$. L is the winding number and gives the vorticity of the system. As we restricted ourselves to circular symmetric configurations, the present states characterize only the giant vortex states. In this case, the number of variables in the GL equations are reduced, which improves the accuracy and shortens the computational time.

Figs. 6.2(a,b) show the ground state free energy and magnetization for the above sample and for the case in the absence of a blind hole with disk thickness $d(= a + b) = 0.6\xi$. In all cases, only a maximum of two vortices can nucleate in the superconductor. The free energy of the Meissner state for the disk is lower than the energy of the other samples which is a consequence of the enhanced penetration of the magnetic field into the superconductor when the blind hole is present. For the same reason, the thermodynamic transition field between the $L = 0$ and $L = 1$ states is higher for the disk. This field is the smallest for the $\eta/\xi = 0.0$ case, i.e. the case of a perfect blind hole (steep edge). The free energy of the $L = 1$ and $L = 2$ states is lower for smaller η/ξ, which illustrates the compression of vortices into the center of the sample. For the $L = 2$ state the value of the free energy of the disk is lower than the energy of the sample with η/ξ =0.1 and 0.2, which results in a higher superconducting/normal (S/N) transition field. This field is $H_{c3}/H_{c2} = 2.11$ for the disk and H_{c3}/H_{c2} =2.04, 2.10, 2.20, 2.40 for the cases η/ξ =0.2, 0.1, 0.05, and 0.0, respectively.

Following the pattern explained above, the magnetization ($-M$) of the disk in the Meissner state is larger than for the samples with a blind hole, which

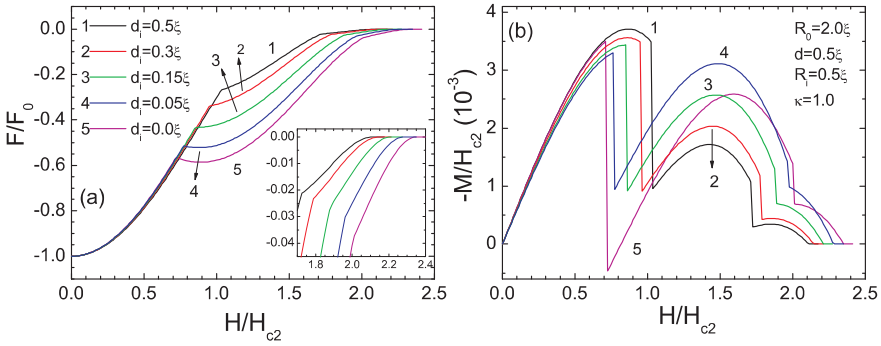

Fig. 6.3: The ground state free energy (a) and the corresponding magnetization (b) as a function of the applied magnetic field, for a disk (curve 1) with radius $R_0 = 2.0\xi$ and thickness $d = 0.5\xi$, a disk with a blind hole in the center with radius $R_i = 0.5\xi$ and thickness $d_i/\xi = 0.3$ (curve 2), 0.15 (curve 3), 0.05 (curve 4), and 0.0 (superconducting ring, curve 5). The inset in (a) is an enlargement of the high magnetic field region where the $L = 2$ state is the ground state.

is due to the larger flux expulsion from the sample. For $L > 0$ the relative position of the different magnetization curves depends on the magnetic field.

Next we consider small superconducting disks with a perfect blind hole in the center, i.e. for $\eta/\xi = 0$ and investigate the effect of the thickness of the blind hole on the superconducting state. Figs. 6.3(a,b) show the ground state free energy and the magnetization of such a superconducting disk with radius $R_0 = 2.0\xi$ and thickness $d = 0.5\xi$ with a blind hole with radius $R_i = 0.5\xi$ and thickness $d_i/\xi = 0.0$, 0.05, 0.15, 0.3, and 0.5. The inset shows the enlargement of the free energy in the region where the $L = 2$ state becomes the ground state. The situation with $d_i = 0.5\xi$ corresponds to the "classical" disk case [88] and $d_i = 0.0\xi$ to the superconducting disk with a hole (superconducting ring) [90]. In all cases the maximal possible vorticity in the sample equals $L_{max} = 2$. When we decrease the blind hole thickness the Meissner state, i.e. the $L = 0$ state becomes less stable and the $L = 0 \rightarrow L = 1$ state transition occurs at lower magnetic field (which is similar to the previous continuous edge case, where decreasing η/ξ implies a decreasing effective thickness of the blind hole, see Fig. 6.2(b)). Also the ground state free energies for the $L = 1$ and $L = 2$ states are lower for the samples with small thickness of the blind hole. Notice that the $L = 1 \rightarrow 2$ transition occurs at higher fields with decreasing d_i (see inset of Fig. 6.3(a)), which is opposite to the $L = 0 \rightarrow 1$ transition and is also different in the case of the continuous edge. With decreasing the thickness of the blind hole the S/N state transition shifts to higher magnetic fields. This field is H_{c3}/H_{c2} =2.11 for the disk, H_{c3}/H_{c2} =2.35 for the ring and H_{c3}/H_{c2} =2.15, 2.21, and 2.29 for a thickness of the blind hole d_i/ξ =0.3, 0.15, and 0.05, respectively.

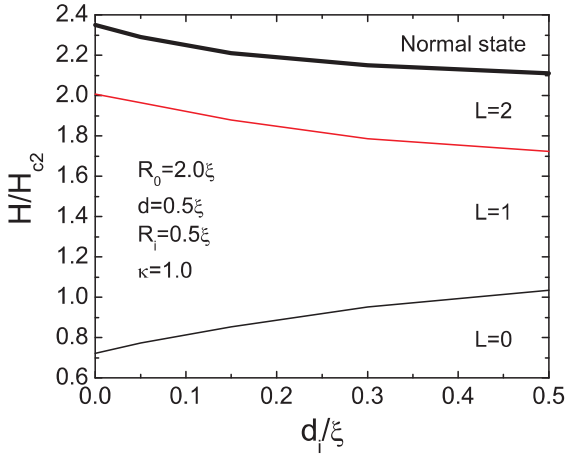

FIG. 6.4: Phase diagram: the relation between the blind hole thickness d_i and the magnetic field H/H_{c2} at which ground state transitions take place for a superconducting sample with radius $R_0 = 2.0\xi$, thickness $d = 0.5\xi$, $\kappa = 1.0$ and with blind hole radius $R_i = 0.5\xi$.

The magnetization, $-M$, (Fig. 6.3(b)) of the $L = 0$ state is higher for the disk than for the other samples, which shows the enhanced expulsion of the field from the disk. However, for the $L = 1$ state the magnetization of the disk is smaller, since the presence of the blind hole in the center favors the appearance of vortices (compression of the flux in the center of the sample). With decreasing the blind hole thickness the magnetization of this state increases. The ground state of the ring with $L = 1$ shows a paramagnetic response, i.e. $-M < 0$. For the other samples this effect occurs only for the metastable states with $L = 1$ and $L = 2$.

Figure 6.4 summarizes these results into a phase diagram which gives the relation between the blind hole thickness d_i and the magnetic field H/H_{c2} at which the ground state transitions take place for a superconducting disk with radius $R_0 = 2.0\xi$, thickness $d = 0.5\xi$, and a blind hole with radius $R_i = 0.5\xi$. The black curve indicates the ground state transition from the $L = 0$ state to the $L = 1$ state, the red curve the $L = 1$ to the $L = 2$ state transition and the thick black curve gives the S/N transition. Notice that the Meissner state is stabilized as being the ground state with increasing thickness of the blind hole, which is opposite to the $L = 1 \rightarrow L = 2$ and the S/N state transition field which moves to smaller fields with increasing d_i.

It was shown in Ref. [90] that with increasing inner radius of the superconducting ring the S/N transition field shifts to higher magnetic fields and more transitions between different vortex states are possible. In Figs. 6.5(a,b)

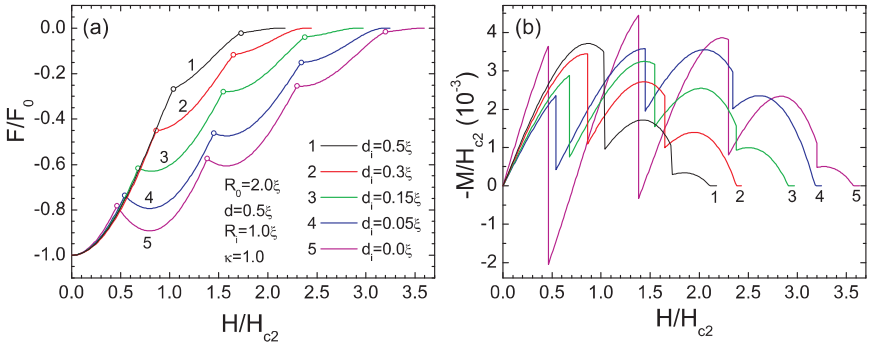

Fig. 6.5: The ground state free energy (a) and corresponding magnetization (b) as a function of the applied magnetic field of a superconducting disk (curve 1) with radius $R_0 = 2.0\xi$ and thickness $d = 0.5\xi$, with a blind hole in the center with radius $R_i = 1.\xi$ and thickness $d_i/\xi = 0.3$ (curve 2), 0.15 (curve 3), 0.05 (curve 4), and 0.0 (superconducting ring, curve 5). Open circles indicate transitions between different vortex states.

the ground state free energy and the corresponding magnetization of a superconducting disk with a larger blind hole ($R_i = 1.0\xi$) is shown while keeping the other parameters the same as before. In this case the maximal number of vortices for the sample with a blind hole of thickness $d_i = 0.3\xi$ is $L_{max} = 2$. For a thinner blind hole more vortices can enter the sample before destroying the superconducting state. The maximal number of vortices for the ring is $L_{max} = 4$. With decreasing the thickness of the blind hole the S/N transition field shifts to higher fields. This field is $H/H_{c2} = 2.11$ in the disk case and $H/H_{c2} = 2.38$, 2.92, 3.21 for the thickness of the blind hole $d_i/\xi = 0.3$, 0.15, 0.05, respectively. The S/N transition field for the ring equals $H/H_{c2} = 3.58$. The transitions between different L states occur at lower fields for the small thickness of the blind hole, and the free energy becomes lower, approaching the free energy of the superconducting ring.

The phase diagram in Fig. 6.6 shows the magnetic field H/H_{c2}, at which ground state transitions take place, as a function of d_i for larger value of the R_i. The thick solid curve gives the S/N transition, which exhibits some oscillatory-like behavior. Notice that the S/N transition moves to higher field with decreasing the blind hole thickness and in that case more vortices can be trapped. Notice that the phase diagram is very different from the $R_i = 0.5\xi$ case (Fig. 6.4) because now all ground state transition fields increase with d_i except for the S/N transition field.

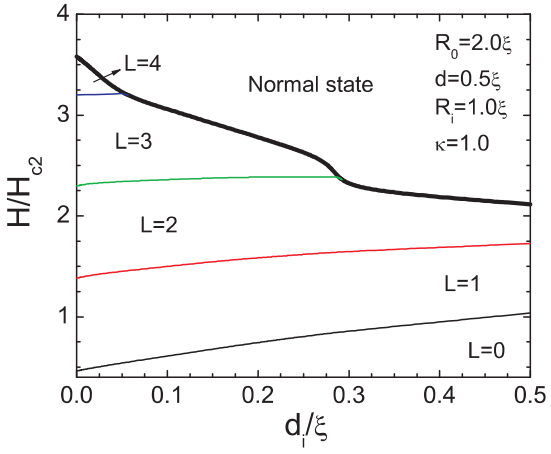

FIG. 6.6: The same as Fig. 6.4, but now for larger radius of the blind hole, $R_i = 1.0\xi$.

6.3.2 Larger disks: multivortex state

Until now, we restricted ourselves to small superconducting samples, where the confinement effects are dominant and only giant vortex states are stable. For larger superconducting disks it is energetically more favorable for the giant vortex to split into separated vortices for certain magnetic fields [78].

As an example we take a superconducting disk with radius $R_0 = 4.0\xi$, thickness $d = 0.1\xi$ and for different values of the radius R_i and thickness d_i of the blind hole. Figs. 6.7(a-d) show the free energy for such a disk containing a blind hole with radius $R_i = 2.0\xi$ and thickness d_i =0.1ξ, 0.05ξ, 0.01ξ, and 0.0ξ (superconducting ring), respectively, as a function of the applied magnetic field. The insets show an enlargement of the free energy close to the S/N boundary. The multivortex states are plotted by dotted curves and the transitions from the multivortex state to the giant vortex state are indicated by open circles. In order to define whether the state is a multivortex state or a giant vortex state, we used the following criterion: if the maximum between two minima in the Cooper-pair density is lower than 0.5% of the maximum Cooper-pair density in the sample, the state is assigned to be a giant vortex state. In all samples vortex states up to $L = 11$ can nucleate. In the case of the uniform disk multivortex states can nucleate for vorticity L =2, 3, 4, 5, and 6, and with increasing external field, these multivortex states transit to a giant vortex state for fixed L. When we include a blind hole into the disk (Fig. 6.7(b)) the free energy of all states becomes lower and the S/N state transition occurs at higher magnetic field. This field is $H_{c3}/H_{c2} = 1.91$ for the disk and $H_{c3}/H_{c2} = 1.92$ for the disk with the blind hole of thickness $d_i = 0.05\xi$. In this case less states are able

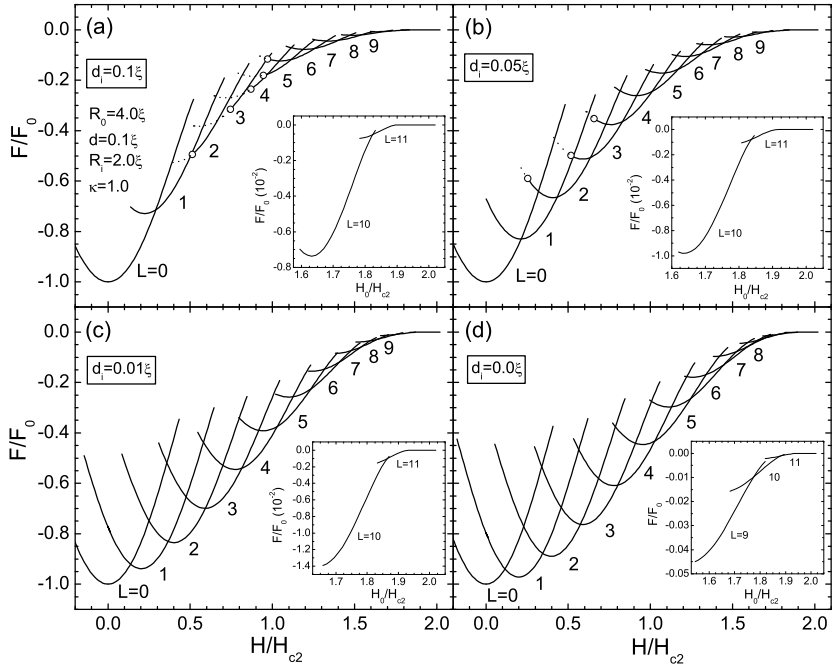

Fig. 6.7: The free energy as a function of the applied magnetic field of the superconducting disk with radius $R_0 = 4.0\xi$, thickness $d = 0.1\xi$ (a) with a blind hole in the center with radius $R_i = 2.0\xi$ and thickness $d_i = 0.05\xi$ (b), 0.01ξ (c), and 0.0ξ (superconducting ring) (d), respectively. The multivortex states are plotted by dotted curves and the transitions from the multivortex state to the giant vortex state are indicated by open circles.

to nucleate into a multivortex state, namely L =2, 3, and 4. Moreover, the magnetic field region over which we found the multivortices is also decreased. When we decrease the thickness of the blind hole (Fig. 6.7(c)) the vortex states become more stable and the ground state transitions occur at lower fields for lower vorticity. Notice that now the $L = 1$ state remains stable even for negative applied fields. The S/N transition field now is $H_{c3}/H_{c2} = 1.95$. In this case all states are giant vortex states. By further decreasing the blind hole thickness the free energy approaches the energy of the superconducting ring (Fig. 6.7(d)). The S/N transition field of the ring is the highest one and equals

$1.96H_{c2}$. It is seen that for the states with lower vorticity ($L \leq 4$) the ground state transition fields are higher for thicker blind holes, i.e. larger d_i, while for states with larger vorticity ($L > 4$) the ground state transition fields increase with decreasing d_i. From Figs. 6.4, 6.6, it is obvious that, regardless on the size of the disk and the blind hole, the thinner blind hole favors penetration of the first vortex in the sample (lower applied field necessary), due to enhanced compression of the field in the blind hole. However, the behavior of the critical field for penetration of the following vortices is determined by a competition between the pinning effects of the blind hole and repulsion between the vortices in the sample. In the case of a larger hole the pinning effects dominate till the fifth vortex penetrates the blind hole, reinforcing the repulsion between vortices. For $L > 4$ vorticity, it is more energetically favorable that the vortices sit further from each other, when the confinement effects of the blind hole are weaker (larger d_i), resulting in a decrease of the threshold applied flux as function of the thickness of the blind hole.

Figs. 6.8(a-d) show the magnetization for the superconducting samples of Figs. 6.7(a-d). The magnetization is calculated using Eq. (2.5) after averaging

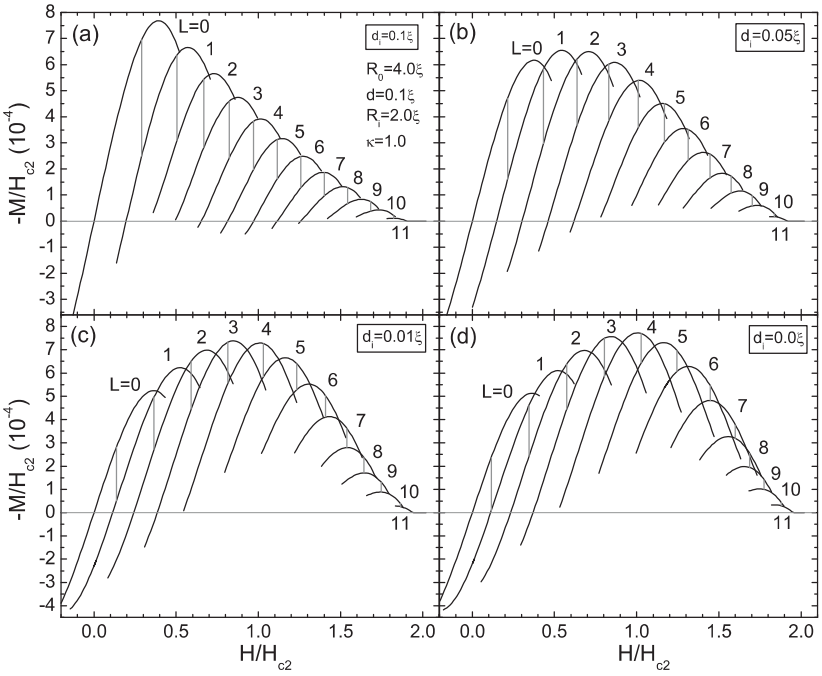

FIG. 6.8: The same as Fig. 6.7, but now for the magnetization. The vertical lines indicate the ground state transition.

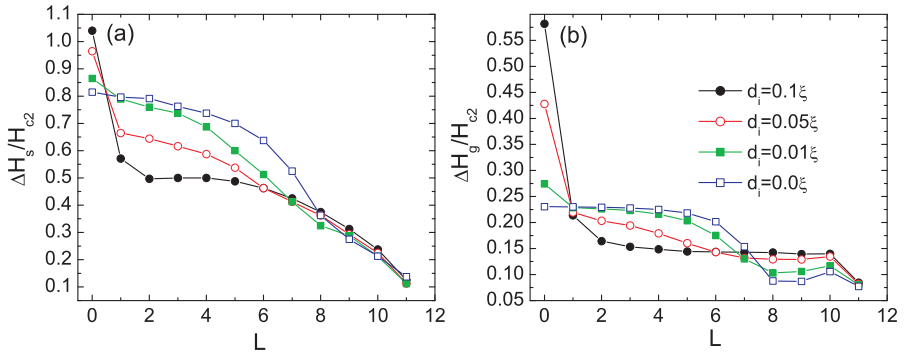

Fig. 6.9: (a) The magnetic-field range ΔH_s over which the vortex state with vorticity L is stable and (b) the magnetic-field range ΔH_g over which the given vortex state is the ground state, as function of the vorticity L. The sample parameters are the same as in Fig. 6.7.

the field only over the superconductor, namely excluding the hole in the superconducting ring case. In these figures the vertical lines indicate the ground-state transitions (see Fig. 6.7). In the case of the superconducting disk (Fig. 6.8(a)) the maxima in the magnetization curve decrease with increasing vorticity L, since most of the applied flux is expelled from the superconductor in the Meissner state. For the given value of the Ginzburg-Landau parameter the states with L =1, 4, 5, 6, 7, and 8 show partly paramagnetic response (i.e. $-M < 0$). Notice that the insertion of a blind hole enhances such a paramagnetic response (Figs. 6.8(b,c)) for the small L-states. The largest amplitude of the magnetization is found for the $L = 1$ state. When we decrease the thickness of the blind hole (Fig. 6.8(c)) (i) the maxima in the magnetization shifts to higher vorticity, (ii) less states show paramagnetic response and (iii) the magnetization approaches the one of the superconducting ring case (Fig. 6.8(d)), which is maximum for the $L = 4$ state.

Figs. 6.9(a,b) show the magnetic-field range $\Delta H_s = H_{penetration} - H_{expulsion}$ over which the vortex state with vorticity L is stable and the magnetic-field range ΔH_g over which the given vortex state is the ground state. For the disk case, the results are given by black curves, for the disk with the blind hole with thickness $d_i = 0.05\xi$ by red curves, $d_i = 0.01\xi$ by green curves and for the superconducting ring by blue curves. Notice that in each case the Meissner state, i.e. the $L = 0$ state, has the largest stability region. For the homogeneous disk ΔH_s exhibits a local maximum at $L = 4$. The Meissner state becomes less stable when the blind hole is present. The transition to the $L = 1$ state occurs at lower magnetic field, indicating that the presence of the blind hole significantly facilitates the penetration of the first vortex in the sample. The lowest stability region of the $L = 0$ state is found for the superconducting ring.

With decreasing the thickness of the blind hole the stability region of the vortex states with $L < 7$ increases, but for $L > 7$ the stability region ΔH_s is almost independent of d_i, which is a consequence of the fact that for large L-values superconductivity is destroyed in the center of the disk and consequently it does not matter whether or not a blind hole is present in that region of the disk. A similar tendency is observed for the ground state magnetic field range $\Delta H_g(L)$ (Fig. 6.9(b)) with the exception that for $L > 7$ $\Delta H_g(L)$ decreases slightly with decreasing d_i. A similar tendency is seen for ΔH_s but to a smaller extent.

In the case of the superconducting rings, the flux is compressed in the hole and this quasi-giant vortex can be recognized only by the phase of the order parameter in the superconductor around the hole. The advantage of blind holes lies in the fact that the real vortex structure inside the pinning center can be visualized. In what follows, we investigate the influence of the thickness of the blind hole on the vortex configurations. The arrangements of vortices in samples containing a blind hole in the center is shown in Fig. 6.10 by the phase of the order parameter for the states with lower vorticity ($L \leq 4$). When the

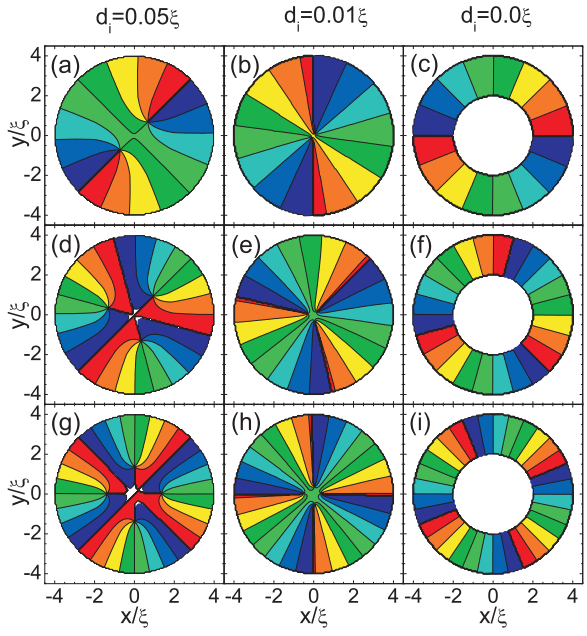

FIG. 6.10: Contour plot of the phase of the order parameter for a superconducting disk with radius $R_0 = 4.0\xi$, thickness $d = 0.1\xi$, $\kappa = 1.0$ for blind holes with radius $R_i = 2.0\xi$ and thickness $d_i = 0.05\xi$ (a,d,g), $d_i = 0.01\xi$ (b,e,h) and $d_i = 0.0\xi$ (c,f,i) for the states with L =2 (a,b,c), 3 (d,e,f) and 4 (g,h,i), at H/H_{c2} =0.22, 0.41, and 0.6, respectively. Phases near zero are given by blue regions, phases near 2π by red regions.

blind hole with thickness $d_i = 0.05\xi$ and radius $R_i = 2.0\xi$ is present in the superconducting disk with $d = 0.1\xi$ and $R_0 = 4.0\xi$, the two vortices are closer to each other (Fig. 6.10(a)) than in the disk case. With decreasing the thickness of the blind hole these two vortices come closer to each other (Fig. 6.10(b)) and form a giant vortex with vorticity $L = 2$. Obviously, when the blind hole is present in the sample vortices are pinned by the hole, and therefore located closer to the center for all vortex states as compared to the disk case. With decreasing the thickness of the hole the vortices are compressed more to the central region of the sample. In the case of the superconducting ring it is not possible to see the vortex structure (Figs. 6.10(c,f,i)).

Until now we considered only cylindrically symmetric superconductors. In the next step we investigate the nonsymmetric case, i.e. when the blind hole is shifted from the center of the sample over a distance a. As an example

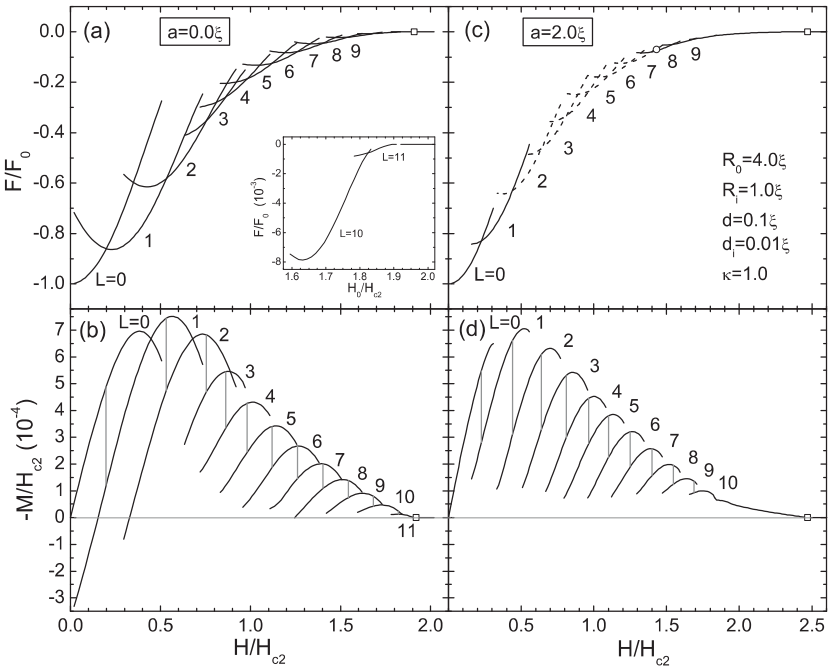

Fig. 6.11: The free energy and magnetization as a function of the applied magnetic field of the superconducting disk with radius $R_0 = 4.0\xi$, thickness $d = 0.1\xi$ with a blind hole with radius $R_i = 1.0\xi$ and thickness $d_i = 0.01\xi$, when the blind hole is in the center (a,b) and moved over a distance $a = 2.0\xi$ in the $-y$-direction (c,d). The multivortex states are plotted by dashed curves and the transition from the multivortex state to the giant vortex state is indicated by open circle in (c). Open squares show the S/N transition fields.

we take a superconducting disk with radius $R_0 = 4.0\xi$, thickness $d = 0.1\xi$ with a blind hole with radius $R_i = 1.0\xi$ and thickness $d_i = 0.01\xi$ moved over a distance $a = 2.0\xi$ in the -y-direction. Figs. 6.11(c,d) show the free energy and magnetization of this sample. To compare with the symmetrical case, we plotted also the free energy and magnetization for the superconductor with a blind hole in the center (Figs. 6.11(a,b)). In the latter case $L = 11$ vortices can be captured into the superconductor while it transits to the normal state at $H/H_{c2} = 1.91$. The breaking of the symmetry changes the superconducting state considerably. In this case the maximal number of vortices in the sample is $L = 15$ and the stability of the states with lower vorticity are decreased. The ground state free energy of the non-symmetric sample is lower for the states with $L > 3$, which leads to a higher critical field $H_{c3}/H_{c2} = 2.47$. It is noticeable that transitions between vortex states after $L = 10$ occur without a jump in the magnetization.

Fig. 6.12 show the distribution of vortices in the samples by Cooper-pair density plots. For the symmetric system, i.e. $a = 0$, we found giant vortex states (Fig. 6.12(a)). By breaking the circular symmetry of the system, multivortex states are stabilized. Figs. 6.12(b-f) show the Cooper-pair density of such multivortex states. The vortex nucleated at the blind hole for $L \geq 5$ is a giant vortex with vorticity 2 (see e.g. Fig. 6.12(f)).

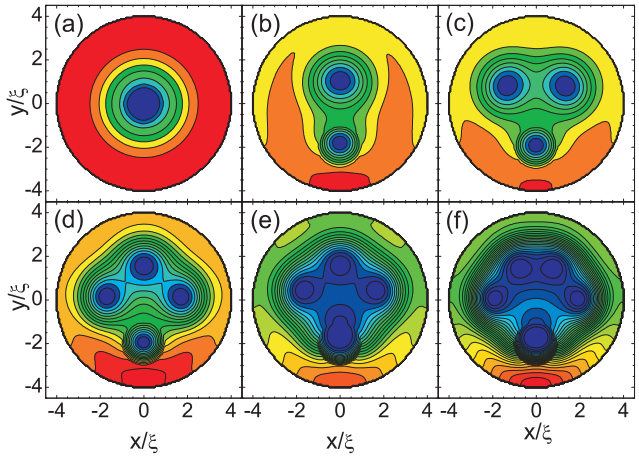

FIG. 6.12: Contour pot of the Cooper-pair density for the superconducting disk with radius $R_0 = 4.0\xi$, thickness $d = 0.1\xi$ with a blind hole with radius $R_i = 1.0\xi$ and thickness $d_i = 0.01\xi$, when the blind hole is in the center (a) and moved over a distance $a = 2.0\xi$ in the y-direction (b-f), corresponding to the vortex states with L =2 (a,b), 3 (c), 4 (d), 5 (e), and 6 (f) at H/H_{c2} =0.55 (a,b) and 0.65 (c), 0.82 (d), 1.0 (e) and 1.12 (f).

6.4 $H-T$ PHASE DIAGRAM

Until now, our calculations were done for fixed temperature T. Now we will include temperature in our numerical calculations through the temperature dependence of the coherence length $\xi = \xi_0/\sqrt{1-T/T_{c0}}$. Therefore, all distances will be expressed in units of $\xi(0)$, magnetic field in $H_{c2}(0)$, and temperature in units of the zero-magnetic-field critical temperature T_{c0}. We consider two samples, namely the superconducting disk with radius $R_0 = 1.5$ μm and thickness $d = 100$ nm, with and without a blind hole with radius $R_i = 0.75$ μm and thickness $d_i = 10$ nm. We choose the coherence length $\xi(0) = 120$ nm and the

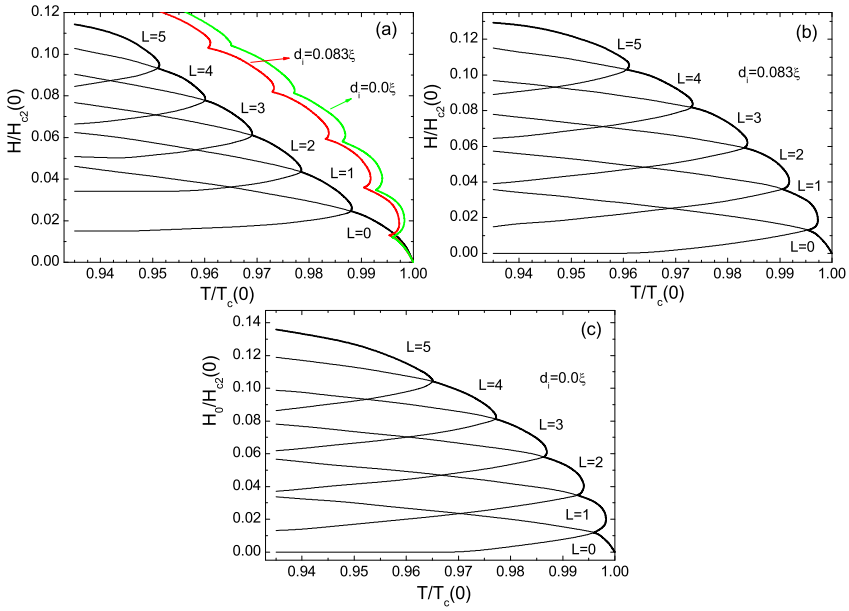

FIG. 6.13: The $H-T$ phase diagram and the stability area for the states with vorticity up to $L = 5$ for the disk (a), the disk with blind hole (b), and the superconducting ring (c). The radius of the disk is $R_0 = 12.5\xi(0)$, the thickness of the disk $d = 0.83\xi(0)$, the radius of the blind hole $R_i = 6.25\xi(0)$, the thickness of the blind hole $d_i = 0.083\xi(0)$ and the GL parameter κ equals 1.167 ($\xi(0) = 120$ nm). Thick solid curves indicate the superconducting/normal transitions.

penetration depth $\lambda(0) = 140$ nm, which are typical experimental values for low temperature mesoscopic superconductors.

The $H - T$ phase diagram is shown in Figs. 6.13(a-c) for the disk (a), the disk with a blind hole (b), and for the superconducting ring (c) for the states with vorticity up to $L = 5$. In the presence of the blind hole vortices enter the sample at higher temperatures and these states have a larger stability region compared to the case of the disk (except for the Meissner state where the opposite tendency is noticed). The S/N transition field at fixed temperature and the critical temperature at the given field is higher for the sample with the blind hole. For values of the parameters used here, the critical field is increased more than 20% and the critical temperature by ∼1.5%. Therefore, introduction of the blind hole in the superconducting sample is a powerful tool for enhancement of the critical parameters. The critical parameters of the sample with a blind hole are close to the parameters of the superconducting ring.

6.5 CONCLUSIONS

We studied the nucleation of superconductivity in superconducting disks containing a blind hole. We found that the increase of the steepness of the edges of the blind-hole-like cavity in the superconductor leads to a shift of the S/N transition field to higher magnetic fields, but the maximal number of vortices remains the same.

We also investigated superconducting disks with a perfect blind hole in the center in the case of relatively small disks ($R = 2.0\xi$). When the radius of the blind hole is much smaller than the radius of the disk, the maximal number of allowed vortices is the same for all considered samples, regardless of the thickness of the blind hole. On the other hand, the decrease of the blind hole thickness leads to higher S/N transition fields, and the free energy of the sample with blind hole approaches the energy of the superconducting ring. For the larger radii of the blind hole the maximal number of vortices in the sample increases with decreasing the thickness of the blind hole and approaches to the number of vortices in the case of he superconducting ring.

In order to investigate the vortex configurations inside the blind hole (as opposed to the hole as a pinning center), we considered superconducting samples with larger sizes. For the value of the Ginzburg-Landau parameter $\kappa = 1.0$ the states with $L \leq 6$ show multivortex states in the disk and a further increase of the applied magnetic field leads to the giant vortex state. When the blind hole is included into the disk the free energy of all vortex states lowers and the S/N state transition occurs at higher magnetic field. A variety of vortex configurations is possible in the blind hole, since the vortices are confined to the hole. In this case less vortex states form a multivortex state and the range

of the magnetic field at which multivortex states are present is also decreased for fixed L. A thinner blind hole leads to more stable vortex states and ground state transitions between different vortex states occur at lower fields. The states with higher vorticity illustrate stronger flux expulsion in samples with a blind hole as compared to the pure disk case. For small radius of the blind hole a limited number of vortices are situated in the hole and other vortices are located in the superconducting region forming a "shell" vortex structure. We also considered the non-symmetric case when the blind hole is moved over some distance from the center of the sample. In this case the maximal number of vortices in the sample is increased and the stability of these states is decreased and multivortex states are favorable.

The $H - T$ phase diagram calculated for the case of the disk and the disk with a blind hole shows that the critical field at a given temperature and the critical temperature at fixed field are higher for samples with a blind hole, and it is close to the phase boundary of the superconducting ring.

Publications. The results presented in this chapter were published as:

- G.R. Berdiyorov, M.V. Milosevic, B.J. Baelus, and F.M. Peeters, *Superconducting vortex state in a mesoscopic disk containing a blind hole*, Phys. Rev. B **70**, 024508 (2004).
- G.R. Berdiyorov, M.V. Milosevic, and F.M. Peeters, *The structure and manipulation of vortex states in a superconducting square with* 2×2 *blind holes*, Journal of low temperature physics **139**, 229 (2005).

7

Superconducting films with arrays of blind holes and pillars

7.1 INTRODUCTION

As we have shown in Chapter 4 of the thesis, the behavior of superconducting vortices in the presence of periodic arrays of antidots reveals a wide range of interesting commensurability and matching effects when the number of vortices is a multiple or rational multiple of the number of pinning sites and these highly ordered vortex configurations lead to a strong enhancement of the critical current. In this chapter we consider a more generale case – superconducting films with arrays of blind holes in the presence of an uniform applied magnetic field. These not fully perforated holes can trap several single quanta vortices whereas all vortices trapped by an antidot fuse in a single multiquanta vortex. The interaction of a flux line with an antidot is different from that with a blind hole. In both cases the normal/superconducting boundary condition which restricts the supercurrents to flow parallel to the walls of the hole leads to an attractive force due to an image antivortex inside the hole [173]. For the antidots, the interaction force acts along the total length of the flux line, whereas for blind holes a smaller force, proportional to the deepness of the hole, is expected. On top of that, once a flux line is trapped by an antidot, the notion of core is lost. In contrast to that, vortices captured by blind holes remain as single-quantum units with a well defined core and are accommodated inside the hole to minimize its repulsive energy [67].

Calculations within the linearized GL theory shows that the critical field of a superconducting film with a blind hole is sensitive to the bottom layer thickness, but the number of vortices which nucleate inside the hole is not influenced by the thickness [67]. Resent *ac* susceptibility measurements [171] also show a weak pinning potential and smaller saturation number provided by the blind holes. However, our calculations for a superconducting disk with a blind hole based on the nonlinear GL equations show that (see Chapter 6) both the critical field and the number of vortices inside the blind hole strongly depend on the radius and bottom thickness of the blind hole and can be equal to the ones for a superconducting ring.

Different vortex states and transition between them in thin superconductors with periodic pinning arrays in which multiple vortices can be trapped at individual sites have been studied in Ref. [151] using molecular dynamic calculations. A rich variety of vortex states, including collective dimer, trimer and composite states with an orientational ordering was obtained as a function of pinning strength and pinning size. Although the general behavior of the vortex lattice was accurately described, made approximations are valid only in certain range of parameters. Namely, those vortices are crudely considered as classical point particles and the pinning was simply introduced through a model, usually a simple attractive potential. However, as was shown in Chapter 5 of the thesis, due to the finite size of the vortex-core and its elastic properties there exists a local repulsive component to the generally attractive pinning force, which has never been considered in such molecular dynamics simulations.

Therefore, in this chapter we study vortex structures in superconducting thin films with arrays of blind holes in the presence of an uniform applied magnetic field using the full nonlinear GL theory. A phase diagram will be given which shows first order phase transitions between states with different blind hole occupation number and second order structural phase transitions. A comparison with the results for an antidot lattice will be given. For large blind holes local vortex shell structures are obtained both in the blind holes and at the interstitials and the evolution of shell formation towards an Abrikosov lattice inside the blind holes are given for different number of pinned vortices.

Real-world superconducting materials, especially high temperature superconductors, which are fabricated through a complex synthesis route, have structural defects at many length scales and in a wide variety of shapes leading to complex static and dynamic processes. Therefore, it becomes of particular interest to model this complex family of defects in a way that allows one to optimize the critical parameters for a given superconducting material. Given such complexity, it is desirable to reduce the problem to the quantitative study of the effectiveness of specific defects types. With this knowledge, it then becomes clear how to either progressively combine them to establish their collective effectiveness or isolate the best pinning sites and remove the others.

In the second part of this chapter we will consider superconducting films with arrays of superconducting pillars instead of blind holes, as a geometrically and

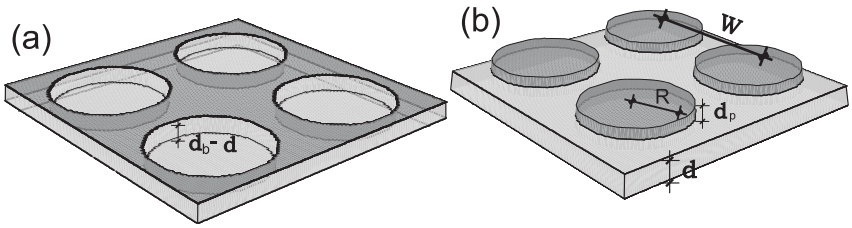

Fig. 7.1: Schematic view of the samples: a superconducting film (thickness d) with a regular array (period W) of blind holes (a) (thickness d_b) and pillars (b) (thickness d_p) with radius R.

physically inverted system, where pillars will serve as anti-pinning sites. The influence of the presence of the pillars to the vortex structure in the interstitials, as well as to the vortex structures in the pillars (for larger radius of the pillars) will be considered.

The chapter is organized as follows. The theoretical formalism of the problem is given in Sec. 7.2. Phase diagrams for different applied magnetic fields will be given in Sec. 7.3.1, which shows first order phase transitions between states with different blind hole occupation number (i.e. number of vortices captured by the blind hole) and second order structural phase transitions (i.e. for continuous transition of vortex configurations). Vortex shell structures inside the blind holes and the process of shell filling for different number of pinned vortices are studied in Sec. 7.3.2. The influence of the superconducting pillars to the vortex distribution in a superconducting film is considered in Sec. 7.4 and all our results are summarized in Sec. 7.5.

7.2 THEORETICAL FORMALISM

We consider superconducting films (of thickness d) with square arrays of blind holes (of radius R, period W and thickness $d_b < d$) and pillars (of radius R, period W and thickness d_p) in the presence of a perpendicular uniform magnetic field (see Fig. 7.1). For the given systems we solved two nonlinear GL equations, which can be written in dimensionless units in the following form (see Chapter 6):

$$(-i\nabla - \mathbf{A})^2 \Psi = \Psi \left(1 - |\Psi|^2\right) + i \left(-i\nabla - \mathbf{A}\right) \Psi \frac{\nabla d(x,y)}{d(x,y)}, \tag{7.1}$$

$$-\Delta \mathbf{A} = \frac{d\xi}{\lambda^2} \delta(z) \mathbf{j}, \tag{7.2}$$

where

$$\mathbf{j} = \frac{1}{2i} \left(\Psi^* \nabla \Psi - \Psi \nabla \Psi^*\right) - |\Psi|^2 \mathbf{A}, \tag{7.3}$$

is the density of superconducting current. The last term in Eq. (7.1) describes the effect of the sample thickness variation on the superconducting condensate in the case of both blind holes and pillars. The periodic boundary conditions (1.57, 1.58) were imposed on the outer edges of the square simulation region, consisting of 2×2 blind holes (pillars). The magnitude of the applied magnetic field $H = n\Phi_0/S$ is determined by the number n of quantum fluxes $\Phi_0 = hc/2e = 2.07 \cdot 10^{-7}\mathrm{Gcm}^2$ piercing through the simulation region area S. The dimensionless Gibbs free energy is calculated as

$$F = V^{-1} \int_V \big[2\big(\mathbf{A} - \mathbf{A}_0\big) \cdot \mathbf{j} - |\Psi|^4 + i\big(-i\nabla - \mathbf{A}\big)\Psi \frac{\nabla d(x,y)}{d(x,y)}\big] d(x,y)dxdy, \tag{7.4}$$

where integration is performed over the primitive cell volume V, and $\mathbf{A}_0$ is the vector potential of the external applied uniform magnetic field.

7.3 ARRAYS OF BLIND HOLES

7.3.1 Small applied fields: vortex phase diagrams

Contrary to the situation for an antidot lattice, where vortices are confined in the hole due to the supercurrent flowing around the hole, vortices trapped inside the blind hole can move freely within the boundaries of the blind hole, interacting with each other repulsively. Although our approach is valid for any integer number of flux-quanta piercing through the simulation region, we will restrict ourselves here to integer matching fields. As an example, we present here the results obtained for blind hole thickness $d_b = 0.01\xi$ and effective GL parameter $\kappa^* = \lambda^2/\xi d \gg 1$.

Fig. 7.2 shows the equilibrium vortex phase diagram for the second matching field as a function of the blind hole radius R and period W, where the solid lines denote the first order transition between states with different hole-occupation number n_o and the dashed ones depict second order configurational transitions. The ground- and metastable states are determined in our calculation by comparing the energy of all stable vortex states found when starting from different randomly generated initial conditions. As in the case of an antidot lattice (see Fig. 4.2) the occupation number (n_o) of each blind hole depends not only on the hole radius R, but also on the proximity of the neighboring blind holes in the lattice. For small radii of the blind holes one vortex is pinned by the blind hole and the second one is located in the interstitial site (inset 1), where the pinned vortices are more suppressed then the ones in the interstitials. In the $n_o = 2$ state we first have a giant vortex trapped in the blind holes (inset 2) and with increasing the radius and the period these giant vortices split into multivortices (note that in bulk superconductors and nonstructured films the

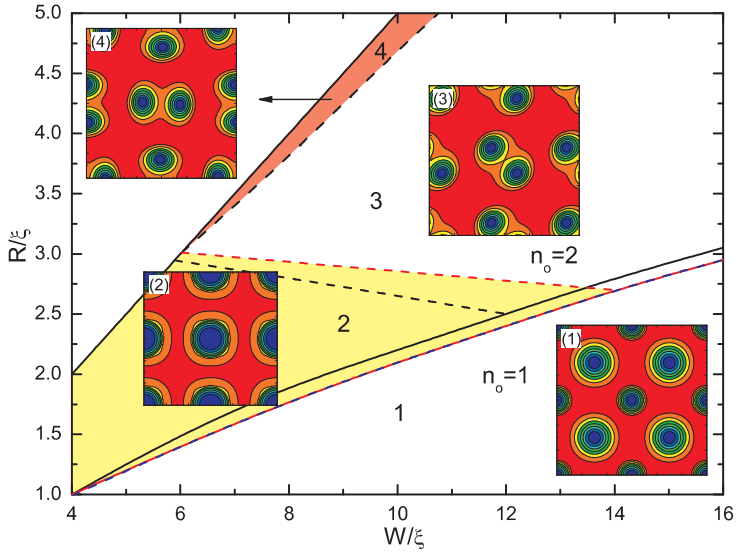

Fig. 7.2: The ground state vortex lattice at $H = H_2$ as a function of the blind hole radius R and period W for the film thickness $d = 0.1\xi$ (black curves) and $d = 0.5$ (red curves) (the thickness of the blind holes is $d_b = 0.01\xi$). The solid lines denote the first order transition between states with different hole-occupation number n_o and the dashed ones depict second order configurational transitions. The insets show the Cooper-pair density plots of the corresponding states indicated by the numbers in the phase diagram (red (blue) color corresponds to large (small) value of the Cooper pair density). The dashed blue line shows the transition between $n_o = 1$ state to $n_o = 2$ states in a superconducting film with an array of antidots.

energy of a giant vortex state is always larger than the energy of a multi-vortex state). The transition between these two states is indicated by the red dashed curve. The vortices inside one blind hole repel each other and move to the edges of the pinning sites. The interaction between vortices in the neighboring blind holes give rise to an orientational ordering between the dimers that are rotated over 45° (inset 3). By further increasing the blind hole radius vortices adjust themselves such that the neighboring dimers are rotated over 90° with respect to each other (inset 4). The blue dashed curve in Fig. 7.2 shows the transition between the $n_o = 1$ to the $n_o = 2$ state for the superconducting film (thickness $d = 0.1\xi$) containing an array of antidots. Notice that in the case of blind hole array there are slightly small number of pinned vortices.

In order to see the influence of the difference between the film thickness and blind hole thickness to the vortex structure we calculated the phase diagram for thicker film ($d = 0.5\xi$), which is shown by the red curves in Fig. 7.2. In this case the threshold blind hole radius for the $n_o = 2$ state decreases compared to the case of a thinner film (solid black curve) due to the enhanced screening of

the applied field. Due to the latter effect the giant vortex state (yellow region in Fig. 7.2) becomes energetically more favorable and is stable over a larger region in the phase diagram. For thicker films we did not find the adjusted vortex state, which was found for thinner films (inset 4 of Fig. 7.2), indicating clearly the weaker interaction between the vortices in neighboring pinning centers in the case of thicker films. Note also that the effective GL parameter $\kappa^* = \lambda^2/\xi d$ decreases (i.e. smaller vortex-vortex interaction) with increasing film thickness d.

The equilibrium vortex lattices for $H = H_3$ are shown in Fig. 7.3 as a function of the radius R and period W of the blind holes. In the $n_o = 1$ state one vortex is pinned by the blind hole and for large W two interstitial vortices in adjacent cells alternate in position, preserving the twofold symmetry (inset 2). This state is identical to the vortex state observed experimentally [38] in a superconducting film with a square array of antidots in the case of the third matching field. With decreasing the period W these two vortices are strongly

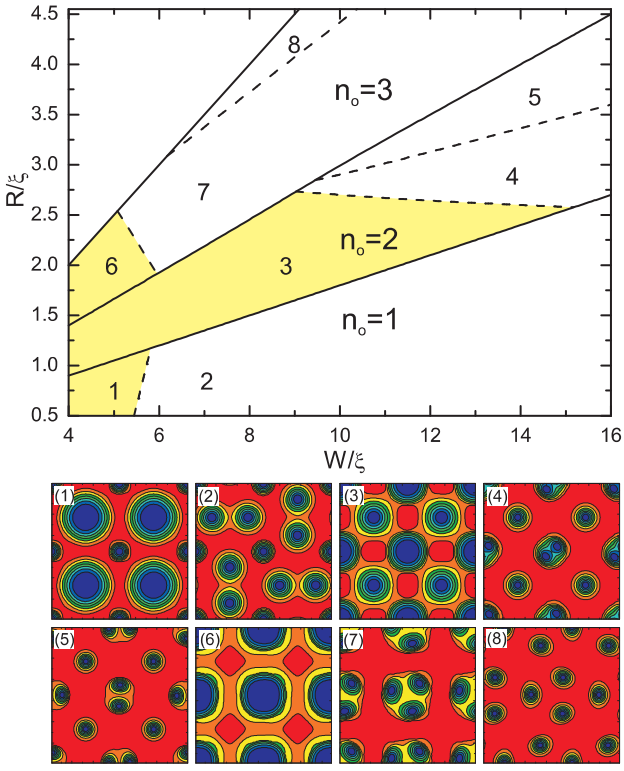

FIG. 7.3: The same as Fig. 7.2 with only the results for the blind hole case for $H = H_3$. The film thickness is $d = 0.1\xi$.

caged by the blind holes, resulting in the formation of giant vortices (inset 1). For increased radius of the blind holes each hole captures two vortices forming a giant vortex in the blind hole. By increasing the blind hole radius and the period these giant vortices split into multivortices with different orientations (insets 4 and 5). Note that the orientation of pinned vortices is the same as was found for $H = H_2$, where no interstitial vortices were present (see insets 3 and 4 of Fig. 7.2). In the $n_o = 3$ state pinned vortices form first a giant vortex (inset 6) and later splits into individual vortices (insets 7 and 8). Vortices show an orientational phase transition with changing lattice parameters. Although, some of the vortex configurations for $H = H_3$ were obtained already using molecular dynamic calculations [151], we found here new configurations with different orientation of vortex dimers and trimers and the coexistence of multivortex states with giant vortex states using our GL calculations, not predicted in Ref. [151]. Because of the large spacing between the blind holes the ordered vortex lattice was not observed in the experiments with blind holes [67].

Fig. 7.4 shows the vortex phase diagram for the fourth matching field ($H = H_4$), as a function of W and R. For small radii each blind hole pins only one vortex and the remaining vortices reside between the holes forming a slightly deformed hexagonal vortex lattice [38] (including the pinned ones) (inset 2). With decreasing the spacing between the blind holes these vortices are compressed into a giant vortex (inset 1). In the lower part of the phase diagram for the $n_o = 2$ state we have giant vortices both inside the hole and at the interstitial sides (inset 3). With increasing the period W first the interstitial giant vortices split into individual vortices (inset 4) and later the pinned ones form multivortices (inset 5). In the latter case we find ordered vortex structures in the blind holes and in the interstitials, while molecular dynamic calculations did not show a completely ordered lattice [151]. The same phase transition is found for the $n_o = 3$ state (insets 6 and 7). In the $n_o = 4$ state the vortices in the blind hole form a square lattice with the same orientation as the pinning lattice (inset 8). Contrary to the cases of smaller matching fields (see Figs. 7.2 and 7.3), here we did not find orientational phase transitions between the pinned vortices. Vortex-antivortex states were not found in the present case of a blind hole array as we found for an antidot lattice (see Fig. 4.2).

7.3.2 Large blind holes: vortex shell structures

In this section we study stable vortex configurations inside the blind holes for the occupation number from $n_o = 1$ to $n_o = 34$, and also for certain n_o up to $n_o = 120$. To systematically determine the stable vortex patterns we did a field-cooling experiment each time starting from random configurations for a given applied magnetic field. Vortex structures in such circular-confined systems (i.e. superconducting disks) have already been studied both theoretically [81,

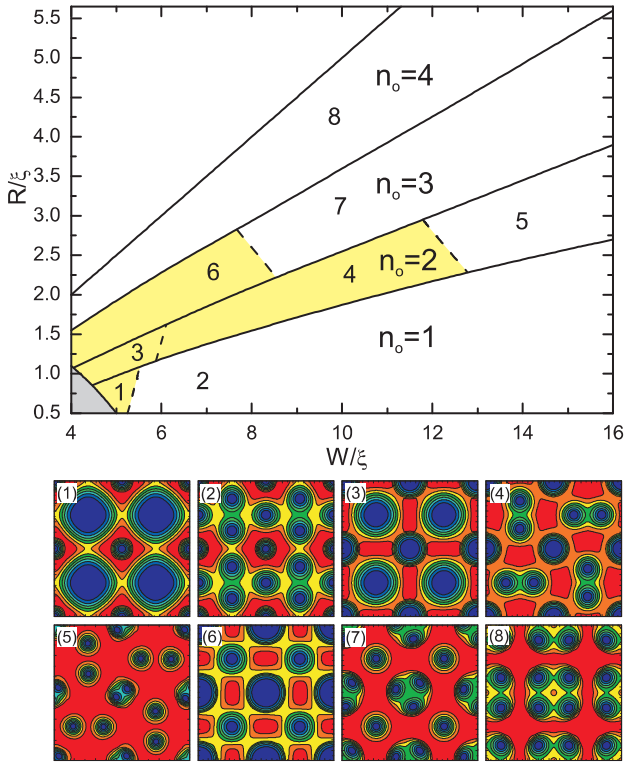

Fig. 7.4: The same as Fig. 7.3 but for $H = H_4$. The gray region shows the normal state region.

174–176] and experimentally [82], which strongly depend on the number of particles involved, which is governed by rich and subtle physics arising due to the competition between particle-particle interaction and confinement, as well as on the radius of the superconducting disk [176]. It was shown that vortices form well-defined "concentric" shell structures, filling these shells according to specific rules (so-called "magic numbers") and formation of these shells resulted in a "periodic table" of formation of shells. The evolution of vortex shells in superconducting disks is as follows: for vorticity (i.e. number of vortices in the disk) $L \leq 5$ all the vortices are arranged in a single shell and the formation of a second shell starts from $L = 6$. Similarly, the formation of a third shell starts at $L = 17$, and of a fourth shell at $L = 33$. Similar shell structures were found earlier in different systems as vortices in superfluids [177], system of charged particles [178] and dusty plasma [179]. Multiple occupation by single quantum vortices in large blind holes was imaged experimentally in Ref. [67] using a Bitter decoration technique. Inside the blind holes the vortices are mostly

concentrated along the perimeter, except the ones which is in the center. It was shown that the density of vortices is considerably higher inside the blind hole, even if the bottom thickness is very close to the film thickness.

Fig. 7.5 shows the distribution of vortices inside a blind hole of radius $R = 6\xi$ for the occupation number ranging from $n_o = 2$ to $n_o = 12$ in the case of closely spaced blind holes ($W = 14\xi$). The evolution of the vortex states is as follows: up to $n_o = 5$ the vortices form regular polygons (Figs. 7.5(a-d)). Contrary to the case of superconducting disks [82, 174], now the first 8 vortices are added one by one to form the first shell (Figs. 7.5(f-i)), the second shell appears only at $n_o = 9$ in the form of one vortex in the center and 8 vortices in the second shell (Figs. 7.5(k)). Using the standard notations for confined geometries [178], we refer to this state as (1,8). This configuration remains stable until the $n_o = 12$ state is reached (Figs. 7.5(p)), i.e. the next 2 vortices are added to the outer shell. Imaging experiments using the Bitter decoration technique [67] shows that the states (8), (1,7), (9) and (1,8) are stable inside

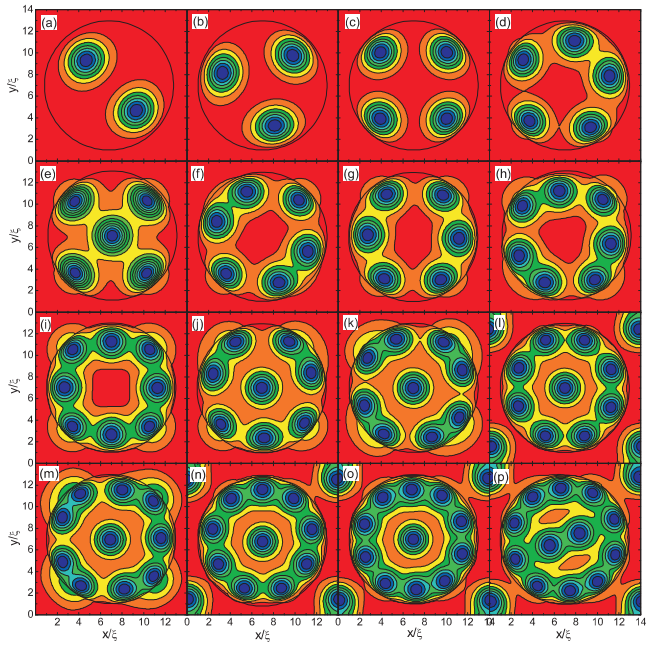

Fig. 7.5: The evolution of vortex configurations in a superconducting film (thickness $d = 0.1\xi$) with arrays of blind holes of radius $R = 6\xi$, thickness $d_b = 0.01\xi$ and period $W = 14\xi$. The number of trapped vortices is $n_o = 2$ (a), $n_o = 3$ (b), $n_o = 4$ (c), $n_o = 5$ (d,e), $n_o = 6$ (f,g), $n_o = 7$ (h), $n_o = 8$ (i,j), $n_o = 9$ (k,l), $n_o = 10$ (m,n), $n_o = 11$ (o) and $n_o = 12$ (p). The black circles indicate the position of the blind holes.

the blind holes and vortices are mostly concentrated along the perimeter of the blind holes, which agrees with our numerical calculations.

It is seen from Fig. 7.5(d) that the pentagon at $n_o = 5$ is not regular. The reason is that the blind holes do not provide a circular confinement due to the close spacing between them, i.e. vortices feel less confinement in the four corners of the unit cell. Because of this asymmetric pinning the (1,4) state at $n_o = 5$ is also stable (but not the ground state), which was found only for the case of vortices in superfluid helium [177]. The effect of the asymmetry in the pinning sites is seen also for the states with larger n_o. For example, the lowest energy states for $n_o = 6$ and $n_o = 8$ has a clear square symmetry (Figs. 7.5(f,i)), having the same fourfold symmetry as the state (4) (Figs. 7.5(c)). This kind of square symmetric (1,8) state was observed experimentally [82] (even more frequently than the circular (1,8) state), which is noticeable exception from the generale rule where, as expected for the disk geometry, vortices form concentric rings. The circular confinement of the blind holes restores if we add extra vortices into the interstitial sites between the holes as

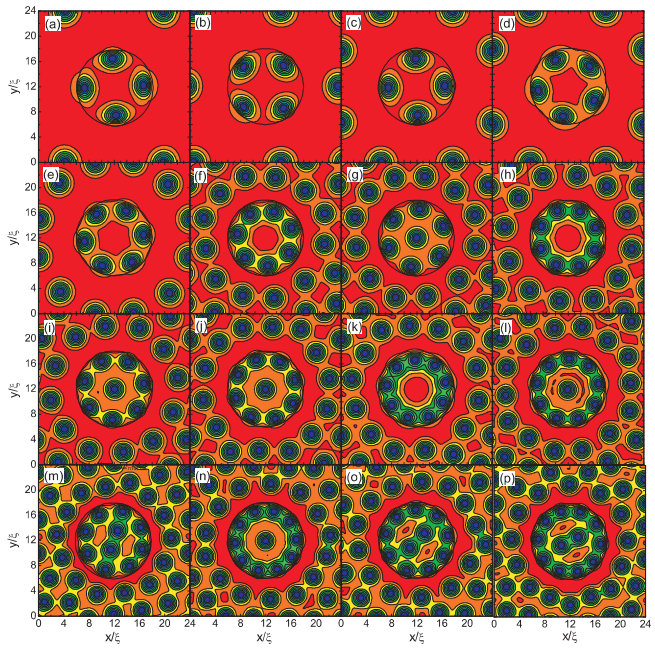

FIG. 7.6: Vortex structures in a superconducting film with an array of blind holes of radius $R = 6\xi$, thickness $d_b = 0.01\xi$ and period $W = 24\xi$. The occupation number $n_o = 4$ (a-c), $n_o = 5$ (d), $n_o = 6$ (e), $n_o = 7$ (f,g), $n_o = 8$ (h,i), $n_o = 9$ (j,k), $n_o = 10$ (l,m), $n_o = 11$ (n,o), and $n_o = 12$ (p). The black circles indicate the position of the blind holes.

illustrated in Figs. 7.5(k,l) and (m,n). To see the influence of these interstitial vortices on the vortex shell structures inside the blind hole, we plotted in Fig. 7.6 vortex distributions in a superconducting film with an array of blind holes of the same radius $R = 6\xi$ but for larger period $W = 24\xi$. Figs. 7.6(a-c) (see also Fig. 7.5(c)) show clearly the influence of the interstitial vortices: a symmetric four fold pattern (4) changes its direction by increasing the number of interstitial vortices. All other states now have circular symmetry. Note that the number of possible shells and the number of vortices in each shell is the same as in Fig. 7.5.

For a small number of pinned vortices ($n_o \leq 4$) we obtained only one vortex configuration (Figs. 7.5(a-c)). For larger n_o, however, at least two or more vortex patterns are found (see Figs. 7.5(d,e), (f,g), (i,j), (k,l), and (m,n), and Figs. 7.6(f,g), (h,i), (j,k), (l,m), and (n,o)). Note that the states with the same n_o are plotted in Fig. 7.5 and Fig. 7.6 in ascending order of the free energy for a given n_o. As another example, the four vortex configurations that we found for $n_o = 19$ are shown in Fig. 7.7 in ascending order of free energy. The ring structure of vortices is quite evident in these pictures. The ground state configuration (Fig. 7.7(a)) consists of one vortex in the center, surrounded by an apparent ring of five vortices, which is surrounded by another ring of thirteen vortices, i.e. (1,5,13) state. The next stable state (Fig. 7.7(b)) have unusual centers with two "rings" of three vortices just slightly different in radius

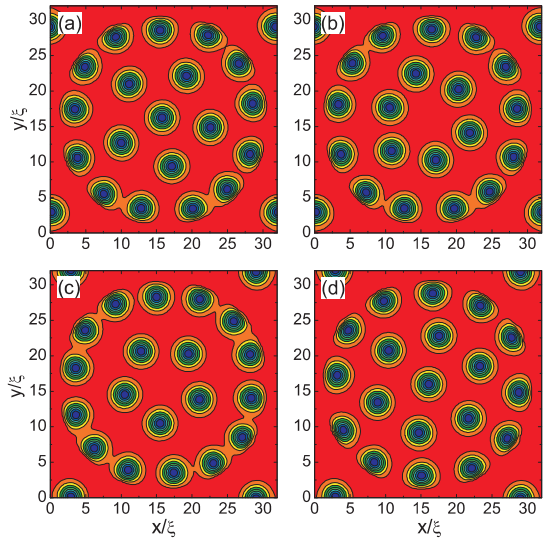

Fig. 7.7: Stable vortex configurations for $n_o = 19$. The free energy of the states is -0.81272 (a), -0.81254 (b), -0.812495 (c) and -0.812421 (d). The radius of the blind holes is $R = 15\xi$ and the period is $W = 32\xi$.

(the (3,3,13) state). In each of these rings the three vortices are symmetrically placed on a perfect circle. This center structure is again surrounded by a ring of thirteen vortices. This kind of vortex structure was obtained in calculation on superfluid helium [177]. However, the outer shells in our case forms perfect rings. The next possible vortex configuration is the one with two shell structure with five vortices in the inner shell and 14 vortices in the outer shell (Fig. 7.7(c)). The three shell (1,6,12) configuration (Fig. 7.7(d)) has the highest energy for $n_o = 19$ state.

An overview of the ground state vortex configurations inside the blind hole for n_o up to 34 is given in Table 7.1. The vortex structures inside the blind holes up to $n_o = 5$ agrees both with previous theoretical calculations in related systems and experimental results. However, the state (6), where all 6 vortices are located in one shell, was found only as a metastable state in the case of the superconducting disks [82, 174, 176], whereas the (1,5) state was found to be the ground state. Similarly, the predictions for superconducting disks and parabolically confined charged particles [180] found (1,8) as a metastable state, while in our case it becomes a ground state as in the case of liquid He. The theoretically predicted and experimentally observed ground state configuration (2,7) for superconducting disks [174] was not found to be stable inside the blind holes both in our calculations and in the experiment [67]. The formation of the second shell starts for larger number of vortices, but the number of vortices in the first shell grows faster than in the case of a superconducting disk. The inner shell changes from 1 to 4 with increasing n_o from 11 to 14 (i.e. states (1,10), (2,10), (3,10) and (4,10)). The third shell in our case appears at $n_o = 19$, which is larger than the theoretical predictions and the experiment. The rule for filling of the first shell (counting from the center) is similar what was found for charged particles in a parabolic potential [178]: the fist shell never exceeds five vortices; when all the shells are filled up to their maximum allowed number of vortices, a new shell consisting of only one vortex appears in the center, when we add one vortex to the system; further adding vortices will increase the number of vortices on the different shells until each of them has reached their maximum.

For larger superconducting disks [81] the structure of the inner shells is very close to the one of a triangular lattice, i.e. all the vortices are sixfold coordinated, whereas outer shells consist of lower-coordinated vortices, which leads to a competition between two types of ordering: ordering into a triangular-lattice structure and ordering into a shell structure. In order to see the transition between these two states in our system we calculated vortex configurations for larger number of pinned vortices, examples of some of them are shown in Fig. 7.8. For small n_o we have a clear shell structure (Figs. 7.8(a-f)) and with increasing n_o vortices in the center "feel" less the presence of the boundary and start forming triangular structures. For $n_o \geq 85$ the vortices are arranged in an Abrikosov lattice in the center of the bind hole, which is surrounded by a perfect circular shell (see Fig. 7.8(h)).

Table 7.1: The ground state vortex configurations inside the blind hole, in the superconducting disks (theoretical results from Ref. [176] and experiment from Ref. [82]), in the system of charged particles [178] and in superfluid He [177].

n_o	blind hole	disk theory	disk exp.	charged particles	vortices in He
1	(1)	(1)	(1)	(1)	(1)
2	(2)	(2)	(2)	(2)	(2)
3	(3)	(3)	(3)	(3)	(3)
4	(4)	(4)	(4)	(4)	(4)
5	(5)	(5)	(5)	(5)	(5)
6	(6)	(1,5)	(1,5)	(1,5)	(1,5)
7	(7)	(1,6)	(1,6)	(1,6)	(1,6)
8	(8)	(1,7)	(1,7)	(1,7)	(1,7)
9	(1,8)	(2,7)	(2,7)	(2,7)	(1,8)
10	(1,9)	(2,8)	(2,8)	(2,8)	(2,4,4)
11	(1,10)	(2,9)	(3,8)	(3,8)	(3,8)
12	(2,10)	(2,10)	(3,9)	(3,9)	(3,3,6)
13	(3,10)	(2,11)	(4,9)	(4,9)	(4,9)
14	(4,10)	(2,12)	(4,10)	(4,10)	(4,10)
15	(4,11)	(3,12)	(4,11)	(5,10)	(4,11)
16	(4,12)	(4,12)	(5,11)	(1,5,10)	(5,11)
17	(5,12)	(1,5,11)	(1,5,11)	(1,6,10)	(1,5,11)
18	(5,13)	(1,5,12)	(1,6,11)	(1,6,11)	(1,6,11)
19	(1,5,13)	(1,6,12)	(1,6,12)	(1,6,12)	(1,6,6,6)
20	(1,6,13)	(1,7,12)	(1,6,13)	(1,7,12)	(1,6,13)
21	(1,6,14)	(1,7,13)	(1,7,13)	(1,7,13)	(1,7,13)
22	(1,6,15)	(1,8,13)	(2,7,13)	(2,8,12)	(1,7,7,7)
23	(1,7,15)	(2,8,13)	(2,7,14)	(2,8,13)	(1,8,14)
24	(2,7,15)	(2,8,14)	(3,7,14)	(3,8,13)	(2,2,4,2,14)
25	(2,8,15)	(3,8,14)	(3,8,14)	(3,9,13)	(3,8,14)
26	(2,8,16)	(3,9,14)	(3,8,15)	(3,9,14)	(3,3,6,14)
27	(2,8,17)	(3,9,15)	(4,8,15)	(4,9,14)	(3,3,6,15)
28	(3,8,17)	(3,10,15)	(5,8,15)	(4,10,14)	(4,9,15)
29	(3,9,17)	(4,10,15)	(5,9,16)	(5,10,14)	(4,10,15)
30	(3,9,18)	(4,10,16)	(6,9,16)	(5,10,15)	(4,4,6,16)
31	(3,9,19)	(5,10,16)		(5,11,15)	
32	(3,9,20)		(6,9,17)	(1,5,11,15)	
33	(3,10,20)		(1,6,9,17)	(1,6,11,15)	
34	(4,10,20)		(1,7,9,17)	(1,6,12,15)	

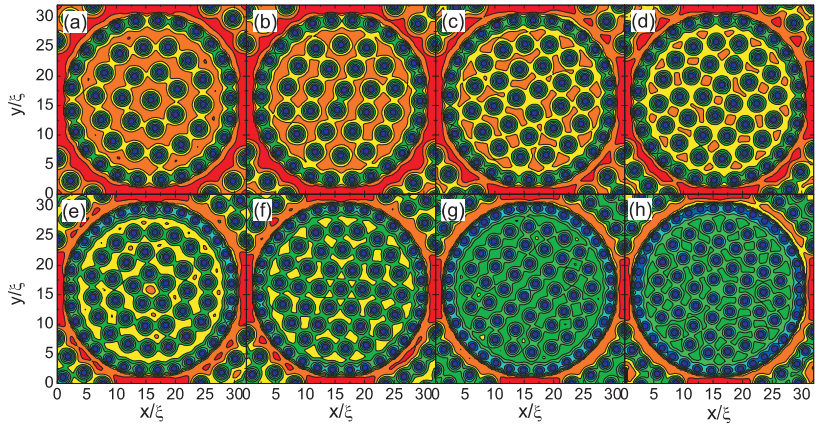

Fig. 7.8: The ground state vortex configurations in a superconducting film (thickness $d = 0.1\xi$) with a square array of blind holes (radius $R = 15\xi$, period $W = 32\xi$ and thickness $d_b = 0.01\xi$) for $n_o = 47$ (a), $n_o = 50$ (b), $n_o = 55$ (c), $n_o = 58$ (d), $n_o = 66$ (e), $n_o = 69$ (f), $n_o = 80$ (g), $n_o = 85$ (h).

This kind of perfect triangular lattice structure for the inner part and circular structure for the outer vortices was also found in a large system of charged particles with parabolic confinement [178]. The density of particles in such a system is nearly constant inside and decreases slightly with radius for the outer shells. However, in the case of hard-wall confinement the density increases with radius and electrons are arranged into well pronounced shells even for large systems [178]. Particles confined in the hard-wall confinement potential tend to occupy first the edge positions at the wall due to the repulsion between particles. When a critical density at the edge is achieved, the remaining electrons form shell structures. In this sense, our system is more similar to the system of hard-wall confined charged particles, because the vortices in our case are mostly located along the perimeter of the blind holes (see Fig. 7.8). However, the density of vortices in the different shells does not increase monotonously (see Fig. 7.9) as in the case of hard-wall confined particles [178]. The inter-vortex distance increase with radius (i.e. density decreases). Note that the density of vortices in the outer shell is always highest. However, the inter-vortex distance may decrease with the number of shell (see pink curve in Fig. 7.9) depending on the stability of the different shells.

As we mentioned above, the interstitial vortices restores the circular confinement of the pinned vortices (see Fig. 7.6). At the same time the pinned vortices also impose their symmetry to the interstitial ones. In order to see this effect we plotted in Fig. 7.10 the vortex structures in a superconducting film for $R = 10\xi$ and $W = 30\xi$ at the matching fields $H = H_{25}$ (a), $H = H_{50}$ (b) and $H = H_{100}$ (c). The ring structure inside the blind hole is quite evident in

these pictures. These vortex rings impose their shape to the interstitial vortices and we obtain also vortex shells outside the blind holes, indicated by white circles in the figure. The number of shells outside the blind holes increases if we increase the distance between the holes and the applied field.

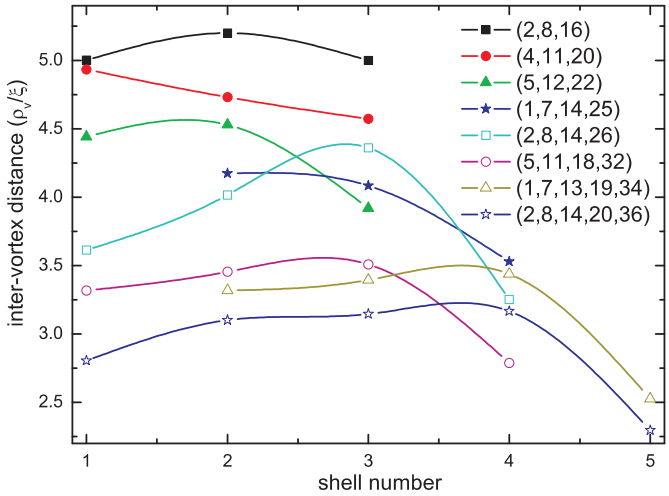

Fig. 7.9: Inter-vortex distance ρ_v as a function of shell number for different number of pinned vortices n_o. The radius of the blind holes is $R = 15\xi$ and the period is $W = 32\xi$.

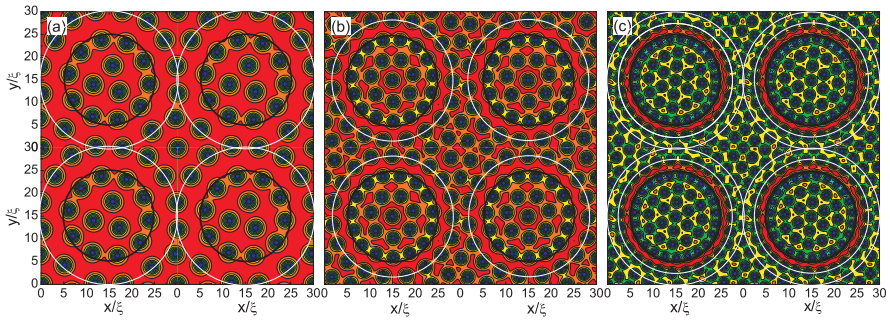

Fig. 7.10: The Cooper-pair density plots for a superconducting film with an array of blind holes of radius $R = 10\xi$ and thickness $d_b = 0.01\xi$ for $H = H_{25}$ (a), $H = H_{50}$ (b) and $H = H_{100}$ (c). The period of the blind holes is $W = 30\xi$. The black circles indicate the position of the blind holes and the white circles show the vortex shell structure outside the blind holes.

7.4 VORTEX STRUCTURE IN A SUPERCONDUCTING FILM WITH A SQUARE ARRAY OF PILLARS

In this section we study vortex configurations in superconducting thin films with a square array of pillars (we refer to them also as disks) in the presence of uniform applied magnetic field. A schematic view of the sample is shown in Fig. 7.1(b). The results we present here are obtained in the limit the GL parameter $\kappa^* \gg 1$, film thickness $d = 0.1\xi$, and thickness of pillars $d_p = 0.1\xi$. The ground state vortex configurations for a given magnetic field are determined by comparing the free energy of all stable vortex states found when starting from different randomly generated initial conditions.

Small disks. Let us first consider small disks, so that no vortex can enter the disks. Fig. 7.11 shows the vortex configurations in such a system for different values of the applied magnetic field. At the first ($H = H_1$, i.e. one vortex per unit cell, which contains one pillar and indicated by dashed lines in Fig. 7.11(a)) and second matching fields (Fig. 7.11(a,b)) vortices form a triangular lattice because of the very small size of the disks (vortex structures are indicated by white lines). At the third matching field we obtained vortex

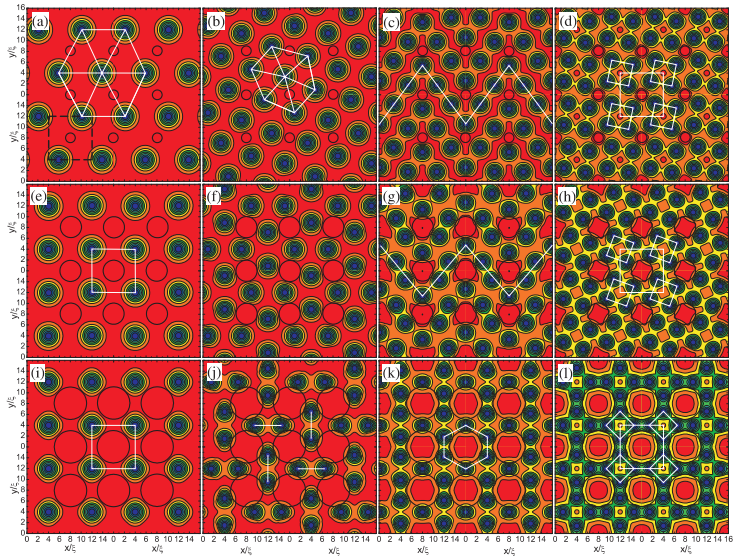

Fig. 7.11: Contour plots of the Cooper-pair density for disks with radius $R = 1\xi$ (a-d), $R = 2\xi$ (e-h), and $R = 3\xi$ (i-l) and for applied field $H = H_1$ (first column), $H = H_2$ (second column), $H = H_3$ (third column), and $H = H_4$ (fourth column). The period is $W = 8\xi$ and the disk thickness is $d_p = 0.1\xi$. The disks are shown by black circles and the vortex lattice structure is made more clear through the white lines.

lines (Fig. 7.11(c)) and at $H = H_4$ vortex clusters are formed at the interstitial sites (Fig. 7.11(d)). By increasing the radius of the disk, vortices transit from a triangular lattice to a square lattice at $H = H_1$ and from a deformed hexagonal lattice to a square lattice of double vortices at $H = H_2$ which are oriented alternatively. For $H = H_3$ a transition from a vortex line structure to a hexagonal structure occurs. The orientation of vortex clusters at $H = H_4$, which consist of 4 vortices in each interstitial site, are repeated periodically in space in a square lattice, and changes with increasing the radius.

Fig. 7.12 shows vortex structures for larger period ($W = 16\xi$) of disks (the radius is $R = 3\xi$). At the fifth matching field (Fig. 7.12(a)) vortex lines are obtained. But we can interpret this vortex structure in a different way: vortices form a cluster of 4 vortices around the disk and one extra vortex is located between them. The orientation of clusters differs from one column to another (solid and dashed white lines in the figure). At $H = H_6$ (Fig. 7.12(b)) two vortices are located between the clusters of 4 vortices with alternating directions. In this case the orientation of clusters changes from one disk to another. At $H = H_7$ (Fig. 7.12(c)) vortex clusters around the disks and vortices between them have different orientation in different columns. For $H = H_8$ we have a perfect square lattice of vortex clusters around the disks and between the

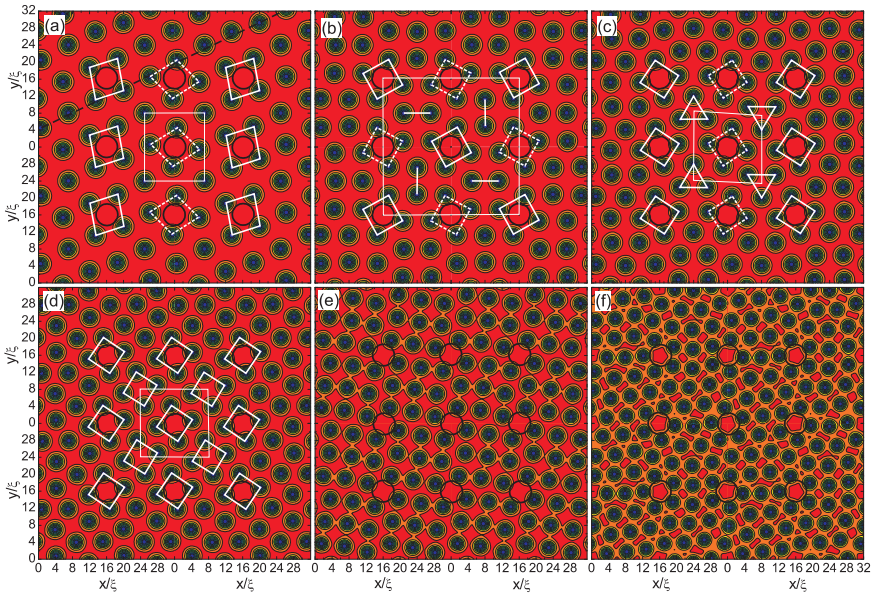

Fig. 7.12: The vortex structure at the applied fields $H = H_5 - H_9$ (a-e) and $H = H_{12}$ (f). The period of the lattice of pillars is $W = 16\xi$ and their radius is $R = 3\xi$.

disks (Fig. 7.12(d)). Many other vortex structures can be found with further increasing the applied field (Fig. 7.12(e,f)).

Larger disks. Let us now see the influence of the disk size on the vortex structure in the superconducting film. When the distance between the disks is larger than the disk size and the applied field is small we have a triangular vortex lattice (Fig. 7.13(a)). If we increase the applied field, a vortex ring is formed around the disk (white circle in Fig. 7.13(b)), i.e. the disk imposes its symmetry to the vortex structure. Moreover, vortex hexagons are formed around this ring. More vortex shells are found around the disk for larger radius of the disks (see Figs. 7.14(a-c)). In order to see the influence of the disk shape to the vortex configurations we did calculations for a superconducting film with an array of square disks. In this case we obtain "square shells" around the pillars (see Figs. 7.14(d-f)). The reason for the vortex shell structures can be both the boundary of the pillars and the vortex distribution inside the pillars.

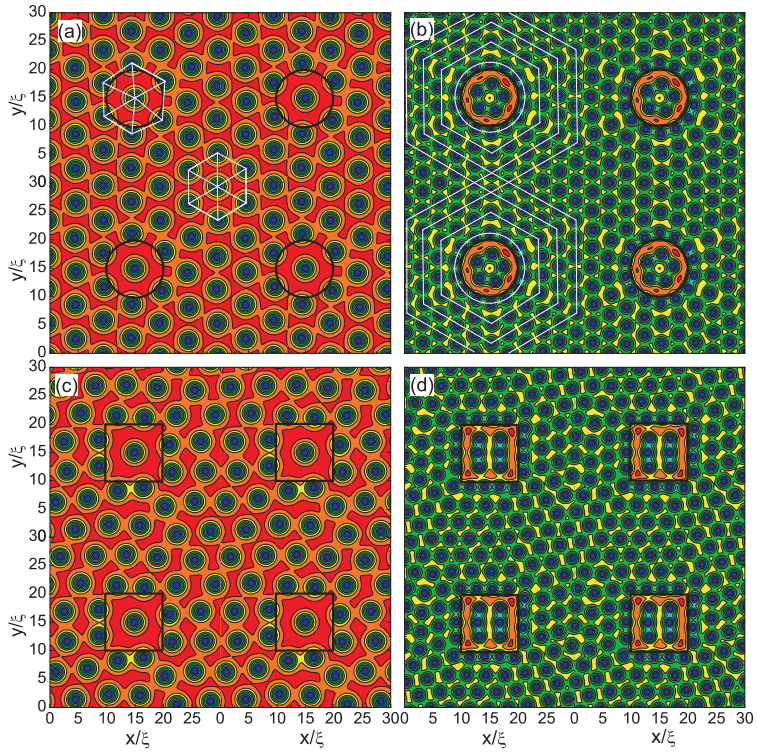

FIG. 7.13: The vortex structure for circular ($R = 5\xi$) (a,b) and square (size $a = 10\xi$) (c,d) pillars with period $W = 30\xi$ at the applied fields $H = H_{30}$ (a,c) and $H = H_{90}$ (b,d).

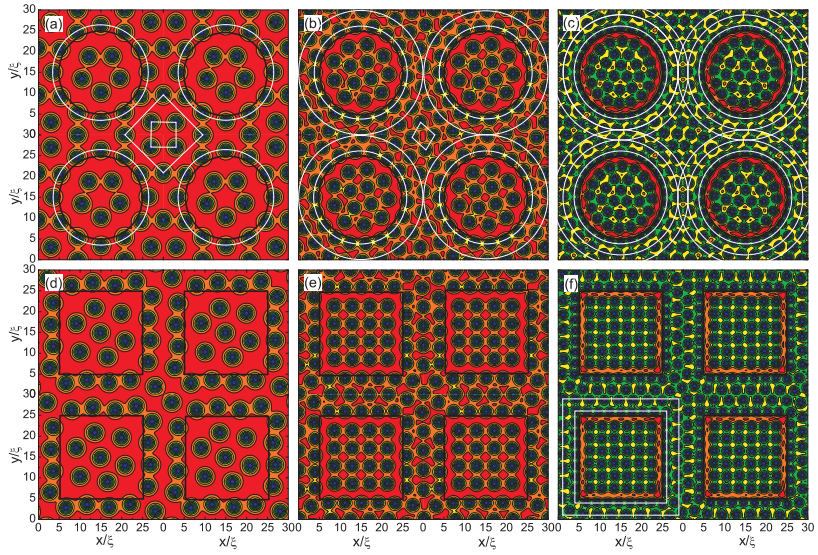

Fig. 7.14: The vortex structure for circular ($R = 10\xi$) (a-c) and square (size $a = 20\xi$) (d-f) pillars with period $W = 30\xi$ at the applied fields $H = H_{25}$ (a,d), $H = H_{50}$ (b,e) and $H = H_{100}$ (c,f).

The latter is confirmed also by the calculations for the blind hole arrays (see Fig. 7.10), where only the pinned vortices interact with the interstitial vortices.

Vortex structures inside the pillars. As we see from the previous figures, vortices form well-defined shell structures inside the disks (see for example Fig. 7.14(c)) as in the case of individual superconducting disks. [82]. Figures 7.15 and 7.16 show different vortex configurations for two values of the disks and different applied magnetic fields. At small applied fields (number of vortices in the disk is small, $L \leq 5$) vortices arrange themselves into simple symmetric structures (Figs. 7.15). As the magnetic field increases further vortices start to form concentric shells. Fig. 7.16 shows the evolution of these vortex shells. We compared these results with the ones for individual disks and found out that the number of vortices in individual disks is smaller than the one for disks placed on top of a superconducting film.

7.5 CONCLUSIONS

We studied the different possible vortex configurations in a thin superconducting film with a square array of blind holes. Although the maximum number of flux quanta trapped by a blind hole is smaller than the corresponding number for antidots, we found that a rich variety of ordered vortex states is possible

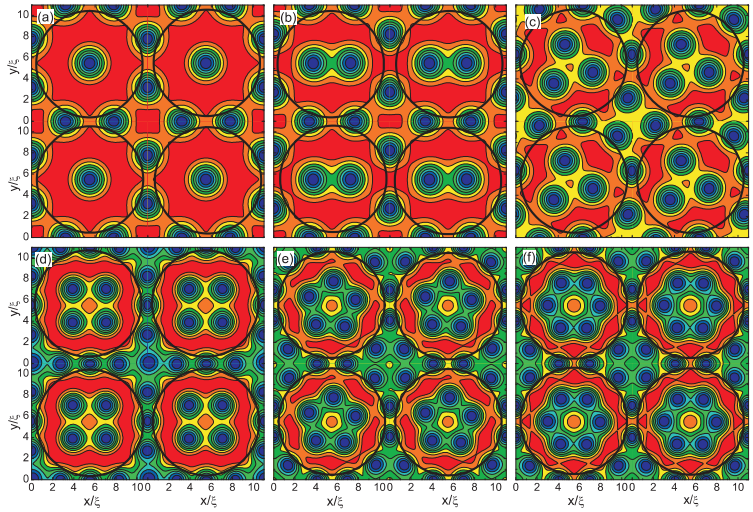

FIG. 7.15: The vortex structure at the applied magnetic fields $H = H_5$ (a), $H = H_6$ (b), $H = H_8$ (c), $H = H_{11}$ (d), $H = H_{13}$ (e) and $H = H_{14}$ (f). The radius of the pillars is $R = 5\xi$ and the period $W = 11\xi$.

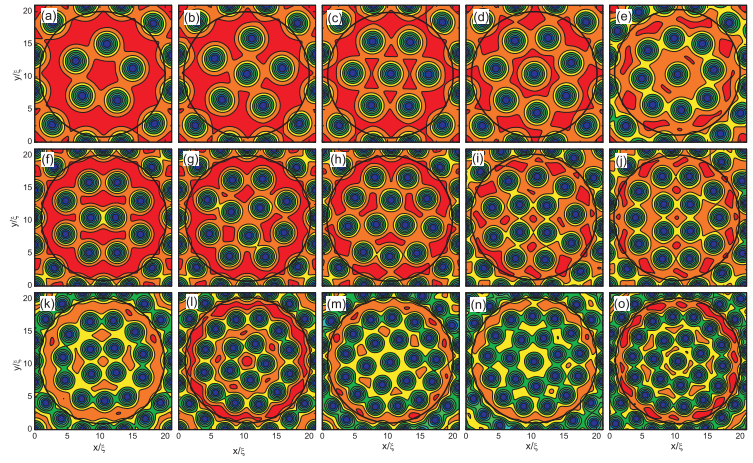

FIG. 7.16: The vortex structure at the fields $H = H_{13} - H_{16}$ (a-d), $H = H_{19}$ (e), $H = H_{21} - H_{23}$ (f-h), $H = H_{25}$ (i), $H = H_{26}$ (j), $H = H_{30}$ (k), $H = H_{32}$ (l), $H = H_{36}$ (m), $H = H_{38}$ (n), $H = H_{40}$ (o). The radius of the holes is $R = 10\xi$ and the period is $W = 21\xi$.

as a function of the size and period of the blind holes. These states include collective dimer, trimer, and composite states in which the vortex structures in the pinning sites exhibit an orientational ordering with respect to each other. Besides these vortex states, combination of giant vortices in the pinning sites and at the interstitials, as well as combination of giant vortices with multi-vortices were obtained. The interaction of the pinned vortices inside a blind hole with the interstitial vortices gives rise to an orientational ordering with respect to the vortex structures in the other pinning sites and the transitions between these ordered vortex states were obtained as a function of blind hole parameters.

For larger radius of the blind holes the vortices are arranged into shells with average inter-vortex distance which depends both on the radius (shell number) for a particular structure and on the total number of vortices. These vortex shells impose their own symmetry to the interstitial vortices. The formation of these concentric shells of vortices was studied for a broad range of blind hole occupation number n_o. For large values of n_o, the vortices are arranged in an Abrikosove lattice in the center of the disk, which is surrounded by the perfect circular outer shell of vortices.

In the second part of this chapter we considered superconducting films with an array of superconducting pillars. Calculations show that different vortex structures can be obtained both in the pillars and interstitial regions depending on the size and shape of the pillars. For example, for small radii of the pillars triangular vortex lattice still exists and with increasing the size of the pillars transition to a square vortex lattice occurs; vortex lines and vortex clusters can be obtained for particular applied magnetic fields. For larger radii of the pillars vortices start to penetrate the pillars forming vortex shell structures. Due to the influence of these shell structures, as well as due to the boundaries of the pillars, vortex rings are formed in the interstitial sites. Vortices in the pillars show structures that are very similar to those found earlier for finite size superconductors.

Summary

The aim of the thesis was to study the superconducting properties of superconducting thin films containing arrays of pinning centers. For such a system the critical parameters strongly depend on commensurability effects between the vortex lattice and the underlying pinning array. Therefore, the main attention was given to the different vortex structures and their stability. Before considering perforated superconducting films, we studied finite size superconducting samples, where the nucleation of superconductivity and the critical parameters are strongly influenced by the topology of the sample.

We started by calculating the **energy barrier for the entry and exit of vortices** into superconducting mesoscopic samples, based on the numerical solution of the coupled nonlinear GL equations using analytical expressions for the phase of the order parameter obtained from the London theory. The understanding of this problem is very important because all the hysteretic effects and different phase transitions [29, 78, 86] originate from this energy barrier. Calculations show that, the energy barrier strongly depends on the GL parameter κ – smaller κ leads to a large range of the applied magnetic field over which the barrier exists. For a superconducting ring we found a minimum in the free energy in the superconducting region of the sample for some range of magnetic field values when there are a number of vortices inside the hole, indicating that a vortex can be trapped in a metastable state in this region. For a superconducting square the vortex feels a larger barrier along the diagonal of the sample, while the lowest barrier is found along the middle of the sides of the square, which confirms the lateral entry of the vortices through the

sample edge [122]. The barrier has a non-linear dependence on temperature, which is in contrast to previous predictions where a linear dependence of the barrier on temperature was assumed [118, 119]. Our results for the energy barrier show clearly the limitations of the London theory which considerably overestimates (underestimates) the barrier for vortex expulsion (penetration). However, the discrepancy between the results from our approach and the one from the London theory decreases with increasing size of the disk.

In Chapter 3 we studied the superconducting state of **mesoscopic square samples containing two and four antidots** in the presence of a uniform perpendicular magnetic field, which were the object of extensive experimental investigations [128, 129]. The presence of the antidots has a considerable influence on the number of possible vortex states, their stability and transitions between them. For example, the states with even vorticity are more stable than the ones with odd vorticity and the vortex states show enhanced stability for commensurate vorticity, i.e. when the number of vortices is a multiple of the number of holes. For the filled square sample only transitions between successive L states, i.e. $\Delta L = 1$ is found in increasing field, while for the two antidot sample transitions between vortex states with higher vorticity occur continuously with possible $\Delta L = 2$ transitions. The critical magnetic field H_{c2} is increased by more than 60% when introducing antidots. The calculated $H - T$ phase diagram for the four-antidot sample shows clear oscillations in the S/N boundary. Contrary to the full square superconductor, in the four-antidot sample the period of the oscillations and the peak amplitude is not the same for all vortex states, which was explained by the stability of the different vortex states. The theoretically calculated $H - T$ diagram shows reasonable good agreement with the experimental results [129].

Next, we studied the vortex structure and critical parameters of **thin superconducting films with a square array of antidots** in a perpendicular applied magnetic field. Together with the matching phenomena [38, 46, 59, 61], a rich variety of ordered vortex lattice configurations was obtained. For small radius of the holes, the vortex configurations with one vortex captured in each hole and the others located at the interstitial sites are realized, where interstitial vortices form regular patterns, either as multi- or giant vortices, or combination of giant- and multi-vortex states. For particular geometrical parameters of the sample and the applied field, a symmetry imposed vortex-antivortex configuration is found. Depending on the ratio between the hole radius R and the interhole distance W, multi-quanta vortices may be forced into the antidots, in spite of their low saturation number at smaller magnetic fields. To illustrate the transition between possible multi-quanta states in the holes we showed a diagram of the *occupation number* n_o as a function of the radius of the holes and interhole distance for different values of the effective GL parameter. n_o increases with decreasing κ^* due to the enhanced expulsion of the magnetic field from the superconductor and giant vortices become energetically favorable because of the attractive interaction between the vortices. The calculated

saturation number n_s ($n_s = n_o$ for larger applied fields) shows clear limitations of the previous theoretical predictions [68, 143] and has good agreement with the experiment [64, 148]. The critical current j_c of the sample shows well defined peaks at different matching H_n and fractional matching fields, indicating that vortices are strongly pinned by antidots. However, the level of j_c enhancement at particular magnetic field strongly depends on the antidot occupation number n_o. For certain parameters of the sample, the critical current becomes larger at higher matching fields, contrary to conventional behavior. We also studied the $T_c(H)$ phase boundary of a regularly perforated superconducting film. When an antidot array is present the critical temperature $T_c(H)$ for non-zero magnetic field is enhanced compared to a non-patterned film and distinct cusps in the phase boundary are found for different matching fields, which is in agreement with experiment [154]. This behavior is in contrast to the Little-Parks like structures found in finite size superconductors. The increase of the antidot size for given lattice period leads to a change of the $T_c(H)$ background from linear to parabolic behavior except for T near T_{c0}.

In Chapter 5 of the thesis we considered the problem of the **interaction of a single vortex with a circular perforation in a superconducting film** taking into account the finite size of the vortex and its elastic properties, which was first solved more than 30 years ago [68] within the London theory. Our calculations based on GL theory shows that due to the local compression of vortex currents and their adhesion to the edge of the perforation, a local repulsive component to the generally attractive pinning force is found. The resulting qualitative behavior of the interaction force therefore depends on the size of the hole and properties of the superconductor. The dynamic consequences of this adhesion effect was considered in the case of a finite size superconductor with external applied current. The obtained results are of great interest in understanding complex dynamic processes [73, 74] in superconducting samples in the presence of different kinds of pinning centers.

Next, we investigate the nucleation of superconductivity in **superconducting disks containing a blind hole**, which is a more general problem than the perforated superconductor. For this system we obtained a simple model based on the GL formalism, which allows one to study superconducting properties of the system taking into account the smoothness, thickness and size of the blind hole. Our calculations show that the increase of the steepness of the edges of the blind-hole-like cavity in the superconductor leads to a shift of the S/N transition field to higher magnetic fields, but the maximal number of vortices that can be captured by the blind hole remains the same. When the radius of a perfect blind hole is much smaller than the radius of the disk, the maximal number of allowed vortices is the same for all considered samples, regardless of the thickness of the blind hole. Decreasing the blind hole thickness leads to higher S/N transition fields, and the free energy of the sample with a blind hole approaches the energy of the superconducting ring. For larger radii of the blind hole the maximal number of vortices in the sample increases with

decreasing thickness of the blind hole and approaches the number of vortices in the case of a superconducting ring. The H-T phase diagram shows that the critical field at a given temperature and the critical temperature at fixed field are higher for samples with a blind hole, and it is close to the phase boundary of the superconducting ring.

In the last chapter of the thesis we presented the results on the pinning properties of **thin superconducting films with a square array of blind holes**, which allow us to study vortex structures inside the pinning centers contrary to the case of antidots. Although the maximum number of flux quanta trapped by a blind hole is smaller than the corresponding number for holes (i.e. antidots) [171], the presence of blind holes gives rise to a rich variety of ordered vortex structures. These states include collective dimer, trimer, and composite states in which the vortex structures in the pinning sites exhibit an orientational ordering with respect to each other. Besides these vortex states, combination of giant vortices in the pinning sites and in the interstitials, as well as combination of giant vortices with multivortices can be obtained, which is unique and has never been observed before. The transitions between these ordered vortex states were obtained as a function of the blind hole parameters. We showed that vortex configurations in the blind holes are determined not only by their mutual repulsion, but also by the influence of the interstitial vortices and the vortices in the neighboring pinning sites. For larger radius of the blind holes the vortices are arranged into shells with average inter-vortex distance which depends both on the radius (shell number) for a particular structure and on the total number of vortices. These vortex shells impose their own symmetry to the interstitial vortices. The formation of these concentric shells of vortices was studied for a broad range of blind hole occupation number n_o. The evolution of shell formation towards an Abrikosov lattice inside the blind holes are studied for different number of pinned vortices.

We also studied the vortex state in **superconducting films with arrays of pillars**, as a geometrically and physically inverted system, where pillars serve as anti-pinning sites. We found that different types of vortex configurations can be obtained depending on the size and shape of the pillars. For example, for small radii of the pillars a triangular vortex lattice still exists and with increasing the size of the pillars transition to a square vortex lattice occurs. Vortex line structures and vortex clusters are formed for particular applied magnetic fields. For larger radii of the pillars vortices start to penetrate the pillars forming vortex shell structures. Due to the influence of these shell structures, as well as due to the boundaries of the pillars, vortex rings are formed at the interstitial sites. Vortices in the pillars show similar shell structures as was found for finite size superconductors.

List of important realizations

In short the **most important realizations of the present thesis** can be listed as follows:

- A new approach for the problem of *surface barriers* for the entry and exit of vortices into the superconductor was presented. This barrier has a non-linear dependence on temperature, which is in contrast to previous predictions, where a linear dependence of the barrier on temperature is assumed.
- The *vortex phase diagram* was obtained for a thin superconducting film containing a square array of antidots, which predicts the following new vortex configurations:
  - lattice of giant vortices;
  - lattice of coexisting giant and individual (i.e. elementary) vortices;
  - lattice containing both vortices and anti-vortices;
  - quasi-Abrikosov lattice of giant vortices for type-I superconducting films.
- It was shown that the *saturation number of a hole* is determined not only by its size, but also by the periodicity (i.e. the size of the unit cell) of the antidot lattice.
- We found the unexpected results that for particular geometric parameters of the antidot lattice and/or temperature the *critical current* becomes

larger at higher magnetic fields, contrary to the conventional behavior. Such a feature is a result of the "caging" of interstitial vortices between the large number of pinned ones.

- The calculations based on the GL theory show that due to the local compression of vortex currents and their adhesion to the edge of the perforation, a *local repulsive component to the generally attractive pinning force* is found, which will necessitate a revisiting of earlier molecular dynamic results for e.g. the ratchet effect, that were based on the London theory.

- A rich variety of ordered vortex structures is obtained in a superconducting film with an array of blind holes, including *collective dimer, trimer, and composite states* in which the vortex structures in the pinning sites exhibit an orientational ordering with respect to each other. For larger radius of the blind holes *vortex shell structures* are obtained both in the blind holes and in the interstitial sites.

Outlook

In the present work I limited myself to a square geometry for the antidot (or blind hole) lattice because it led to a very interesting interplay with the triangle lattice symmetry of the Abrikosov vortex lattice in macroscopic pinning free superconductors. As a direct extension one may consider **other geometries for the pinning lattice** (e.g. triangle, rectangle, hexagonal) and other shapes for the holes (e.g. elongated, elliptic). Some of these geometries have been already realized experimentally.

As a continuation of the present work one can investigate static and **dynamic** properties of vortices in superconducting films in the presence of different **pinning centers**, e.g. antidots, blind holes and pillars (as anti-pinning sites) **of various shapes**. These investigations will help to understand the origin of different dynamic processes such as creation of vortex-antivortex pairs in the presence of an applied current [49] and vortex rectification effects [73, 74]. Although the dynamic behavior of vortices are accurately described by molecular dynamic simulations [139–142, 151], approximations made are valid only in certain range of parameters. For example, vortices are considered as classical point particles and the pinning is simply introduced through a model potential. However, our calculations within GL theory show that the interaction of vortices with defects is considerably changed due to the finite size of the vortex-core and its elastic properties (see Chapter 5 of the thesis). Such a study within GL theory, where vortices are extended objects, will give more accurate results and further insights into the dynamics of vortices in the presence of artificial pinning.

It would be interesting to extend these theoretical studies to the case of **superconducting-normal metal bilayers with arrays of pinning centers** [50], as a nobel metal covering layer is often employed against rapid oxidation of superconductors.

Another area of interest would be the interplay between the **finite size of a 3D type-I superconductor** and the relationship between the topology of the flux structures and their macroscopic properties. The intermediate state of type-I superconductors is a very rich study object - it consists of coexisting normal state, flux bearing domains and superconducting domains, which originates from the balance between the short-range attractive interaction associated with the interfacial tension between the two phases and the long-range interaction between domains. In addition, these two states strongly depend on the external conditions and the topology of the samples [181]. Although different theoretical models for the bulk intermediate state were developed (see e.g. Ref. [182] and references therein), fitting properly these complex patterns into a topologically confined mesoscopic type-I superconductor remains an unresolved issue.

Samenvatting

Het onderwerp van deze thesis is de studie van de supergeleidende eigenschappen van dunne supergeleidende films met pinning centra. Voor zo'n systeem hangen de kritische parameters sterk af van de commensurabiliteitseffecten tussen het vortexrooster en de onderliggende pinning centra. Daarom gaat de aandacht in deze thesis vooral uit naar de verschillende vortexstructuren en hun stabiliteit. Vooraleer echter geperforeerde supergeleidende films te behandelen, werden eindige supergeleidende samples bestudeerd, waarin de nucleatie van de supergeleiding en de kritische parameters sterk beïnvloed worden door de topologie van het sample.

We zijn gestart met de berekening van de **energiebarrière voor de in- en uittrede van vortices** in mesoscopische supergeleidende samples, gebaseerd op de numerieke oplossing van de gekoppelde niet-lineaire Ginzburg-Landau (GL) vergelijkingen waarbij gebruik gemaakt werd van de analytische uitdrukkingen voor de fase van de orde-parameter uit de London-theorie. Het begrijpen van dit effect is erg belangrijk omdat alle hysteresis-effecten en de verschillende fase-overgangen in eerste intantie bepaald worden door deze energiebarrières [29, 78, 86]. De berekeningen tonen aan dat de energiebarrière sterk afhangt van de GL parameter κ – kleinere κ waarden leiden tot een groot interval van het magneetveld waarbij de barrière bestaat. Voor een supergeleidende ring vonden we een minimum in de vrije energie in het supergeleidende gebied van het sample voor een bepaald interval van het magneetveld waarvoor er vortices aanwezig zijn binnen in de ring. Dit toont aan dat in dit gebied een

vortex opgesloten kan worden in een metastabiele toestand. In een supergeleidend vierkant ondervindt de vortex een grotere barrière langs de diagonaal van het sample, terwijl de laagste barrière gevonden werd langs het midden van de zijden van het vierkant, hetgeen de laterale intrede van vortices door de wand van het sample bevestigt [122]. De barrière hangt op een niet-lineaire wijze af van de temperatuur, in tegenstelling tot eerdere voorspellingen waarbij een lineaire afhankelijkheid werd gevonden [118, 119]. Onze resultaten voor de energiebarrière tonen duidelijk de beperkingen aan van de London-theorie die de barrière voor de uittrede (penetratie) van een vortex duidelijk overschat (onderschat). De afwijking tussen onze aanpak en de London-theorie verkleint met toenemende grootte van het sample.

In Hoofdstuk 3 bestudeerden we de supergeleidende toestand van **mesoscopische vierkante samples met twee en vier antidots** in de aanwezigheid van een uniform loodrecht magnetisch veld, die reeds onderwerp waren van extensieve experimentele studies [128, 129]. De aanwezigheid van antidots heeft een aanzienlijke invloed op het aantal mogelijke vortextoestanden, hun stabiliteit en overgangen tussen hen. De toestanden met even vorticiteit zijn bijvoorbeeld stabieler dan die met oneven vorticiteit, d.w.z. wanneer het aantal vortices een veelvoud is van het aantal gaten. Voor het volle vierkant sample vinden we enkel overgangen tussen opeenvolgende L-toestanden, d.w.z. $\Delta L = 1$, voor toenemend veld, terwijl voor het sample met twee-antidots overgangen tussen vortextoestanden met hogere vorticiteit continu optreden met de mogelijkheid van $\Delta L = 2$ overgangen. Het kritisch magnetisch veld H_{c2} neemt met meer dan 60% toe wanneer antidots geïntroduceerd worden. Het berekend H-T fasediagram voor het vier-antidot sample vertoont duidelijke oscillaties in de S/N grens. In tegenstelling tot de volle vierkant supergeleider is de periode van de oscillaties en de piekamplitude voor het vier-antidot sample niet gelijk voor alle vortextoestanden. Het theoretisch berekende H-T diagram vertoont goede overeenkomtst met de experimentele resultaten [129].

Vervolgens bestudeerden we de vortexstructuur en de kritische parameters van **dunne supergeleidende films met een vierkante matrix van antidots** in een loodrecht aangelegd magnetisch veld. Naast de matchingfenomenen [38, 46, 59, 61] werd een rijke verscheidenheid aan geordende vortexroosterconfiguraties verkregen. Voor kleine straal van de gaten worden configuraties met vortices gevangen in elk gat en de anderen vortices zijn gelokaliseerd op de interstitiële plaatsen, waarbij interstitiële vortices regelmatige patronen vormen, ofwel als multi- of giant-vortices, ofwel als combinaties van giant- en multi-vortextoestanden. Voor bepaalde geometrische parameters van het sample en het aangelegde veld wordt een door symmetrie opgelegde vortex-antivortexconfiguratie gevonden. Afhankelijk van de verhouding tussen de straal R van het gat en de afstand W tussen de gaten kunnen multi-quanta-vortices in antidots gedwongen worden, ondanks hun laag verzadigingsgetal

bij lagere magnetische velden. Om de overgang tussen mogelijke multi-quanta-toestanden in de gaten te illustreren toonden we een diagram van het bezettingsgetal n_o als functie van de straal van de gaten en de afstand tussen de gaten voor verschillende waarden van de effectieve GL-parameter. n_o neemt toe met afnemende κ^* vanwege de verhoogde uitdrijving van het magnetisch veld van de supergeleider en giant-vortices worden energetisch gunstig vanwege de attractieve wisselwerking tussen de vortices. Het berekende verzadigingsgetal n_s ($n_s = n_o$ voor grotere aangelegde velden) toont duidelijke beperkingen van de voorgaande theoretische voorspellingen [68, 143] en vertoont goede overeenkomst met het experiment [64, 148]. De kritische stroom j_c van het sample toont welgedefinieerde pieken bij verschillende matching velden H_n en fractionele matching velden, wat aantoont dat vortices sterk gepind worden door antidots. Echter, de mate van j_c-verhoging bij een bepaald magnetisch veld hangt sterk af van het antidotbezettingsgetal n_o. Voor bepaalde parameters van het sample wordt de kritische stroom groter bij hogere matching velden, in tegenstelling tot het conventioneel gedrag. We bestudeerden eveneens de $T_c(H)$ fasegrens van een regelmatig geperforeerde supergeleidende film. Wanneer een antidotmatrix aanwezig is wordt de kritische temperatuur $T_c(H)$ verhoogd in vergelijking met een film zonder patroon en duidelijke punten in de fasegrens worden gevonden voor verschillende matching velden, wat in overeenkomst is met het experiment [154]. Dit gedrag staat in contrast met de Little-Parks-achtige structuren die men in supergeleiders van eindige grootte aantreft. De toename van de antidotgrootte voor een gegeven roosterperiode leidt tot een verandering van de $T_c(H)$ achtergrond van lineair naar parabolisch gedrag behalve voor T dicht bij T_{c0}.

In Hoofdstuk 5 van deze thesis beschouwden we het probleem van de **interactie van een vortex met een cirkelvormige opening in een supergeleidende film**. Hierbij werd er rekening gehouden met de eindige grootte van de vortex en met zijn elastische eigenschappen . Dit probleem werd meer dan 30 jaar geleden [68] opgelost met de London theorie. Onze berekeningen gebaseerd op de GL theorie tonen aan dat door de lokale compressie van de vortex stromen en door hun adhesie aan de rand van de opening er een lokale repulsieve component ontstaat van de in het algemeen attractieve pinning kracht. Het resulterende kwalitatief gedrag van de interactiekracht hangt daarom af van de grootte van de opening en de eigenschappen van de supergeleider. De dynamische gevolgen van deze adhesie bij een eindige supergeleider met een extern aangelegde stroom werden beschouwd. De verkregen resultaten zijn van groot belang om de complexe processen [73, 74] in supergeleidende samples in de aanwezigheid van verschillende soorten pinningscentra te begrijpen.

Vervolgens onderzochten we de nucleatie van supergeleiding in **supergeleiders met een blind gat** vertonen, wat een algemener probleem is dan een geperforeerde supergeleider. Voor dit systeem gebruikten we een eenvoudig model gebaseerd op het GL formalisme. Dit model laat ons toe om de supergeleidende eigenschappen van het systeem te bestuderen, rekening houdend

met de gladheid, de dikte en de grootte van het blind gat. Onze berekeningen tonen aan dat een toename van de steilheid van de randen van de blinde gaten-achtige caviteit in de supergeleider leidt tot een verschuiving van het S/N transitie veld naar hogere magnetische velden, maar dat het maximaal aantal vortices dat gebonden kan worden door het blinde gat hetzelfde blijft. Als de straal van een perfect blind gat veel kleiner is dan de straal van de schijf dan blijft het maximaal aantal vortices hetzelfde voor alle beschouwde samples, ongeacht de dikte van het blinde gat. Een afname van de dikte van het blinde gat leidt tot hogere S/N transitievelden en de vrije energie van het staal benadert de energie van een supergeleidende ring. Voor grotere stralen neemt het maximaal aantal vortices toe bij afnemende dikte van het blinde gat en het aantal benadert het aantal vortices in een supergeleidende ring. Het $H-T$ fasediagram toont aan dat het kritisch veld bij een gegeven temperatuur en de kritische temperatuur bij een gegeven veld hoger zijn voor een staal met een blind gat en dat dit dicht bij de fasegrens van een supergeleidende ring is.

In het laatste hoofdstuk van de thesis hebben we de resultaten voorgesteld van de **'pinning'-eigenschappen van dunne supergeleidende films met een vierkant rooster van blinde gaten, die ons toelaten de vortex-structuren in de 'pinning'-centra tegenover de antidots te bestuderen**. Hoewel het maximum aantal fluxquanta dat gevangen zit in een blind gat kleiner is dan het corresponderende aantal gaten (i.e. antidots) [171], zorgt de aanwezigheid van blinde gaten voor een rijke variëteit van geordende vortex-structuren. Deze toestanden bevatten dimeer, trimeer en samengestelde toestanden waarin de vortex-structuren in de 'pinning'-locaties zich ten opzichte van elkaar oriënteren. Naast deze vortex-toestanden kunnen zowel combinaties van giant vortices in de 'pinning'-locaties en de tussenliggende ruimtes als giant vortices met multivortices verkregen worden. Dit is uniek en is nooit eerder geobserveerd. De overgang tussen deze geordende vortex-toestanden werd verkregen als functie van de parameters van de blinde gaten. We hebben aangetoond dat de vortex-configuraties in de blinde gaten niet alleen bepaald worden door hun onderlinge afstoting, maar ook door de invloed van de vortices in de tussenliggende ruimten en de vortices in naburige 'pinning'-locaties. Voor grotere stralen van de blinde gaten groeperen de vortices zich in ringen. De gemiddelde afstand tussen de vortices hangt af van de straal van de vortexstructuur en het aantal vortices. De vorming van deze concentrische ringen van vortices werd bestudeerd voor een grote spreiding in het bezettingsnummer n_o van de blinde gaten. De evolutie van de ringvorming tot het Abrikosov-rooster in de blinde gaten is bestudeerd voor verschillende aantallen van vastgepinde vortices.

We hebben ook de vortex-toestand bestudeerd in **supergeleidende films met roosters van pilaren**, als een geometrisch en fysisch geïnverteerd systeem, waar de pilaren als 'pinning'-locaties dienst doen. We vonden dat verschillende types van vortex-configuraties kunnen verkregen worden naargelang de grootte en de vorm van de pilaren. Zo bestaat bijvoorbeeld voor kleine

stralen van de pilaren een driehoekig rooster van vortices dat met het groter worden van de pilaren overgaat in een vierkant rooster. Vortex lijnstructuren en vortexclusters worden gevormd bij bepaalde magnetische velden. Bij grotere stralen van de pilaren beginnen de vortices de pilaren binnen te dringen en vormen ze ring structuren. Door zowel de invloed van deze ringstructuren als door de grenzen van de pilaren vormen de vortices ook ringstructuren in de tussenliggende ruimten. Vortices in de pilaren vormen dezelfde structuren als gevonden voor supergeleiders met eindige afmetingen.

References

1. H. Kamerlingh Onnes, Leiden Comm. **122b**, 124 (1911).
2. W. Meissner and R. Ochsenfeld, Naturwiss. **21**, 787 (1933).
3. Per Fridthof Dahl, *Superconductivity. Its Historical Roots and Development from Mercury to the Ceramic Oxides* (American Institute of Physics, New York, 1992).
4. US Department of Energy report (2006), *Basic Research Needs for Superconductivity*, *www.er.doe.gov/bes/reports/files/SC_rpt.pdf*.
5. J. Nagamatsu, N. Nakagawa, T. Muranaka, Y. Zenitani, and J. Akimitsu, Nature (London) **410**, 63 (2001).
6. D. Jerome, A. Mazaud, M. Ribault, and K. Bechgaard, J. Physique Lett. **41**, 95 (1980).
7. W.A. Little, Phys. Rev. **134**, A1416 (1964).
8. A.F. Hebard, M.J. Rosseinsky, R.C. Haddon, D.W. Murphy, S.H. Glarum, T.T.M. Palstra, A.P. Ramirez, and A.R. Kortam, Nature (London) **350**, 600 (1991).
9. J.G. Bednorz and K.A. Müller, Z. Phys. B **64**, 189 (1986).
10. A. Schilling, M. Cantoni, J.D. Guo, and H.R. Ott, Nature (London) **363**, 56 (1993).

11. S.N. Putilin, E.V. Antipov, A.M. Abakumov, M.G. Rozova, K.A. Lokshin, D.A. Pavlov, A.M. Balagurov, D.V. Sheptyakov, M. Marezio, Physica C **338**, 52 (2000).

12. EU report, *SCENET roadmap for superconductor digital electronics*, Physica C **439**, 1 (2006).

13. M.F. Bocko, A.M. Herr, and M.J. Feldman, IEEE Trans. Appl. Superconductivity **7**, 3638 (1997).

14. J.E. Mooji, T.P. Orlando, L. Levitov, L. Tian, C.H. van der Wal, and S. Lloyd, Science **285**, 1036 (1999).

15. J.R. Friedman, V. Patel, W. Chen, S.K. Tolpygo, and J.E. Lukens, Nature **406**, 43 (2000).

16. Y. Makhlin, G. Schon, and A. Shnirman, Rev. Mod. Phys. **73**, 357 (2001).

17. F. London and H. London, Proc. Roy. Soc. **A149**, 71 (1935).

18. J. Bardeen, L.N. Cooper, and J.R. Schrieffer, Phys. Rev. **108**, 1175 (1957).

19. L.N. Cooper, Phys. Rev. **104**, 1189 (1956).

20. L.P. Gor'kov, Sov. Phys. JETP **9**, 1364 (1959).

21. V.L. Ginzburg and L.D. Landau, Zh. Eksp. Teor. Fiz. **20**, 1064 (1950).

22. L.D. Landau and E.M. Lifshitz, *Statistical Physics*, 3rd edn., part 1 (Nauka, Moscow 1976) [English transl.: Pergamon Press, Oxford 1980].

23. M. Tinkham, *Introduction to superconductivity* (McGraw Hill, New York, 1975).

24. P.-G. de Gennes, *Superconductivity of Metals and Alloys* (Benjamin, New York, 1966).

25. H.B. Nielsen and P. Olesen, Nucl. Phys. B. **160**, 380 (1979).

26. G. Stenuit, S. Michotte, J. Govaerts, and L. Piraux, Supercond. Sci. Technol. **18**, 174 (2005).

27. P.S. Deo, V.A. Schweigert, F.M. Peeters, and A.K. Geim, Phys. Rev. Lett. **79**, 4653 (1997).

28. B.J. Baelus, A. Kanda, F.M. Peeters, Y. Ootuka, and K. Kadowaki Phys. Rev. B **71**, 140502 (2005).

29. A.K. Geim, I.V. Grigorieva, S.V. Dubonos, J.G.S. Lok, J.C. Maan, A.E. Filippov, and F.M. Peeters, Nature (London) **390**, 256 (1997).

30. A.A. Abrikosov, Sov. Phys. JETP **5**, 1174 (1957).

31. W.H. Kleiner, L.M. Roth, and S.H. Autler, Phys. Rev. **133**, A1226 (1964).

32. U. Essmann and H. Träuble, Sci. Am. **224**, 75 (1971).

33. M.R. Eskildsen, A.B. Abrahamsen, D. Lopez, P.L. Gammel, D.J. Bishop, N.H. Andersen, K. Mortensen, and P.C. Canfield, Phys. Rev. Lett. **86**, 320 (2001).

34. P. Nozieres and W.F. Vinen, Philos. Mag. **14**, 667 (1966).

35. M.R. Eskildsen, M. Kugler, S. Tanaka, J. Jun, S.M. Kazakov, J. Karpinski, and O. Fischer, Phys. Rev. Lett. **89**, 187003 (2002).

36. P.E. Goa, H. Hauglin, M. Baziljevich, E. Il'yashenko, P.L. Gammel, and T.H. Johansen, Supercond. Sci. Technol. **14**, 729-731 (2001).

37. S.B. Field, S.S. James, J. Barentine, V. Metlushko, G. Crabtree, H. Shtrikman, B. Ilic, and S.R.J. Brueck, Phys. Rev. Lett. **88**, 067003 (2002).

38. K. Harada, O. Kamimura, H. Kasai, T. Matsuda, A. Tonomura, and V.V. Moshchalkov, Science **274**, 1167 (1996).

39. Y.B. Kim and M.J. Stephen, *Superconductivity* (edited by R.D. Parks, Marcel Dekker, New York, 1969).

40. J. Evetts (ed.), *Concise Encyclopedia of Magnetic and Superconducting Materials* (Pergamon Press, Oxford, 1992).

41. Ž. Radović and L. Dobrosavjević, in *Recent Development in Condensed Matter Physics*, **4**, Ed. J.T. Devreese (Plenum Publishing Corporation, 1981).

42. G. Blatter, M.V. Feigelman, V.B. Geshkenbein, A.I. Larkin, V.M. Vinokur, Rev. Mod. Phys. **66**, 1125 (1994).

43. A. Silhanek, L. Civale, S. Candia, G. Nieva, G. Pasquini, and H. Lanza, Phys. Rev. B **59**, 13620 (1999).

44. D. Niebieskikwait, A.V. Silhanek, L. Civale, G. Nieva, P. Levy, and L. Krusin-Elbaum, Phys. Rev. B **63**, 144504 (2001).

45. A. Castellanos, R. Wördenweber, G. Ockenfuss, A. v.d. Hart, and K. Keck, Appl. Phys. Lett. **71**, 962 (1997).

46. V.V. Moshchalkov, M. Baert, V.V. Metlushko, E. Rosseel, M.J. Van Bael, K. Temst, R. Jonckheere, and Y. Bruynseraede, Phys. Rev. B **54**, 7385 (1996).

47. V.V. Moshchalkov, M. Baert, V.V. Metlushko, E. Rosseel, M.J. Van Bael, K. Temst, Y. Bruynseraede, and R. Jonckheere, Phys. Rev. B **57**, 3615 (1998).

48. L. Van Look, B.Y. Zhu, R. Jonckheere, B.R. Zhao, Z.X. Zhao, and V.V. Moshchalkov, Phys. Rev. B **66**, 214511 (2002).

49. R. Villar, V.V. Pryadun, J. Sierra, F.G. Aliev, E. Gonzalez, J.L. Vicent, D. Golubovic and V.V. Moshchalkov, Physica C **437**, 345 (2006).

50. V. V. Metlushko, L. E. DeLong, V. V. Moshchalkov and Y. Bruynseraede, Physica C **391**, 196 (2003).

51. J.I. Martin, M. Velez, J. Nogues, and I.K. Schuller, Phys. Rev. Lett. **79**, 1929 (1997).

52. M.J. Van Bael, J. Bekaert, K. Temst, L. Van Look, V.V. Moshchalkov, Y. Bruynseraede, G.D. Howells, A.N. Grigorenko, S.J. Bending, and G. Borghs, Phys. Rev. Lett. **86**, 155 (2001).

53. M.J. Van Bael, K. Temst, V.V. Moshchalkov, and Y. Bruynseraede, Phys. Rev. B **59**, 14674 (1999).

54. A. Hoffmann, P. Prieto, and I.K. Schuller, Phys. Rev. B **61**, 6958 (2000).

55. M. Lange, M.J. Van Bael, Y. Bruynseraede, and V.V. Moshchalkov, Phys. Rev. Lett. **90**, 197006 (2003).

56. O. Daldini, P. Martinoli, J.L. Olsen, G. Berner, Phys. Rev. Lett. **32**, 218 (1974).

57. A.F. Hebard, A.T. Fiory, and S. Somekh, IEEE Trans. Magn. **1**, 589 (1977).

58. A.T. Fiory, A.F. Hebard, and S. Somekh, Appl. Phys. Lett. **32**, 73 (1978).

59. M. Baert, V.V. Metlushko, R. Jonckheere, V.V. Moshchalkov, and Y. Bruynseraede, Phys. Rev. Lett. **74**, 3269 (1995).

60. V. Metlushko, U. Welp, G.W. Crabtree, Zhao Zhang, S.R.J. Brueck, B. Watkins, L.E. DeLong, B. Ilic, K. Chung, and P.J. Hesketh, Phys. Rev. B **59**, 603 (1999).

61. V. Metlushko, U. Welp, G.W. Crabtree, R. Osgood, S.D. Bader, L.E. DeLong, Zhao Zhang, S.R.J. Brueck, B. Ilic, K. Chung, and P.J. Hesketh, Phys. Rev. B **60**, R12585 (1999).

62. V. Metlushko, U. Welp, G.W. Crabtree, R. Osgood, S.D. Bader, L.E. DeLong, Zhao Zhang, S.R.J. Brueck, B. Ilic, K. Chung, and P.J. Hesketh, Phys. Rev. Lett. **41**, 333 (1998).

63. A. Volodin, K. Temst, C. Van Haesendonck, and Y. Bruynseraede, Appl. Phys. Lett. **73**, 1134 (1998).

64. A.N. Grigorenko, G.D. Howells, S.J. Bending, J. Bekaert, M.J. Van Bael, L. Van Look, V.V. Moshchalkov, Y. Bruynseraede, G. Borghs, I.I. Kaya, R.A. Stradling, Phys. Rev. B **63**, 052504 (2001).

65. S.J. Bending, G.D. Howells, A.N. Grigorenko, M.J. Van Bael, J. Bekaert, K. Temst, L. Van Look, V.V. Moshchalkov, Y. Bruynseraede, G. Borghs and R.G. Humphreys, Physica C **332**, 20 (2000).

66. A.N. Grigorenko, S.J. Bending, M.J. Van Bael, M. Lange, V.V. Moshchalkov, H. Fangohr, and P.A.J. de Groot Phys. Rev. Lett. **90**, 237001 (2003).

67. A. Bezryadin, Yu.N. Ovchinnikov, and B. Pannetier Phys. Rev. B **53**, 8553 (1996).

68. G.S. Mkrtchyan and V.V. Shmidt, Sov. Phys. JETP **34**, 195 (1972).

69. H. Nordborg and V.M. Vinokur, Phys. Rev. B **62**, 12408 (2000).

70. I.B. Khalfin and B. Ya. Shapiro, Physica C **207**, 359 (1993).

71. V. Misko, S. Savelev, and F. Nori, Phys. Rev. Lett. **95**, 177007 (2006).

72. A.V. Silhanek, W. Gillijns, and V.V. Moshchalkov, Appl. Phys. Lett. **89**, 152507 (2006).

73. C.C. de Souza Silva, J. Van de Vondel, M. Morelle, and V.V. Moshchalkov, Nature (London) **440**, 651 (2006).

74. J. Van de Vondel, C.C. de Souza Silva, B.Y. Zhu, M. Morelle, and V.V. Moshchalkov, Phys. Rev. Lett. **94**, 057003 (2005).

75. A. Wahl, V. Hardy, J. Provost, Ch. Simon, and A. Buzdin, Physica C **250**, 359 (1995).

76. F.M. Araujo-Moreira, C. Navau, and A. Sanchez, Phys. Rev. B **61**, 6334 (2000).

77. A.C. Rose-Innes and E.H. Rhoderick, *Introduction to Superconductivity* (Second edition, Pergamon Press. Oxford, 1978).

78. V.A. Schweigert, F.M. Peeters, and P.S. Deo, Phys. Rev. Lett. **81**, 2783 (1998).

79. B.J. Baelus and F.M. Peeters, Phys. Rev. B **65**, 104515 (2002).

80. Y.E. Lozovik and E.A. Rakoch, Phys. Rev. B **57**, 1214 (1998).

81. L.R.E. Cabral, B.J. Baelus, and F.M. Peeters, Phys. Rev. B **70**, 144523 (2004).

82. I.V. Grigorieva, W. Escoffier, J. Richardson, L.Y. Vinnikov, S. Dubonos, and V. Oboznov, Phys. Rev. Lett. **96**, 077005 (2006).

83. A. Kanda, B.J. Baelus, F.M. Peeters, K. Kadowaki, and Y. Ootuka, Phys. Rev. Lett. **93**, 257002 (2004).

84. M.M. Doria, J.E. Gubernatis, D. Rainer, Phys. Rev. B **39**, 9573 (1989).

85. R. Kato, Y. Enomoto, S. Maekawa, Phys. Rev. B **47**, 8016 (1993).

86. A.K. Geim, S.V. Dubonos, J.G.S. Lok, M. Henini, and J.C. Maan, Nature (London) **396**, 144 (1998).

87. C.A. Bolle, V. Aksyuk, F. Pardo, P.L. Gammel, E. Zeldov, E. Bucher, R. Boie, D.J. Bishop, D.R. Nelson, Nature (London) **399**, 43 (1999).

88. V.A. Schweigert and F.M. Peeters, Phys. Rev. B **57**, 13817 (1998).

89. J.J. Palacios, Phys. Rev. B **58**, R5948 (1998); *ibid.* Phys. Rev. Lett. **84**, 1796 (2000).

90. B.J. Baelus, F.M. Peeters, and V.A. Schweigert, Phys. Rev. B **61**, 9734 (2000).

91. F.M. Peeters, V.A. Schweigert, B.J. Baelus, and P.S. Deo, Physica C **332**, 255 (2000).

92. C.P. Bean and J.D. Livingston, Phys. Rev. Lett. **12**, 14 (1964).

93. L. Burlachkov, Phys. Rev. B **47**, 8056 (1993).

94. V.P. Galaiko, Zh. Eksp. Teor. Fiz. **50**, 1322 (1966) [Sov. Phys. JETP **23**, 878 (1966)].

95. E.H. Brandt, Phys. Rev. B **58**, 6506 (1998).

96. E. Akkermans, D.M. Gangardt, and K. Mallick, Phys. Rev. B **63**, 064523 (2001).

97. A.L. Fetter, Phys. Rev. B **22**, 1200 (1980).

98. A.I. Buzdin and J.P. Brison, Phys. Lett. A **196**, 267 (1994).

99. S. Pedersen, G.R. Kofod, J.C. Hollingbery, C.B. Sorensen, and P.E. Lindelof, Phys. Rev. B **64**, 104522 (2001).

100. J.R. Kirtley, C.C. Tsuei, V.G. Kogan, J.R. Clem, H. Raffy, and Z.Z. Li, Phys. Rev. B **68**, 214505 (2003).

101. D.Y. Vodolazov, F.M. Peeters, S.V. Dubonos, and A.K. Geim, Phys. Rev. B **67**, 054506 (2003).

102. V.G. Kogan, J.R. Clem, and R.G. Mints, Phys. Rev. B **69**, 064516 (2004).

103. V.G. Kogan, Phys. Rev. B **49**, 15 874 (1980).

104. E. Zeldov, A.I. Larkin, V.B. Geshkenbein, M. Konczykowski, D. Majer, B. Khaykovich, V.M. Vinokur, and H. Shtrikman, Phys. Rev. Lett. **73**, 1428 (1994).

105. E.H. Brandt, Phys. Rev. B **54**, 4246 (1996).

106. E.H. Brandt, Phys. Rev. B **59**, 3369 (1999).

107. A.V. Kuznetsov, D.V. Eremenko, and V.N. Trofimov, Phys. Rev. B **59**, 1507 (1999).

108. P.S. Deo, V.A. Schweigert, and F.M. Peeters, Phys. Rev. B **59**, 6039 (1999).

109. V.A. Schweigert and F.M. Peeters, Phys. Rev. Lett. **83**, 2409 (1999).

110. V.A. Schweigert and F.M. Peeters, Physica C **332**, 266 (2000).

111. B.J. Baelus, F.M. Peeters, and V.A. Schweigert, Phys. Rev. B **63**, 144517 (2001).

112. A.D. Hernandez and D. Dominguez, Phys. Rev. B **65**, 144529 (2002).

113. E.H. Brandt, Phys. Rev. Lett. **74**, 3025 (1995).

114. L. Prigozhin, J. Comp. Phys. **144**, 180 (1998).

115. G. Stenuit, PhD thesis (Université Louvain-la-Neuve, 2004).

116. P.M. Morse and H. Feshbach, *Methods of Theoretical Physics* (McGraw-Hill Book Company, Inc., 1953), Chapt. 10.

117. B.J. Baelus, A. Kanda, N. Shimizu, K. Tadano, Y. Ootuka, K. Kadowaki, and F.M. Peeters, Phys. Rev. B **73**, 024514 (2006).

118. M. Konczykowski, L.I. Burlachkov, Y. Yeshurun, and F. Holtzberg, Phys. Rev. B **43**, 13707 (1991).

119. L. Burlachkov, A.E. Koshelev, and V.M. Vinokur, Phys. Rev. B **54**, 6750 (1996).

120. W.A. Little and R.D. Parks, Phys. Rev. Lett. **9**, 9 (1962); *ibid.* Phys. Rev. **133**, A97 (1964).

121. C.C.S. Silva, L.R.E. Cabral, and J.A. Aguiar, Physica C **404**, 11 (2004).

122. B.J. Baelus, K. Kadowaki, and F.M. Peeters, Phys. Rev. B **71**, 024514 (2005).

123. V.V. Moshchalkov, L. Gielen, C. Strunk, R. Jonckheere, X. Qiu, C. Van Haesendonck, and Y. Bruynseraede, Nature **373**, 319 (1995).

124. J. Berger and J. Rubinstein, Phys. Rev. B **59**, 8896 (1999).

125. D.Y. Vodolazov, B.J. Baelus, and F.M. Peeters, Phys. Rev. B **66**, 054531 (2002).

126. V.M. Fomin, V.R. Misko, J.T. Devreese, and V.V. Moshchalkov, Solid State Communication **101**, 303 (1997); Phys. Rev. B **58**, 11703 (1998).

127. P.G. de Gennes and C.R. Seances, Acad. Sci., Ser. II **292**, 279 (1981).

128. T. Puig, E. Rosseel, L. Van Look, M.J. Van Bael, V.V. Moshchalkov, Y. Bruynseraede, and R. Jonckheere, Phys. Rev. B **58**, 5744 (1998).

129. V. Bruyndoncx, J. G. Rodrigo, T. Puig, L. Van Look, V. V. Moshchalkov, and R. Jonckheere, Phys. Rev. B **60**, 4285 (1999).

130. B. Baelus, S.V. Yampolskii, and F.M. Peeters, Phys. Rev. B **66**, 024517 (2002).

131. V.A. Schweigert and F.M. Peeters, Phys. Rev. B **60**, 3084 (1999).

132. A.K. Geim, S.V. Dubonos, I.V. Grigorieva, K.S. Novoselov, F.M. Peeters, and V.A. Schweigert, Nature (London) **407**, 55 (2000).

133. V.M. Fomin, V.R. Misko, J.T. Devreese, and V.V. Moshchalkov, Phys. Rev. B **58**, 11703 (1998).

134. M. Brunner and C. Bechinger, Phys. Rev. Lett. **88**, 248302 (2002).

135. J.L. Vioy, Rev. Mod. Phys. **72**, 813 (2000).

136. P. Zeppenfeld, J. Goerge, V. Diercks, R. Halmer, R. David, G. Comsa, A. Marmier, C. Ramseyer, and C. Girardet, Phys. Rev. Lett. **78**, 1504 (1997).

137. C.S. Lent, P.D. Tougaw, W. Porod, and G.H. Bernstein, Nanotechnology **4**, 49 (1993).

138. J.W. Reijnders and R.A. Duine, Phys. Rev. Lett. **93**, 060401 (2004).

139. C. Reichhardt, J. Groth, C.J. Olson, Stuart B. Field, and Franco Nori, Phys. Rev. B **54**, 16108 (1997).

140. C. Reichhardt, C.J. Olson, and Franco Nori, Phys. Rev. B **57**, 7937 (1998).

141. C. Reichhardt, G.T. Zimanyi, and N. Gronbech-Jensen, Phys. Rev. B **64**, 014501 (2001).

142. C. Reichhardt and N. Gronbech-Jensen, Phys. Rev. B **63**, 054510 (2001).

143. A.I. Buzdin, Phys. Rev. B **47**, 11416 (1993).

144. A. Bezryadin and B. Pannetier, J. Low Temp. Phys. **98**, 251 (1995).

145. L.F. Chibotaru, A. Ceulemans, V. Bruyndoncx, and V.V. Moshchalkov, Nature **408**, 833 (2000); *ibid.* Phys. Rev. Lett. **86**, 1323 (2001).

146. T. Mertelj and V.V. Kabanov, Phys. Rev. B **67**, 134527 (2003).

147. V.R. Misko, V.M. Fomin, J.T. Devreese, and V.V. Moshchalkov, Phys. Rev. Lett. **90**, 147003 (2003).

148. A.V. Silhanek, S. Raedts, M.J. Van Bael, and V.V. Moshchalkov, Phys. Rev. B **70**, 054515 (2004).

149. W.V. Pogosov, A.L. Rakhmanov, and V.V. Moshchalkov, Phys. Rev. B **67**, 014532 (2003).

150. G. Coupier, M. Saint Jean, and C. Guthmann, cond-mat/0611582 (unpublished).

151. C. Reichhardt and N. Gronbech-Jensen, Phys. Rev. Lett. **85**, 2372 (2000).

152. M.V. Milošević and F.M. Peeters, Phys. Rev. Lett. **93**, 267006 (2004).

153. A.V. Silhanek, L. Van Look, R. Jonckheere, B.Y. Zhu, S. Raedts, and V.V. Moshchalkov, Phys. Rev. B **72**, 014507 (2005).

154. E. Rosseel, T. Puig, M. Baert, M.J. Van Bael, V.V. Moshchalkov, and Y. Bruynseraede, Physica C **282-287**, 1567 (1997).

155. D.R. Link, S.L. Anna, D.A. Weitz, and H.A. Stone, Phys. Rev. Lett. **92**, 054503 (2004).

156. T. Shinjo, T. Okuno, R. Hassdorf, K. Shigeto, and T. Ono, Science **289**, 930 (2000).

157. T. Uhlig, M. Rahm, C. Dietrich, R. Hollinger, M. Heumann, D. Weiss, and J. Zweck, Phys. Rev. Lett. **95**, 237205 (2005); M. Rahm, R. Höllinger, V. Umansky, and D. Weiss, J. Appl. Phys. **95**, 6708 (2004).

158. M.N. Walters and J.M. Papadimitriou, Crit. Rev. Toxicol. **5**, 377 (1978).

159. D.J. Priour, Jr. and H.A. Fertig, Phys. Rev. B **67**, 054504 (2003).

160. G.S. Park, C.E. Cunningham, B. Cabrera, and M.E. Huber, Phys. Rev. Lett. **68**, 1920 (1992).

161. L. Kramer and R.J. Watts-Tobin, Phys. Rev. Lett. **40**, 1041 (1978).

162. B.J. Baelus, L.R.E. Cabral, and F.M. Peeters, Phys. Rev. B **69**, 064506 (2004); *ibid.* Phys. Rev. B **70**, 144523 (2004).

163. T. Mertelj and V.V. Kabanov, Phys. Rev. B **67**, 134527 (2003).

164. A.S. Melnikov, I.M. Nefedov, D.A. Ryzhov, I.A. Shereshevskii, V.M. Vinokur, and P.P. Vysheslavtsev, Phys. Rev. B **65**, 140503(R) (2002).

165. R. Geurts, M.V. Milosevic, and F.M. Peeters, Phys. Rev. Lett. **97**, 137002 (2006).

166. F.M. Peeters, V.A. Schweigert, and B.J. Baelus, Physica C **369**, 158 (2002).

167. V. Bruyndoncx, L. Van Look, M. Verschuere, and V.V. Moshchalkov, Phys. Rev. B **60**, 10468 (1999).

168. J.E. Bonevich, K. Harada, T. Matsuda, H. Kasai, T. Yoshida, G. Pozzi, and A. Tonomura, Phys. Rev. Lett. **70**, 2952 (1993).

169. S. Behler, S.H. Pan, P. Jess, A. Baratoff, H.J. Guntherodt, F. Levy, G. Wirth, and J. Wiesner, Phys. Rev. Lett. **72**, 1750 (1994).

170. A. Bezryadin and B. Pannetier, J. Low Temp. Phys. **102**, 73 (1996).

171. S. Raedts, A.V. Silhanek, M.J. Van Bael, and V.V. Moshchalkov, Phys. Rev. B **70**, 024509 (2004).

172. Qiang Du, Max D. Gunzburger, and J.S. Peterson, Phys. Rev. B **51**, 16194 (1995).

173. A. Buzdin and D. Feinberg, Physica C **256**, 303 (1996).

174. B.J. Baelus, L.R.E. Cabral, and F.M. Peeters, Phys. Rev. B **69**, 064506 (2004).

175. A.I. Buzdin and J.P. Brison, Phys. Lett. A 196, 267 (1994).

176. V.R. Misko, B. Xu, and F.M. Peeters (unpublished).

177. L.J. Campbell and R.M. Ziff, Phys. Rev. B **20**, 1886 (1979).

178. V.M. Bedanov and F.M. Peeters, Phys. Rev. B **49**, 2667 (1994).

179. Y.J. Lai and L.I, Phys. Rev. E **60**, 4743 (1999).

180. M. Kong, B. Partoens, and F.M. Peeters, Phys. Rev. E **65**, 046602 (2002).

181. R. Prozorov, R.W. Giannetta, A.A. Polyanskii, G.K. Perkins, Phys. Rev. B **72**, 212508 (2005); *ibid.* cond-mat/0612135 (2006) (unpublished).

182. C.R. Reisin and S.G. Lipson, Phys. Rev. B **61**, 4251 (2000).

Curriculum Vitae

Berdiyorov Golibjon

Born on September 20, 1976
in Samarkand / Uzbekistan

September 1993 - June 1998: Diploma in Physics, Tashkent State University, Tashkent, Uzbekistan.

July 1998 - September 2002: Research Assistant, Institute of Applied Physics, National University of Uzbekistan, Uzbekistan.

October 2002 - September 2007: Research Assistant, Condensed Matter Theory group, Physics Department, University of Antwerpen, Belgium.

Promotor: Prof. dr. F. M. Peeters
Co-promotor: Dr. M. V. Milošević

Scientific award

2006 The best poster presentation in Joint International Workshop on "Nanosensors and Arrays of Quantum Dots and Josephson Junctions for space applications", 1-8 April 2006, Bjorkliden, Kiruna, Sweden.

List of publications

1. G.R. Berdiyorov, B.J. Baelus, M.V. Milosevic, and F.M. Peeters, *Stability and transition between vortex configurations in square mesoscopic samples with antidots*, Phys. Rev. B **68**, 174521 (2003) (19 pages).

2. G.R. Berdiyorov, B.J. Baelus, M.V. Milosevic, and F.M. Peeters, *The superconducting state in square mesoscopic samples with two and four antidots*, Physica C **404**, 56-60 (2004) (5 pages).

3. G.R. Berdiyorov, M.V. Milosevic, B.J. Baelus, and F.M. Peeters, *Superconducting vortex state in a mesoscopic disk containing a blind hole*, Phys. Rev. B **70**, 024508 (2004) (15 pages).

4. G.R. Berdiyorov, M.V. Milosevic, and F.M. Peeters, *The structure and manipulation of vortex states in a superconducting square with 2x2 blind holes*, Journal of Low Temperature Physics **139**, 229 (2005) (10 pages).

5. G.R. Berdiyorov, L.R.E. Cabral, F.M. Peeters, *Surface barrier for flux entry and exit in mesoscopic superconducting systems*, Journal of Mathematical Physics **46**, 095105 (2005) (17 pages).

6. M.V. Milosevic, G.R. Berdiyorov, and F.M. Peeters, *Mesoscopic field and current compensator based on a hybrid superconductor-ferromagnet structure*, Phys. Rev. Lett. **95**, 147004 (2005) (4 pages).

7. G.R. Berdiyorov, M.V. Milosevic, and F.M. Peeters, *Vortex lattice in effective type-I superconducting films with periodic arrays of submicron holes*, Physica C **437-438**, 25-28 (2006) (4 pages).

8. G.R. Berdiyorov, M.V. Milosevic, and F.M. Peeters, *Superconducting films with antidot arrays -Novel behavior of the critical current*, Europhys. Lett. **74** (3), 493-499 (2006) (7 pages).

9. G.R. Berdiyorov, M.V. Milosevic, and F.M. Peeters, *Novel Commensurability effects in superconducting films with antidot arrays*, Phys. Rev. Lett. **96**, 207001 (2006) (4 pages).

10. G. R. Berdiyorov, M. V. Milosevic, and F. M. Peeters, *Vortex configurations and critical parameters in superconducting thin films containing antidot arrays: Nonlinear Ginzburg-Landau theory*, Phys. Rev. B **74**, 174512 (2006) (14 pages).

11. M. V. Milosevic, G. R. Berdiyorov, and F. M. Peeters, *Stabilized vortex-antivortex molecules in a superconducting microdisk with a magnetic nanodot on top*, Phys. Rev. B **75**, 052502 (2007) (4 pages).

12. G. R. Berdiyorov, M. V. Milosevic, and F. M. Peeters, *New commensurate vortex structures in type-I and type-II superconducting films with antidot arrays*, to appear in Physica C (2007) (4 pages).

13. G. R. Berdiyorov, M. V. Milosevic, and F. M. Peeters, *Qualitative Modification of the Pinning Force due to Vortex-Cavity Adherence* (submitted to Phys. Rev. Lett.) (4 pages).